A versatile spin- and angle-resolved inverse photoemission setup : application to Rashba effect

Abraham Campos Contreras

université PARIS-SACLAY

A versatile spin- and angle-resolved inverse photoemission setup: application to Rashba effect

Un dispositif versatile de photoémission inverse résolue en spin et en angle : application à l'effet Rashba

Thèse de doctorat de l'université Paris-Saclay

École doctorale n°564 : physique en Île-de-France (PIF)
Spécialité de doctorat: Physique
Graduate School : Physique , Référent : Faculté des sciences d'Orsay

Thèse préparée dans la unité de recherche LPS (Université Paris-Saclay, CNRS), sous la direction de Antonio TEJEDA (DR)

Thèse soutenue à Paris-Saclay, le 5 Juillet 2022, par

Abraham Federico Campos Contreras

Composition du jury

Véronique Brouet Directrice de Recherche, Université Paris-Saclay	Présidente
Christine Richter Professeure, Université de Cergy-Pontoise	Rapportrice & examinatrice
Jean-Marc Themlin Professeur, Aix-Marseille Université	Rapporteur & examinateur
Daniel Malterre Professeur, Université de Lorraine	Examinateur
Francine Solal Professeure, Université de Rennes	Examinatrice
Jacques Peretti Directeur de Recherche, École Polytechnique	Examinateur
Antonio Tejeda Directeur de Recherche, Université Paris-Saclay	Directeur de thèse

THESE DE DOCTORAT
NNT : 2022UPASP067

université PARIS-SACLAY

ÉCOLE DOCTORALE
Physique en Île-de-France (PIF)

Titre: Un dispositif versatile de photoémission inverse résolue en spin et en angle : application à l'effet Rashba.

Mots clés: états inoccupés, photoémission inverse, polarisation de spin, pérovskite hybride, effet Rashba.

Résumé: La bande de conduction est la clef de voûte d'une multitude d'applications car elle définit les excitations électroniques permises. Cette bande reçoit les électrons excités dans les processus laser, les électrons photoexcités dans une cellule solaire, ou les électrons de conduction dans les transistors et les jonctions p-n. D'un point de vue fondamental, de nombreuses questions de base sur la bande de conduction doivent encore être résolues, en particulier dans les systèmes à corrélation électronique forte. Les bandes inoccupées sont souvent étudiées par des techniques indirectes, tandis que la technique la plus appropriée pour explorer les états électroniques vides avec une résolution en k est la photoémission inverse, une technique rare dans le monde, et encore moins avec une résolution en spin. Cette technique est particulièrement nécessaire pour l'étude des matériaux présentant un effet Rashba au-dessus du niveau de Fermi.

La photoémission inverse résolue en spin et en angle avait une limite majeure : les dispositifs existantes ne permettaient pas de découpler la direction du spin de l'angle d'incidence du faisceau d'électrons sondant l'échantillon. Par conséquent, la technique était extrêmement limitée pour décomposer la symétrie orbitale des états inoccupés polarisés en spin pour des vecteurs d'onde arbitraires. La première partie de ce manuscrit concerne les résultats du développement, de la caractérisation et de la validation d'une source d'électrons polarisés en spin pour la photoémission inverse, qui permet de découpler la direction du faisceau d'électrons de la direction de sa polarisation. Ce dispositif élimine ainsi les restrictions existantes sur la photoémission inverse résolue en spin et en angle.

La deuxième partie de la thèse est consacrée à la compréhension du mécanisme de photoexcitation et de relaxation subséquente de la pérovskite hybride $CH_3NH_3PbI_3$ et à la manière dont ce processus est affecté par l'effet Rashba-Dresselhaus dans la bande de conduction. Dans ce but, des expériences de photoémission inverse au Laboratoire de Physique des Solides et de diffraction des rayons X résolue en temps au synchrotron SOLEIL ont été réalisées. L'ensemble des mesures fournit des informations sur le caractère centrosymétrique de la structure pendant la relaxation, la réorganisation des cations méthylammonium, et l'effet Rashba-Dresselhaus dans la bande de conduction.

Title: A versatile spin- and angle-resolved inverse photoemission setup: application to Rashba effect.

Keywords: unoccupied states, inverse photoemission, spin polarization, hybrid perovskite, Rashba effect.

Abstract: The conduction band is the cornerstone of a multitude of applications since it defines the permitted electronic excitations. This band receives excited electrons in laser processes, photoexcited electrons in a solar cell, or conduction electrons in transistors and p-n junctions. From a fundamental point of view, many basic questions about the conduction band still need to be answered, especially in systems with strong electronic correlation. Unoccupied bands are often studied by indirect techniques, while the most suitable technique to explore electronic empty-states with k-resolution is inverse photoemission, a rare technique in the world, and even less with spin resolution. This technique is particularly needed for the study of materials with Rashba effect above the Fermi level.

Spin- and angle-resolved inverse photoemission had a major limitation: existing setups did not allow decoupling the spin direction from the incidence angle of the electron beam probing the sample. As a result, the technique had extreme limitations to decompose the orbital symmetry of spin-polarized unoccupied states at any arbitrary wavevector. The first part of this manuscript concerns the results of the development, characterization, and validation of a spin-polarized electron source for inverse photoemission, which allows decoupling the direction of the electron beam from the direction of its polarization. This device eliminates thus the restrictions on existing spin- and angle-resolved inverse photoemission.

The second part of the thesis is dedicated to understanding the mechanism of photoexcitation and subsequent relaxation of the hybrid perovskite $CH_3NH_3PbI_3$ and how this process is affected by the Rashba-Dresselhaus effect in the conduction band. For this purpose, inverse photoemission experiments at the *Laboratoire de Physique des Solides* and time-resolved X-ray diffraction at the SOLEIL synchrotron were performed. All the measurements provide information on the centrosymmetric character of the structure during the relaxation, the reorganization of the methylammonium cations, and the Rashba-Dresselhaus effect in the conduction band.

Contents

Acknowledgments

I am very grateful to my supervisor Antonio Tejeda who accepted me as his Ph.D. student. I thank him for his trust on the commissioning for developing an inverse photoemission setup with total spin resolution. It was only with the passing of time that I realized the impact of this ambitious project. His mentorship has allowed me to grow scientifically and his collaboration has been more than pleasant during these years.

I acknowledge the support of the permanent members of the LUTECE group: Vincent Jacques, David Le Bolloc'h, Luc Ortega, Olivier Plantevin, and Sylvain Ravy for their uninterested support during my journey within the group. I really appreciate your critical observations that allowed me to analyze the subjects from different perspectives. I always found a very friendly environment with the non-permanent LUTECE members: Antoine Gallo-Frantz, Antoine Loncle, Darine Ghoneim, Jairo Obando and Lipin Chen. Interesting exchange with Antoine Gallo-Frantz about the XRD results on MAPI perovskite was very beneficial for the discussion in Chapter 4. Jairo Obando was always available for giving me a hand while working on the UHV chambers and tuning the optical setup whenever it was necessary. I acknowledge the investment of Lipin Chen in our common projects by providing first-principles calculations. The scientific discussions have been very rewarding and I am eager to continue our collaboration. I also acknowledge Min-I Lee (former group member) for allowing me to continue with her ongoing project on the structural dynamics in MAPI perovskite.

I am very in debt to Philippe Duret who assisted me during the initial stage of my Ph.D. and allowed me to learn from him about the subtleties in UHV technology. The know-how of Stanislas Rohart allowed me to test the unique capability of longitudinal tuning of the polarization vector by the supply of well-characterized Co thin-films.

The yearly meetings with my *comité de suivi*, conformed by Véronique Brouet and André Thiaville, were very important to assess my performance thanks to their experience and expertise.

Thomas Duden is a team player in the development of the spin-polarized electron source, the core of the spin-resolved inverse photoemission setup at the LPS. From the conception to the fine-tuning of the electron-optics, his presence in the project has been fundamental. I do really appreciate his problem-solving strategies and accurate advice.

Special thanks to the Mechanics group of the LPS conformed by Marc Bottineau, Stéphane Cabaret, Christophe Courtot, Vira Davouloury and Ismaël Nimaga. Interesting results are now being harvested thanks to your commitment in the fabrication phase of the spin-polarized electron source. The work of the Instrumentation group of the LPS, conformed by Vincent Klein, Jérémie Sanchez, Sambath Saranga and Yannic Simon, was also fundamental to optimize my experimental routine in the SPIPES setup. Thank you for being very kind and helpful without hesitation.

I acknowledge Claire Lauhlé (Synchrotron SOLEIL) for her commitment to the CRISTAL beamline and the time-resolved XRD experiments. The results we have gathered allowed me to discuss very interesting physics in Chapter 4 of my manuscript concerning MAPI perovskite.

Often, successful experiments are correlated to exceptional samples. I appreciate the skills of Emmanuelle Deleporte and Gaelle Trippé-Allard, who have continuously supplied us with the perovskite crystals to accomplish our investigations.

Un dispositif versatile de photoémission inverse résolue en spin et en angle : application à l'effet Rashba (version de diffusion)

On s'intéresse dernièrement à l'exploration des systèmes qui présentent des états de dédoublement de spin au-dessus du niveau de Fermi en raison de leurs applications potentielles à la spintronique. Le spin des électrons de conduction est censé agir comme un support d'information avec une consommation d'énergie moindre par rapport à l'électronique conventionnelle. Les transistors de spin peuvent être fabriqués à partir de matériaux dans l'élément actif du dispositif qui présentent interaction spin-orbite et effet Rashba. Grâce à cela, avec des faibles tensions de déclenchement il est posible de: (i) filtrer le courant de spin et (ii) augmenter/diminuer la séparation de bande polarisée en spin. Les matériaux permetant cela sont très variés (Fig. 1). Par exemple, (i) les interfaces métal/semiconducteur, dans lesquelles on prédit des états de surface divisés en spin-orbite avec une texture de spin, (ii) les interfaces entre un metal et une couche moléculaire, dans lesquelles, selon le couplage de la molécule à la surface, les états moléculaires peuvent ou non être ajustés au-dessus du niveau de Fermi, (iii) les isolants topologiques, avec ses états inoccupés non dégénérés et topologiquement protégés, et (iv) les semi-conducteurs bidimensionnels, avec un dédoublement Rashba géant attendu.

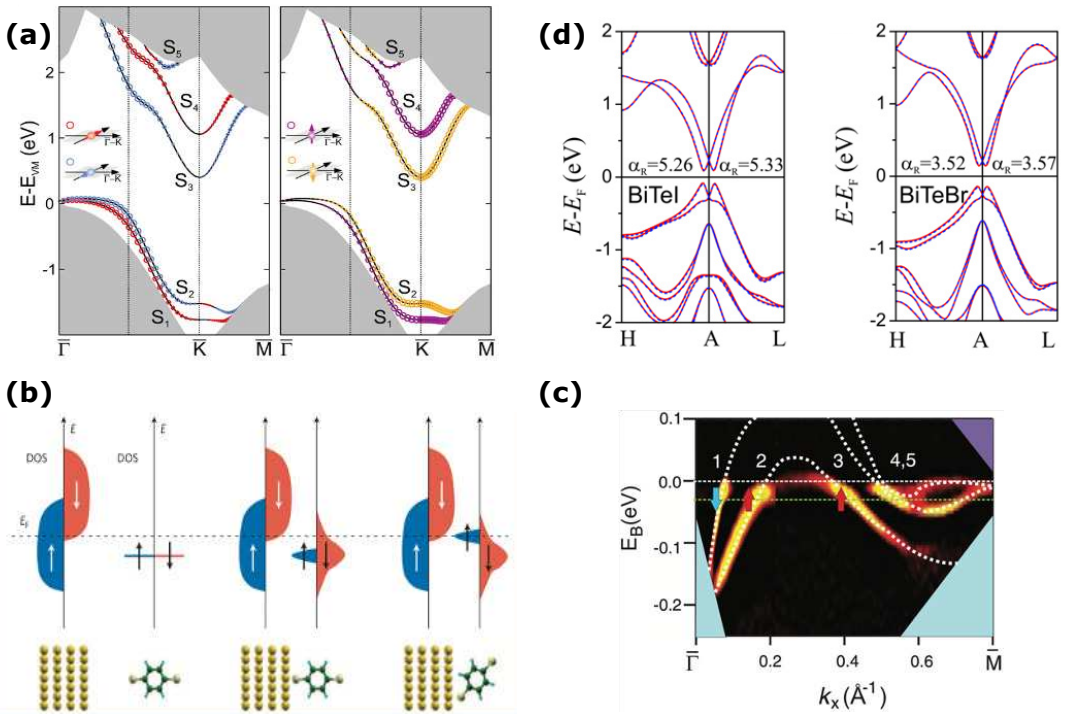

Figure 1: Exemples de systèmes de matière condensée avec des états inoccupés non dégénérés en spin. (a) Interface Tl/Si avec texture de spin le long de la $\overline{\Gamma M}$, adapté de [1]. (b) Schéma d'interface entre métal ferromagnétique et couche moléculaire où la durée de vie infinie des états moléculaires est réduite en fonction du couplage à la surface et change selon l'hybridation avec celle-ci, adapté de [2]. (c) Isolant topologique $Bi_{1-x}Sb_x$ avec prédictions d'une bande de conduction non-dégénéré en spin, adapté de [3]. (d) Tellurohalogénures de bismuth avec un effet Rashba géant prédit dans la bande de conduction, adapté de [4].

La manière la plus directe d'accéder à ces états inoccupés avec une résolution de spin est d'utiliser la spectroscopie de photoémission inverse en incorporant une source d'électrons polarisés en spin. La photoémission inverse (IPES) peut être décrite comme le processus d'inversion temporelle de la photoémission (Fig. 2), c'est-à-dire une technique ou des électrons sondent le matériau et font émettre des photons. La technique est basée sur la conservation du vecteur d'onde parallèle à la surface à l'extérieur ($K_{\parallel}$) et à l'intérieur ($k_{\parallel}$) du solide. La dispersion de bande du solide est donc déterminée par l'utilisation des conditions cinématiques de conservation de l'énergie et du vecteur d'onde et, dans l'expérience, l'angle d'incidence du faisceau d'électrons θ et son énergie cinétique E_{kin} doivent être définis sans ambiguïté. La conservation de la quantité de mouvement dans IPES est donc,

$$\hbar k_{\parallel} = \hbar K_{\parallel} = \sqrt{2m(E_f + \hbar\omega - \Phi_s)} sin\theta = \sqrt{2m(E_{kin})} sin\theta, \quad (1)$$

où E_f est l'énergie de l'état final, $\hbar\omega$ l'énergie du photon et Φ_s le travail de sortie de l'échantillon.

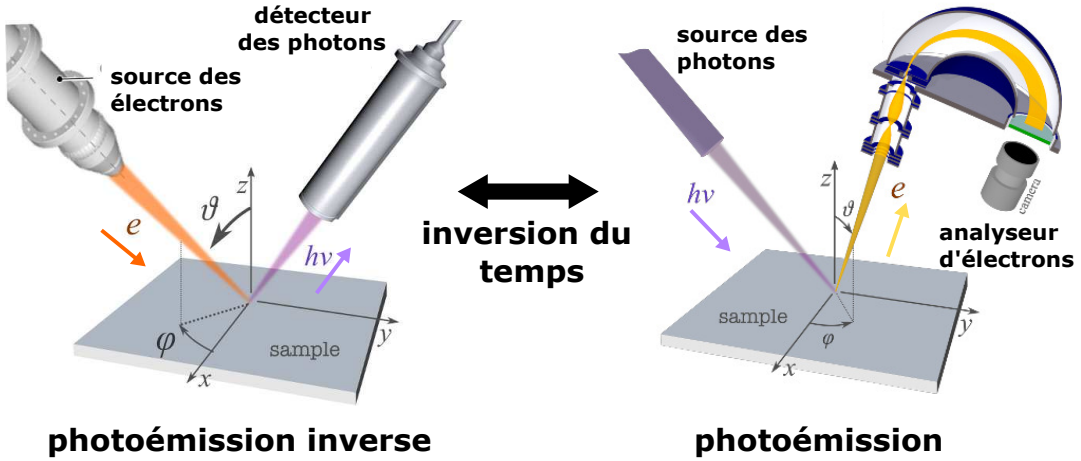

Figure 2: IPES est le moyen le plus direct d'accéder aux états inoccupés des solides et il est complémentaire de la photoémission. Les modèles inversés à une ou trois étapes de la théorie de la photoémission sont valables pour décrire l'IPES en raison de la symétrie par inversion temporelle des processus.

Une partie importante de ce travail de thèse a été centrée sur le développement d'une source d'électrons polarisés en spin avec un contrôle total de l'orientation du spin. La clé repose sur une optique électronique pour produire un faisceau d'électrons parallèle à la surface de la cible, tout en préservant la résolution en momentum nécessaire à la photoémission inverse résolue en angle. Avant ce développement instrumental, il y avait une limitation majeure pour l'étude des systèmes avec des textures de spin non triviales en raison des contraintes de la polarisation du faisceau électronique. Dans les dispositifs habituels qui incorporent des déflecteurs électrostatiques, le vecteur de polarisation de spin et le vecteur d'onde de l'électron sont couplés par l'angle d'incidence du faisceau d'électrons. Cela résulte en une double limitation:

- impossibilité de mesurer la composant de spin hors plan près de Γ (incidence normal de faisceau),
- la necessité d'analyser précisement les intensités des spectres pour remonter à la composant hors plan et dans le plan a partir d'une mesure qui couple les deux.

La source décrite dans cette thèse, grâce au contrôle totale de la direction du spin, résout ces limitations qui existaient auparavant.

Dans une première partie de cette thèse, nous démontrons le fonctionnement du dispositif en mesurant les états inoccupés de : Cu(001), Au(111) avec dédoublement de Rashba et de couches minces de Co. Les paramètres les plus importants du dispositif experimental ont été déterminés : résolution en énergie, résolution en momentum, polarisation en spin du faisceau d'électrons et son ajustement dans une direction arbitraire.

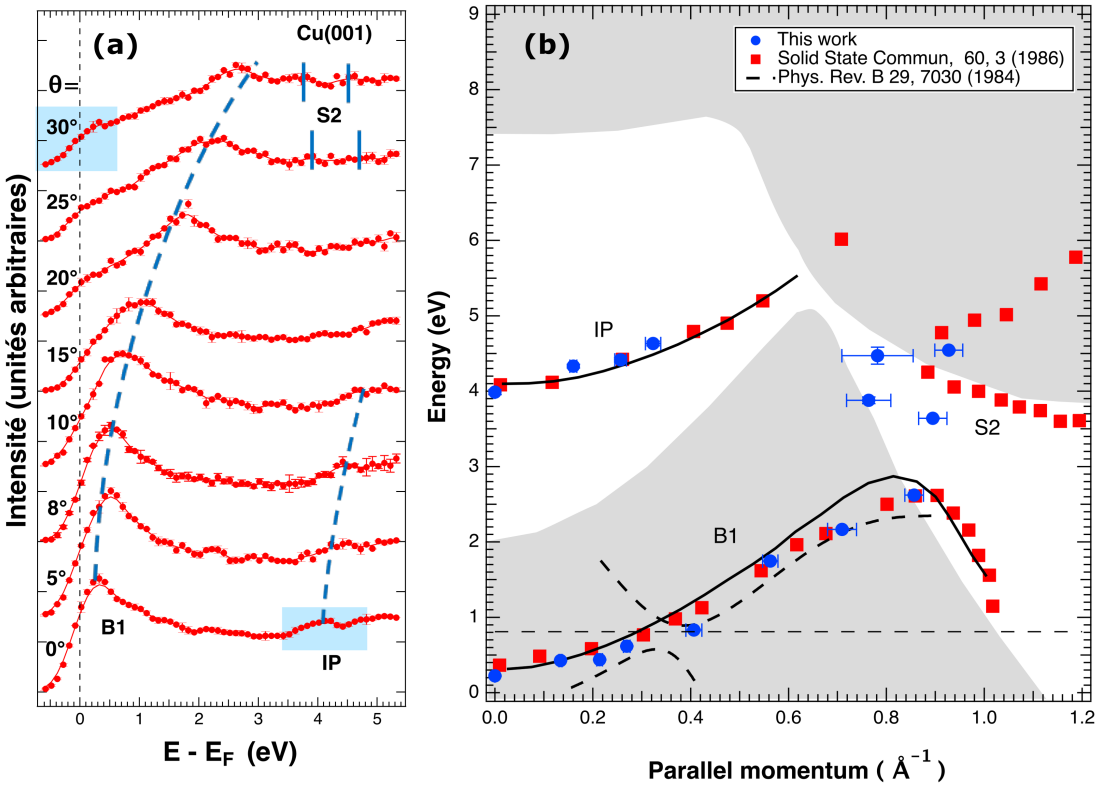

Figure 3: (a) Spectres IPES integrés au spin de Cu(001) sur la direction ΓX à température ambiante et (b) sa dispersion de bandes respective.

À partir de mesures sur Cu(001), nous avons déterminé une résolution énergétique de 200 meV en utilisant des méthodes différentes: de la largeur d'un état potentiel image, de la modelisation du niveau de Fermi et d'un estimation de la largeure du niveau. Par ailleurs, ces mesures reproduisent celles de la littérature et démontrent le bon fonctionnement du dispositif (Fig. 3).

La résolution en spin de la configuration SPIPES a été ensuite démontrée par des mesures de l'état de surface (SS) polarisé en spin dans le gap L de Au(111). La polarisation en spin de l'état de surface est due à l'effet Rashba-Bychkov induit par l'absence de symétrie d'inversion à la surface. La dispersion de l'Au(111) est montrée sur la Fig. 4(a), obtenue à partir des spectres de photoémission inverse polarisé en spin (SPIPES). Nous observons une différence entre les spectres des deux spins là où ils sont censés apparaître : lorsque l'état de surface est au-dessus E_F et loin des bandes de volume. Ensuite, l'ajustement de la polarisation a été démontré sur l'état de surface Shockley. A titre d'example, la Fig. 4(b) de ce résumé montre l'évolution du spectre correspondant à l'état de surface lorsque la direction du spin incident est variée par rapport à celle de l'état.

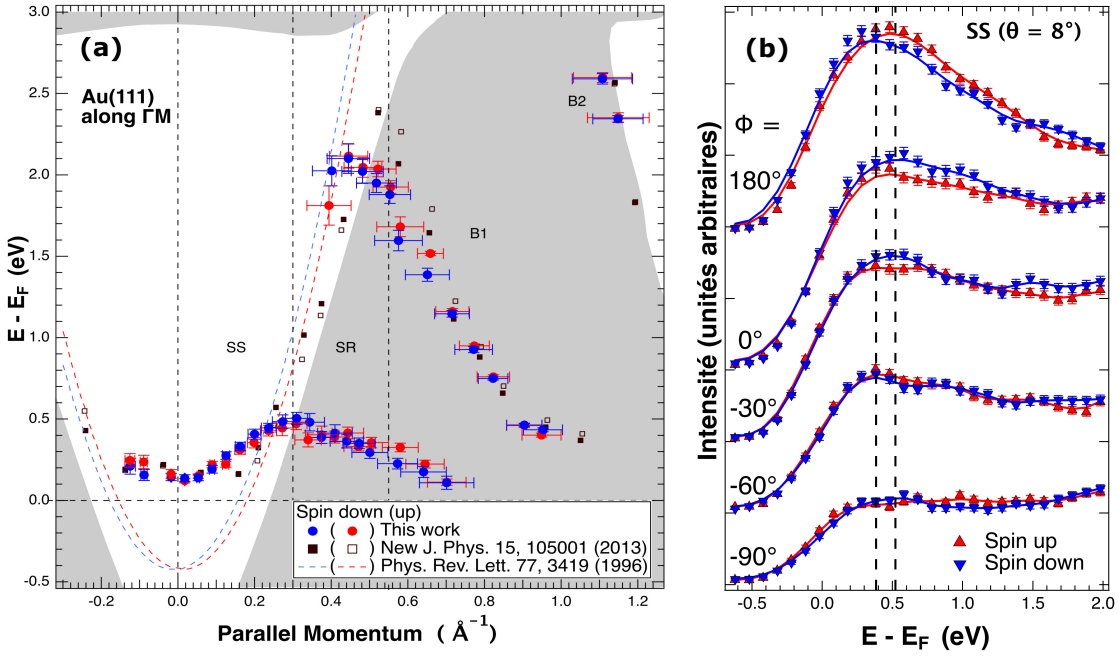

Figure 4: (a) Relation de dispersion de Au(111) sur la direction ΓM. L'état de surface Shockley s'écarte de la dispersion parabolique attendue en raison d'une forte hybridation avec les états de volume projetés en surface (régions grises). (b) Spectres SPIPES de l'état de surface de Shockley en fonction de l'angle transversal de la polarisation du faisceau d'électrons. Comme prévu, il y a une inversion des énergies de liaison entre les composantes de spin up et de spin down lorsqu'il y a une rotation de 180° de la polarisation du faisceau.

Dans une seconde partie, nous avons utilisé le nouveau dispositif pour étudier une controverse à propos des propriétés de conduction de la pérovskite métallorganique $CH_3NH_3PbI_3$ (connue comme MAPI). En effet, l'existence et l'origine d'un dédoublement Rashba sur la bande de conduction dans sa phase tétragonale est controversée. L'absence ou l'existence de ce dédoublement est liée à la structure atomique et donc au groupe d'espace du système. Trois scénarios ont été proposés dans la littérature pour expliquer l'effet Rashba dans la bande de conduction : (i) une structure centrosymétrique (I4/mcm) avec des réseaux apolaires des cations MA (CH_3NH_3) (et donc pas de dédoublement Rashba), (ii) une structure non centrosymétrique (I4/cm) avec une disposition polaire de l'ensemble des cations MA et une dédoublement Rashba et, (iii) une structure centrosymétrique avec une dédoublement Rashba dû à la dynamique des cations MA. Pour aborder ce problème expérimentalement, nous avons utilisé des techniques complementaires : XRD résolue en temps (TR-XRD), réalisée à la ligne CRISTAL du synchrotron SOLEIL, et IPES résolue en spin, réalisée au Laboratoire de Physique des Solides. Par TR-XRD, nous avons observé que l'excitation optique vers la bande de conduction avec des photons de 400 nm favorise un changement structural correspondant à une réorientation des cations MA entre configurations apolaires vers polaire. Le temps de photoexcitation caractéristique que nous avons trouvé est en accord avec le temps de relaxation moléculaire observé par diffusion de neutrons. Enfin, nos résultats SPIPES montrent un dédoublement Rashba dans la bande de conduction dont l'amplitude est en accord avec des calculs DFT.

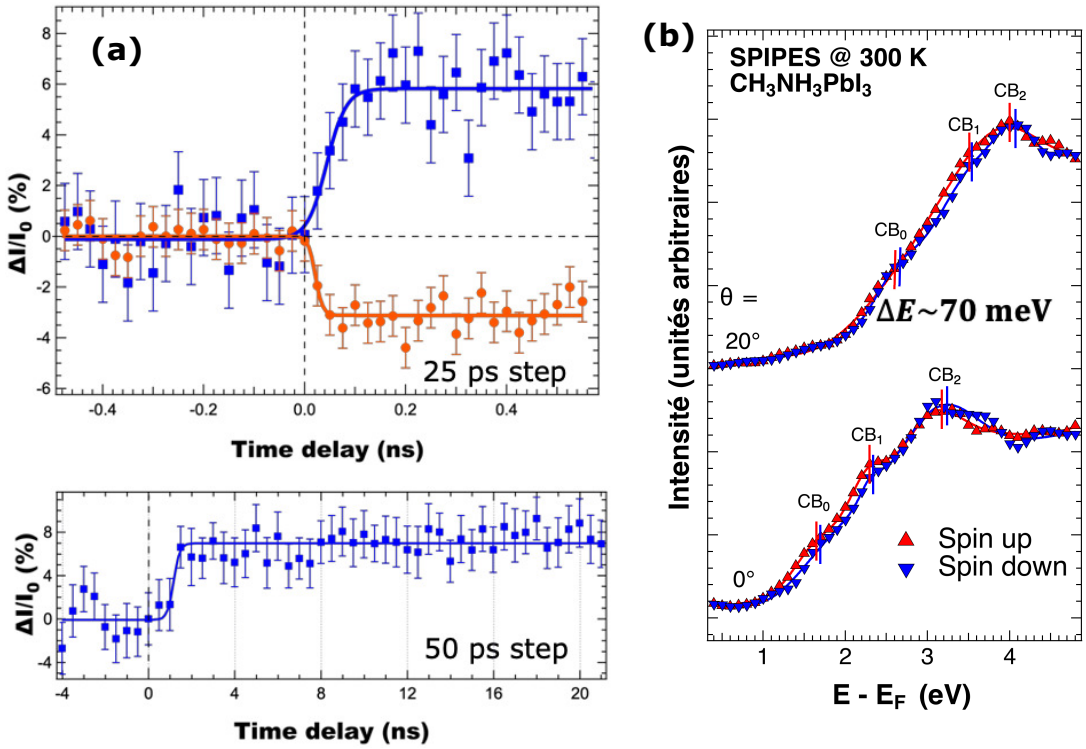

Figure 5: (a) Dynamique de diffraction de MAPI dans la phase tétragonal en fonction du délai entre l'excitation laser et la sonde RX. Intensité diffractée des réflexions de Bragg (312) et $(2\overline{2}\overline{2})$ avec des intervals de 25 ps (haut) et 50 ps (bas). La fluence laser est de 0.5 mJ·cm^{-2}. (b) Spectres SPIPES mesuré avec notre dispositif de la pérovskite MAPI le long de $\overline{\Gamma M}$.

L'ensemble de nos résultats expérimentaux comparés aux calculs de premiers principes, nous permettent de suggérer que la phase tétragonal de MAPI est centrosymétrique dans sa condition statique et possiblement un effet Rashba dynamique.

En résumé,nous avons demontré sur tout un ensemble de systemes les performances d'un nouveau dispositif unique de photoémission inverse résolue en spin. Ce dispositif SPIPES avec un contrôle complet du vecteur de polarisation du faisceau électronique qui sonde le materiél ouvre de nouvelles perspectives dans l'étude de la bande de conduction avec résolution en spin.

Acronym	Name
AES	*Auger Electron Spectroscopy*
ARPES	*Angle-Resolved Photoemission Spectroscopy*
BZ	*Brillouin Zone*
DOS	*Density Of States*
dRD	*Dynamical Rashba-Dresselhaus*
EDC	*Energy Distribution Curve*
FM	*Ferromagnetic*
FWHM	*Full-Width at Half-Maximum*
GM	*Geiger-Müller*
IP	*Image Potential*
IPE(S)	*Inverse Photoemission (Spectroscopy)*
LEED	*Low-Energy Electron Diffraction*
LEIPES	*Low-Energy Inverse Photoemission Spectroscopy*
MBE	*Molecular Beam Epitaxy*
MOKE	*Magneto-Optical Kerr Effect*
ML	*Monolayer*
N(P)EA	*Negative (Positive) Electron Affinity*
NEG	*Non-Evaporable Getter*
NFE	*Nearly-Free Electron*
NIR	*Near Infrared*
PES	*Photoemission Spectroscopy*
QE	*Quantum Efficiency*
RT	*Room Temperature*
SOC	*Spin-Orbit Coupling*
SPIPES	*Spin-Polarized Inverse Photoemission*
SR	*Surface Resonance*
SS	*Surface State*
TMD(T)C	*Transition-Metal Di(Tri)Chalcogenide*
UHV	*Ultra-High Vacuum*
vdW	*van der Waals*
VUV	*Vacuum Ultraviolet*
XRD	*X-Ray Diffraction*
2PPE	*Two-Photon Photoemission*
ND	*N-Dimensional,* $N \in \{1, 2, 3\}$.

1 - INTRODUCTION

1.1 . MOTIVATION AND SCOPE

Surface science studies the physical properties of the finite-thickness selvedge region. The discovery of graphene by K. Novoselov in 2004 [6] induced to revisit the impossibility of long-range order in perfect 2D crystals in the Mermin-Wagner theorem [7]. Yet, the carbon honeycomb array does not possess an electronic bandgap despite its unusual electronic, optical, and mechanical properties. The challenge of incorporating the high-carrier mobility of graphene in present-day electronic devices has opened the venue for the search of alternative two-dimensional (2D) materials with tunable bandgap properties and spin-orbit coupling (SOC). Topological insulators, 2D ferromagnets, and organic photovoltaics are an essential part of contemporary condensed matter physics accentuated since the advent of single-layer exfoliated graphene.

Tunable bandgap and the spin character of bands are to be explored. The first major step for using the electron spin as an information carrier is by revealing the spin character of the electronic states. Once the spin of electronic bands is well known, it is possible to further manipulate spin textures in spintronic applications with low energy consumption and without the need of applied voltages. Rashba-type materials [8, 4], topological insulators [9, 10], molecular interfaces [2, 11], embedded transition-metals in dichalcogenides [12, 13, 14], single-layered trichalcogenides [15, 16, 17] and even three-dimensional organic-inorganic compounds [18, 19, 20] are relevant examples where a spin resolution is fundamental while probing their electronic states.

There is therefore a major interest in studying the electronic states of all those systems with spin resolution. While spin resolution in photoemission is relatively common, spin-resolved inverse photoemission is even more rare due to the scarcity of inverse photoemission setups. Here, we have developed an electron source for inverse photoemission spectroscopy that incorporates spin resolution. Our setup grants access to the unoccupied band dispersion on surfaces and interfaces with k-resolution and total spin-resolution.

1.2 . OUTLINE OF THE THESIS

This manuscript consists of two parts. The first one corresponds to Chapter 2 and Chapter 3 and is related to the development of a spin-polarized electron source with unique capabilities for tuning the electron beam polarization. The source was implemented at the *Laboratoire de Physique des Solides* to perform spin- and k-resolved inverse photoemission spectroscopy to gain insight into unoccupied spin textures in non-degenerated states in surfaces and interfaces.

In Chapter 2, the generalities on the inverse photoemission spectroscopy (IPES) are presented. The development of the technique and the governing equations of the process are also introduced. The elementary components of the IPES system i.e., the generation and the detection of polarized electrons are also discussed, together with a description of the methods to enhance the energy resolution. In Chapter 3, the spin-resolved inverse photoemission setup was fully characterized by measuring on prototypical low-index metal surfaces. The energy and momentum resolution were obtained from bulk and surface features in Cu(001) whereas the spin-resolution was tested on the Shockley surface state of Au(111). Chapter 3 starts with the aspects related to the electron optical elements of the electron source that permit the

rotation of the spin polarization vector. Additionally, the Shockley surface state of the L-gap in the Au(111) allows for demonstrating the tuning of the polarization vector into transverse and longitudinal rotations with respect to the propagation vector. Complementary results on out-of-plane magnetized Co thin-films reinforce the unique characteristic of longitudinal tuning. The new implementations permit tuning the polarization vector to any desired orientation in space by electromagnetic interactions with service energies between 5 to 200 eV.

In a second part, we performed combined studies of the atomic and electronic structure of the photovoltaic halide perovskite $CH_3NH_3PbI_3$ to shed light on the complex dilemma of the optoelectronic function of the methylammonium $CH_3NH_3^+$ ions and its interplay within the inorganic PbI sublattice. In Chapter 4, we present picosecond-resolved XRD studies on monocrystalline $CH_3NH_3PbI_3$ to unveil the structure and dynamics of the methylammonium cations while mimicking visible-light absorption. The structural studies, conducted in synchrotron facilities, revealed the transient structural state of the tetragonal phase by single-spot Bragg dynamics. The results on the lattice parameter and diffracted intensity strongly indicate an apolar disposition of the methylammonium cations in the equilibrium state while the cations reorganize in a polar distribution in the photoexcited state. More fundamental insight into the electronic properties of $CH_3NH_3PbI_3$ was also revealed by the spin-resolved conduction band of the hybrid perovskite. Since our SPIPES measurements on the conduction band of $CH_3NH_3PbI_3$ show spin-splitting effects, the hypothesis of an apolar-to-polar cation reorganization is further supported. An energy splitting of 70 meV, in agreement with first-principle calculations, indicates a random orientation of the organic cations in the tetragonal static phase and probably related to a dynamical Rashba-Dresselhaus effect. The manuscript ends with the general conclusions and future experimental work in Chapter 5. We present the perspectives for enhancing the energy resolution of the SPIPES setup by controlling the GaAs photocathode temperature. Finally, perspectives on the unoccupied spin-split states of 2D systems, $CrSiTe_3$ and $CrGeTe_3$ ferromagnetic semiconductors and the low-dimensional $CH_3NH_3PbI_3$ perovskite, are presented.

1.3 . SPIN-ORBIT INTERACTION AND RASHBA EFFECT

Spin-orbit coupling (SOC) is a relativistic effect in the form of an effective magnetic field in the reference frame of a moving electron. SOC leads to fine structure splitting on the spectral lines of atoms and also degeneracy on the energy levels of solids. The one-electron Hamiltonian in a crystal is

$$H_e = \frac{\hbar^2}{2m^*}\mathbf{k}^2 + V(\mathbf{r}), \tag{1.1}$$

where $\hbar$ is the reduced Planck constant, m^* is the effective mass of the electron, $\mathbf{k}$ is the wavevector and V is the lattice potential. With the spin-orbit correction H_{SOC}, the Hamiltonian is

$$H = H_e + H_{SOC} = H_e + \frac{\hbar^2}{4m^{*2}c^2}(\nabla V \times \mathbf{k}) \cdot \boldsymbol{\sigma}, \tag{1.2}$$

where c is the velocity of light in free space and $\boldsymbol{\sigma}$ is the Pauli spin operator whose components are the Pauli matrices:

$$\sigma_j = \begin{pmatrix} \delta_{j,3} & \delta_{j,1} - i\delta_{j,2} \\ \delta_{j,1} + i\delta_{j,2} & -\delta_{j,3} \end{pmatrix}, j \in \{1, 2, 3\}. \tag{1.3}$$

From Eq. 1.2, it follows that the one-electron Schrödinger equation accepts Bloch states $\Psi^s_{n,\mathbf{k}}(\mathbf{r})$, as solutions with corresponding eigenvalues $E^s_n(\mathbf{k})$, where $s \in \{\uparrow, \downarrow\}$ represents the spin degree of freedom and n is the principal quantum number. Moreover, the Pauli matrices, $\boldsymbol{\sigma} = 2\hbar^{-1}\mathbf{S}$, permit to rewrite the SOC interaction rather as a perturbation [21] in terms of the orbital and the spin angular momentum operators:

$$H_{SOC} = \lambda \mathbf{L} \cdot \mathbf{S}, \tag{1.4}$$

making explicit a twofold (spin) degeneracy of the energy levels on lattices with inversion symmetry. The SOC-induced spin degeneracy is removed when $V(\mathbf{r})$ does not possess a center of inversion and $E(\mathbf{k}) = E(-\mathbf{k})$, so the periodic part of the Bloch function does not satisfy the condition $u_{-\mathbf{k}}(\mathbf{r}) = u_{\mathbf{k}}(-\mathbf{r})$ [22].

At the surfaces of crystals there is no inversion symmetry since there is an asymmetric charge distribution so spin states are never degenerated. However, the magnitude of the effect depends on the atomic potential and it is notably larger in heavy-element compounds. Therefore, when SOC is high enough, an asymmetric distribution in the normal direction to the surface can be observed and described by the Rashba-Bychkov model.

In the bulk, a representative example of SOC splitting is found in the III-V semiconductor GaAs where the topmost valence band (VB) splits into heavy-hole and light-hole around the Γ-point due to the lack of inversion center[1]. The inversion asymmetry in GaAs arises because the compound has a zinc-blend structure consisting of two interpenetrating fcc cubic sublattices and each sublattice possess a unique atomic species, so there is no inversion symmetry in the whole system. On the contrary, if the two basis on the zinc-blend structure were identical, a diamond structure with inversion symmetry would result and the SOC splitting would not emerge as it is the case for diamond or silicon.

Let us explain more precisely the spin degeneracy removal due to the Rashba effect. Let us start with a crystal with inversion symmetry. These lattice sites are unaffected by the transformation $r \to -r$ so

$$E(\mathbf{k}, \uparrow) = E(-\mathbf{k}, \uparrow) \tag{1.5}$$

and time reversal symmetry in a crystal leads to [23, 24]

$$E(\mathbf{k}, \uparrow) = E(-\mathbf{k}, \downarrow). \tag{1.6}$$

That is to say, after the time reversal transformation $t \to -t$, the energy of a spin-up ($\uparrow$) electron with a momentum $\mathbf{k}$ is equal to the energy of an electron with an opposite spin and momentum $-\mathbf{k}$. From Eq. 1.5 and Eq. 1.6 it is evident that if a system has both time and inversion symmetry then $E(\mathbf{k}, \uparrow) = E(\mathbf{k}, \downarrow)$ i.e., the electronic state is spin degenerated. On the other hand, when one of the above symmetry conditions is not satisfied, the degeneracy on the energy state is lifted.

[1] In this case, the spin-orbit interaction leads to an energy splitting of valence bands with different total angular momentum J, which is different from the spin splitting of bands in surfaces with SOC.

An asymmetric potential at the surface of a crystal is a condition for the appearing of surface states. Therefore, the absence of an inversion center at the crystal surface permits surface state levels with the same parallel wavevector $\mathbf{k}_{\parallel}$, and opposite spins to have different energies [25]. The surface state dispersion can sometimes be described in the nearly free electron (NFE) framework as a 2D electron gas. This model assumes a free movement of the electrons on the plane of the surface (x, y) whereas the presence of a potential, $V = V(z)$, forbids the access to the remaining z direction. The SOC is basically quantified by $\nabla V = \frac{dV}{dz}\hat{\mathbf{e}}_z$, being $\hat{\mathbf{e}}_z$ a unitary vector along z, and controlled by the atomic potential gradient affecting the surface state. More explicitly, the SOC Hamiltonian in the NFE model

$$H_{SOC} = \hbar\alpha_R(\hat{\mathbf{e}}_z \times \mathbf{k}) \cdot \boldsymbol{\sigma}, \tag{1.7}$$

lifts the spin degeneracy at $\mathbf{k} \neq \mathbf{0}$ and determines the spin splitting nearby $\mathbf{k} = \mathbf{0}$ [26, 27] as:

$$E(\mathbf{k}_{\parallel}, \uparrow) = E_0 + \frac{\hbar^2}{2m*}\mathbf{k}_{\parallel}^2 + \alpha_R|\mathbf{k}_{\parallel}|, \tag{1.8}$$

$$E(\mathbf{k}_{\parallel}, \downarrow) = E_0 + \frac{\hbar^2}{2m*}\mathbf{k}_{\parallel}^2 - \alpha_R|\mathbf{k}_{\parallel}|. \tag{1.9}$$

The coefficient α_R, usually known as the Rashba term, is proportional to the atomic SOC α,

$$\alpha_R = \frac{\alpha}{m*}\frac{dV}{dz} = \frac{\alpha\sigma}{m*}. \tag{1.10}$$

The states from the Rashba model are found in two parabolic bands with opposite polarization as shown in Fig. 1.1(a). The polarization of each state is always tangent to the Fermi surface that consists of two concentric circles (1.1(b)). Thus, the energy dispersion can be written in terms of the momentum splitting $\Delta k = 2k_0$ [28]:

$$E(\mathbf{k}_{\parallel}, \uparrow) = E_0 + \frac{\hbar^2}{2m*}\left(\mathbf{k}_{\parallel} + \frac{\Delta k}{2}\right)^2, \tag{1.11}$$

$$E(\mathbf{k}_{\parallel}, \downarrow) = E_0 + \frac{\hbar^2}{2m*}\left(\mathbf{k}_{\parallel} - \frac{\Delta k}{2}\right)^2. \tag{1.12}$$

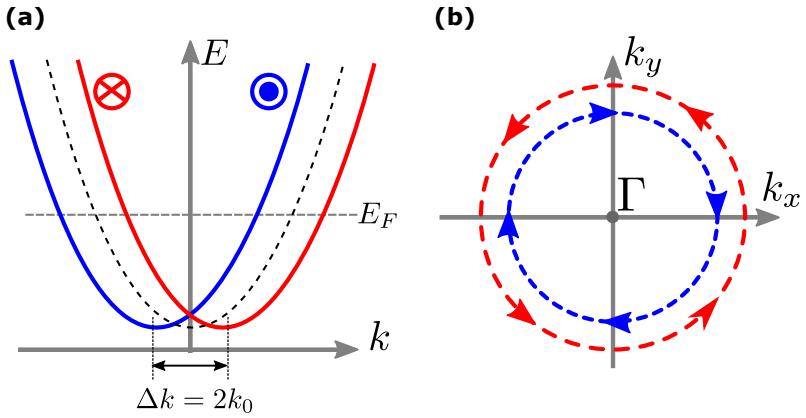

Figure 1.1: (a) Schematic representation of energy bands in free-electron dispersion with Rashba splitting Δk. The degenerated band is marked by a dashed black parabola. (b) Corresponding Fermi surface formed by two concentric circles with indicated (arrows) spin helicity.

2 - SPIN- & ANGLE-RESOLVED INVERSE PHOTOEMISSION

This Chapter serves as an introduction to generalities on the inverse photoemission technique. The concepts related to spin-splitting effects on the energy bands, the generation of polarized electrons, and the techniques for detecting VUV radiation, are introduced. The parameters characterizing our spin-polarized electron source, such as the electron beam polarization and the current density, are presented as a necessary preliminary commissioning of our spin- and angle resolved inverse photoemission setup.

2.1 . INVERSE PHOTOEMISSION

The pioneering work of J. Pendry [29] in 1980 highlighted that inverse photoemission spectroscopy (IPES) is the most direct way to investigate the unoccupied band structure in solids and surfaces. IPES is the time-reversal process of photoemission, so it determines the band structure by detecting the photons after injecting well-characterized electrons into the empty states of the solid. More specifically, in IPES, when electrons emitted from a source at a given energy E_i relax to lower-lying unoccupied levels E_f, the empty-band dispersion $E(\mathbf{k}_{\parallel})$ can be reconstructed by integrating the emitted photons during the relaxation from E_i to E_f ($E_i - E_f = \hbar\omega$). The IPE process is summarized in Fig. 2.1. The spectral signatures of these *photon-emission* events may result from bulk-projected, surface and even absorbate-induced states. The mapping of $E(\mathbf{k}_{\parallel})$ is only possible if the kinetic energy of the electron beam E_{kin}, and its impinging angle with respect to the surface θ, are both unambiguously defined. The surface sensitivity of IPES is achieved because at the low-energy regime ($E_{kin} < 30$ eV) the electrons injected at the surface have a penetration depth into the material of about 10 Å [30].

As previously indicated, IPE can be treated as the time-reversal process of photoemission [29, 31]. This assumption permits to exploit the formalism behind the photoelectric effect for the sake of interpreting IPES data without the need of a separated theory. Thus, the three-step model, approximation for understanding band structures in PES, can be *inverted* and summarized as in the following [31]:

- Coupling of the incoming electron into an unoccupied state of the system.
- Competition between radiative and non-radiative decay. Non-radiative events correspond mainly to inelastic electron-electron scattering.
- Radiative decay through a direct (vertical and $\mathbf{k}$-conserving) transition.

The three-step process can be reduced to a single and coherent quantum mechanical event as described by J. Pendry [32]: (i) wavefunction matching at the surface between the external plane waves and the internal electron waves, (ii) strong probability of non-radiative inelastic electron decay (wavefunction attenuation) due to electron-electron interactions with the solid, and (iii) radiative transition. The inequivalence between the initial state in PE and the final state in IPE (with an additional electron) can be neglected in systems with non-localized states, e.g. metals, but not for systems with strong electronic correlation, although many information can also be obtained there despite this fact. In strongly-correlated systems, some caution must

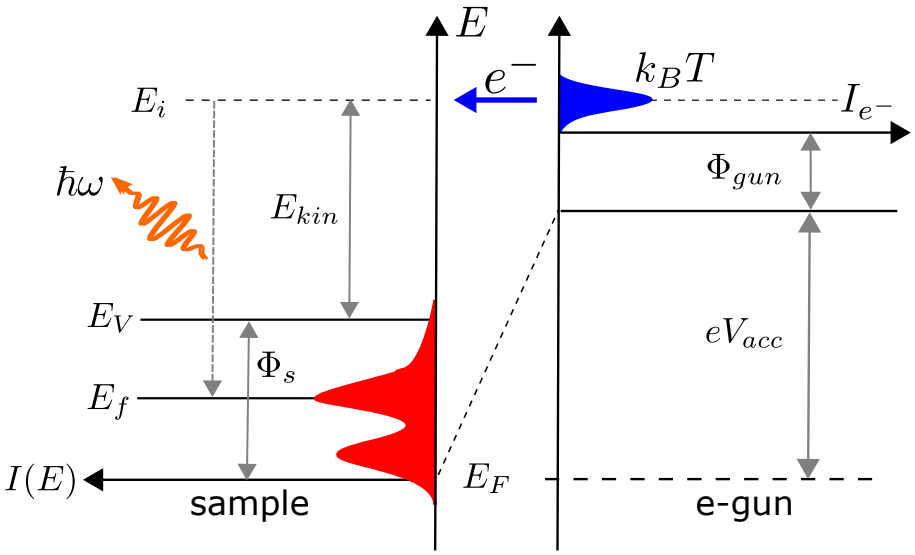

Figure 2.1: Energy diagram of the IPES experiment. An electron gun, with workfunction Φ_{gun}, provides electrons of thermal distribution k_BT that are further accelerated by an applied potential V_{acc} towards the sample surface. Electrons are thus coupled to unoccupied states of the solid. The VUV radiation of elastic and direct transitions, allows to obtain the spectral intensity $I(E)$ of the final state energies at the corresponding wavevector $k_i(\theta_i)$. Integrating the spectra for distinct k_i's allows to obtain the band dispersion of the solid.

be taken when comparing IPES and 2PPE that can both report on unoccupied states, although with particularities in each technique. Indeed, in the two-step excitation 2PPE goes from a neutral (initial state) to a cation (final state) whereas IPES goes from also a neutral to an anionic state.

The governing equations of IPES are summarized as the kinematical conditions that follow from conservation rules of photoemission theory. In direct analogy to angle-resolved photoemission spectroscopy (ARPES), the parallel-to-the-surface component of the electronic wavevector outside the solid $\mathbf{K}_{\parallel}$ is conserved after traversing the surface potential of the solid $V(z)$. In other words,

$$\mathbf{K}_{\parallel} = \mathbf{k}_{\parallel}, \tag{2.1}$$

where $\mathbf{k}_{\parallel}$ is the parallel-to-the-surface momentum component inside the solid. On the other hand, the surface potential is responsible of breaking the symmetry along the perpendicular-to-plane direction, implying that the corresponding wavevector is not conserved ($\mathbf{K}_{\perp} \neq \mathbf{k}_{\perp}$). Of course, the optical transitions are limited by the interband energy difference. If the workfunction of the sample is Φ_s, the energy conservation for a radiative transition of an electron with kinetic energy E_{kin}, is

$$E_f(\mathbf{k}) = E_i(\mathbf{k}) - \hbar\omega = E_{kin} + \Phi_s - \hbar\omega, \tag{2.2}$$

where $\hbar\omega$ is the photon energy and E_i (E_f) is the initial (final) state energy (see Fig. 2.1). In other words, E_f is the excitation energy associated to adding one electron to the system:

$$E_f(\mathbf{k}) = E_f^{N+1}(\mathbf{k}) - E_i^{N}(\mathbf{k}). \tag{2.3}$$

The intensity distribution from the radiative transitions is governed by the matrix elements [33], that can be written as

$$H_{if} \approx A_\sigma \langle E_f, \mathbf{k_f}, 1 | e^{i\mathbf{q}\cdot\mathbf{r}} \nabla V a^+_{\mathbf{q},\boldsymbol{\sigma}} | E_i, \mathbf{k_i}, 0 \rangle, \tag{2.4}$$

where A_σ is the vector potential amplitude and $a^+_{\mathbf{q}}$ is the creation operator of a photon with wavevector $\mathbf{q}$ and polarization $\boldsymbol{\sigma}$ [34]. For monocrystalline solids V can be expanded in Fourier series over reciprocal lattice vectors $\mathbf{G}$ such that,

$$V(\mathbf{r}) = \sum_{\mathbf{G}} V_{\mathbf{G}} \cdot e^{i\mathbf{G}\cdot\mathbf{r}}, \tag{2.5}$$

the assumption of Bloch waves within the crystal implies that:

$$H_{if} \approx A_\sigma \sum_{\mathbf{G}} V_{\mathbf{G}} \int e^{-i\mathbf{k_f}\cdot\mathbf{r}} e^{i\mathbf{q}\cdot\mathbf{r}} e^{i\mathbf{G}\cdot\mathbf{r}} e^{i\mathbf{k_i}\cdot\mathbf{r}}, \tag{2.6}$$

which is distinct to zero only if

$$\mathbf{k_f} - \mathbf{k_i} = \mathbf{G} + \mathbf{q}, \tag{2.7}$$

indicating the momentum conservation in the radiative transition and the wavefunction matching at the surface. In the VUV regime, the momentum balance is simplified by neglecting the photon momentum [30, 34], i.e $\mathbf{q} = \mathbf{0}$. The assumption on $\mathbf{q} = \mathbf{0}$ indicates that the observed emission intensity in IPES is dominated by primary emission rather than secondary surface *umklapp* scattering [35] in which $\mathbf{G} \neq \mathbf{0}$. This is why the direction of the VUV photons is not explicitly treated in IPES but only the direct transitions in the reduced zone scheme ($\mathbf{G} = \mathbf{0}$). The momentum conservation in IPES is thus,

$$\hbar k_\parallel = \hbar K_\parallel = \sqrt{2m(E_f + \hbar\omega - \Phi_s)} sin\theta = \sqrt{2m(E_{kin})} sin\theta, \tag{2.8}$$

where θ is the polar angle of the electron beam with respect to the sample surface (Fig. 2.2). The dispersion relation $E(\mathbf{k}_\parallel)$ is obtained by varying the angle θ. With the usual units of E_{kin} (eV) and $k_\parallel$ (Å^{-1}), Eq. 2.8 can be simplified as [36]

$$k_\parallel = 0.512\sqrt{E_{kin}} sin\theta. \tag{2.9}$$

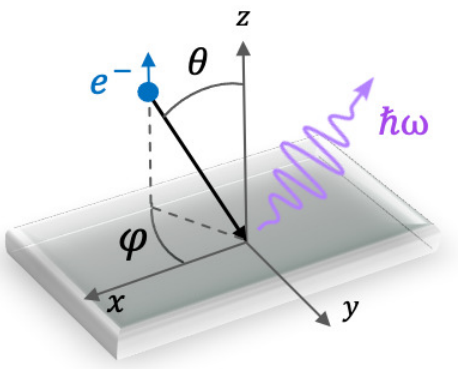

Figure 2.2: Schematic representation of IPE process in a crystalline solid. Electrons of kinetic energy E_{kin} impinge on the solid with a polar angle θ. The azimuthal angle ϕ allows to orient along high-symmetry directions in reciprocal space.

IPES is less widespread than photoemission because the fewer number of counts in the IPE process, inherent to the lower cross section σ_{IPES}. The difference in PES and IPES arises due to the distinct availability of phase space for photon creation as opposed to electron creation [31]. The ratio r of the respective cross sections [30, 37] is:

$$r = \frac{\sigma_{IPES}}{\sigma_{PES}} \sim \left(\frac{\lambda_e}{\lambda_{\hbar\omega}}\right)^2 \equiv \frac{\hbar\omega^2}{2mc^2E_e} \equiv \alpha^2 \frac{(\hbar\omega/R)^2}{4(E_e/R)}, \tag{2.10}$$

where λ_e ($\lambda_{\hbar\omega}$) is the wavelength of the created electron (photon), E_e the kinetic energy of the electron and $\hbar\omega$ the energy of the photon. Here, R and α are the Rydberg and the fine-structure constants, respectively. Taking r for the VUV case, for instance with $E = E_{kin} = \hbar\omega = 10$ eV as a representative value, we have that $\lambda_{\hbar\omega} \sim 1240$ Å and $\lambda_e \sim 4$ Å, therefore $r \sim 10^{-5}$. Conventional IPES has therefore 4 or 5 orders of magnitude less counts. However, both techniques are comparable when dealing with spin-resolved measurements. Although the phase space factors in IPES imply longer acquisition times with respect to PES, the addition of spin-resolution does not cause losses in the counting rate. This is because the spin information is encoded in the excitation rather than the detection channel as in SARPES, where the small efficiency of spin detection reduces the signal by $10^{-3} - 10^{-4}$ [38].

We can now compare IPES to other techniques sensitive to empty states. Scanning tunneling spectroscopy (STS), X-ray absorption (XAS), and near-edge structure spectroscopy (XANES) are examples of other *empty-state* techniques with surface sensitivity. However, they all differ from IPES because of their lack of k-resolution. STS has much higher energy resolution (below 1 meV) although its range of action is limited to the vicinity of E_F. XAS and XANES probe only symmetry selected unoccupied DOS [39]. Finally is two-photon photoemission (2PPE), a technique with k-resolution that has succeeded in unveiling image potential (IP) states [40], where the electron pumping mechanism constrains the k-resolution to narrow regions of the Brillouin Zone (BZ) and its interpretation assumes a previous knowledge of $E(k)$ in the photoexcited filled band [32].

2.1.1 . Bulk and surface states

IPES benefits from surface sensitivity because the probing depth of the low-energy electrons can be up to some atomic layers in a nominal application range ($5 - 20$ eV). Yet, in metal surfaces, the emission from the second layer and beyond is essentially dominated by the bulk due to the short metal screening lengths [41]. The observable bulk bands correspond to kinematically allowed transitions satisfying $E_i(\mathbf{k}) = E_f(\mathbf{k}) + \hbar\omega$ where $\mathbf{k} = (\mathbf{k}_\parallel, \mathbf{k}_\perp)$ constraining $\mathbf{k}_\parallel$ to be a constant [35]. Therefore, identifying whether the IPES emission is due to a bulk state or a surface state (SS) is not straightforward.

Before discussing the experimental criteria to distinguish surface from bulk states, let us first recall that a SS is a bound state with a large local DOS at the surface atom [42]. The surface states are localized in the direction normal to the surface and they are categorized depending on the decaying behavior of the wavefunction while approaching the bulk. From the bulk side, the solutions of the Schrödinger equation are Bloch states that form the ordinary volume states. Normally, in a SS the wavefunction decays exponentially approaching the crystal but if its amplitude persists through the crystal it becomes a surface resonant (SR). One can picture the SS as a wave that is confined between the crystal and the surface barrier. Therefore, if a wave Ψ^+ carries unit flux towards the crystal part of this will be reflected as $A_c e^{i\phi_c}\Psi^-$ towards the surface barrier. Then again, because the wave is confined, there will be a further

reflection at the barrier Ψ^- with contribution $A_b A_c e^{i(\phi_b+\phi_c)}\Psi^+$. Summing the amplitude due to the repeated reflection the total amplitude of Ψ^+ is A_T [43]:

$$A_T = [1 - A_b A_c e^{i(\phi_B+\phi_C)}]^{-1}. \tag{2.11}$$

Thus, a pole in Eq. 2.11 corresponds to a bounded surface state. Non-resonant SS are categorized into Shockley or Tamm states whether they are described by a tight binding or nearly-free electron (NFE) model, respectively. A second type of SS is given by the image potential (IP) states that do arise in metallic surfaces and are bounded to the vacuum level. IP states are weakly bounded to the metal and they can have relatively long lifetimes (> 10 fs) [44]. They are described by an infinite series due to the surface potential $V(z) = -\frac{e^z}{4(z-z_0)}$.

In the experiment, some criteria can be applied to attribute surface and bulk binding energies when theoretical calculations are not available. In a SS:

(i) The spectral intensity is influenced by the adatom concentration at the surface, as seen in noble metals [45, 46], and also more sensitive to temperature due to the terminating dangling bonds.

(ii) The angular distribution of the emitted photons can be characterized by the degree of polarization of the emitted light. For instance, sp-like surface states are polarized with electric vector along the surface normal [47].

(iii) The $k_\perp$ is undefined because the binding energies are independent of the detection bandpass energy and pinned with respect to E_F when $\hbar\omega$ is varied [48].

Criterion (iii) is exemplified in Fig. 2.3 where the SPIPES spectra of a surface band and a bulk band of Au(111) were acquired with two distinct bandpass detectors at different take-off angles. The surface state maintains the same binding energy whereas the bulk derived band (B1) shifts towards lower binding energies while increasing the bandpass energy. This result is consistent with the conservation of energy (Eq. 2.2) because $E_{kin} = (E_f + \hbar\omega) - \Phi_s$ when E_{kin} is hold as a constant. Thus, the particular setup characteristics can shift the energy reference (E_F) of bulk bands [35] but, ultimately, their dispersion relation is setup-independent.

The expectation values of IPE events are linked to the spectral intensity observed in IPES. For the interpretation of the spectral intensity, the geometrical parameters of the experiment have to be considered. Indeed, their influence may lead to symmetry-breaking of the states and even hindering of the spin asymmetry [50]. In angle-resolved IPES, the electron incidence is varied by rotating the sample so that the take-off angle of the photons is modified respect to a fixed detector. In particular, having a fixed photon energy makes very suitable the isochromat IPES mode[1] for the study of SS's in 2D systems where $k_\perp$ is undefined. Surface spin textures can also be studied by adding spin resolution to isochromat IPES by incorporating a spin-polarized electron beam. In the following, we present the generalities on the generation of spin-polarized electrons from GaAs photocathodes that are directly incorporated in the electron sources of spin-resolved IPES.

2.2 . SPIN-POLARIZED ELECTRONS PRODUCTION

In usual spin-polarized IPES setups, the wavevector and the spin polarization vector $\mathbf{P}$ are coupled through the angle of incidence θ. In other words, $\mathbf{k} = \mathbf{k}(\theta)$ and $\mathbf{P} = \mathbf{P}(\theta)$ hold simultaneously. The intrinsic relation between $\mathbf{P}$ and $\mathbf{k}$ is evidenced in Fig. 2.4 where it is

[1] See Section 2.4.

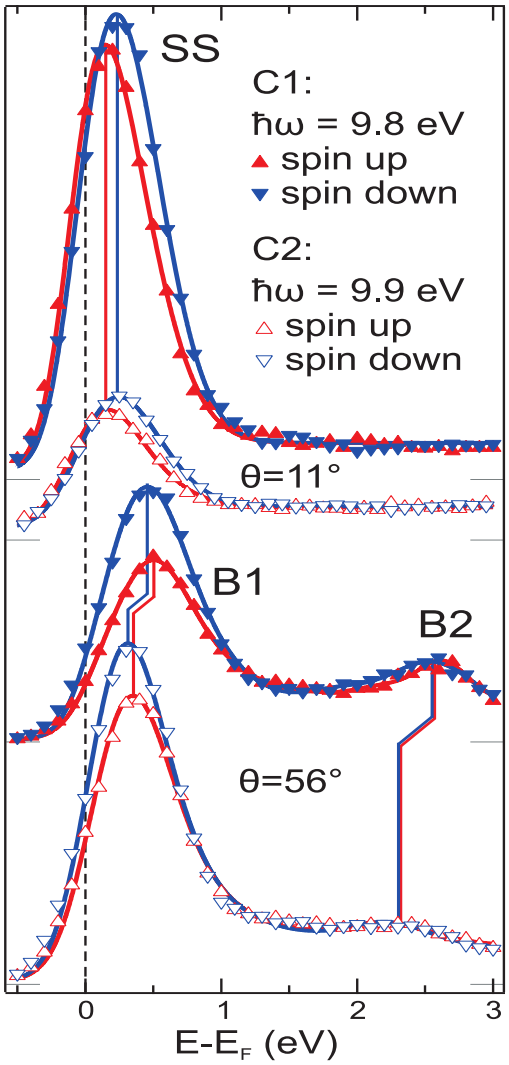

Figure 2.3: SPIPES of Au(111) surface state ($\theta = 11°$) and bulk state ($\theta = 56°$) taken with GM counters of 9.8 eV (C1) and 9.9 eV (C2) bandpass energy. The take-off angle modifies the intensity of both spectral linewidths, whereas the bandpass energy only shifts the binding energy of bulk-related bands (B1) as seen in the lower spectra. Adapted from [49] under a CC attribution license.

clear that any variation of the wavevector $\mathbf{k}$ modifies the projection of $\mathbf{P}$ onto the surface of the crystal. It is thus compulsory to decouple $\mathbf{P}$ from $\mathbf{k}(\theta)$ to determine unoccupied states with both, k- and spin-resolution. If not, it is impossible to probe any polarization $\mathbf{P}$ at any wavevector $\mathbf{k}$.

To exploit the capabilities of spin-polarized IPES, a three-dimensional (3D) control of the spin-polarization vector $\mathbf{P}$ is needed. This is not a trivial task especially in the low-energy regime, where the momentum resolution and the parallel beam condition are ought to be maintained. We will describe the development and characterization of such a source in Chapter 3.

The spin resolution in IPES is obtained by injecting spin-polarized electrons in the sample. GaAs photocathodes are commonly used to generate spin-polarized electrons. The use of GaAs crystals as high-efficiency photocathodes is widely established since the first realization of p-doped photoemitters by J. J. Scheer and J. van Laar [51]. The spin-orbit interaction and the lack of inversion center in this zinc-blend semiconductor are responsible of an intrinsic Dresselhauss splitting Δ_{SOC} of the topmost VB. The heavy-hole (VB1) and light-hole (VB2) bands are degenerated at Γ_8 with an energy splitting of $\Delta_{SOC} = \Gamma_8 - \Gamma_7 \sim 0.34$ eV [52, 53], as shown in Fig. 2.5(a). By increasing the photon energy the transition wavevector magnitude is also

increased and the modifications to the wavefunctions, for instance by transitions VB(2)3-CB1, do also modify the net polarization [54]. The $\Gamma_7 - \Gamma_6$ transitions are energetically allowed with equal probability of spin up and spin down electrons and thus a zero net polarization. Therefore, in order to obtain spin-polarized electrons, a photon energy of ~ 1.4 eV (at RT) must be used.

Monochromatic and spin-polarized electrons can be produced [55, 56, 57] by optical transitions induced by circularly polarized light. The excitation energy follows from the temperature-dependent direct bandgap E_g [58, 59],

$$E_g(T) = 1.519 - 5.405 \times 10^{-4} T^2 (T + 204)^{-1}, \tag{2.12}$$

where the units of E_g are given in eV with an standard deviation of about 3 meV for $0 < T < 1000$ K. At 300 K, the intrinsic bandgap $E_g \sim 1.422$ eV (872 nm) is within the near-infrared (NIR) regime as shown in Fig. 2.5(b).

Since IR photons cannot extract electrons due to the intrinsic GaAs workfunction, the GaAs surface has to be set either into a negative electron affinity (NEA) or a positive electron affinity (PEA) [60] depending on the doping nature of the crystal. The electron affinity χ (usually ~ 2.5 eV [61]) is defined as the potential barrier that an electron at the CB minimum must overcome to escape into the vacuum level as depicted for a pristine crystal in Fig. 2.6(a). The effects of NEA are schematized in the band diagram of Fig. 2.6(b).

In GaAs in NEA, the hole carriers lower the E_F nearby the VBM and χ is decreased at the photocathode surface [51, 55, 57, 62, 63]. The NEA activation can be achieved by alkali deposition with small quantities of an oxidizing gas such as NF_3 or O_2. In the most common case, also used in this work, an alternated evaporation of Cs and O_2 ("yo-yo") forms a Cs_2O dipole layer with a strong field V_{dip}, located at the surface, that lowers E_V down below the conduction band (CB) edge. The evolution of the photocurrent (emission) during the NEA activation process is summarized in five different steps (Fig. 2.7). To maintain the surface at equilibrium, a downward bending of the bands stabilizes E_F [51, 64] with a potential change V_{bb} in the so-called depletion region d_{bb} inside the semiconductor. The depletion region is given by

$$d_{bb} = \left(\frac{2\epsilon\epsilon_r}{(N_a - N_d)e^2} V_{bb} \right)^{1/2}, \tag{2.13}$$

where $\epsilon\epsilon_r$ is the dielectric permittivity of the crystal. The distance of the p-doped GaAs band bending depends on the acceptor (donor) concentration N_a (N_d). Typically, $d_{bb} \sim 10$ nm for

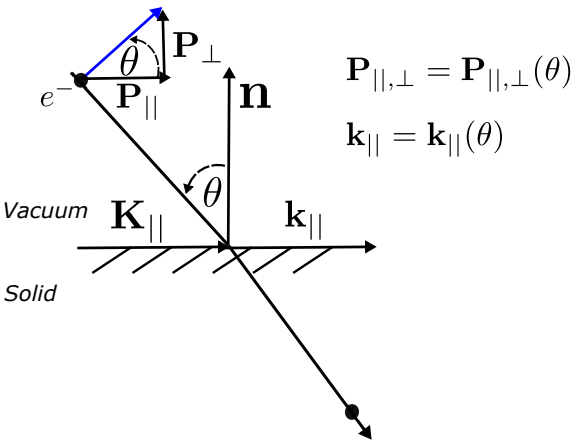

Figure 2.4: Dependency of $\mathbf{k}_{\|}$ and $\mathbf{P}$ (blue arrow) on the (polar) angle of incidence θ over the crystal surface in the inverse photoemission process. The electron optical system of the spin polarized electron source can decouple $\mathbf{P}$ from $\mathbf{k}$ allowing to probe with the same magnitude of either $\mathbf{P}_{\|}$ or $\mathbf{P}_{\perp}$ in a k-resolved measurement.

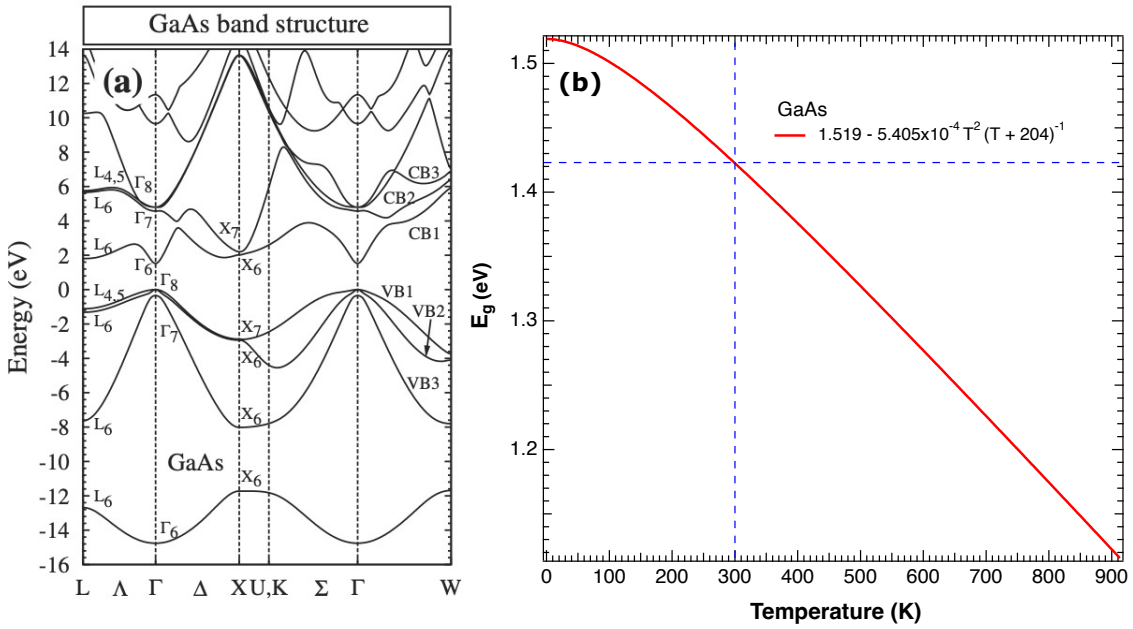

Figure 2.5: (a) Band diagram calculation of GaAs showing the degeneracy and band splitting at Γ adapted from [53] with permission from APS Physics. (b) Temperature-dependent GaAs bandgap from numerical model [58]. Dashed blue lines intersect the bandgap energy at RT.

$V_{bb} \sim 0.5$ eV and $N_a \sim 10^{19}$ cm^{-3} [54].

Once that Φ is below the CB edge, electrons promoted to the conduction band by optical transitions escape to vacuum. Experimentally, this can be seen as a gradual saturation on the photocurrent, for a given incoming photon flux, that is reached after some cycles of alternated evaporation as shown in Fig. 2.7 (step II).

Once the GaAs is in NEA, and therefore NIR photons can extract electrons, lets focus on the process of spin-polarized electron generation. Electrons could be initially pumped to CBM either from the hole-degenerated VB or from the SOC-induced VB3. Nevertheless, only the electrons from the uppermost VB are of polarized nature.

In GaAs, the spin polarization of the emitted electrons is constrained to $P = 0.5$ [55, 65]. The fractions of photoelectrons with $m_s = \pm\frac{1}{2}$ is determined through the probabilities of each transition that are calculated by the dipole matrix elements [66]. The selection rules for the optical transitions with circularly polarized light are schematized in Fig. 2.8 indicating the allowed transitions $\Delta M_J = 1$.

The produced electron beam can be depolarized by several mechanisms [67, 68, 69] taking place mainly at the surface before ejection to vacuum as a consequence of the Cs_2O dipole layer. Experimental values of spin polarization of GaAs-based sources are typically found between 0.2 and 0.35 at RT. To go beyond this polarization value, strained superlattices e.g. GaAs/GaAsP, can be used to reach an electron beam polarization up to more than 90% [70] but this does not compensate the diminishing of the quantum efficiency in the NIR regime [71] so, at the end, the counting statistics are decreased.

When preparing the photocathode, thermal treatments favor the removal of adatoms on the surface and are quite advisable before each NEA activation. In our system, the highly p-doped ($N_a = 2.5 \times 10^{19}$ cm^{-3}) GaAs(100) crystal is attached to a manipulator by Mo clamps and it can be annealed by passing a current through it. A proper NEA activation depends on

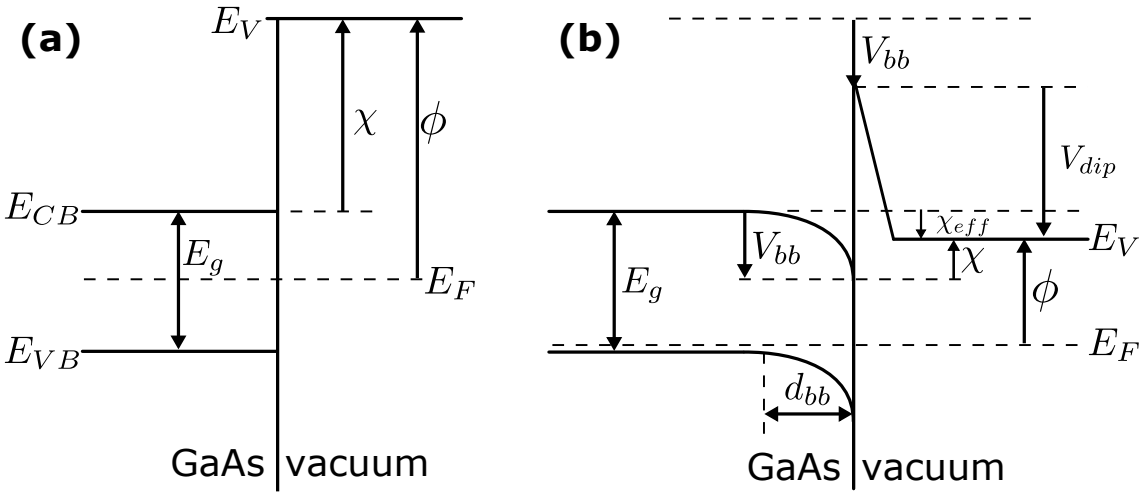

Figure 2.6: Energy diagram of GaAs crystal: (a) pristine and (b) p-doped in negative electron affinity (NEA) where electrons are ejected to vacuum from the conduction band after optical transitions take place.

the annealing temperature with better performance just below the melting point (~ 910 K), a tricky issue since non-stoichiometrical As evaporation (920 K) [72] could permanently damage the GaAs surface. After the thermal treatment, we evaporate Cs (SAES evaporable getter) and expose the photocathode to high-purity O_2 (Messer 99.999%). Alternated deposition, by a dedicated leak valve on the O_2 inlet, favors the formation of a Cs_2O dipole layer on the GaAs surface. Thus, Γ-valley electrons can be photoemitted to vacuum by the assistance of a 830 nm (40 mW) diode laser. The quantum yield, or quantum efficiency (QE), defined as the probability of a photon to generate a detectable electron of elementary charge e, is expressed as [73]:

$$QE = \left|\frac{hcI_p}{W\lambda e}\right|, \tag{2.14}$$

where I_p is the photocurrent produced by an incident laser of wavelength λ and power W over the sweet spot of the GaAs crystal. Feeding Eq. 2.14 with the experimental parameters of this work: $W = 40$ mW, $\lambda = 830$ nm and $I_p = 10$ μA, we obtain $QE \sim 0.005$. This value is in agreement with the yield of non-strained GaAs photocathodes [55, 74, 75], where usually $0.01 < QE < 0.1$, and high-QE electron sources [76]. The PL emission of our GaAs photocathode at RT, obtained in Olivier Plantevin's setup (LPS), is presented in Fig. 2.9. The spectrum, obtained with a 554 nm (10 mW·cm^{-2}) photoexcitation, confirms that a photon energy of 1.42 eV (873 nm) [74] enhances the QE of the photoemitter.

We have further characterized our photocathode by determining its workfunction. A simple energy balance from the IPE process (Fig. 2.1) allows to corroborate the photocathode workfunction Φ_c:

$$\Phi_c + eV_{acc} = E_{kin} + (E_V - E_F) = E_{kin} + \Phi_s. \tag{2.15}$$

Recalling that $E_{kin} = E_f + \hbar\omega - \Phi_s$ and taking $E_f = 0$, it can be seen that $\Phi_c = \hbar\omega - eV_{acc}$. From SPIPES measurements on the (111) facet of Au we obtained $eV_{acc} \sim 8.41$ eV (Section 3.3.3) and considering the photon energy $\hbar\omega \sim 9.90$ eV detected by our photon counters, we

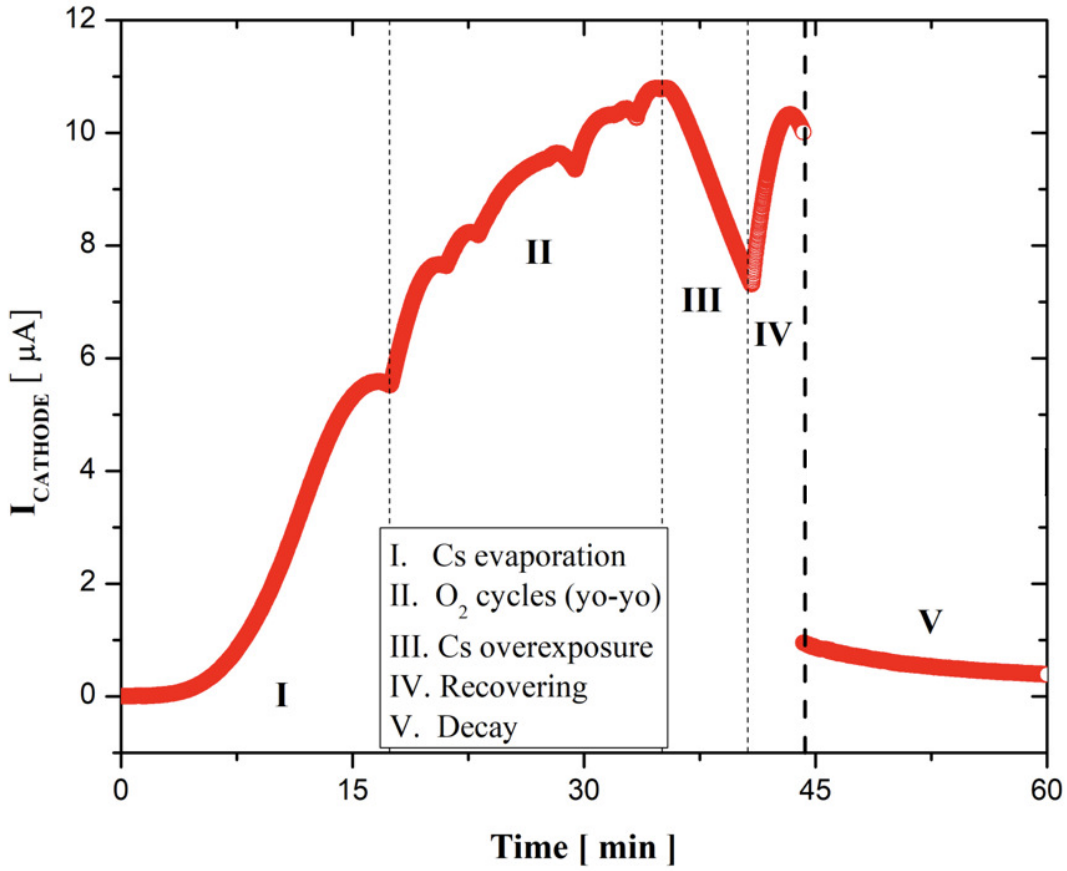

Figure 2.7: Emission current from our GaAs photocathode in the NEA activation steps. (I) Cs is evaporated until saturation is reached. (II) An alternated evaporation of Cs and O_2 increases the emission threshold. (III) Overexposure of Cs decreases the emission current signaling the end of the activation process. (IV) The emission current stabilizes to a maximum threshold in the equilibrium state i.e with no evaporation. Natural or photoinduced desorption decrease the emission current. (V) Decaying of photocurrent by an attenuated NIR laser (10% power).

determined $\Phi_c \sim 1.49$ eV. As expected, Φ_c is close to the pristine GaAs direct bandgap. The emission from the CBM is assisted by NIR radiation if a correct NEA activation is achieved.

When preparing the photocathode, the emission current is monitored in a high resolution electrometer (~ 50 pA) until saturation, with typical activation value for NIR light between 1 and 4μA. Once the photocathode is prepared, it is transferred to the extraction position, where the surface can be reactivated with a low-rate Cs evaporation. The idea of using a second dispenser is twofold: (i) to feed the photocathode in critical experiments and, (ii) to reduce the frequency of chamber opening for dispenser replacement. The low-rate evaporation getter is positioned nearby the extraction lenses of the electron-gun and proximity discharges might occur but this is easily prevented by using moderate input power through the alkali getter feedthrough.

The gaseous co-adsorption method renders high-efficient GaAs photocathodes for the visible and the NIR spectra. However, the efficiency and lifetime may be affected by residual agents inside the vacuum chamber which increase the probability of electron scattering. For instance, CO and CO_2 are the most harmful residual gases for the efficiency stability of the photocathode

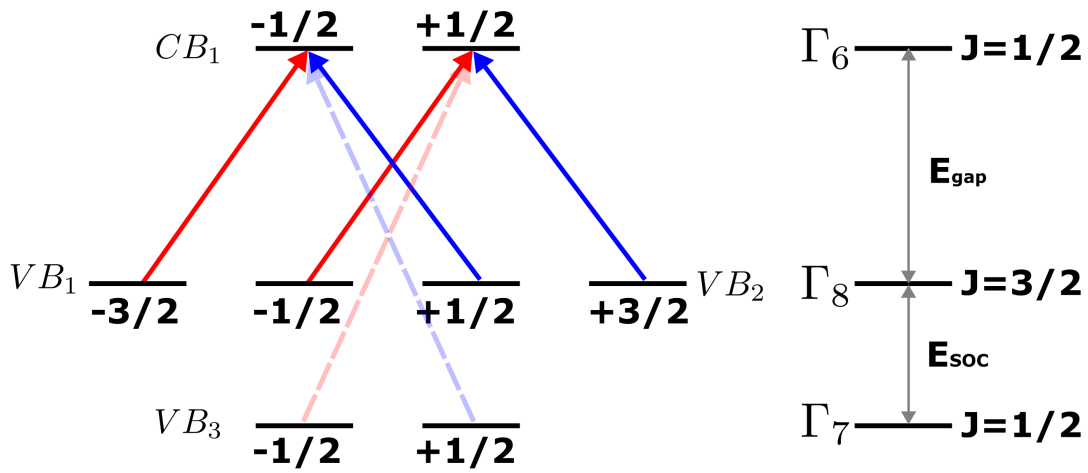

Figure 2.8: Selection rules for the optical transitions in GaAs crystal around Γ. Circularly right (left) polarized light is depicted by red (blue) arrows signaling the allowed transitions with angular momentum conservation: VB1(2)-CB1. Conversely, in the VB3-CB1 transitions (light-colored arrows), the angular momentum is not conserved resulting in an unpolarized electron beam.

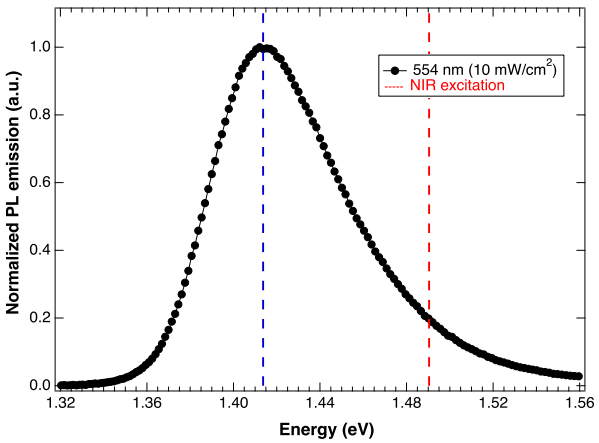

Figure 2.9: Photoluminescence spectra of our p-doped GaAs single crystal photocathode at RT. The maximum emission is found at 1.41 eV as marked by the dashed blue line. Polarized electrons are ejected from the CB with a 1.49 eV NIR laser to perform SPIPES. The measurement was taken in the setup of Olivier Plantevin (LPS).

[77]. Another factor having an impact on the efficiency are the extraction fields that shape the electron beam. Eventual deviations on the trajectory of surrounding ions in the residual vacuum towards the active surface may occur because of the HV tension. The ionic back-bombardment of the photocathode could disrupt the dipole bilayer by breaking Cs_2O bonds and reducing the photocathode lifetime [78, 79]. Disregarding external factors affecting lifetime, it is usual to consider an exponential decay of the emission current such that $I_e(t) = I_0 exp(-t/\tau)$, due to natural Cs desorption, that imposes a finite lifetime τ of the emission current $I_e(t)$. The emission lifetime depends on parameters such as the crystal quality, doping concentration, power of light excitation, base pressure, and other factors where consensual literature is hard to establish. On average, the lifetime can be better than eight hours for a continuous emission but it can be further extended to 24 hours if we use low-rate cesiation. We have considered an empirical expression for the exponential argument of the current emission as a third order polynomial $P_3(t)$ that satisfies our experimental observations. Therefore, the emission current is expressed as:

$$I_e(t) = I_0 exp\left[P_3(t)/\tau\right], \tag{2.16}$$

where I_0 is the initial current just after the activation. Therefore,

$$\tau = log\left[\frac{I_e(t)}{I_0}\right]^{-1} P_3(t). \tag{2.17}$$

The current decay of an individual activation (annealing and Cs-O_2 exposure) is shown in Fig. 2.10(a) where P_3 has been fitted with Eq. 2.17 to match the normalized emission current. The lifetime was calculated by assuming an *inactive* photocathode at $I_e(t) = 0.1 \times I_0$. Consecutive activations increase the photocathode lifetime as shown in Fig. 2.10(b). Our results agree with former observations [60, 65, 74] in where repeated NEA preparations improved the photocathode lifetime reaching saturation after ~ 30 activations. The enhanced lifetime may be attributed to surface restructuration and assisted desorption of contaminants by the Cs atoms. Here we have found that flushing the surface with O_2 while annealing did improve the photocathode performance.

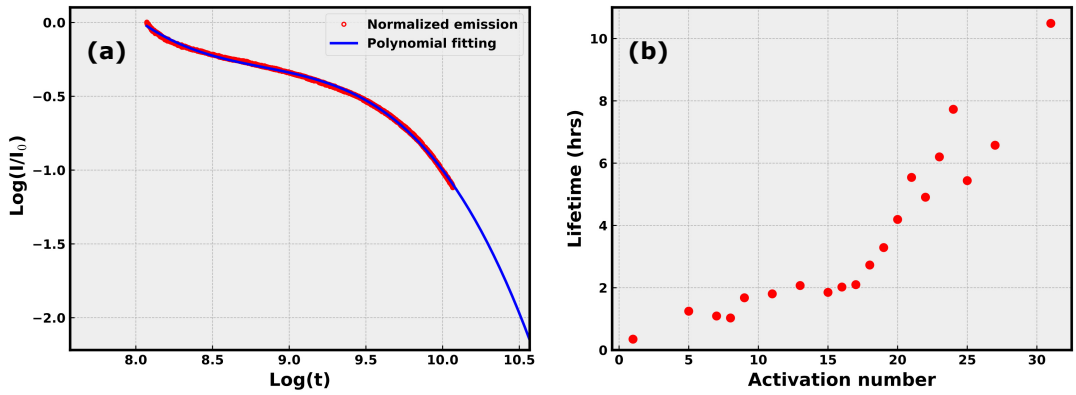

Figure 2.10: Lifetime characterization of NEA activated GaAs photocathode. (a) Logarithmic plot of the emission current as function of elapsed time after NEA cycle. (b) Lifetime as function of activation number. The GaAs photocathode can emit during 10 hours without further Cs evaporation.

From the phase space considerations of the IPE process it would then be desirable to have a high intensity source with a high electron transmission. Yet, even when samples could stand higher currents, space-charge phenomena [80, 81] may modify the electron distribution at the surface and the beam cross section so that not only the energy but also the momentum resolution could be affected. The electron-electron repulsion becomes important in low-energy and high-brightness [2] beams where the energy resolution is impacted by the chromatic aberration caused by the Boersch effect. These space-charge forces can be treated as an external force consisting of a linear and a non-linear term. The former is responsible for defocusing the beam whereas the second one for distorting the phase space distribution [82]. Since high beam intensities also reduce lifetime and induce proximity discharges, high-intensity beams should be

[2]The brightness of a charged beam is defined as the current density divided by its subtended solid angle. The source parameters are not modified (electron optics) to change the intensity of the electron beam so that the current density is, in this case, equivalent to the brightness. These terms will be used interchangeably.

avoided while performing IPES. To avoid charging effects, current densities $j < 1$ μA·mm^{-2} are suggested in non-organic samples such as ferromagnets [83]. We have therefore studied the effect of the laser current density in the spectral width of the Au(111) bulk transition ($\theta = 46°$) shown in Fig. 2.11(a). Each spin pair data set is normalized to maximum intensity. The lineshape is well defined for $0.1 < j < 0.6$ μA·mm^{-2} with a clear spin asymmetry at the binding energy (see Section 3.3.5). On the other hand, for $j = 1.0$ μA·mm^{-2}, the spin asymmetry vanishes and the spectral broadening makes difficult the determination of the final-state energy. This is therefore the upper limit for the current density in a meaningful operation of the source. This can be better observed in Fig. 2.11(b), where the FWHM of the pseudo-Voigt fitting of each spectra is shown. We have thus taken 0.6 μA·mm^{-2} as a nominal value to perform SPIPES without compromising the counting rate. The effect of the spectral broadening by the current density is also frequent for conventional IPES electron sources with Stoffel-Johnson design [80] observed e.g., on the image potential states of Cu(100) [81]. The IPES spectral broadening is mainly affected by two parameters: the thermal energy spread of the beam and the space-charge effects of the cathode. In one hand, the transverse thermal energies of the electrons broaden the beam size [84] especially at the low-energy regime [3] as observed in conventional BaO IPES sources, where the FWHM Maxwellian momentum distribution projected along one transverse direction is given by [80]:

$$\Delta k(T) = \frac{2}{\hbar}\sqrt{2mk_BTln(2)}, \tag{2.18}$$

where T is the cathode temperature. On the other hand, the maximum current I_{max} that limits the space-charge effects is related to the retarding potential at the exit of the electron source V_0 by a coefficient defined as the perveance P [85]:

$$P_{max} = I_{max}V_0^{-3/2}, \tag{2.19}$$

with usual units 1 $\mu perv \equiv 1$ $\mu A/V^{3/2}$. Because the retarding potential basically controls the final energy of the electron beam to perform isochromat IPES, the maximum perveance thus indicates the maximum service current of the electron source without undesired space-charge effects. An equivalent expression for the maximum perveance is [80, 81]:

$$P_{max}(\mu perv) = 38 \cdot tan^2(\delta/2), \tag{2.20}$$

where δ is the full angular width of the beam. Considering $\delta = 6°$ from our experimental estimations (see Section 3.3.3), it follows $P_{max} = 0.10$ $\mu perv$ for our electron source.

Although the figures for the quantum efficiency and perveance of our electron source validate its correct functioning for performing IPES, the spin polarization is a necessity for incorporating SPIPES operation. In the following, the concept of spin polarization is introduced whereas the effective polarization of our electron source will be quantified in Section 3.3.4.

2.3 . POLARIZATION OF THE ELECTRON BEAM

The proportion of equally aligned spins is quantified by the polarization. The notion of spin polarization P is only meaningful in the electron beam generated by the photocathode.

[3] See for instance the simulations of the beam profile as function of the beam energy in Fig. 3.21.

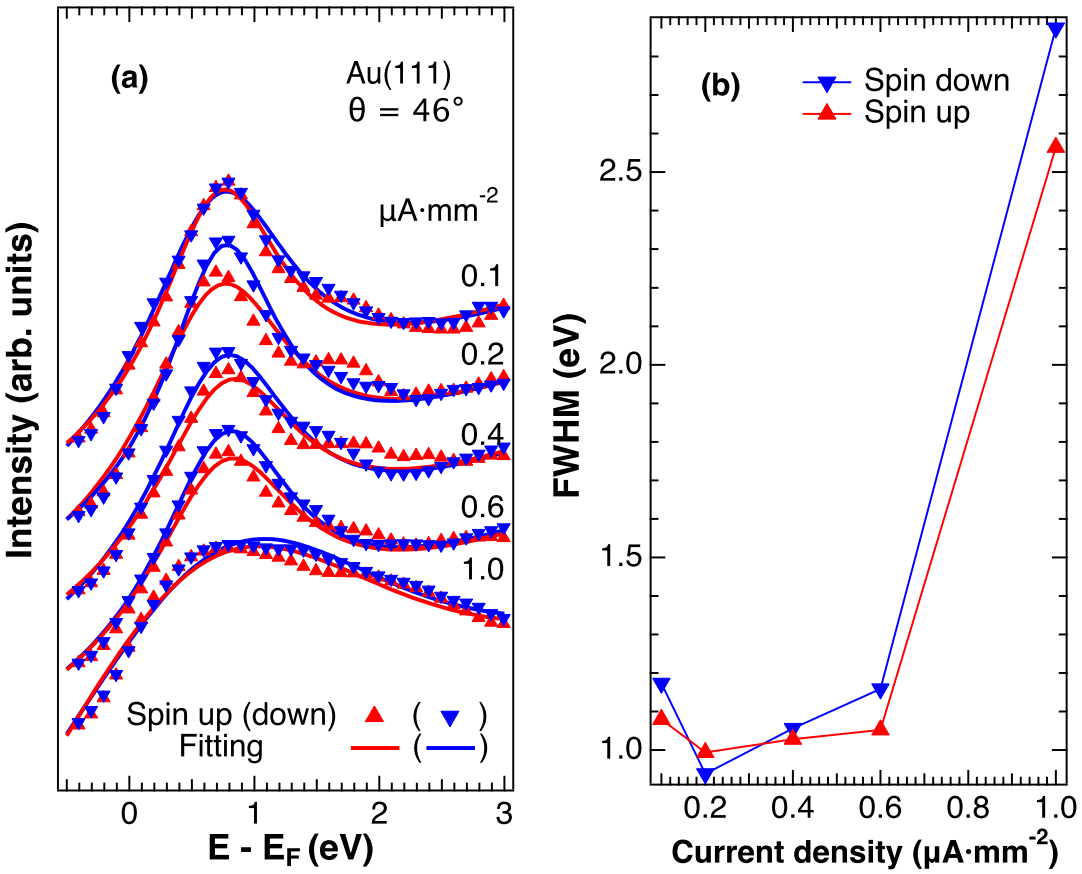

Figure 2.11: (a) SPIPES spectra of Au(111) bulk state ($\theta = 46°$) as a function of the current density j. Data are normalized (triangles) to maximum intensity and fitting lines are shown. High density currents increase the uncertainty of determining the final state energy, see $j = 1.0\ \mu$A·mm^{-2}. The peak broadening is attributed to space-charge effects occurring at the sample surface. (b) FWHM of fitted spectra as function of the current density.

Statistically, an electron beam is said to be polarized if the two spin subsets, spin up ($\uparrow$) and spin down ($\downarrow$), are not equally populated [86] and a resulting state of polarization is described by a polarization vector $\mathbf{P}$. A quantization axis must be chosen to define the spin polarization of an electron beam [87]. Of course, the reference frame will depend on the nature of the experiment. In a polarized beam of $n = n_\uparrow + n_\downarrow$ electrons, the projections of spin up and spin down along the quantization axis are not identical and the polarization of the beam is simply

$$P = \frac{n_\uparrow - n_\downarrow}{n_\uparrow + n_\downarrow}, \tag{2.21}$$

where n_i ($i \in \{\uparrow, \downarrow\}$) accounts for the number of electrons with magnetic moment parallel or anti-parallel to the quantization axis. On the other hand, for an unpolarized electron beam, the projection of the spin components in any random reference axis is just the same so that $P = 0$.

The polarization of an electron beam is usually accessed by Mott polarimetry. In this technique, an electron beam is accelerated by a high voltage against a heavy metal target. Electrons feel then the spin-orbit coupling of atoms in the target and backscatter asymmetrically in what it is known as Mott diffusion [36]. The Sherman function S is the asymmetry that would be observed in the case of a totally polarized electron beam and it is inherent to the spin

detector. It is related to the asymmetry A by

$$A = P \cdot S. \tag{2.22}$$

In Mott detectors, S depends on the energy of the electrons, the atomic number of the scatterer and the particular geometry of the device [88, 89]. It follows that P can only be determined if S is an a priori known parameter (usually between 0.1 and 0.3) [90].

In SPIPES, the polarization of the electron beam is linked to the difference of photon counts, for spectra of the same state for opposite polarizations of the electron beam, rather than the intrinsic polarization of the electron source.

Let us consider $I_\uparrow$ ($I_\downarrow$) as the total counts per incident charge of the spin up (down) component for the hypothetical case of a completely polarized electron beam ($P = 1$). It follows that $I = I_\uparrow + I_\downarrow$ is the total photon count number per unit of incident charge and the spin asymmetry is given by

$$A \equiv \frac{I_\uparrow - I_\downarrow}{I_\uparrow + I_\downarrow}, \tag{2.23}$$

and therefore, the total counts for each spin are expressed as

$$I_{\uparrow,\downarrow} = \frac{I}{2}\left(1 \pm A\right). \tag{2.24}$$

Since in any real situation the electron beam has incomplete polarization ($P < 1$), Eq. 2.24 is not longer valid. If only the polarization is changed but not the number of counts by an incompletely polarized electron beam, $i = i_\uparrow + i_\downarrow$, and the totally polarized beam, the same total intensity is generated:

$$I = I_\uparrow + I_\downarrow = i_\uparrow + i_\downarrow. \tag{2.25}$$

The asymmetry is renormalized as [91, 92]:

$$A = \frac{I_\uparrow - I_\downarrow}{I_\uparrow + I_\downarrow} = \frac{i_\uparrow - i_\downarrow}{i_\uparrow + i_\downarrow} \cdot \frac{1}{Pcos\theta}, \tag{2.26}$$

where the factor $cos\theta$ modulates P due to the beam incidence with respect to the sample surface (Fig. 2.4). In particular situations, appropriated quantization axes exist, like in domain structures with an in-plane magnetization [92]. The asymmetry is renormalized by the projection of $\mathbf{P}$ onto $\mathbf{M}$. If ψ is the angle between $\mathbf{M}$ and $\mathbf{P}$ then Eq. 2.26 becomes

$$A = \frac{i_\uparrow - i_\downarrow}{i_\uparrow + i_\downarrow} \cdot \frac{1}{Pcos\theta cos\psi}. \tag{2.27}$$

This expression highlights that the asymmetry and therefore the spin sensitivity decrease due to the experimental geometry. In order to maximize the asymmetry, it is compulsory to tune the spin in any arbitrary direction. This is precisely the case of our spin-resolved electron source, so angular corrections in Eq. 2.27 can be neglected due to the 3D tuning capabilities and only the spin polarization module has to be considered while analyzing spectral intensities.

2.4 . ULTRAVIOLET PHOTON DETECTION

Once the spin-polarized electron beam excites the sample, VUV photons are emitted with information about the empty states. IPES can be performed with two extremely different experimental modes, the *isochromat* or the *fluorescent* mode. The isochromat is based on detecting photons of a single energy, so it consists of varying the kinetic energy of electrons to perform a spectrum similarly to EDC's in ARPES (Fig. 2.12(a)). This mode uses GM tubes as gas scintillators counters. On the other hand, the fluorescent mode detects, by using a monochromator before a microchannel plate (MCP), photons of different energy (Fig. 2.12(b)). The isochromat mode is nowadays primarily used since the low IPES cross-section requires high counts and the high gain in photocurrent by MCP's does not compensate for the loss of solid angle in monochromators [93]. Very few IPES setups have operated in the fluorescence mode [94, 95] and, to our knowledge, do not provide spin resolution.

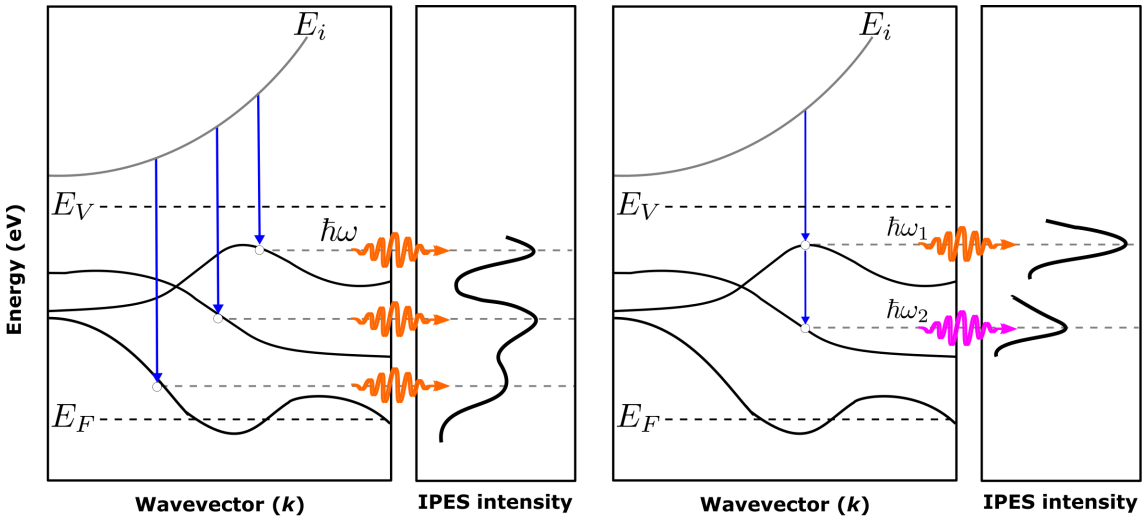

Figure 2.12: IPES operation modes: (a) Isochromat detection where E_{kin} is varied for a fixed photon energy and (b) Tunable photon energy, where the energy of the impinging electrons is kept fixed while acquiring photons of distinct energy.

Fig. 2.13 shows a GM counter that is used to detect VUV photons in isochromat IPES. This design is a variation of the initial configuration proposed by V. Dose [34, 96]. The principle of operation relies on detecting VUV photoionization events of a filling gas triggered by the photons entering the detector through the window. The ion-electron pairs are separated by the presence of an electric field that accelerates the electrons to an axial anode, generating a current that is converted into analogical pulses. In IPES, the primary ionization is due to a single VUV photon, resulting in a single electron-ion pair [97]. However, the cathode-anode potential accelerates the free electron from the primary ion pair and, if its kinetic energy exceeds the ionization potential of the molecule, the electron may cause another ionization generating a secondary electron-ion pair. The process can be further repeated now by the two free electrons creating more free electrons whose population growing rate is an exponential function of their distance to the central anode [98]. The effect of subsequent ionizations triggered by a single electron is known as *Townsend avalanche* and they occur in the GM counter. Therefore, the raw output of the GM is often preamplified by charge-sensitive operational elements and further processed to discriminate noise levels so that only IPE pulses are counted. The discriminated

transistor-transistor logic (TTL) pulses are further registered in e.g. nuclear instrumentation modules, in our case an Ortec® 994 model.

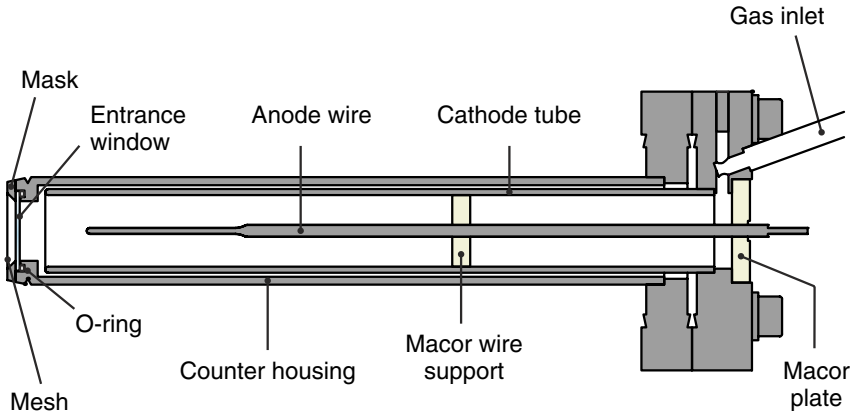

Figure 2.13: Geometrical design and elements of a Geiger-Müller bandpass counter for IPES. Reproduced from [97] with permission from IOP publishing.

The active elements of the GM counter are a stainless steel tube (cathode) and a coaxial filament (anode wire). The outer cathode is grounded so a positive high voltage assures that the electrons are attracted towards the anode. MACOR® plates are adapted to fix the position of the electron collector at the axis of the outer cylinder. This is crucial to avoid unwanted discharges due to an heterogeneous field distribution. Also, the surface of the electrodes is polished to avoid corona discharge and a highly transparent mesh ($T \sim 80\%$ [93]) of Mo, Au, or Ti is placed on the UHV side of the photon window to prevent charge accumulation provoked by the electron gun. The ionization potential of the filling gas (high-pass) and the transmission of an insulating photon window (low-pass) define the energy cutoff of the GM detector. Thus, final states whose energy is below the bandpass threshold can be explored. Usual materials for the low-pass filter are alkaline earth fluorides such as CaF_2, SrF_2 and MgF_2. Table 2.1 summarizes the existing gas-window combinations for VUV photon detection.

For isochromat IPES, GM counters can work either in the *Geiger-Müller* mode or the *proportional* mode. The main difference of these modes is their counting statistics whose typical distributions are compared in Fig. 2.14(a) since it is necessary to acquire enough statistics in a reasonable time frame where the measured surface remains free of external impurities. Considering an isotropic photon distribution, the count rate is proportional to $1/d^2$ [97] where d is the counter distance to the sample. Therefore, the most direct way to enhance the counting rate is by increasing the detector solid angle by approaching the window to the sample. In the following, we present more in detail each operation mode.

Geiger-Müller mode

The Geiger-Müller mode operates with a continuous flow of ionizing/quenching gases and it is characterized by a multiplication mechanism of the detected photons and an optimal voltage plateau regime. In this work, GM counters (OmiVac) with CaF_2 window and Ar-C_3H_6O were operated in the Geiger-Müller mode. A wire mesh of Au was located in the UHV side of the silica window to avoid charging effects. For these particular specifications, VUV photons of $\hbar\omega = 9.90$ eV and 330 meV bandpass are detected at RT [107]. A pressure of 130 mbar was

Filling gas	Window material	Detection energy (eV)	Bandpass width (meV)
Iodine + He/Ar [96, 99]	CaF_2	$9.6 - 9.7$	~ 800
Dimethyl ether + Ar [100, 101]	MgF_2	$10.47 - 10.6$	$600 - 750$
1-butanol + Ar [102]	MgF_2	10.53	550
Methanol + Ar [102]	MgF_2	10.76	520
Acetone [39, 93, 103, 104]	CaF_2	9.9	$320 - 480$
1-propanol + Ar [102, 105]	MgF_2	$10.54 - 10.76$	$410 - 439$
Iodine + Ar [41, 106]	SrF_2	$9.4 - 9.5$	~ 400
Ethanol + Ar [102, 105]	MgF_2	$10.61 - 10.89$	$355 - 370$
Acetone + Ar [107]	CaF_2	9.9	330
Iodine + Ar [106]	SrF_2 †	9.3	280
Acetone + Ar [107]	CaF_2 ‡	9.8	190
Acetone [93]	CaF_2 + Kr gas filter	9.72	115
Acetone + Ar [107]	SrF_2 *	9.75	110
Acetone [39]	$Ca_{0.7}Sr_{0.3}F_2$	9.7	82

Table 2.1: Bandpass combinations for Geiger-Müller photon counters in the VUV range ordered by decreasing energy width. The temperature of the alkaline earth fluoride windows is 300 K unless otherwise stated: ($\star$) 243 K, (†) 350 K and (‡) 380 K. If only one gas species is present, proportional counting is being considered.

held with an steady-flow of 70 sccm regulated by a dosing valve facing a primary scroll pump. A $[96 : 4]$ ratio of Ar/acetone provided a reasonable voltage plateau (see Appendix B) without compromising the counting stability. Higher HV tensions increase the counting rate but they are also more prone to spark discharge avalanches and unstable operation. The photoionization threshold in the acetone is 9.69 eV [108] which is smaller than the continuum emission line of Ar ~ 9.75 eV (Fig. 2.14(b)). Thus, the acetone has a twofold purpose: it triggers the ignition but also serves as quenching agent in subsequent ionization events. Another possibility (not used here) is to use iodine vapor, that provides a similar sensitivity to acetone [103] but leads to higher corrosion levels on the GM case. In addition to the detection agent, it is common to add a quenching gas typically not exceeding 5% of partial pressure since the counting rate depends on the quenching gas content [97], to avoid Townsend discharges, because the ionization rate is damped by the breaking of its covalent bonds. Yet, quenching gases may lead to a reduction on the GM counting sensitivity by carbon contamination. Carbonaceous remnants can coat the polished electrodes, producing an anisotropic field distribution of the HV tension along the cylinder and subsequently causing undesired discharges of the GM counter. Baking the GM detector out does not eliminate the carbon contamination. Plasma baths may recover the initial detector sensitivity but this requires venting the GM vessel.

Proportional mode

The detector hardware design is equivalent to the one in the Geiger-Müller mode. In this case, the detector is filled with spectroscopy grade C_3H_6O (99.8% purity) at ~ 8 to 10 mbar of vapor pressure. The proportional mode is stationary meaning that a permanent primary pumping is not needed reducing the consumption of C_3H_6O and improving the mechanical

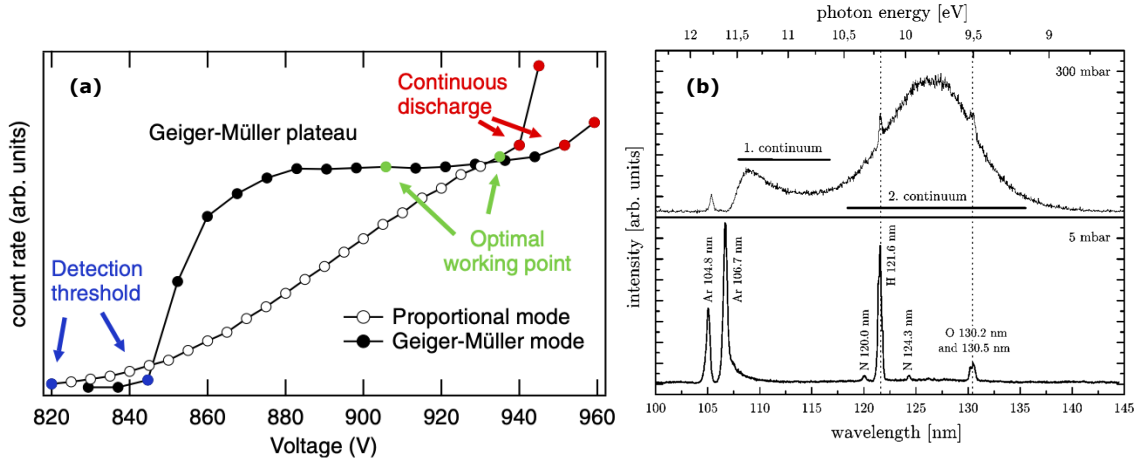

Figure 2.14: (a) Counting statistics as function of HV for the isochromat and the Geiger-Müller modes in isochromat IPES. Reproduced from [97] with permission from IOP publishing. (b) Emission lines of Ar at typical counting pressure values in IPES. Reproduced from [93] with the permission of AIP Publishing.

stability of the system.

In the proportional mode, single-photon-induced pulses can be detected and, if the statistics follows a Poisson distribution, a one-to-one correspondence between photon detection and counting rate can be assumed. Typical dead-time is around 30 μs [97] but it can be shortened to about 4 μs in modified acetone/CaF_2 detectors [104]. For this work, the CaF_2 window is attached to the housing via a Ti wire mesh sealed with a perfluorelastomer O-ring so that a high chemical and thermal resistance is reached for operating with the corrosive acetone.

3 - DEVELOPMENT & COMMISSIONING OF A SPIN- AND ANGLE-RESOLVED IPES SETUP

3.1 . INTRODUCTION AND STATE-OF-THE-ART

In recent years, the IPES technique has experienced significant advances, for instance, energy resolution better than 170 meV has been achieved by modifying the electron source and the bandpass detectors [107]. Also, the technique has been adapted to very low energies to study sensitive molecular systems (Low-Energy IPES, LEIPES) [109]. Moreover, major advances have been made concerning rotatable spin-polarized sources for probing systems with a net polarization with longitudinal and transverse components at particular points of reciprocal space [5]. Here we will focus on further development of spin-polarized electron sources. The development of polarized electron sources for IPES emerged as a necessity to elucidate exchange-splittings in ferromagnetic surfaces and thin films [110]. Out-plane magnetized samples reflected the need of sources with sensitivity to longitudinal polarization. Thus, the spatial manipulation of $\mathbf{P}$ in a low-energy electron beam is necessary to perform SPIPES without restriction on the orbital character of the system. Even though spin-polarized IPES setups are still very scarce, a whole variety of systems have been studied [5, 111, 112, 113, 114, 115, 116]. More recently, the investigation of spin-split unoccupied bands on hybrid systems of metal-semimetal or even metal-semiconductor has proliferated. We can mention studies on surface states with giant spin splitting of about 0.6 eV in the K-valley of the metal-semiconductor Tl/Si(111) [1] or WS_2/Au(111) [111], mixed orbital symmetries on Bi/Ag(111) [112], 3D topological insulators [113] or even graphene interfaces [116].

To fully exploit the capabilities of spin-resolved IPES, unrestricted control of the polarization vector is necessary and was lacking. Sampling a crystalline surface with any desired spin orientation is problematic in existing setups. The reason is that the sources control the direction of $\mathbf{P}$ with respect to the sample [5], but they cannot decouple $\mathbf{P}$ from the incidence angle of the electron beam, which controls the wavevector k that is explored in angle-resolved IPES. Therefore, the polarization vector is normal to the sample far from normal incidence, i.e. far from the Γ point in reciprocal space, particularly important for studying complex spin textures. This is a limitation for systems whose spin is normal of the surface. Also, the projection of the polarization $\mathbf{P}$ varies when changing θ or equivalently, when exploring a high-symmetry direction of reciprocal space.

Polarized electron sources have been developed to assist linear accelerators with high-brightness and highly-energetic (keV) electron beams. Landing on the side of low-energy applications, e.g. IPES, requires further adaptation to preserve the momentum resolution. Current SPIPES-dedicated electron sources supply transversely polarized electrons ($\mathbf{P}_{\parallel} \equiv \mathbf{P} \perp \mathbf{v_e}$) [5, 114] whose spin polarization is either perpendicular to or within the plane of incidence[1] depending on the geometrical configuration of the electron source. Some electron sources have a rotation axis that allows partial tuning of the polarization with respect the surface. Fig. 3.1 shows that if the electron source is in a vertical (horizontal) configuration the spin polarization of the beam is perpendicular (parallel) to the plane of incidence depending on the position of

[1]The plane of incidence is defined by the propagation vector of the electron beam and the normal vector of the surface.

the electrostatic deflector [5]. The horizontal configuration allows to measure a signal from which the out-of-plane polarization component of the sample can be extracted for $\theta \neq 0°$ and the magnitude of $\mathbf{P}$ increases in the out-of-plane while approaching a more grazing incidence.

Besides the delicate mechanical rotation of a macroscopical element (electron source) under UHV environment, there are further limitations on this approach: (i) it is not possible to study out-of-plane polarized states in the vicinity of Γ, (ii) there is a necessity of disentangling the contribution of each spin polarization (transverse, longitudinal) from the entangled experimental spectra and (iii) there is an inherent loss in the IPES intensity in the horizontal configuration associated to the projection of $\mathbf{P}$ (Eq. 2.26).

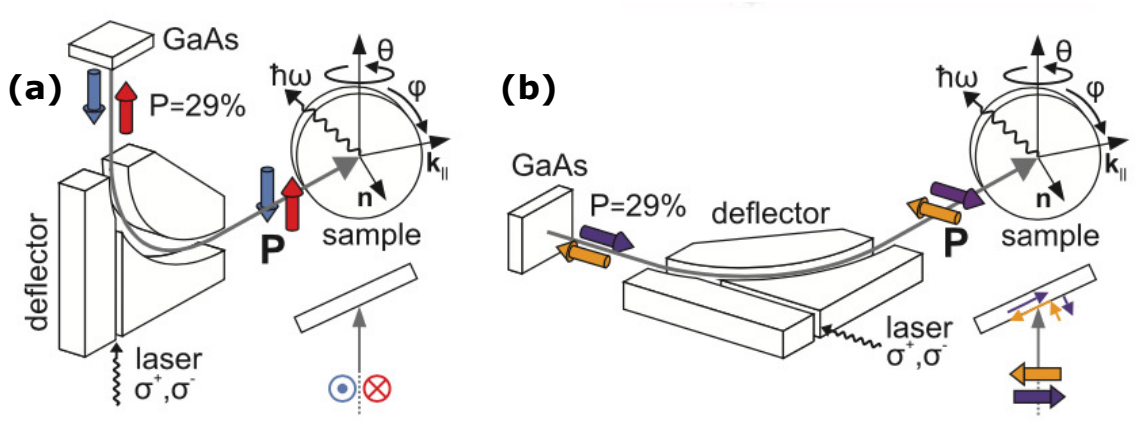

Figure 3.1: Schematic representation of a rotatable spin-polarized electron source in (a) vertical and (b) horizontal configuration. The spin polarization of the electron beam is perpendicular (parallel) to the plane of incidence in the vertical (horizontal) setup. The spin sensitivity is (a) in-plane and (b) out-of-plane polarization of the sample. Additionally, out-of-plane sensitivity is reached in the horizontal configuration for $\theta \neq 0°$ incidences. Reproduced from [5] with the permission of AIP publishing.

In order to go beyond the state-of-the-art IPES setups, a GaAs photocathode-based electron gun where $\mathbf{P}$ is independent of the incoming beam angle was constructed at the *Laboratoire de Physique des Solides* (LPS, Orsay France) and designed in collaboration with T. Duden (Constructive Solutions for Science and Technology, Bielefeld Germany). Our low-energy electron source allows to spatially tune the spin polarization $\mathbf{P}$ independently of the incidence of the parallel electron beam. The beam is controlled by a series of electron optic lenses, as firstly proposed by T. Duden [117]. Yet, the principle was adapted here to the delicate low-energy regime ($E_{kin} < 200$ eV). On isochromat IPES, the direction of the electron beam along with its kinetic energy must be known to yield $E(k)$ relationships. In addition, the k-resolution should be preserved while tuning the spin polarization vector. Also, the source must provide a high intensity current at low-energies with a narrow energy distribution. In this Chapter, we present the development of a GaAs-based electron source fulfilling the above requirements.

The instrument was characterized in terms of the energy resolution, the momentum resolution and the beam polarization through the investigation of unoccupied states in prototypical low-index noble metal surfaces exhibiting Rashba effect:

- Spin-integrated IPES on Cu(001) to determine the energy resolution from the image potential surface state and the Fermi edge.

- Spin-resolved IPES on Au(111) to obtain the effective polarization of the electron source, the wavevector resolution and also to demonstrate the spin tuning while orienting the beam polarization differently with respect the Au(111) Shockley surface state spin.

3.2 . EXPERIMENTAL SETUP AT LPS

3.2.1 . Experimental apparatus at LPS

In this Section, we describe the elements of the spin-polarized IPES setup at LPS. We will describe the UHV setup where the IPES chamber is located, the optical system for the photocathode excitation and finally, the spin-polarized electron gun.

Ultra-high vacuum setup

Our experimental setup consists of two interconnected stainless-steel vessels as shown in Fig. 3.2. One of the chambers is dedicated to perform SPIPES (analysis chamber) whereas the other serves for preparing and characterizing samples and surfaces (preparation chamber). These chambers need to be pumped to UHV conditions to preserve the surface clean from adsorbates as long as possible. Surface adsorbates modify the coupling between free electron wavefunctions (vacuum) and even Bloch bulk states [45, 118]. Also, in the analysis chamber, UHV is necessary in order that the electron beam reaches the sample without any significant losses. Therefore, a pumping system consisting of a turbomolecular pump (Agilent TwisTorr 305 FS) and an ion pump (Agilent StarCell®) with Ti sublimators, was installed on the analysis chamber. The pumping capacity was calculated by Philippe Duret (LPS, Orsay). A non-evaporable getter (NEG) pump was also included (SAES CapaciTorr Z400) to further improve the H_2 sorption capacity. A base pressure of 2×10^{-10} mbar is hold while SPIPES operation. Similarly, a base pressure better than 5×10^{-10} mbar can be achieved in the preparation chamber.

The analysis chamber includes a 5-axis cryogenic manipulator (Prevac) for the sample, that can vary the temperature between 10 K and RT. This chamber is connected to a Mott detector for characterizing the beam polarization, to two GM detectors and to the spin-polarized electron gun, located in a μ-metal chamber. The spin-polarized electron gun chamber is connected to a photocathode preparation chamber that can be isolated from the rest of the volume by a UHV gate valve so that the sample surface is preserved during the activation process (annealing/evaporation) of the photocathode. The GaAs photocathode is covered by a Mo mask with a circular hole for emitting electrons, as proposed by U. Kolac and coworkers [60]. Our photocathode is heated by an electrical current induced by a voltage drop between the GaAs clamps. The gate valve is also convenient for the replacement of degraded GaAs crystals and alkali dispensers preserving the base pressure in the electron-optics volume. The electron gun chamber also includes a slow-rate Cs dispenser to reactivate the GaAs surface and increase its lifetime. A moderated Cs exposure (yield < 1 mg/cm) can maintain steady emission current for more than 24 hours. The dosing is carefully regulated because of the proximity between the dispensers and the extractor lens (see Section 3.2.2), that might induce abrupt discharges of the photocathode. The two cylindrical GM detectors are installed such that their axes are coplanar to the electron gun axis. They are placed at azimuthal angles of $\phi = -75°$ (GM1) and $\phi = +35°$ (GM2) within the plane, $\phi = 0°$ being the electron gun axis. The counters are mounted on linear transfer lines and can be approached about 20 mm away from the sample surface.

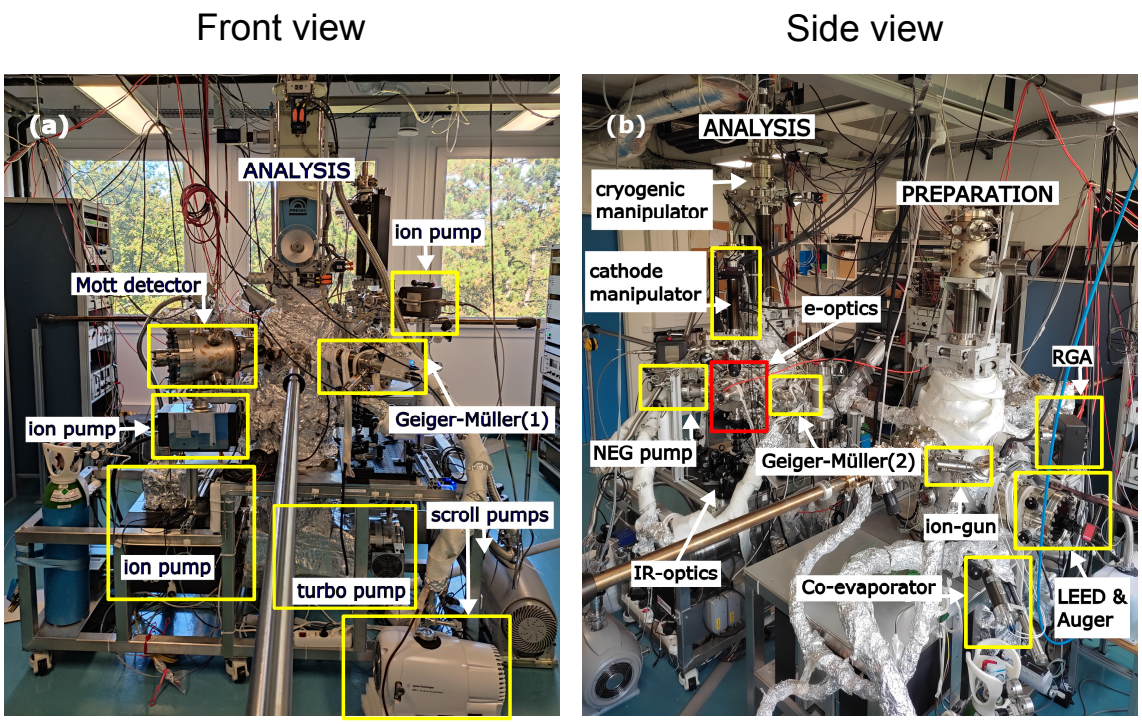

Figure 3.2: Experimental SPIPES apparatus at LPS. (a) Front view of analysis chamber with pumping elements. (b) Side view of analysis and preparation chambers with main elements. The core of the setup (electron optics) is highlighted by a red square.

The optical excitation of the photocathode

As indicated in Section 2.2, spin-polarized electrons in the electron source are photoemitted from negative electron affinity (NEA) GaAs by exciting transitions with circularly-polarized near infrared (NIR) radiation [51, 55, 56, 57]. The angular momentum conservation of either clockwise (σ^+) or anticlockwise helicity (σ^-) is used to select a component of the spin polarization in the electron beam. The optical setup for polarizing the NIR beamlight is schematized in Fig. 3.3. For the photoexcitation of the GaAs, we use a diode laser (830 nm) of 30 mW of CW power. The laser intensity on the photocathode and the helicity of the laser can be controlled by two liquid crystal (LC) retarders in alternating sequence with two Glan-Thompson polarizers. The nematic retarders are electrically operated to allow automation of the experimental process. The principle of operation of the laser system controlling the light polarization follows from an adjustable phase shift on the $\lambda/4$ waveplates and is presented in Appendix A. In summary, the first LC retarder is located between two crossed Glan-Thompson polarizers and allows the adjustment of the transmission by its variable birefringence. The second LC retarder receives linearly polarized light from the second Glan-Thompson polarizer. By invoking an adjustable phase shift, which is either set to quarter wave or three quarter wave delay, σ^+ or σ^- helicity is respectively imposed on the outgoing laser beam. Conventional IPES can be easily retrieved by changing the light source to a 630 nm red diode laser by flipping a $90°$ mirror mount. Of course, with this source the net polarization of the electron beam is zero.

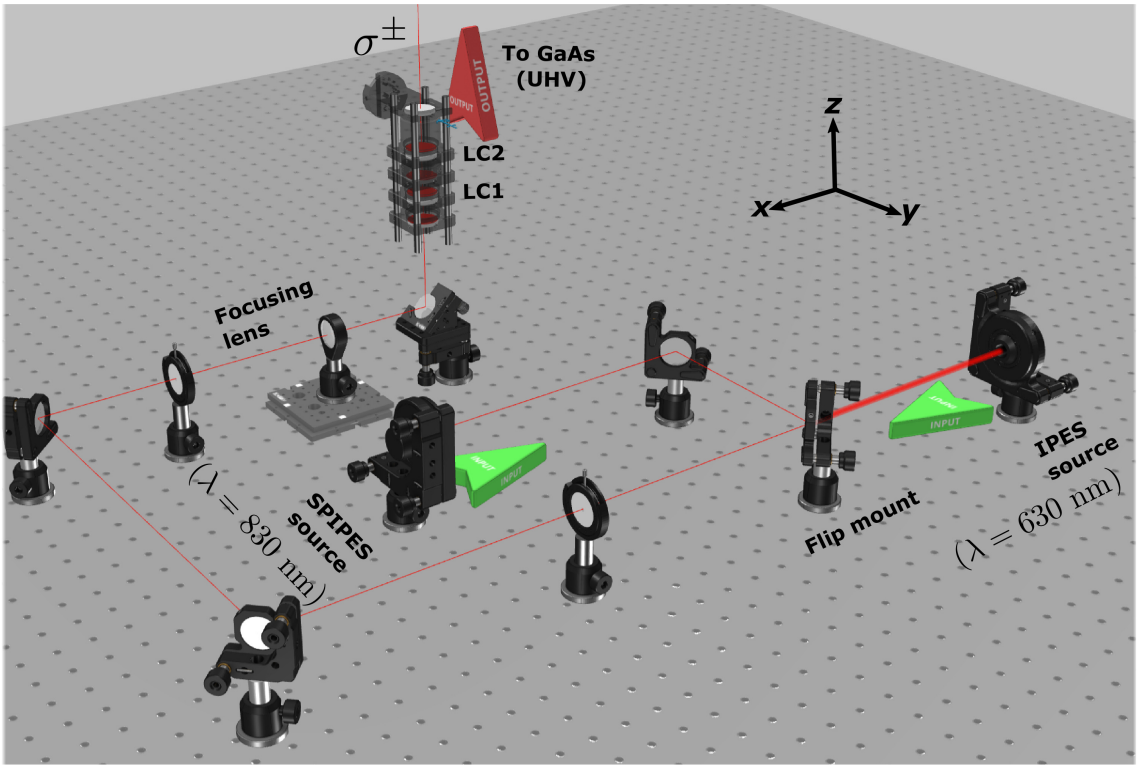

Figure 3.3: Optical arrangement for the photoexcitation of the GaAs photocathode. Nematic retarders (LC1 and LC2) are installed to automatize the control of the helicity of the NIR light. A focusing lens system permits to vary the focal position along z for vertical translations of the photocathode and to space-filter the light beam with additional pin-holes. A flipping mounting permits to easily select the light excitation source to release either polarized (SPIPES) or non-polarized electrons (IPES), depending on the wavelength of the excitation laser.

3.2.2 . The Spin-polarized electron gun

As summarized in Fig. 3.4(a), the electrons are photoemitted from the front-illuminated GaAs photocathode with $\mathbf{P}$ parallel or antiparallel to the quantization axis of the NIR light i.e., with a spin polarization parallel to their momentum. Having a proper alignment in the NIR beam is fundamental to: (i) maximize electron transmission to sample and (ii) reduce the beam depolarization by electron scattering on the UHV chamber walls.

Working with the spin of low-energy electrons is rather tricky. While tuning the polarization direction magnetic stray fields may alter the angular distribution, limiting the achievable momentum resolution, or even depolarize the electron beam [86]. Canceling the Lorentz force over the charged particles is necessary to maintain the desired trajectory of the beam. To preserve an electron beam of high quality, the electron beam is operated at 1 keV in the electron optics and only decelerates to the energies necessary for IPES at the electron gun nose, close to the sample. In addition, there is a double magnetic field screening of the electron optics. First, the electron gun is housed in a μ-metal chamber. Second, the sector field is embedded in a Permenorm® case further assuring the shielding of the electron trajectory (Fig. 3.5). A Ti extractor lens (3.4(a), pink) accelerates the electrons towards the core of the electron gun. After the extractor and a focusing, the sector field region is found. In the sector field, the superposition of electrostatic and magnetic deflecting fields, the angle between $\mathbf{P}$ and the momentum vector $\mathbf{k}$ of the transmitted electron beam can be tuned without changing the direction of the outgoing beam [119]. The electron optics allows tuning in transverse and longitudinal

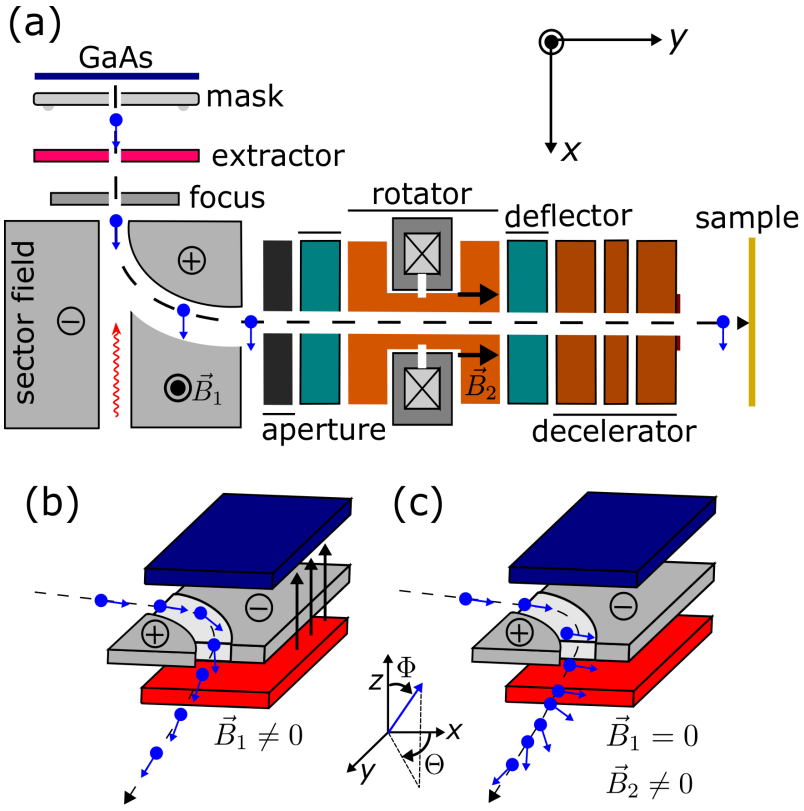

Figure 3.4: Simplified schematics of the low-energy spin-polarized electron source. (a) Photoemission from NEA-activated GaAs is produced with a circularly polarized NIR laser beam (red arrow). The electrons (blue circles) are extracted with a voltage of 2 kV in a Ti electrode (pink) and subsequently deviated in a sector field (gray). The orientation of $\mathbf{P}$ (blue arrows) is selected according to the magnetic action in the sector field as shown below. (b) Θ-rotation: magnetic deflection from the polepiece in the sector field (black arrows) allows turning the beam polarization up to longitudinal orientation ($\mathbf{P} \parallel \mathbf{v_e}$). (c) Φ-rotation: in an electrostatic deflection, in the absence of magnetic field, transverse polarization ($\mathbf{P} \perp \mathbf{v_e}$) holds after the sector field. A subsequent $\mathbf{P}$ precession around the propagation axis by applying a field $\mathbf{B_2}$ in the rotator permits to fully map $\mathbf{P}$ onto the surface.

polarization or any intermediate orientation.

The first stage of the electron gun is a compact $90°$ electromagnetic sector field (Fig. 3.4(a), gray) where secondary electrons are suppressed as in hemispherical analyzers [120]. In a non-relativistic situation as in the present case, the electrostatic field does not interact with the magnetic moment of the electrons so that the spin polarization of the beam is unaffected. In the case of purely electrostatic deflection, the initial orientation of $\mathbf{P}$ would be preserved in the laboratory frame, and the resulting beam therefore has a transverse polarization, as depicted in Fig. 3.4(c). Let us see what happens when the magnetic field $\mathbf{B_1}$ is applied. Before entering the sector field, the electron velocity $\mathbf{v_e}$ is perpendicular to a tunable magnetic field $\mathbf{B_1}$ as depicted in Fig. 3.4(b). Thus, when the field is applied ($\mathbf{B_1} \neq \mathbf{0}$), $\mathbf{P}$ rotates towards the momentum vector, allowing to obtain a longitudinal electron beam polarization. In this way, after the $90°$ circular sector, the angle Θ between the electron beam polarization and the propagation vector is controlled in between the limiting cases (i) $\mathbf{P} \parallel \mathbf{v_e}$ and (ii) $\mathbf{P} \perp \mathbf{v_e}$.

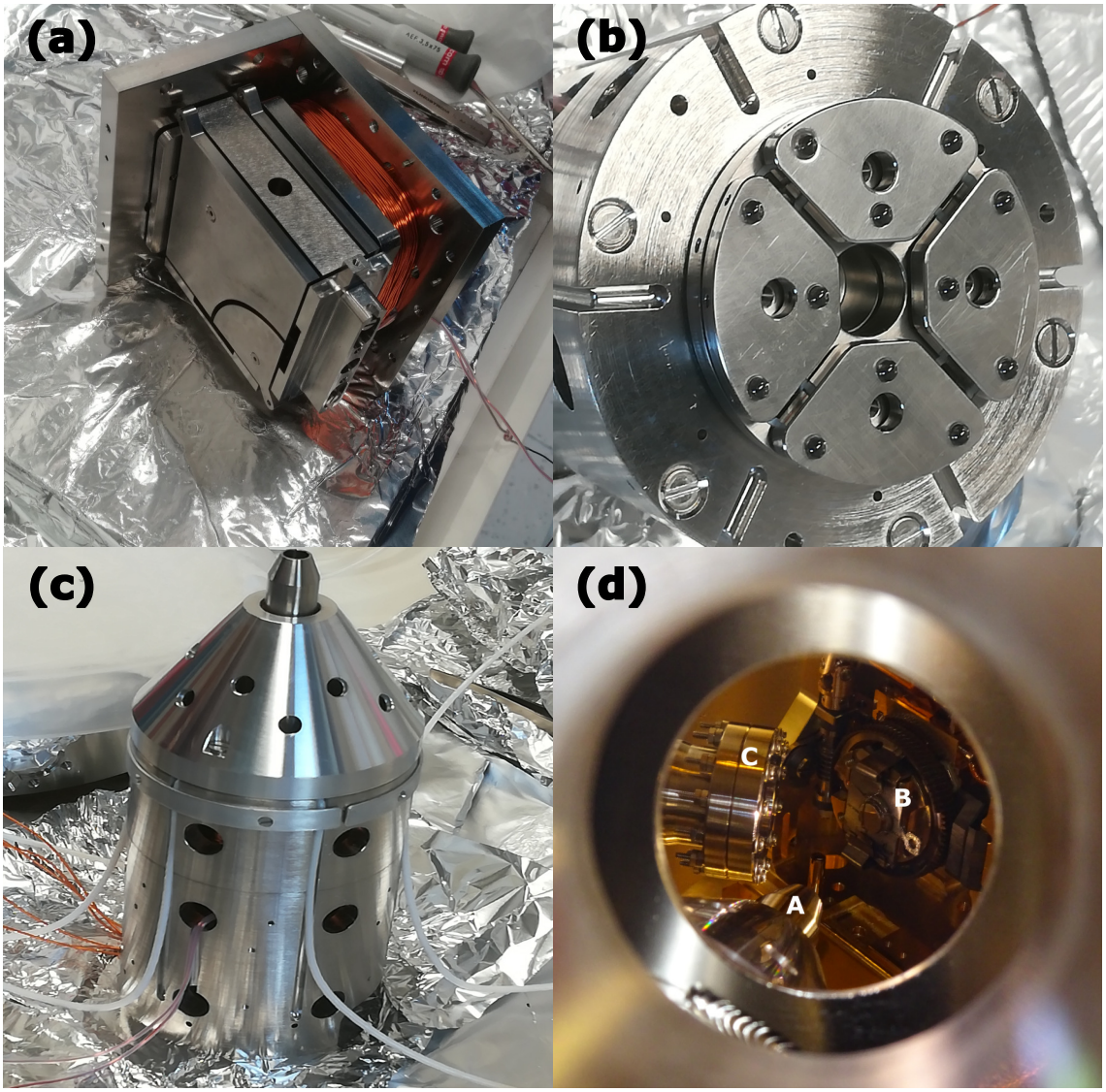

Figure 3.5: Electron optical elements during the assembly of the electron gun. (a) Electromagnetic deflector with semispherical electron spectrometer and the coils that tune Θ. (b) Rotator lens to induce $\mathbf{B_2}$ field, longitudinal to the electron trajectory. (c) Decelerator lens with the conical shielded case at the gun nose. (d) Final disposition of core components: A. Electron gun nose embedded in a conical decelerator stage (with μ-metal case), B. 5-axis manipulator with a mounted sample, C. GM1 detector entrance window. The outer (inner) circumference is a CF40 inspection window (μ-metal field shielding case).

Let us see now the polarization tuning more in detail. In the sector field, the electrons enter into a tunable magnetic field $\mathbf{B_1}$ perpendicular to their trajectory and therefore perpendicular to the electron velocity $\mathbf{v_e}$. The magnitude of $\mathbf{B_1}$ defines the direction of $\mathbf{P}$ after the sector field. When $\mathbf{B_1}$ is equal to zero, transversal polarization ($\mathbf{P} \perp \mathbf{v_e}$) is achieved. On the other hand, if $\mathbf{B_1} \neq \mathbf{0}$ the spin direction can vary between transversal to longitudinal polarization ($\mathbf{P} \parallel \mathbf{v_e}$) at the end of the sector field.

After the electromagnetic sector field, an aperture follows (Fig. 3.4(a), black), which selects only the electrons close to the beam center. Thereby, stray electrons are removed from the beam profile which would travel too far from the axis to be properly transferred through the following electron optics. In order to decrease the sensitivity to stray magnetic fields, a transfer

energy of 1 keV is set in most parts of the electron optical system, which is, for the same reason, housed inside a μ-metal screen. The selected transfer energy also aims at reducing the effects of space charge at the electron source, which could have a negative effect on the transmission [80, 81].

Then, electrons enter into the rotator stage (Fig. 3.4(a), orange) that, in analogy to the Wien-type spin twisters [121, 122], can turn at will $\mathbf{P}$ around the electron beam axis in clockwise or counterclockwise transversal rotations. The rotation angle is defined as Φ, where $\Phi \in (0°, \pm 180°)$, and it depends on the field $\mathbf{B_2}$, provided by the current in the rotator solenoid I_{rot} and the rotator voltage V_{rot}. Two additional electrostatic deflecting lenses (Fig. 3.4(a), green) preserve the location of the focal planes behind the rotator forming a focal spot on its center.

After the rotator, the electrons travel through the decelerator stage (3.4(a), brown) where E_{kin} is decreased from the transfer voltage to desired service values, below 200 eV, before reaching the sample. Refocusing lenses are positioned strategically throughout the electron trajectory.

The source was firstly operated using the theoretical parameters for currents and voltages controlling the electron optics [2]. These initial field parameters were experimentally optimized by maximizing the beam transmission T to the sample with a tightly focused beam. Rotator voltage values V_{rot} that provided with maximized T were obtained for equidistant swept steps on the rotator coils current I_{rot}. The results of the $T = T(I_{rot}, V_{rot})$ surface are shown in Fig. 3.6(a) for an electron beam of 10 eV. The optimization procedure was assisted by the Nelder-Mead (NM) method [123] in the case of Φ-rotations. Gradient-based methods e.g., Newton or the genetic algorithm, were discarded because the presence of saddle points on the $T = T(I_{rot}, V_{rot})$ surface difficult a satisfactory convergence to global maxima values. Fig. 3.6(b) shows satisfactory convergence with the NM method to $T = T_{max}$ when varying I_{rot} along different paths. The symmetry of V_{rot} with respect to the initial condition ($\mathbf{B_2} = \mathbf{0}$) can be observed. An iterative loop between the result of NM interpolation and the fine-tuning of the voltage parameters was later performed to find the parallel beam with smaller spot size on a dedicated (low-energy) phosphorescent screen at the sample position.

The variation Φ with respect the rotator current ($I_{rot} > 0$) and the corresponding transmission are shown in Fig. 3.7 for clockwise (positive) rotations with respect to the propagation vector. Conversely, the number of parameters that are to be considered for the Θ-rotation experimental optimization makes difficult to find an analytical representation of T. Yet, the transmission at the limiting angle $\Theta = 90°$ drops to approximately 20% which is a similar figure corresponding to a $\Phi = 180°$ rotation. Therefore, the spin-polarized electron source has an overall electron transmission between 60% to 20% for typical IPES experiments, i.e. for energies of $5 - 20$ eV and for current densities ($j < 0.6$ μA·mm^{-2}) that do not cause strong space-charge effects.

[2] The theoretical electron trajectories were calculated by T. Duden (Bielefeld, Germany).

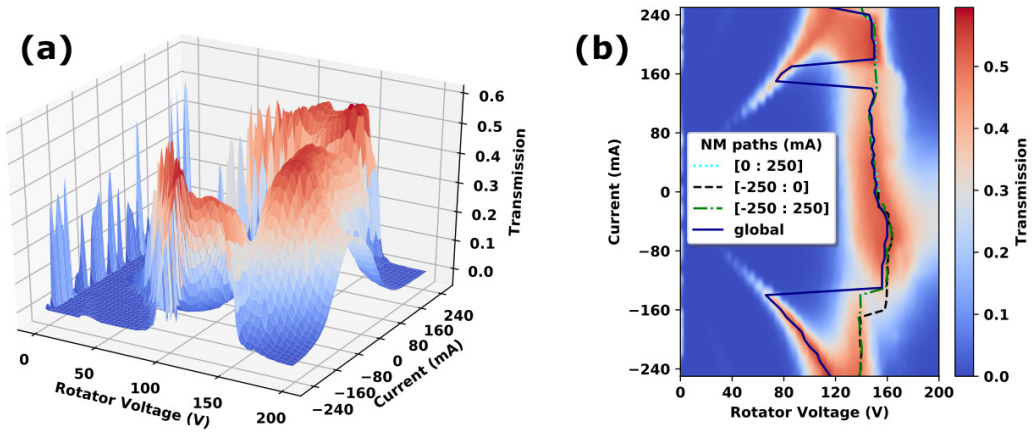

Figure 3.6: (a) Surface distribution of the experimental electron transmission as function of V_{rot} and I_{rot}. The data was gathered for a mesh of $(\Delta I_{rot}, \Delta V_{rot})$=(2 V, 10 mA). (b) Bicubic-interpolated 2D map of $T(I_{rot}, V_{rot})$. The jacobian-free NM method was applied along three paths of I_{rot} converging to maximum transmission in all the cases.

In summary, we have described how the $\mathbf{P}$ vector of a quasimonoenergetic beam can be spatially manipulated by combinations of Φ and Θ rotations while holding a particular $\mathbf{k}(\theta)$.

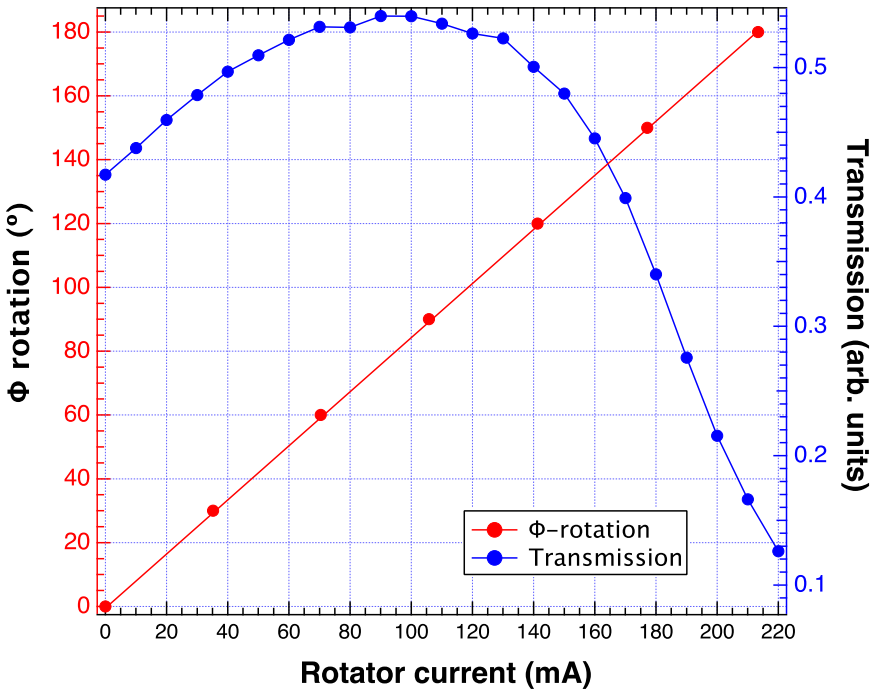

Figure 3.7: Transversal rotation of $\mathbf{P}$ and electron transmission as function of the rotator current for clockwise (positive) rotations with respect to the propagation vector.

3.3 . SPIN- AND ANGLE-RESOLVED IPES SETUP COMMISSIONING

The fabrication of the spin-polarized electron gun, after the drawings of Thomas Duden, was coordinated at LPS by Stephan Cabaret. A total of 204 non-commercial parts in different

materials (316LN, 316L, Al, Cu, CuBe, Mo, μ-metal, Permenorm, PtIr, PVC, sapphire, teflon, Ti...) were machined mainly at the LPS workshop[3] and also in the *Laboratoire Aimé Cotton*[4] and the *Laboratoire des Sciences Moleculaires d'Orsay*[5]. The assembly was then done in collaboration with Thomas Duden. Once the electron gun was assembled and mounted in the UHV chamber, the commissioning started. The commissioning has been done in two surfaces with Rashba effect on the unoccupied states: Cu(001) and Au(111). Our measurements of the unoccupied states of the noble-metal surfaces reproduce those of the literature. The total energy resolution ΔE_{tot} and the momentum resolution Δk of the setup were determined by IPES and SPIPES measurements on those surfaces. The effective polarization P of the electron source was also determined. This characterization, essential to perform IPES measurements with spin resolution, demonstrates the correct functioning of the setup.

3.3.1 . Unoccupied states in Cu(001)

Noble metal fcc surfaces are prototypical systems to assess the functioning of IPES spectrometers. In this work, a freshly prepared Cu(001) surface was used to reproduce IPES measurements from the literature and characterize the total energy resolution of our recently-built setup. The Cu surface was prepared by iterative sputtering/annealing. The sample was bombarded with Ar ions (1 keV) and annealed at 770 K until a clear LEED pattern was obtained as shown in Fig. 3.8(a). The $\overline{\Gamma X}$ along the [100] high-symmetry direction of the BZ fcc cubic lattice was explored (Fig. 3.8(b)).

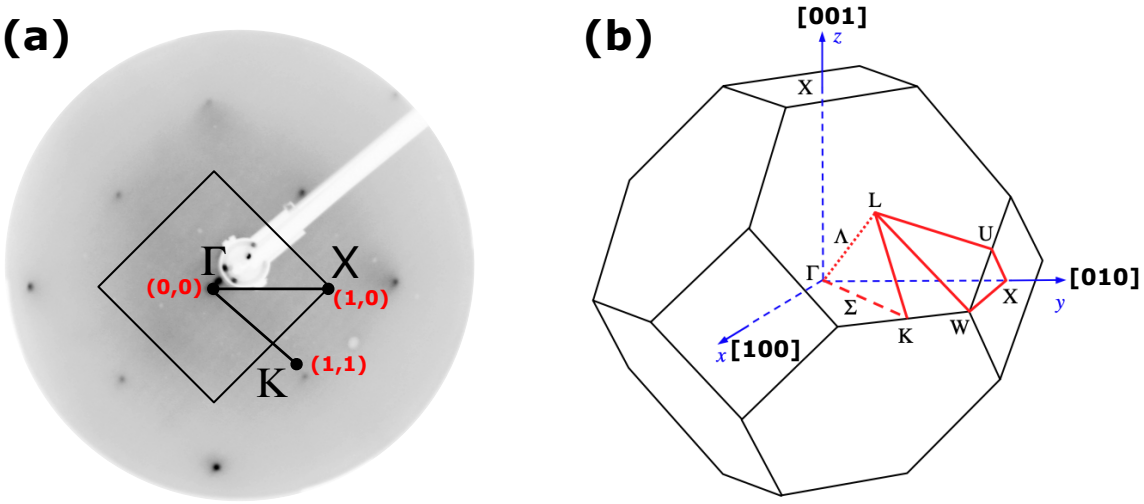

Figure 3.8: (a) Experimental LEED pattern of Cu(001) at 120 eV. (b) First BZ of the ffc structure to determine orientation of Cu(001).

A preliminary study of the integration statistics helped to determine the error bars of our IPES measurements. IPES spectra were performed with a 100 meV step and a total integration time of one minute per data point. A representative IPES spectrum of Cu(001) ($\theta = 15°$) is shown in Fig. 3.9. The raw photon counts were normalized to the sample current[6]. Error bars,

[3]Marc Bottineau, Christophe Courtot, Vira Davouloury and Ismaël Nimaga.
[4]Guillaume Dolgotworoff, Lionel Marriaux, Henri Pezard and Daniel Civiale.
[5]Jean-Philippe Dugal and Jérôme Guigand.
[6]Hereafter, the *raw* IPES data is considered as already normalized to the impinging current, unless stated otherwise.

corresponding to the standard deviation at each energy, span between 5% to 8% of the total intensity. The spectrum shows the *sp* bulk transition (B1) and the image potential (IP) surface state at ~ 1.1 eV and ~ 4.1 eV, respectively. The background, increasing at higher kinetic energies, is attributed to inelastic scattering of the incident electrons [124] *before* the radiative transition since energy losses make the electrons appear at lower energies. The one-dimensional IPES spectra can be denoised from high-frequency signals by the use of nonparametric methods e.g., Gaussian filtering [125] or singular-value decomposition [126] with minimal assumptions on the signal and the noise. This is demonstrated by the clear overlap of the averaged sweeps and the Gaussian filtered spectrum (Fig. 3.9).

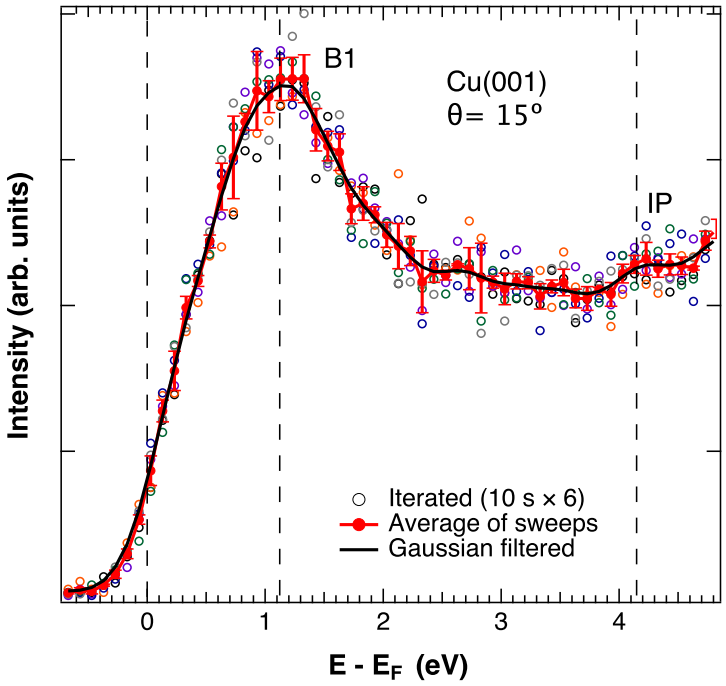

Figure 3.9: Typical IPES spectrum with the energy scale referred to the Fermi level and a 100 meV acquisition step. The data corresponds to Cu(001), at $\theta = 15°$, with one minute integration per data point.

When the incidence angle θ is varied, a particular $E(k)$ relationship can be obtained from the angle-resolved spectra. Fig. 3.10 shows spectra along the $\overline{\Gamma X}$ direction: the dispersion of the projected bulk band sp-transition (B1) and the $n = 1$ IP state. The overall dispersion is in agreement with previous studies [47, 127, 128] as observed from the comparison of panels (a) and (b). The evolution of the spectral lineshape while varying θ demonstrates the momentum resolution of the setup.

In order to compare to the literature more precisely, we extracted the $E(k)$ relationship from the binding energies of the spectral features (Fig. 3.10) and the incidence angle of the beam for each spectrum. The Cu(001) workfunction $\Phi_s = 4.6$ eV [129] and the detector bandpass energy $\hbar\omega = 9.9$ eV were considered in Eq. 2.9. The $E(\mathbf{k}_{\parallel})$ dispersion is shown in Fig. 3.11. Three features can be extracted from our IPES data (blue circles): (i) the sp bulk state (B1), (ii) the $n = 1$ image potential (IP) surface state and (iii) the Tamm (S2) surface state. Our data is in good agreement with one-step model calculations (solid-black lines) [45] and experimental IPES data (red squares) [47]. Moreover, from the four spectra where we observe the IP state,

we obtain the expected effective mass of $\frac{m*}{m} = 1$. Similarly, the sp-bulk (B1) state is also in agreement with the kinematically allowed bulk transitions (dashed-black lines) [35]. An energy shift of ~ -200 meV of the B1 band is perfectly explained by the photon detector energies that were used for the experiment: our data was taken with $\hbar\omega = 9.9$ eV whereas the reference detected photons of $\hbar\omega = 9.7$ eV. Finally, the S2 band corresponds to a Tamm surface state with $\frac{m*}{m} \sim 0.7$ [47, 130] and, due to the noise level of our data, it is difficult to clearly identify it. We have anyway shown the most plausible binding energies of the S2 state according to our data.

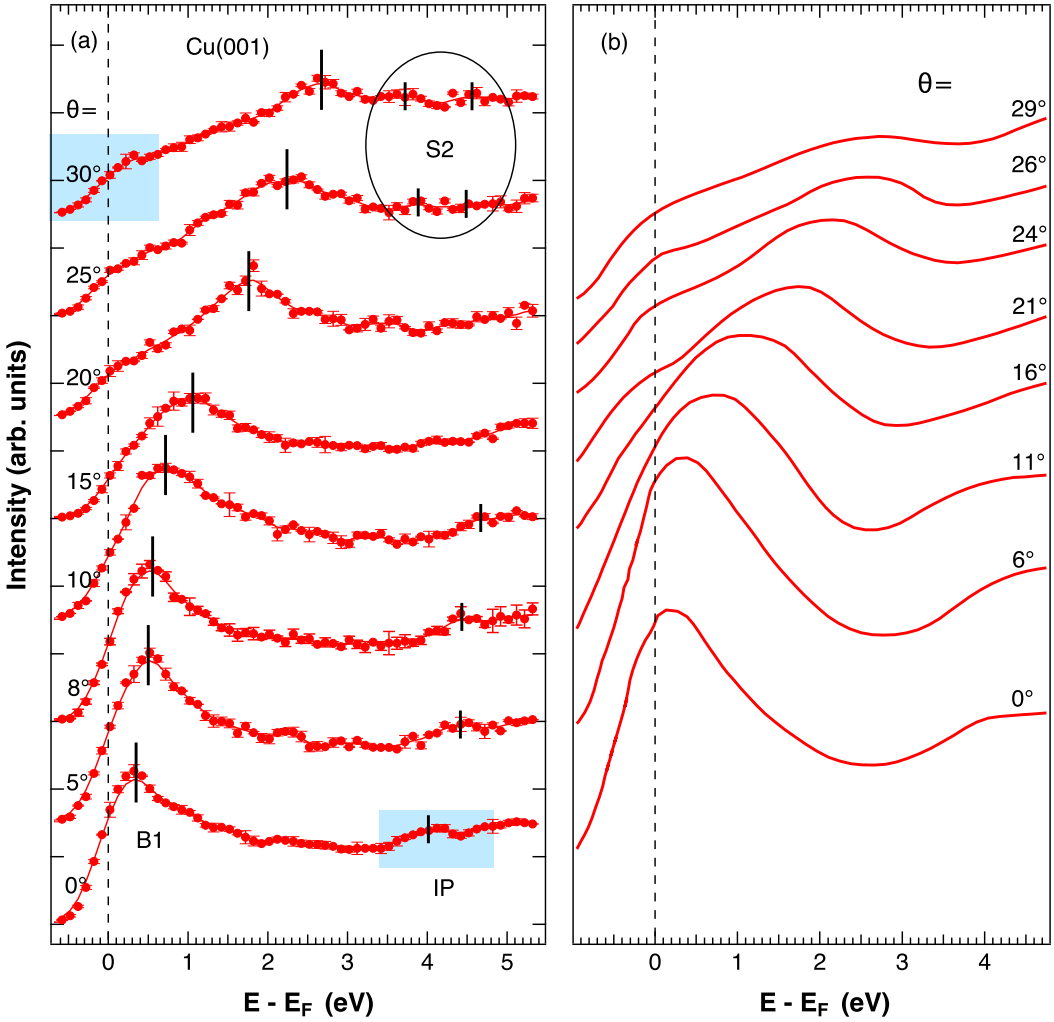

Figure 3.10: Room-temperature IPES spectra of Cu(001) along $\overline{\Gamma XUL}$. (a) Spin-integrated mode of the SPIPES setup at LPS. The $n = 1$ IP state and the Fermi step (blue-shaded insets) are used to determine the energy resolution of the setup. The raw data is compared to earliest literature [128] presented in (b), showing an overall good agreement despite a different energy reference in both experiments.

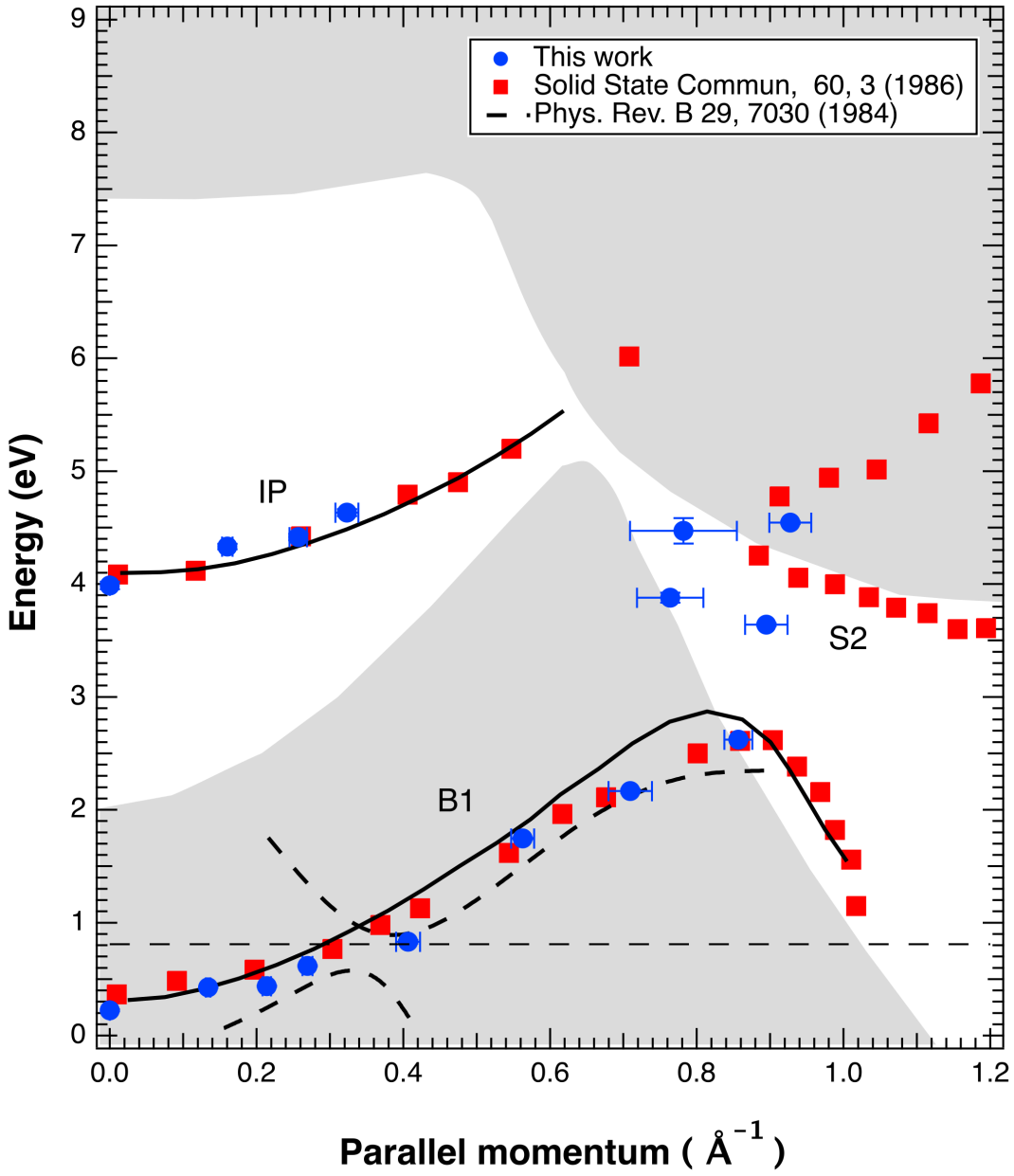

Figure 3.11: Unoccupied band dispersion of Cu(001) along $\overline{\Gamma X}$ for: (i) the sp-bulk transition (B1), (ii) the $n = 1$ image potential (IP) and the (iii) Tamm (S2) surface states. Our experimental data (blue circles) are compared to existing literature. The surface-projected bulk band structure (solid-gray full regions) and its kinematically allowed transitions (dashed-black lines) [35] are also shown. The agreement of our data with the literature demonstrates the correct operation of the IPES setup and its momentum resolution.

3.3.2 . Energy resolution

The energy resolution is a fundamental parameter in any electron spectroscopy. The inverse photoemission community has often adopted the FWHM of the Gaussian-convoluted Fermi edges [90, 107] or the FWHM of IP surface states [47, 90, 131] to characterize the energy resolution in IPES setups. The analysis of the IP width does not allow comparison to direct photoemission. We propose to estimate the energy resolution in IPES by $k_B T_{eff}$, being T_{eff} the effective temperature of the Fermi level. This parameter can be evaluated without any

further fitting, by measuring the Fermi-Dirac function in the $[10-90]$% intensity interval which corresponds to a $4k_BT_{eff}$ width. We have thus estimated the energy resolution of our setup by the usual methods for IPES and also by determining k_BT_{eff}. The three standard methods in IPES for obtaining observables related to the energy resolution are: (i) from a modified apparatus Gaussian broadening the Fermi level, (ii) from the width of image potential states and (iii) from the Fermi edge of polycrystalline metals.

One way to obtain the total resolution ΔE_{tot} of IPES setups is by considering the Fermi edge via an experimental apparatus function. The IPES spectra is described, in analogy to photoemission, by an spectral function $A(E,T)$ multiplied by the temperature-dependent Fermi-Dirac distribution for unoccupied states [5, 111]:

$$f_D(E,T) = [1 + e^{-\beta(E-\mu)}]^{-1}, \tag{3.1}$$

where $\beta = 1/K_BT$ and μ is the chemical potential. In the general case, the spectral intensity is thus

$$I(E) = G(E) \star [f_D(E,T) \cdot (\sum L_i + B)], \tag{3.2}$$

where $B(E)$ is the inherent background of the IPES signal which is

$$B(E) = a + bE, \tag{3.3}$$

where the constant a is due to *dark* counts from either cosmic radiation (γ-rays) or decaying of radioactive material in the laboratory[7] and unfortunately, it cannot be avoided [98]. The bE term is a linear inelastic scattering from the almost-constant DOS of a free-electron metal close to the Fermi level [107]. Finally, $L_i, (i \in \{1,2,...\})$ are the final-state energies that are often considered as Lorentzian peaks centered on the corresponding binding energies. Of course, for a system with no dispersion around the Fermi edge, L_i can be discarded reducing the fitting parameters of $I(E)$ and consequently those of ΔE_{tot}.

Experimentally, the finite energy resolution of the spectrometer is considered via an apparatus function $G(E)$ [107, 109] which is equal to the convolution of the optical bandpass (photon detector) and the electron energy distribution (electron source). The analytical expression of $G(E)$ is difficult to determine but it can be approximated by a Gaussian distribution [132]. Without loss of generality, the optical bandpass and the electron energy distribution can also be described by a Gaussian function. Thus, the variance σ_{tot} of the experimental apparatus can be written as

$$\sigma_{tot} = \sqrt{\sigma_o^2 + \sigma_e^2}, \tag{3.4}$$

where σ_o and σ_e are the variances of the optical bandpass and the electron energy distribution, respectively. The full-width at half maximum (FWHM) of $G(E)$, that will be represented by ΔE_{tot}, is

$$\Delta E_{tot} = 2\sqrt{2ln(2)} \cdot \sigma_{tot} = 2.35 \cdot \sigma_{tot}. \tag{3.5}$$

In Fig. 3.12(a) we present the Fermi level for $\theta = 30°$ from which is also possible to determine the energy resolution. At this angle, the bulk sp-band is well above the Fermi level

[7] Usual dark signal levels do not surpass 0.5 Hz as in the case of our setup.

so the width of the apparatus function can be obtained by a fit to the IPES signal close to E_F, as explained above. The HWHM of the apparatus function is 240 ± 20 meV.

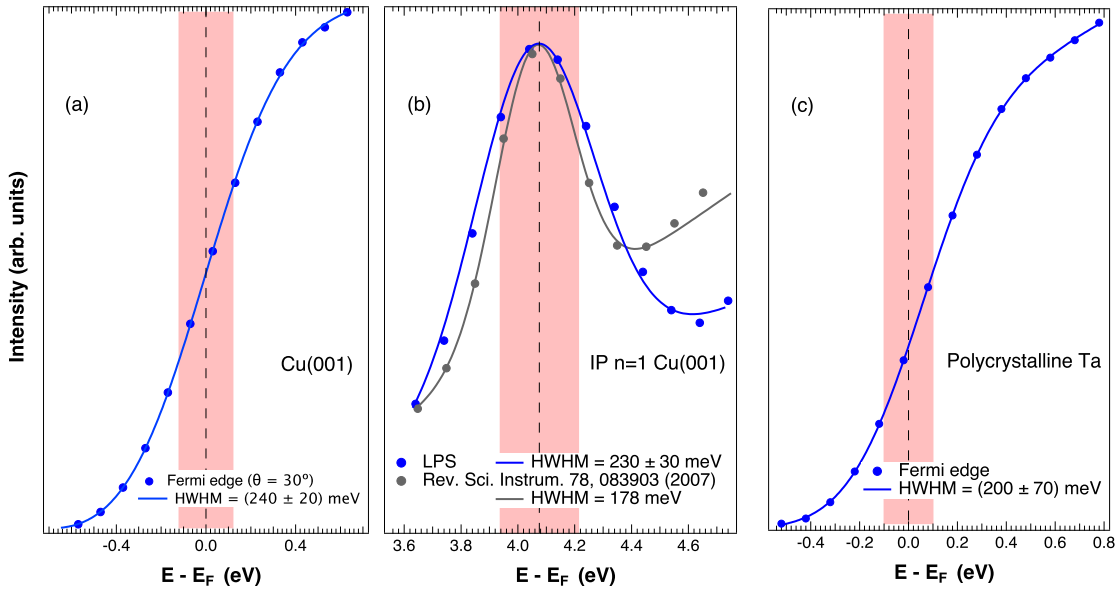

Figure 3.12: Spectra to estimate the energy resolution of our SPIPES setup: (a) Cu(001) Fermi level onset, (b) Cu(001) IP $n = 1$ state and (c) Fermi edge of polycrystalline Ta sample. The data points are fitted to experimental apparatus functions whose respective HWHM's are represented by red-shaded areas.

Another way to evaluate the energy resolution is by measuring the spectral width of $n = 1$ image potential states of metal surfaces, because they have a narrow intrinsic linewidth (very high particle lifetime) [48, 93, 107] and a unique dependency on $k_{\parallel}$. IP states are long-range interactions experienced by an electron in front of a metal surface and the small binding energies, relative to the vacuum level, indicate a weak coupling to the metal [44]. This is shown in Fig. 3.13, where the Cu(001) $n = 1, 2$ IP states are pinned to the vacuum level. IP states on low-index Cu surfaces were explored in the early days of IPES [47, 118] and they have been used to determine the energy resolution of IPES setups [93, 107]. The blue-shaded region of Fig. 3.10 at $\theta = 0°$ highlights the IP state with $n = 1$. The IP state is shown in more detail in Fig. 3.12(b). The linewidth of this state was fitted with a Gaussian over a linear background and it has a Half Width at Half Maximum (HWHM) of 230 ± 30 meV, in good agreement with previous findings [47, 131]. In particular, we contrast our data to an equivalent measurement in a more recent IPES/PES setup [90, 107] with a similar energy resolution.

A third method to characterize the energy resolution consists on measuring polycrystalline metals [133] because their spectra can be fitted by a Fermi function. Thus, we have performed IPES on a polycrystalline Ta sample, that was prepared by Ar^+ sputtering (1 keV) and annealing at 900 K before the measurement. The IPES signal, presented in Fig. 3.12(c), is deconvolved in a region close to the Fermi level and simulations are performed until a satisfactory fitting is achieved. The deconvolved Gaussian has a HWHM $= 200 \pm 70$ meV, in agreement to measurements [112] taken with an equivalent source (GaAs) and photon window (CaF_2).

All the above methods are consistent to each other and correspond to a FWHM of 540 meV as in other IPES setups. This value underestimates the resolution since the standard deviation of the Gaussians is closer to the HWHM, because $\sigma_{tot} = 0.85 \times$HWHM. Assuming that σ_{tot} is

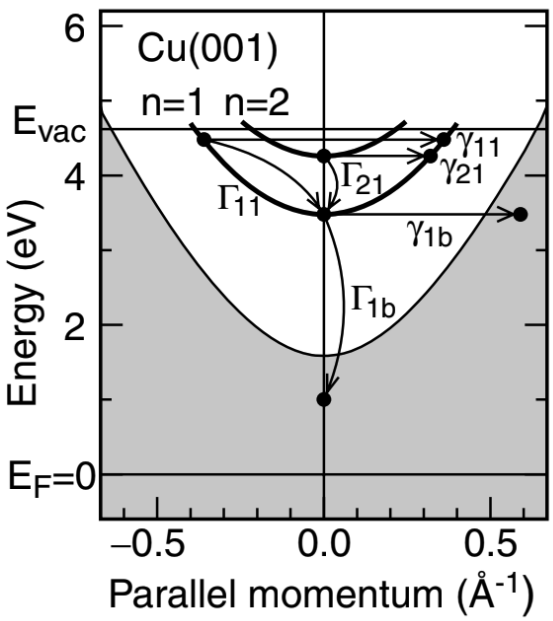

Figure 3.13: Projected band structure of Cu(001) with bulk dispersion (shaded area) and $n = 1, 2$ IP states with arrows indicating possible scattering processes. The binding energy of the IP states is scaled by a factor of 2. Adapted from [44] with permission of John Wiley and Sons Publishing.

a direct measure of the energy resolution, we get ~ 230 meV as the upper limit of ΔE_{tot}.

Finally, a straightforward way to compare the experimental resolutions of different experimental setups, valid also for photoemission, is to evaluate the effective thermal energy $k_B T_{eff}$ of the experimental Fermi level that includes all the broadening sources in the setup. The convolution of the Fermi-Dirac function with $G(E)$ corresponds to a new Fermi function with an effective temperature T_{eff} [134] where,

$$T_{eff} = \sqrt{T^2 + \left(\frac{\Delta E_{tot}}{4k_B}\right)^2}. \tag{3.6}$$

In order to obtain a value for ΔE_{tot} without any mathematical treatment or fitting to a Fermi function, we have measured the width of the Fermi edge between 10% and 90% of its intensity (Fig. 3.12(a)), obtaining that $4k_B T_{eff} \sim 680$ meV and therefore $k_B T_{eff} = 170$ meV. With this value in mind, it should be noticed that the ability to distinguish spin up from spin down electrons by using alternated probing beams allows the observation of splittings even smaller than the energy resolution [92, 135].

Taking into account all the above estimations, an overall energy resolution of $\Delta E_{tot} = 200 \pm 30$ meV is obtained. Even though the resolution has been determined from spin-integrated measurements (Fig. 3.12), it turns out that, ΔE_{tot} is equivalent for either spin-resolved or spin-integrated IPES (see Section 2.2). In IPES, the spin information is encoded in the excitation (probe). There is no need of analyzing the polarization of the VUV photons so the energy resolution is directly obtained from a spin-integrated spectrum. It would not have been the case for ARPES where the energy resolution is relaxed when spin-resolved measurements are performed due to the low efficiency of the detection of spin polarized electrons [38]. For instance, an intensity loss of about three orders of magnitude decreases the resolution from 10 meV to 100 meV [107].

Once the total resolution is determined, we can wonder whether the photon detector or the electron beam are limiting the resolution. Since the bandpass energy of detectors similar to ours have a FWHM of 330 meV when operated at RT [97] (see Table 2.1) we get that $\sigma_o = 140$

meV. From Eq. 3.4 and considering $\Delta E_{tot} \sim 200$ meV, we obtained an energy width of the electron beam of $\sigma_e = 143$ meV and we conclude that the energy resolution is affected almost equally by the optical bandpass and the thermal distribution of the electron beam.

The energy resolution of the setup can be enhanced by modifying the temperature of the alkaline earth window in isochromat detectors which decreases the detection bandpass [107]. Another possibility is to reduce the energy bandwith of the electron distribution. This can be achieved by decreasing the aperture diameter before the rotator lens (Section 3.2.2) but this directly impacts the counting statistics because of the reduction of the electron transmission. In our setup, the aperture can be modified by diaphragms of 5, 10 and 100 μm diameter and for example, changing the aperture from 100 μm to 5 μm drops the transmission $\sim 60\%$. We have therefore monochromatized the electron beam by decreasing the photocathode temperature. This has been already studied in photoemission experiments where the energy distribution of GaAs photoelectrons is highly reduced when the photocathode is at 77 K [54]. The consequences of a low-temperature photocathode are understood from the relation $E_g(T)$ (Fig. 2.5): (i) the GaAs bandgap energy increases and limits the available transitions for the fixed NIR excitation, (ii) the energy distribution of the electron beam is narrowed and therefore, (iii) the energy resolution of IPES increased (see for instance Eq. 3.4). We observed the effect of the photocathode temperature on IPES data on the Au(111) Shockley surface state (Fig. 3.14). The measurements were performed at two temperatures of the GaAs photocathode, 77 K (solid triangles) and 300 K (empty triangles), both taken with the same current density over the sample. In the high temperature case, the linewidth is broadened and the intensity decreased for both spin components of the state. At 300 K (77 K) the FWHM of the polarized states are 1.73 (0.83) eV and 1.53 (0.91) eV for the spin up and spin down, respectively.

We can assume that the electrons arriving to the sample are free electrons so that their dispersion relation is $E(k) = \hbar^2 k^2/2m$. Therefore their distribution is simply:

$$\Delta E = \frac{\hbar^2}{m} k \Delta k. \tag{3.7}$$

Considering the transverse momentum distribution of the electron beam Δk (Eq. 2.18) in Eq. 3.7 we get that

$$\Delta E(k,T) = \frac{2\hbar}{m} k \sqrt{2 m k_B T ln(2)}. \tag{3.8}$$

If only the photocathode temperature is varied the change between energy distributions can be quantified at each k_i-point:

$$\Delta E(k_i,T_1) - \Delta E(k_i,T_2) = \frac{2\hbar k_i \sqrt{2 m k_B ln(2)}}{m} (T_1^{1/2} - T_2^{1/2}). \tag{3.9}$$

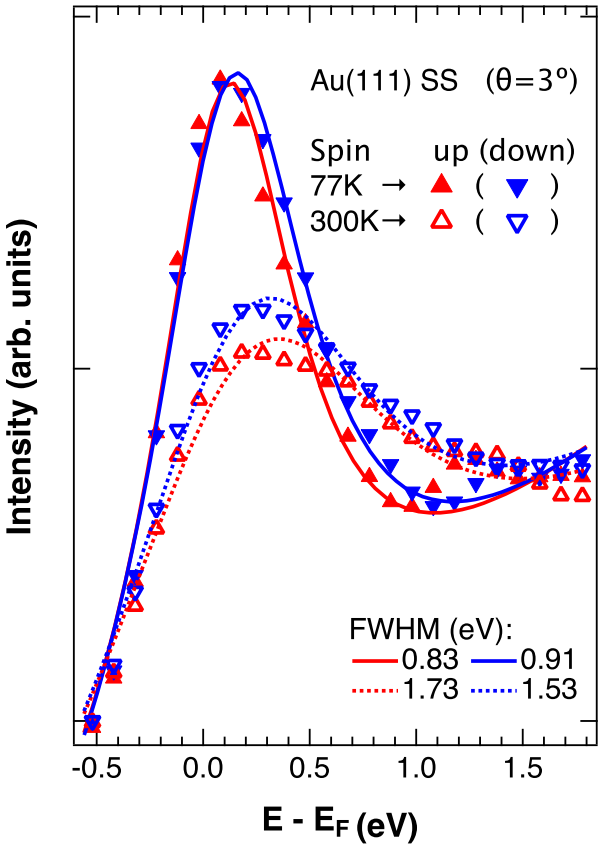

Figure 3.14: Shockley SS of Au(111) at $\theta = 3°$ incidence as a function of the photocathode temperature. The linewidths of the spin-polarized spectra are reduced when the photocathode is held at 77 K, as shown in the FWHM of the fitting (lines), due to the better monochromatism of the electron beam.

Let us estimate the energy distribution due to the variation of the photocathode temperature. Considering the binding energy of the spin down state in Fig. 3.14 as $E^{\downarrow} \sim 0.2$ eV we get that $k_{\parallel} \sim 0.06$ Å^{-1} and feeding this value in Eq. 3.9 we get that $\Delta E(300) - \Delta E(77) = 62 - 32 = 30$ meV. In other words, the electron beam increases its energy distribution by about 30 meV if operated at room temperature with respect to 77 K. An energy distribution of the electron beam of ~ 60 meV (300 K) is slightly underestimated since previously we calculated that $\sigma_e \sim 40$ meV.

3.3.3 . Spin resolution

In the following, we will demonstrate the spin resolution of the SPIPES setup by considering a spin-polarized surface state in Au(111). Low-index Au systems host a spin-polarized SS. The inversion asymmetry at the surface raises a spin-split SS at the L-gap consistent with the Rashba-Bychkov spin-orbit coupling of 2D gases, observed in the Au(111) [38, 136] or in the Au(110) [137] surfaces. The spin splitting emerges from the atomic field and its magnitude is influenced by adsorbates at the surface [138] and herringbone reconstruction [139]. Initially, the surface reconstruction was considered the cause of the band splitting but the debate was closed after ARPES measurements by S. LaShell and collaborators [25] that demonstrated the existence of the sp-derived SS splitting along $\overline{\Gamma K}$ but also along $\overline{\Gamma M}$, where no effect of the reconstruction should appear.

For analyzing the spin resolution of our setup, we have thus determined the electronic structure of Au(111) by spin- and k-resolved IPES at RT. The Au(111) surface was prepared by Ar ion sputtering (1 keV) and annealing at 800 K and this cycle was repeated over ten times until a clear LEED pattern was visible. The orientation of the surface was determined by the LEED pattern with sixfold symmetry (Fig. 3.15(a)). The $\overline{\Gamma M}$ direction was selected for measurements to avoid any influence of the herringbone reconstruction on the SS [139]. The experimental geometry in real space is presented in 3.15(b) where θ_i is the polar angle of the sample. The angle between the electron beam and the GM detector is fixed ($75°$). The GaAs photocathode was illuminated with NIR light of positive and negative helicity to invert the spin polarization of the electron beam (see Fig. 3.3) with an integration time of 30 s per data point. The polarization $\mathbf{P}$ of the electron beam is indicated by red-up and blue-down arrows that are perpendicular to the plane of incidence. In this configuration, the polarization of the beam remains in the Au(111) surface but it is always perpendicular to $\mathbf{k}_{\|}$.

The normalized-to-target-current SPIPES spectra are summarized in Fig. 3.15(c)-(d) for $-7° \leq \theta \leq 65°$. Fig. 3.15(c) shows the Shockley SS dispersion while Fig. 3.15(d) shows the surface resonance (SR) and B1 and B2 bulk states. Pseudo-Voigt fitting curves on top of a linear background (color lines) are included as a guide to the eye.

From Fig. 3.15 we can extract the dispersion relationships $E(k)$ for spin up and spin down (Fig. 3.16) from the binding energies (peak positions) at each corresponding wavevector related to θ according to:

$$\theta = sin^{-1}\left(\frac{k}{0.512\sqrt{E_f + \hbar\omega - \Phi_s}}\right), \tag{3.10}$$

where the detection energy of our GM counter ($\hbar\omega = 9.9$ eV) and the Au(111) workfunction ($\Phi_s = 5.26$ eV [140, 141]) have to be considered. The Shockley SS crosses the Fermi level at $k_F^{\downarrow} = 0.153$ Å^{-1} and $k_F^{\uparrow} = 0.177$ Å^{-1} in agreement with [25]. These wavevectors correspond to the angles $\theta^{\downarrow} = 8.0°$ and $\theta^{\uparrow} = 9.2°$. The band dispersion $E(\mathbf{k}_{||})$ is then extracted from the fitted pseudo-Voigt peaks on top of a linear background function [25].

Fig. 3.16 shows the SS, the SR and B1 and B2. In principle, the SS should be observed for $k > k_F$ (at the $k > 0$ branch). However, it can be seen that the SS is experimentally observed by SPIPES in occupied k-points at the center of the surface BZ, i.e. in reciprocal space regions where, a priori, the SS is only observable by photoemission. This is a consequence of the finite energy resolution in IPES that allows to probe occupied states close to the Fermi level.

Fig. 3.16 also shows the surface resonance (SR) within the projected bulk bands [142, 143]. Surface resonances have been extensively observed by inverse photoemission in fcc (111) metallic surfaces such as Cu [144, 145], Ag [146] and Ni [41, 147]. Finally, sp-like bulk transitions B1 and B2 are observed at $k > 0.55$ Å^{-1}. A clear spin asymmetry is observed in the B1 state ($\theta \geq 49°$). This state should not be spin-polarized but it has been experimentally observed before [49] and explained by a pseudo Rashba-effect for the unoccupied bulk transition ascribed to initial-state effects.

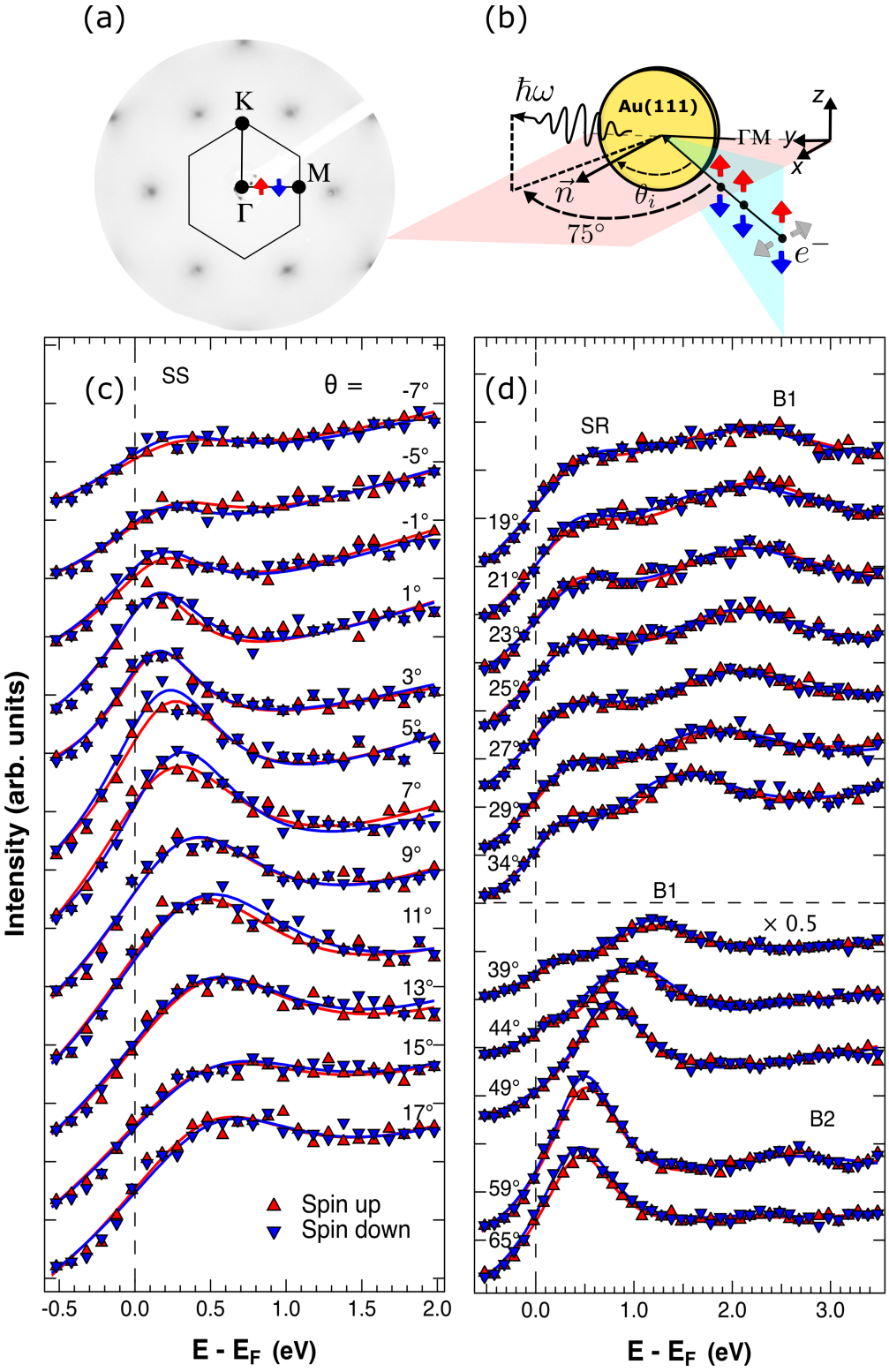

Figure 3.15: (a) LEED pattern of Au(111) at 150 eV with sixfold symmetry. The up-red (down-blue) arrow depicts the spin up (down) component of $\mathbf{P}$. (b) Experimental geometry of the SPIPES on Au(111) measured with the GM1 detector. SPIPES on Au(111) at RT along $\overline{\Gamma M}$ showing (c) SS and (d) surface resonance and bulk states (B1 and B2). The data is normalized to the beam current and the spectral intensities are multiplied by 0.5 intensity for $\theta \geq 39°$. Fitting curves (color lines) are also shown.

A priori, the SS should have the same intensity along the spanning k-space. However, this is not the case for the data in Fig. 3.15. For instance, the spectra of $\theta = -7°$ and $\theta = 11°$ have significant differences in their signal-to-noise ratio. In fact, in Fig. 3.15(c) the SS spectral intensity: (i) highly reduces at negative θ, (ii) increases and keeps more or less constant in between $\theta = 5°$ to $\theta = 11°$ and, (iii) further decreases until reaching $\theta = 17°$. This variation of intensity is explained by the matrix element effects and the particular experimental geometry that was used for acquiring the data. Indeed, the SPIPES spectra are affected by the take-off angle of the photons and the position of the GM1 detector that, in this case, favors the counting statistics for higher values of reciprocal space. With these considerations, the spectral intensity of the SS is consistent up to the $\theta = 11°$ spectrum but contradicts the intensity diminution of the $\theta = 15°$ and $\theta = 17°$ spectra. It turns out that, despite that the Au(111) SS follows the nearly-free-electron (NFE) model [24], it becomes a SR and projects into the bulk band region, dispersing towards lower energies. Thus, the $\theta = 17°$ spectrum marks the interface between the pristine SS and the SR and its intensity diminution is merely related to a migrated spectral weight into the bulk. The SR is continued in Fig. 3.15(d) where its intensity further decreases until it is no longer detectable at $\theta > 39°$. Similarly, B1 and B2 disperse to lower energies but with an increasing signal intensity that was multiplied by 0.5 for $\theta \geq 39°$.

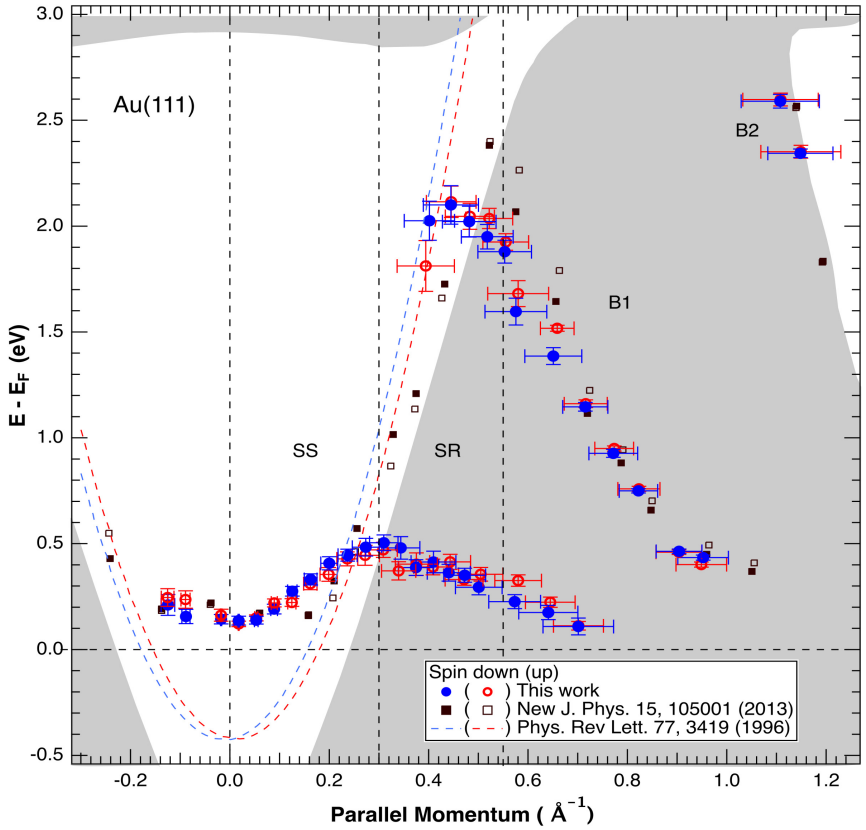

Figure 3.16: Spin-polarized energy dispersion of Au(111) along $\overline{\Gamma M}$ derived from the fitted data of Fig. 3.15. Three states are observed: the Shockley surface state (SS) that follows the NFE model, the spin-resonance (SR) and the bulk states (B1 and B2). Discrete values of the spin down (up) component are shown as solid (empty) circles. Reference data are shown as squares from [49]. The calculated projection of the spin down (up) SS is shown as a dashed-blue (dashed-red) line reprinted from [25]. The surface-projected bulk band structure is depicted by solid-gray regions (reprinted from [142]).

Now we will discuss on the spectral intensity of the spin up and spin down components. In a first approach, the spin up and spin down components of their respective θ spectrum should have the same intensity. Our data is consistent in most of the spectra except at the $\theta = 5°$ and $\theta = 7°$ spectra where the intensity of the spin down state is favored over the spin up state. This effect could be explained by the k-resolution, considering that both probing angles are in fact closer to the excitation of the spin down state ($\theta^{\downarrow} = 8.0°$) than the spin up state ($\theta^{\uparrow} = 9.2°$). This trend is not followed at the subsequent incidences, $\theta = 9°$ and $\theta = 11°$, where both states have an equivalent intensity. In order to give more insight into this effect and test our assumption, we take advantage of the symmetry of the SS dispersion at $\theta = 0°$ in Fig. 3.17. A small but noticeable intensity difference is inverted at the $\theta = \pm 4°$ spectra as expected. The symmetry of the SS with respect to the sample normal can be nicely observed in Fig. 3.15. The spectra at $k = \pm 0.134$ Å^{-1} exemplify the inversion of binding energies between spin down and spin up states respect to the normal incidence ($\theta = 0°$).

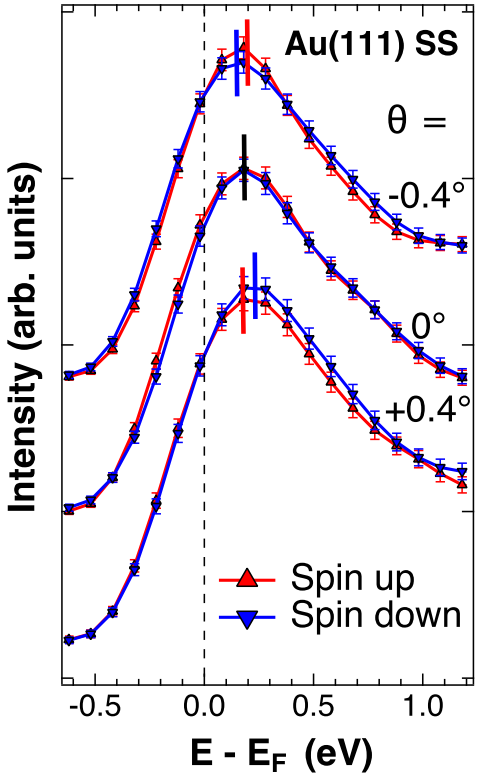

Figure 3.17: SPIPES spectra of Au(111) surface state around the Γ-point ($\theta = 0°$) from where $k_F^{\uparrow}$ and $k_F^{\downarrow}$ are at the same distance. As expected, the intensity of the spin down (up) spectrum at $\theta = +0.4°$ ($\theta = -0.4°$) is higher at the binding energy marked by vertical lines of corresponding colors. At Γ, the binding energy of both states appears at the same energy (vertical black line).

An alternative way of representing Fig. 3.16 while including the intensities of the spectra in Fig. 3.15 is by doing a 2D color plot of $E(k)$ where the color represents the intensity. In order to enhance dispersive features and to localize extreme points in $E(k_{\parallel})$ dispersion plots, the ARPES community has developed a representation of the second derivative of these color plots. Similarly, the curvature method can be used and it renders more precise results [148] in 2D dispersive plots as compare to the second derivative. We have applied this to the Au(111) SPIPES data and the resulting dispersion relation is summarized in Fig. 3.18 for the spin up, spin down and their difference.

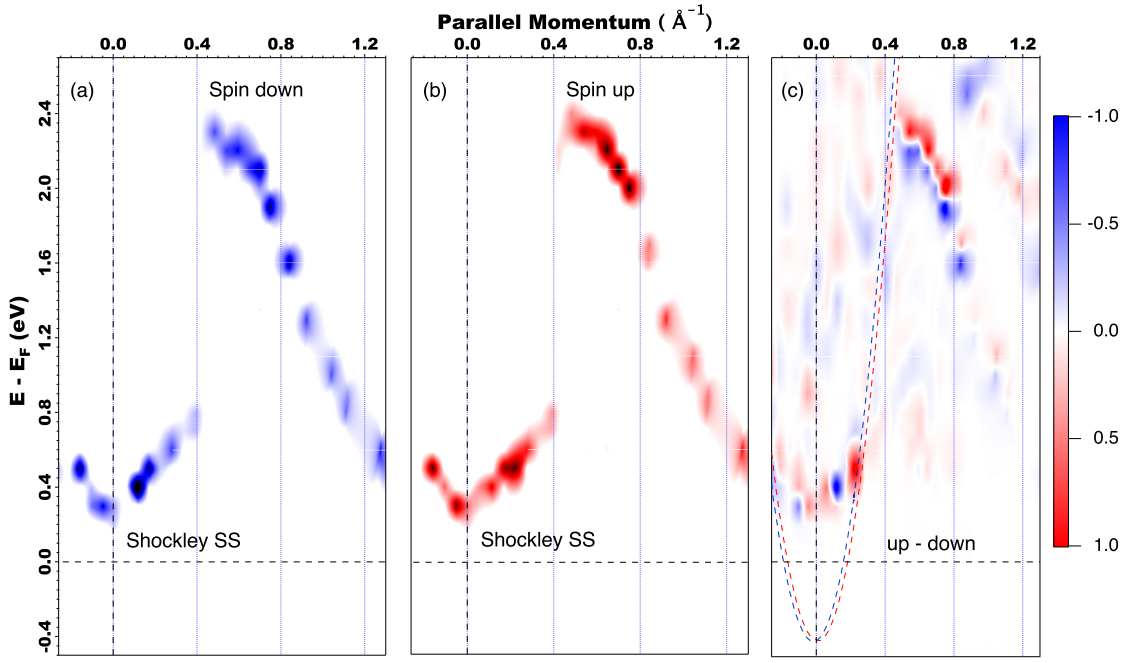

Figure 3.18: Curvature of the Au(111) dispersion relation above E_F for (a) spin down and (b) spin up component. Voronoi interpolation has been applied to the discrete data sets. (c) $I_\uparrow - I_\downarrow$ dispersion with intensity color bar (spin up: red, spin down: blue).

3.3.4 . Effective polarization

In order to estimate the polarization P of the electron source, we have compared the spin asymmetry of the Au(111) SPIPES spectra to those of the literature. The B1 state of Au(111) has a prominent spin asymmetry at $\theta = 56°$ [49] as observed in Fig. 3.15. The detail of this state ($\theta = 56°$) is shown in Fig. 3.19(a). The intensity ratio between the spin down and spin up contributions can be simulated [92] by considering the effective source polarization as a free parameter in Eq. 2.24. We have then compared our data with an already P-calibrated electron source [49] of similar energy resolution and geometry of the photon detector. Without loss of generality, the intensity of the spin down component is normalized to one so that the changes of the spin up component intensity are due to the polarization (Fig. 3.19(b)).

An effective polarization of $P = 0.30 \pm 0.03$ follows from the comparison of the simulated spectra in Fig. 3.19(b) as experimentally expected in GaAs-based electron sources. Even though the theoretical polarization of a GaAs source should be 0.5 according to only the optical transitions, the experimental polarization is always smaller because of depolarization processes, such as: (i) electron beam reflections in the chamber walls, (ii) electron scattering at the Cs_2O layer and (iii) non-homogeneous field distribution of the polepieces. Naturally, (i) can be minimized by NIR laser alignment and by maximizing the electron transmission to the sample. On the contrary, (ii) is an intrinsic consequence of the experiment and cannot be eradicated and (iii) may be even difficult to quantify but particular attention has been paid to the manufacture of the active elements that act on $\mathbf{P}$.

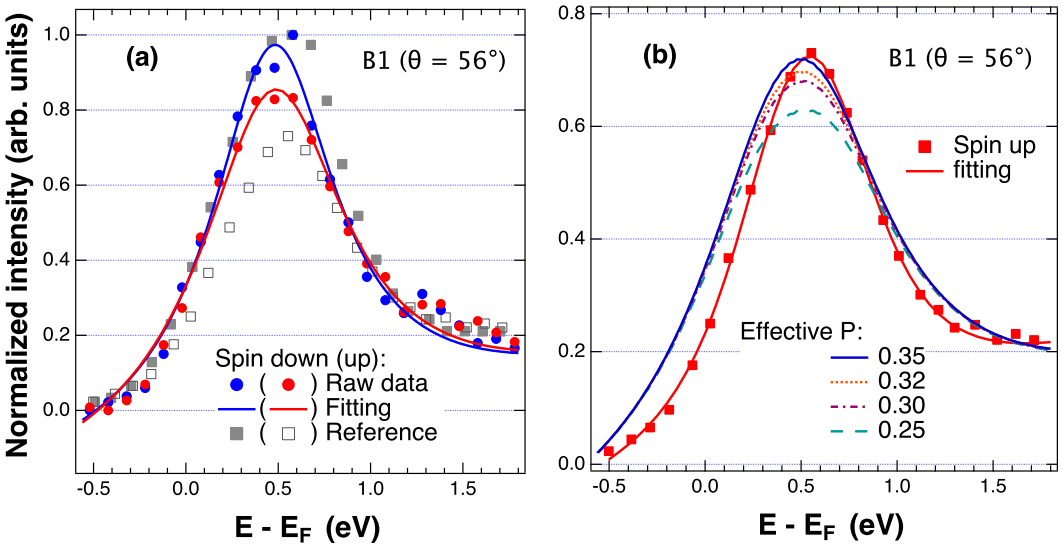

Figure 3.19: SPIPES spectra of Au(111) bulk state at $\theta = 56°$ of our data (circles and lines) with an integration time of one minute per point. Reference data ($P = 0.33$) (squares) from [49]. The spin down (up) component is represented by solid (empty) markers. (b) Polarization-dependent simulation (lines) on the spin up component of reference with calibrated polarization. An effective polarization of $P = 0.30 \pm 0.03$ is estimated for the electron source.

Let us just double check our estimation of P by normalizing the Au(111) SS as if the beam had a 100% polarization [92, 5]. For that, we consider the spectra at $\theta = 8°$ with the polarization vector of the electron beam parallel and anti-parallel to the polarization of the state. The normalized-to-current spectra are presented in Fig. 3.20(a) with error bars that indicate the standard deviation at each binding energy. We can remark a nonzero asymmetry precisely at the SS binding energy with a partial overlap of the error bars. When considering a totally polarized electron beam by normalization to $P = 0.30$, the asymmetry is magnified as shown in 3.20(b). After the treatment, there are two features that demonstrate the correct calibration of the effective polarization:

- A spin asymmetry $A \sim 1.6$ in agreement with reported observations [49].

- The energy splitting of $\Delta E \sim 120 \pm 20$ meV, from the pseudo-Voigt fitting (lines) is in agreement with the experimental (110 meV) and theoretical estimations (~ 150 meV) [25]. The slight difference with respect the expected experimental value can be due to surface adsorbates, specially by rare gases [149] or Cs or O_2 coming from the photocathode activations. It is known that O_2 adsorption enhances the exchange-splitting in ferromagnetic systems [150] but, to our knowledge, this has not been clarified for the case of noble metals.

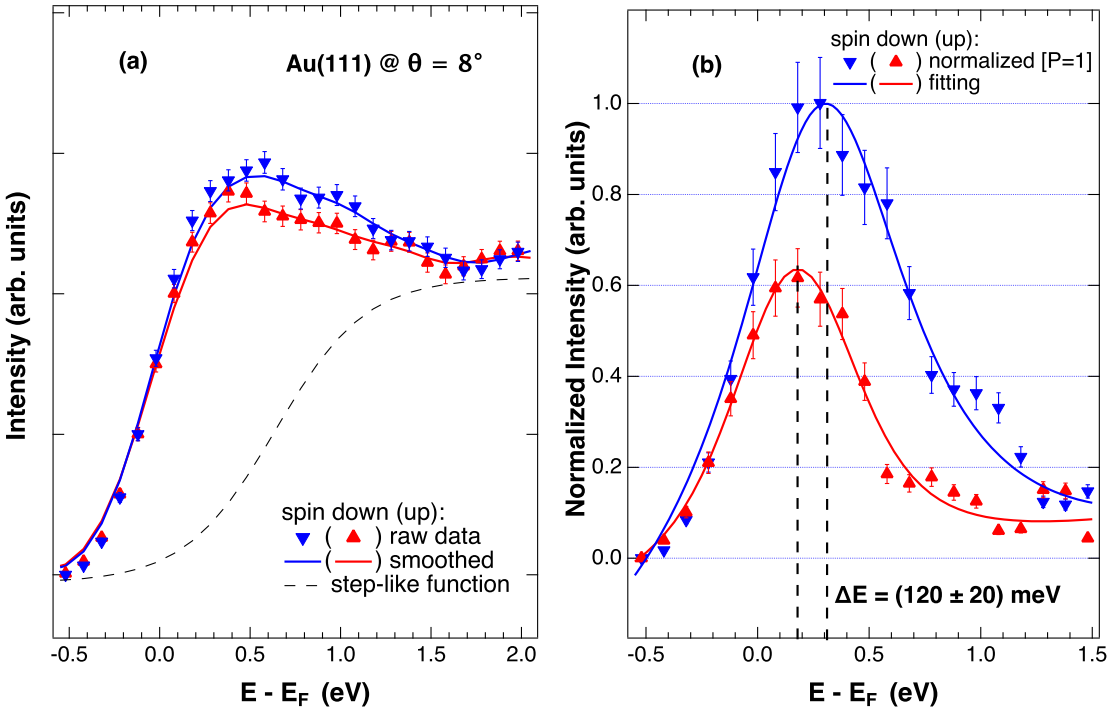

Figure 3.20: Spin-split SS at $\theta = 8°$ with the spin down (up) component depicted by solid (empty) circles with standard deviation bars. (a) Normalized-to-current data with non-zero spin asymmetry at the binding energy of the SS. (b) Resulting spectra after linear background removal and polarization normalization to account for 100% beam polarization. Pseudo-Voigt fittings are included as continuous and dashed lines for the spin down and spin up components, respectively.

3.3.5 . Wavevector resolution

The finite angular resolution of the SPIPES setup is clearly evidenced in the $E(k_{\parallel})$ dispersion of Au(111) (Fig. 3.15) where the SS appears at $\theta < \theta_F^{\uparrow,\downarrow}$ $(k_{\parallel} > 0)$ and in principle it should not be observed in IPES. For example, the SS is already visible at $\theta = 0°$ although its expectation value is zero because the SS is merged below the Fermi level with an energy of $E - E_F = -0.47$ eV [25]. This is an effect of finite energy and wavevector resolution of the setup. The intrinsic relation between the wavevector resolution and energy resolution follows from the IPES equation (Eq. 2.8).

The wavevector resolution depends on the angular divergence of the electron beam [128, 151]. Likewise, the angular divergence is a function of the electron energy as can be seen in the simulations[8] of the beam diameter at the sample D_{sample} of Fig. 3.21 where an asymptotical behavior of the beam diameter with respect to the beam energy is observed. The same profile is present in different principal plane positions H, into which the Φ-rotator images the beam crossover from the aperture plane. Our electron source design has a principal plane of $H = -32.14$ mm which is the lowest practical value above a critical threshold of 5 eV. Below this threshold the beam diameter rapidly increases. The beam diameter at the sample is $D_{sample} < 700$ μm without considering lens aberration, even for the lowest reachable energy.

[8]The simulations were performed by Thomas Duden.

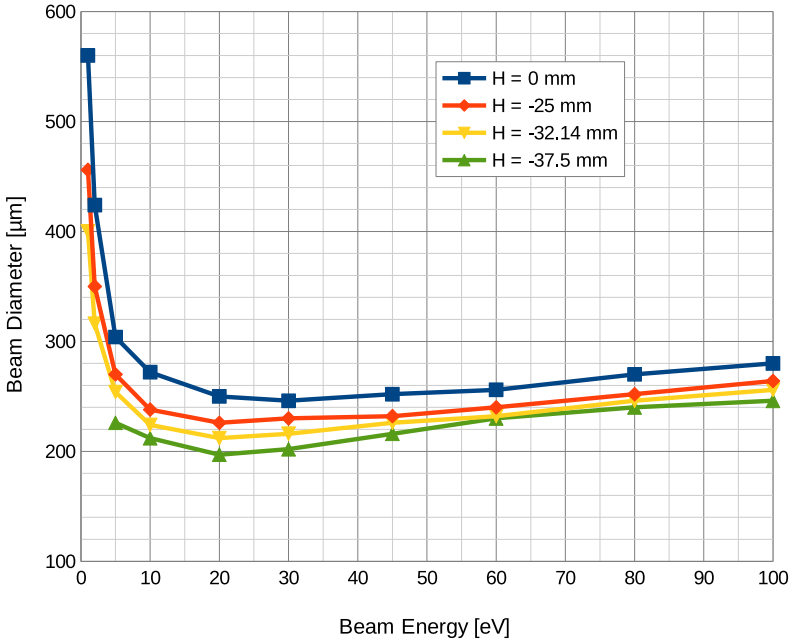

Figure 3.21: Ideal beam diameter at the sample as function of beam energy. The curves were calculated for different principal plane positions H.

The experimental angular divergence of the electron beam can be obtained by determining the beam profile with a Faraday cup [151]. Here we measured it from the beam diameter at two points: at the aperture point located before the decelerator and at the sample. The beam diameter was measured at the aperture with standard operation energy of 10 eV as follows: (i) the beam is sent to the sample target with maximum transmission, (ii) the vertical (z) position of the aperture was tuned while simultaneously reading the sample current in a high-resolution electrometer, (iii) the displacement of the aperture is iterated along the vertical until maximum and minimum values of the sample current are found. With the aforementioned method the spot diameter at the decelerator lens is $D_{dec} = 410$ μm. In the other hand, the spot diameter at the sample was estimated from the beam projection over a phosphorescent screen placed at the nominal working distance of 20 mm from the decelerator and at a normal incidence of the beam. In this case we found the spot diameter at the sample to be $D_{sample} = 1.0 \pm 0.2$ mm. There is therefore a factor of five in the beam diameter at the sample with respect to the simulations. The discrepancy may be due to the light dispersion on the phosphor screen and the lens aberration. From this real space analysis and considering the above parameters, an angular divergence of $\Delta\theta \sim \pm 2.3^{\circ}$ is obtained, corresponding to $\Delta k_{\parallel} = 0.06$ Å^{-1}.

Another way of determining the angular divergence is from spectral intensities of surface states in photoemission [152] and inverse photoemission [48, 151]. In particular, Cu(111) surface states have been used for obtaining the wavevector resolution in IPES. The unoccupied band dispersion of Cu(111) (Fig. 3.22(a)) allows to follow the dispersion of S_1 (Shockley state) and S_2 (image potential state) to compare their effective masses. Therefore, it can be determined how *fast* S_1 ($m* = 0.42$ [35, 153]) emerges with respect to S_2 ($m* = 1.0$ [35]) when θ is varied. The growing rate of S_1 is influenced by the beam divergence. Let us consider the transitions at $k_{\parallel} = 0$: (i) S_1 is below E_F ($E - E_F = -0.39$ eV) and it cannot be observed by IPES, (ii) S_2 is above E_F ($E - E_F = +4.1$ eV) and thus, it is an IPES observable. From this kind of analysis, a correspondence between angular divergence and intensity ratio can be

achieved by comparison of the surface states at each θ incidence. Yet, experimental parameters that might influence the IPES intensity, such as the energy resolution, photon take-off angle and surface preparation, still need to be considered, so we did not use this method. We will just mention that, since the intensity of S_1 is smaller than the one of S_2 at normal incidence (Fig. 3.22(b)), the momentum resolution of the setup is quite acceptable.

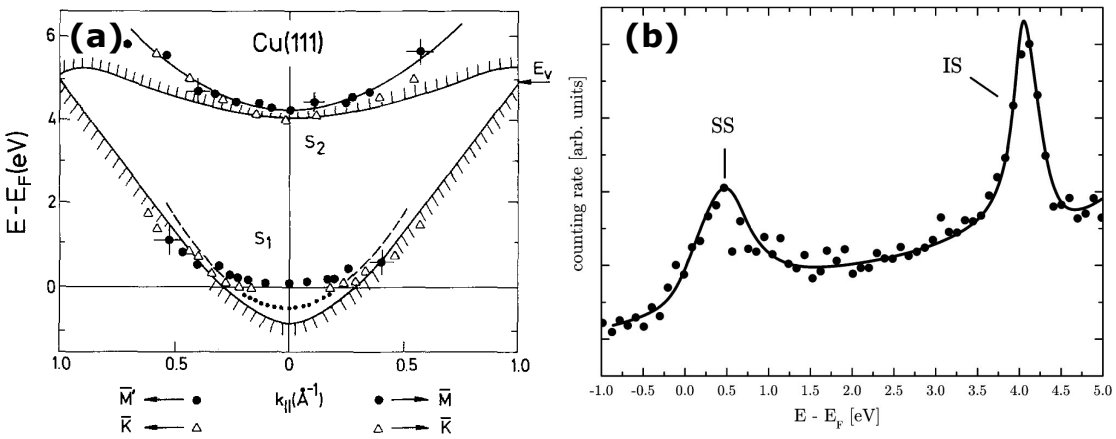

Figure 3.22: (a) Energy dispersion of Cu(111) where S_1 and S_2 are the Shockley SS and the IP band, respectively. Notice that at $k_{\parallel} = 0$, the S_1 band is below E_F and in principle only detectable by photoemission. Reproduced from [35] by permission from Springer Publishing. (b) IPES isochromat of Cu(111) at normal incidence. The intensity of the image potential state (IS) is higher than the Shockley SS in a spectrometer with small angular divergence. Reproduced from [93] with the permission of AIP Publishing.

Instead, we take advantage of the spin resolution of our spectrometer and we use a simple yet powerful method, firstly proposed by Zümbulte et al. [151]. In this method, the asymmetry of just one spin-polarized state is enough to determine the momentum resolution, and the aforementioned experimental parameters are not relevant. We will consider again the spin-polarized Shockley SS of Au(111) at E_F crossing (Fig. 3.20). The Shockley surface state has already been simulated as function of the beam divergence [151] for correlating the spin down/up intensity ratio with respect to $\Delta\theta$. At E_F crossing, we observe that $I_{\downarrow}/I_{\uparrow} \sim 1.6$ at the respective binding energies. The angular divergence for a 1.6 ratio is $\Delta\theta = \pm 3.0^{\circ}$. Besides $\Delta\theta$, the uncertainty in the manipulator angle $\Delta\theta_{manip}$ has to be considered to obtain the momentum resolution:

$$\Delta^2 k_{\parallel} = \Delta^2\theta + \Delta^2\theta_{manip}. \tag{3.11}$$

In our setup, $\Delta\theta_{manip} = 0.1^{\circ}$, so negligible for the Δk estimation. Therefore, we conclude that $\Delta k_{\parallel} = 0.08$ Å^{-1}.

In order to double check our estimation of $\Delta k_{\parallel}$, we follow the spectral features of Au(111) SS when varying θ. The Au(111) SS was measured nearby $k = 0$ with a minimum angular step of 0.2°. Noticeable differences between the binding energy start at about 1°-steps in the spin-integrated ($i^{\uparrow} + i^{\downarrow}$) spectra of Fig. 3.23. For instance, the difference between the binding energies of $\theta = 0^{\circ}$ and $\theta = 1^{\circ}$ is already $\Delta E = 0.16$ eV. This shows that $\Delta\theta = \pm 3^{\circ}$, from the aforementioned calculations, may be slightly overestimated. Anyway, we have considered both methods to claim $\Delta k_{\parallel} = 0.07 \pm 0.01$ Å^{-1} for our setup.

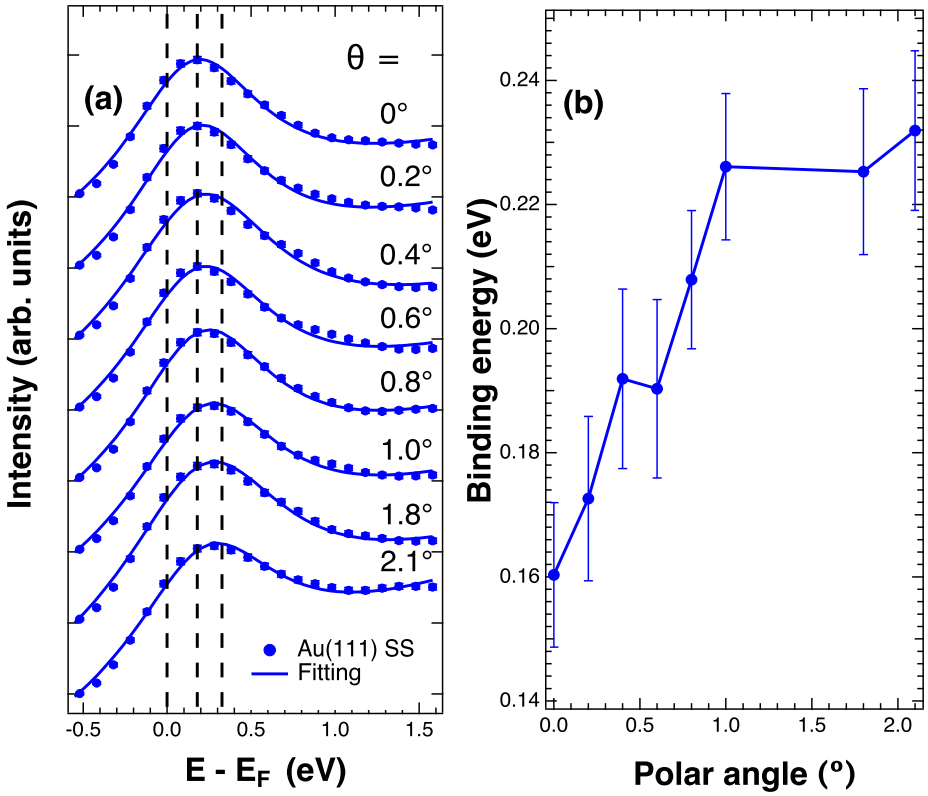

Figure 3.23: (a) Spin-integrated spectra of the Au(111) SS in the vicinity of $k = 0$. The data corresponds to the integration of spin up and spin down components ($i_\uparrow + i_\downarrow$). Solid cyan lines depict the spectral fitting to extract the binding energies. (b) Binding energies of left panel with uncertainty bars.

3.3.6 . Orientation tuning of the spin polarization

Once the effective polarization of the electron source was obtained, the tuning of the spin polarization vector of the electron beam at any desired orientation in 3D was demonstrated. Both the angle with respect to the propagation axis (Θ) and the angle in the plane perpendicular to the propagation (Φ) can be tuned. The parallel beam condition is preserved as observed by a low-energy phosphor screen placed at the sample position. The SPIPES experiments were again performed on the Au(111) surface due to its single crystallinity and quality.

Transverse tuning

The spin polarization of the Au(111) Shockley SS is tangent to the Fermi surface (Fig. 1.1(right)). We will take advantage of this fact to analyze the polarization of the electron beam, perpendicularly to the beam propagation, i.e. transverse (Φ) tuning. The evolution of the SPIPES spectra was studied when the beam polarization is parallel($\Phi = 0°$)/anti-parallel($\Phi = 180°$) to the spin of the SS. Between these two orientations, intermediate Φ angles were also considered. Fig. 3.24(a) summarizes the SPIPES spectra of the SS at $\sim k_F$ ($\theta = 8°$) for rotations of $\mathbf{P}$ within the plane perpendicular to the propagation. Both the spectral intensity and the asymmetry of the spin-polarized state increase when the beam polarization is aligned to the SS spin direction. This result is also reproduced for an incidence of $\Phi = 180°$ where, as expected: (i) the spin up and spin down components of the state change their binding

energy with respect to the $\Phi = 0°$ condition and (ii) an energy splitting of $\Delta E = 120$ meV follows from the peak positions. Conversely, when the beam polarization is perpendicular to the SS spin ($\Phi = -90°$), the overall intensity decreases and the energy splitting cannot be clearly appreciated. In between these extreme situations, the spectral lineshape evolves smoothly with a similar background lineshape. Qualitatively, the evolution of the spectral intensity is in agreement with the expectations. Electrons are less injected when their spin orientation is not aligned with that of the surface state so the surface state intensity is decreased.

Further proof of Φ tuning is found in the B1 state of Au(111) at $\theta = 56°$ presented in Fig. 3.24(b). In this case, both the asymmetry and the overall intensity of the degenerated B1 state are maximized (minimized) at $\Phi = 0°$ ($\Phi = 90°$). It can be observed that the signal/noise ratio decreases for high Φ angles. The signal/noise ratio for $\Phi = 0°$ ($\Phi = 90°$) spectra is 2.5 (1.6). Consider the spectral differences of the SS and the B1 states at $\Phi = 0°$. The reason of the signal/noise ratio variation (signal/noise of SS is ~ 1.3) is the taking-off angle of the photons with respect to the center of the GM1 detector.

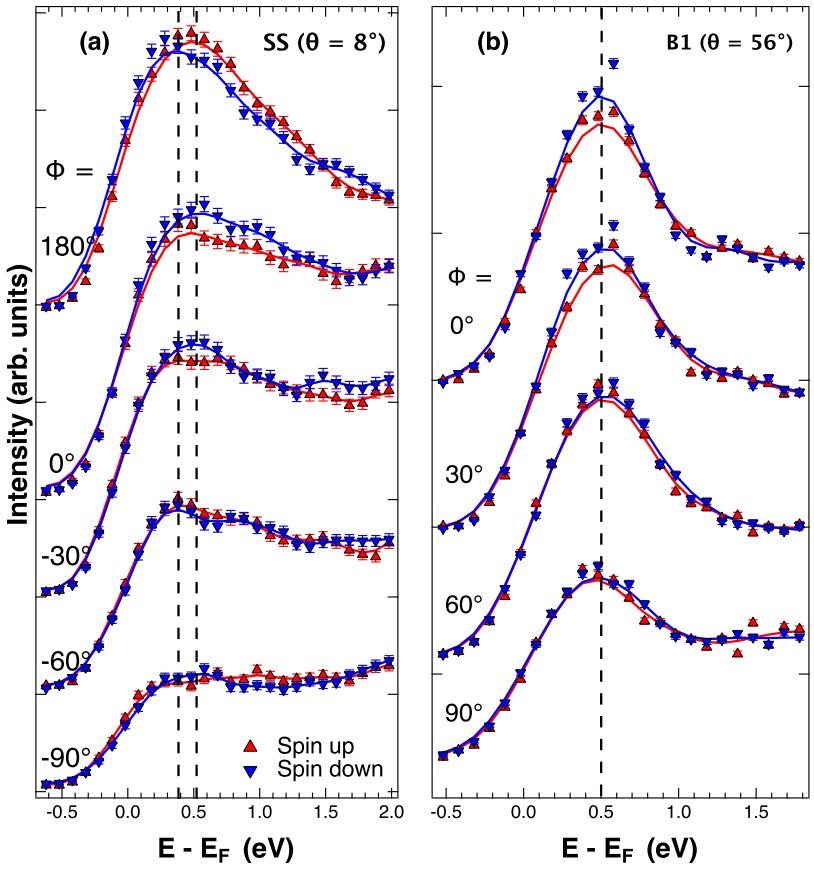

Figure 3.24: Dependency of Au(111) SPIPES spectra on the transversal (Φ) spin polarization with a current density of $\sim 0.8\,\mu$A·mm^{-2}. Smoothed spectra are shown as a guide to the eye. (a) Shockley SS: the inversion between the spin down and spin up components appears after a $\mathbf{P}$ rotation of $\Phi = 180°$. The energy splitting is ~ 120 meV. (b) The spin asymmetry of B1 vanishes after a rotation of $\Phi = 90°$. All the spectra were taken with $\Theta = 0°$. The electron source parameters are specified in Appendix C.

Longitudinal tuning

The in-plane spin of the Au(111) surface state can be also used to corroborate the tuning of the spin polarization in the longitudinal orientation i.e. a polarization along the propagation direction of the electron beam. The comparison of the spectral intensity of the SS, at $\theta = 16°$, for longitudinal and transversal spin orientations, is shown in Fig. 3.25. The intensity of both spin components is highly reduced when probing with a longitudinal spin orientation ($\Theta = 90°$) which is roughly perpendicular to the spin state. Conversely, the state emerges when retrieving a transversal polarization ($\Theta = 0°$), i.e. when the electron beam spin is in-plane, aligned with the SS spin.

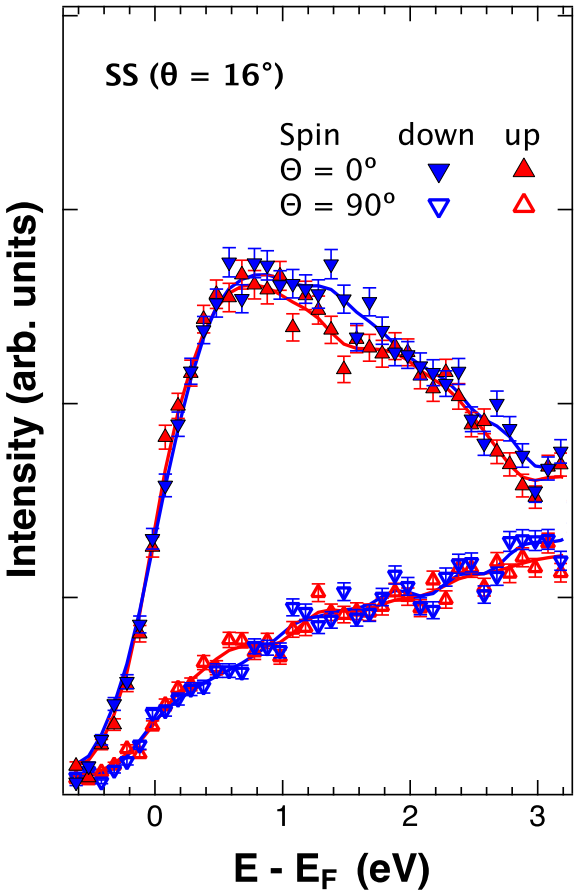

Figure 3.25: SPIPES spectra of the Shockley SS ($\theta = 16°$) for transverse ($\Theta = 0°$) and longitudinal ($\Theta = 90°$) polarization of the electron beam. Solid lines depict the high-frequency filtered data that serves as a guide to the eye.

The intensity decrease of surface states when turning the beam polarization is something already observed in the literature. For example, in Tl/Si(111) the Γ-valley unoccupied surface states decrease their intensity [1] when the spin of the beam is at $\Phi = 90°$ with respect to the spin of the state. An equivalent effect of intensity decreased has been observed in photoemission studies on the Shockley SS in Cu(111) where about 94% of its intensity is decreased while changing the excitation light from p to s polarization [154] (Fig. 3.26).

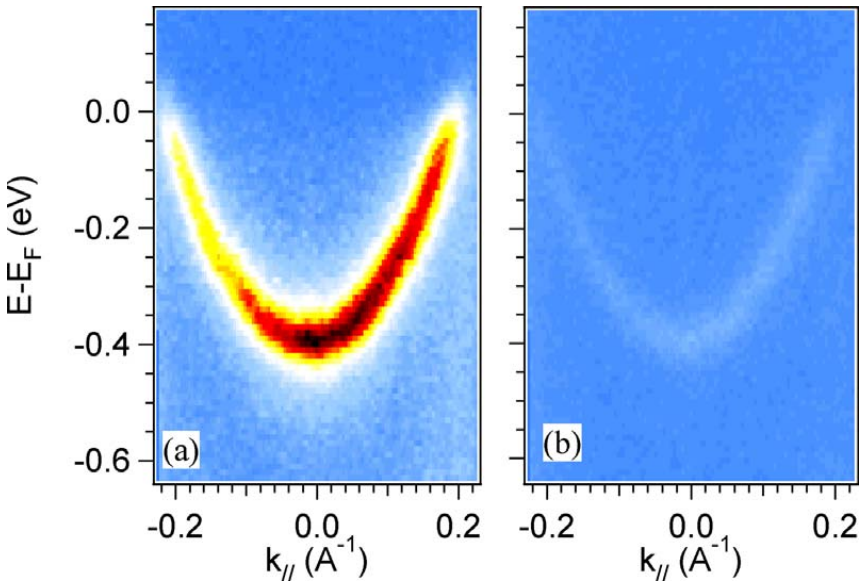

Figure 3.26: Angle-resolved photoemission maps of the Cu(111) Shockley surface state measured with a photon energy of $\hbar\omega = 18$ eV with (a) p and (b) s polarization. Reproduced from [154] with permission from APS Physics.

The tuning from longitudinal to transverse spin polarization was also tested on a Au|Co|Au sample with k-integrated SPIPES measurements. The magnetic anisotropy of ultra-thin magnetic films depends on the thicknesses of the individual layers [155]. For $d_{Co} = 3$ nm the magnetization is out-the-plane of the sample surface, while for $d_{Co} = 1$ nm the magnetization is in-plane. We have therefore studied thin Co films grown by molecular beam epitaxy (MBE) in a multi-evaporator setup with the support of Stanislas Rohart (IDMAG, LPS). In this work, we have measured an Au(7nm)|Co(3nm)|Au(4nm) sample with an out-of-plane magnetization. The Au external layer serve as protection against oxidation of the Co surface when transferring it to the UHV environment and, in principle, it does not affect the spin polarization of the beam [156]. Ex-situ magneto-optical Kerr hysteresis loops, shown in Fig. 3.27(a), corroborate the out-of-plane direction of the magnetization of the Co layer [155].

The experimental geometry is shown in Fig. 3.27(b). Normal incidence ($\theta = 0°$) SPIPES spectra is summarized in Fig. 3.28(a) as function of longitudinal incidence in steps of $\Theta = 15°$. An intensity correction was applied to the spin-dependent DOS from $\mathbf{P} \cdot \mathbf{M} = PMsin\Theta$ (Eq. 2.27) as shown in the inset of Fig. 3.28(b). It can be observed that the spectra is much more structured when the spin is aligned with the magnetization ($\Theta = 90°$). The interplanar distance of epitaxially-growth fcc Co in Cu(100) is about 1.774 Å [157] from which we can roughly estimate the number of Co monolayers of our system to be ~ 17 monolayers. Three spin-polarized states are in good agreement with the quantum-well states appearing in a 16-layered Co system [158] (Fig. 3.28(b)), with binding energies of ~ 0.6 eV, ~ 1.4 eV and ~ 1.7 eV. Variations on the spectra are expected because the systems are not totally equivalent. For instance, it is obvious that the peak corresponding to the emission of the Cu(100) surface (~ 0.2 eV) is absent in the spin-resolved DOS since we have evaporated Co over polycrystalline Au. Moreover, a strong depolarization is likely to happen when electrons travel, for instance, through the Au capping layer. This reasoning is based on the spin torque mechanism [159, 160] that occurs when a spin current flows from a nonmagnet (vacuum) into a ferromagnet where the

absorbtion of spin components depends on $\mathbf{M}$. The absorption arises from (i) spin-dependent reflection and transmission, (ii) rotation of reflected and transmitted spins and (iii) spatial precession of spins in the ferromagnet.

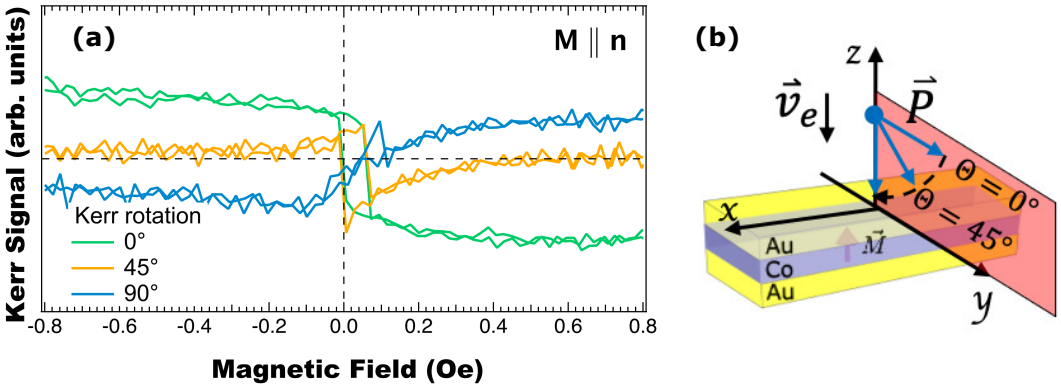

Figure 3.27: (a) Magneto-optical Kerr hysteresis loops of Co films: polar-Kerr for out-of-plane magnetization ($d_{Co} = 3$ nm). The $0°$ Kerr rotation coincides with the $\mathbf{M}$ easy-axis and defines a $\mathbf{P}$ reference for k-integrated SPIPES at normal incidence. (b) Experimental arrangement of normal incidence with the relative orientation of the spin polarization (blue arrow) and the magnetization (violet arrow).

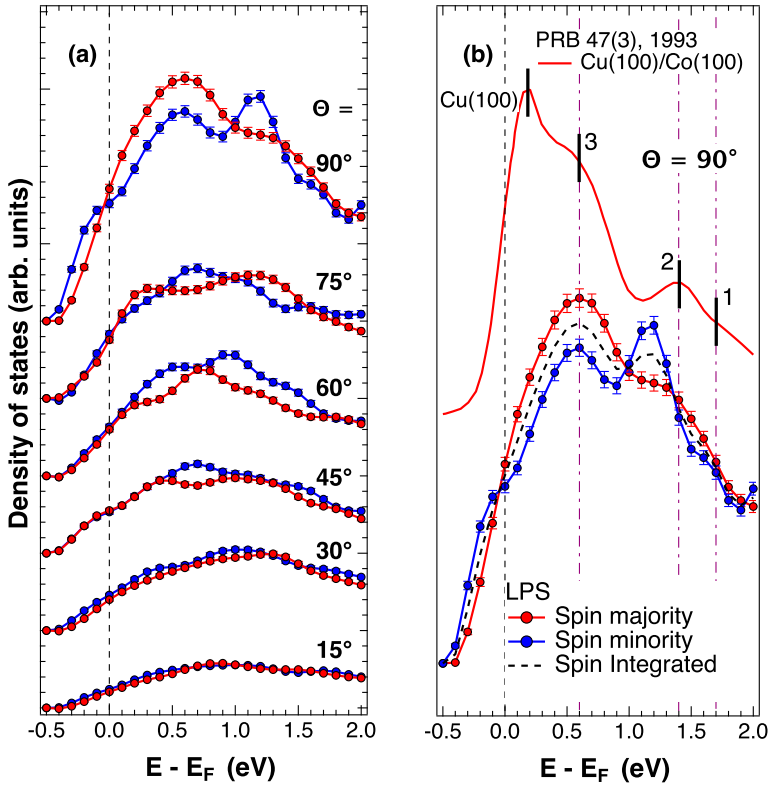

Figure 3.28: (a) Normal incidence SPIPES spectra of Au(7nm)|Co(3nm)|Au(4nm) system with out-of-plane magnetization. The spectral intensity is modulated by a factor of $sin\Theta$. (b) Direct comparison of the $\Theta = 90°$ spectra (solid circles) with a 16 ML of Co on Cu(100) [158] (red line). A spin-integrated spectrum is also added as dashed black lines.

3.4 . CONCLUSIONS

We have demonstrated the operation of a spin- and k-resolved inverse photoemission setup. The energy resolution of the instrument was obtained from the bulk and surface dispersion in Cu(001). It is around 200 meV in good agreement with similar setups. Moreover, by analyzing the Shockley surface state of the Au(111) we demonstrated:

- The spin-resolution on the SPIPES setup by the observation of the Rashba-Bychkov effect.
- The determination of its spin-polarization of 0.3.
- The 3D polarization tuning of the electron beam.

We have therefore demonstrated the decoupling of $\mathbf{P}$ from $\mathbf{k}$. It is thus possible to perform spin- and angle-resolved IPES without any restriction as in current setups.

4 - PHOTO-INDUCED DYNAMICS OF ORGANIC CATION IN $CH_3NH_3PbI_3$

Organometallic halide perovskites are outstanding semiconductors with a strong solar-light absorption and potential application for next-generation photovoltaics and light-emitting low-cost devices [161, 162]. An adapted direct bandgap and a long carrier diffusion length, of hundreds of micrometers in single crystals (SC) [163], allow for an impressive light-to-power conversion efficiency (PCE) now even surpassing 25% in cell structures [164]. In order to go beyond the actual limits on the PCE in perovskite solar cells (Fig. 4.1), an understanding of the mechanisms of charge-transfer upon light absorption is fundamental. A key component of hybrid lead-halide perovskites is the spatial configuration of organic cations, e.g. methylammonium (MA) in the prototypical $CH_3NH_3PbI_3$ (usually named $MAPbI_3$ and henceforth MAPI) perovskite, impacting on the dielectric and electronic properties. DFT calculations ascribe ferroelectric order to polar structures [165] so the orientational flexibility of the organic cation may promote (i) a reduction of the bandgap due to the formation of charged domain walls [166] and (ii) an indirect bandgap inhibiting carrier recombination [167]. The absence of such properties in purely inorganic perovskites [168] highlights the fundamental role of studying the organic cation dynamics.

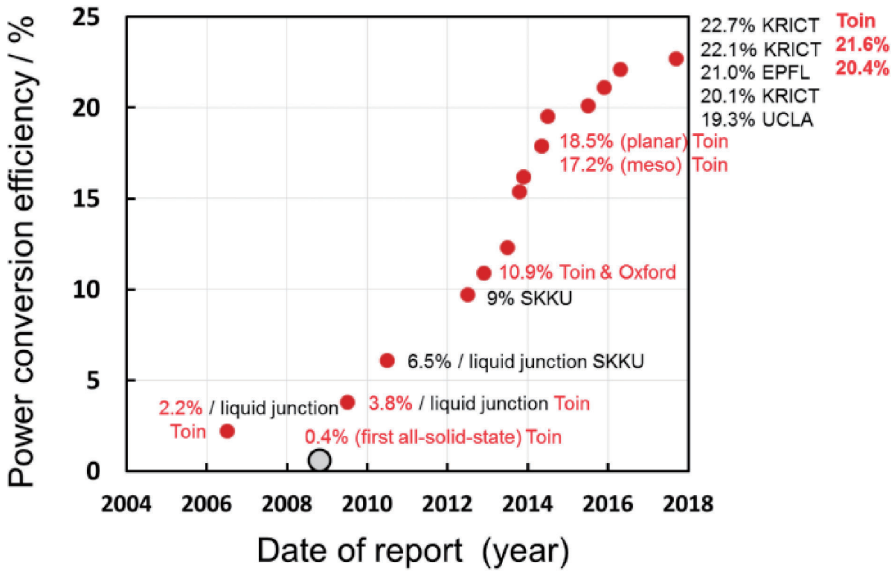

Figure 4.1: Progression of the power conversion efficiency in perovskite solar cells. Figure adapted from [169].

The optoelectronic functionality of the organic framework has been mostly investigated by ab-initio calculations [170, 171, 172, 173, 174, 175, 176]. Very recently, a strong coupling between the inorganic and organic sublattices, having an effect in the conduction band of MAPI monocrystals, was revealed by resonant Auger spectroscopy [177]. Indeed, the organic-inorganic interplay is probably mediated by the spin-orbit coupling of the heavy atoms, that affects mainly the CB, so a direct access to the conduction band with spin resolution is necessary. A dynamical Rashba-Dresselhaus (dRD) effect has been proposed to explain the band splitting in MAPI

perovskite [178] even in centrosymmetric structures, which is the most accepted structure for MAPI (I4/mcm, Table 4.1). The dRD effect is promoted by time-dependent lattice fluctuations affecting to the SOC Hamiltonian

$$V_{SOC} = -\frac{e\hbar}{4m^2c^2}\mathbf{E}\cdot\sigma\times\mathbf{p}. \tag{4.1}$$

This can be seen by replacing $\mathbf{E}$ by the gradient of the single-particle potential energy, i.e. $\mathbf{E} = (1/e)\nabla V$, where the atomic potential is fluctuating with time. In the dynamical Rashba effect, the inorganic-organic degrees of freedom are coupled and give rise to a local Rashba effect due to the orientational disorder of the molecular cations in centrosymmetric structures I4/mcm [178, 170]. The effect thus splits the bands in k-space as schematically represented in Fig. 4.2. Another possibility to settle a Rashba-Dresselhaus effect in the system is a static distortion of the PbI sublattice from a set of ideal corner-sharing octahedra, in the called static bulk Rashba effect, ascribed to non-centrosymmetric structures [171]. The occurrence of either a dynamical or static Rashba-Dresselhaus in MAPI has not been established.

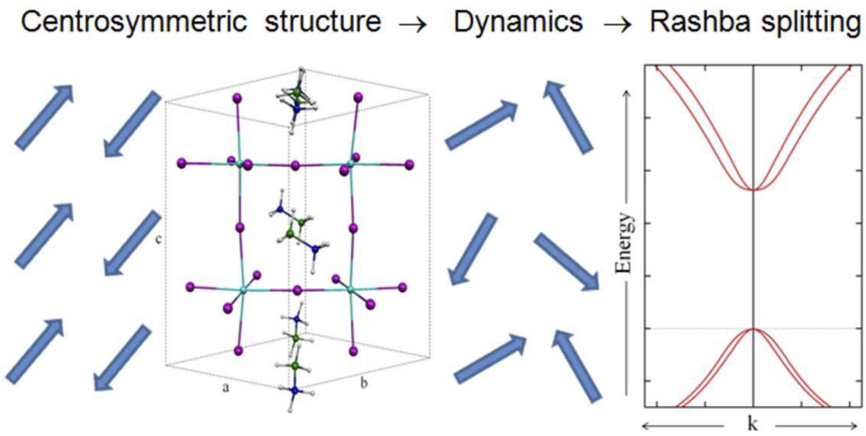

Figure 4.2: Schematics representing centrosymmetric MAPI structure with blue arrows indicating the methylammonium dipole orientations. In the dynamical Rashba-Dresselhaus effect, molecular rotations in the picosecond scale give rise to band splitting effects in the conduction and valence band nearby the bandgap. Adapted from [170].

To date, no direct experimental evidence on the MAPI CB spin-splitting has been reported. Very recently, J. Yang et al. could resolve the CB of MAPI for the first time using a very low-energy electron beam [179]. The very-low energy inverse photoemission (LEIPES) spectra at 300 K and 170 K of MAPI (tetragonal) reveal good agreement with an anomalous bandgap: $E-E_F$ of the CB minimum is reduced from high-temperature (1.66 eV) to low-temperature (1.25 eV) (Fig. 4.3). This bandgap renormalization is compatible with static Rashba-Dresselhaus effect. However, the aforementioned LEIPES experiments lack spin resolution so the presence or absence of static Rashba-Dresselhaus effect cannot be concluded.

Therefore, in this Chapter we present electronic and structural studies on $CH_3NH_3PbI_3$ monocrystals to shed light into the complex dilemma of the optoelectronic function of the organic cations. On one hand, we performed time-resolved XRD (TR-XRD) to unveil the structure and the dynamics of the methylammonium cations upon light excitation. Our experimental results indicate an apolar-to-polar dynamics of the MA cations by the temporal evolution of the lattice parameter and diffracted intensity. The cation reorganization occurs in the picosecond

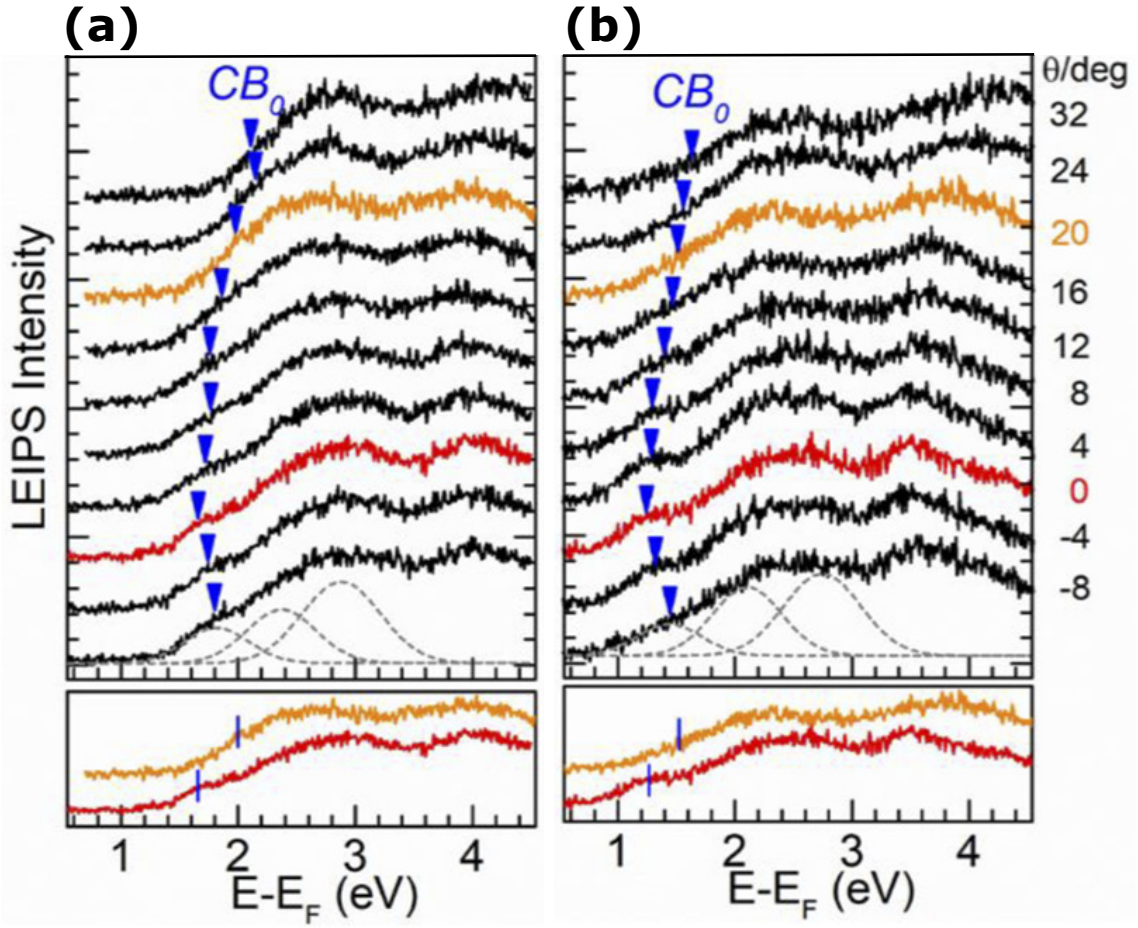

Figure 4.3: Angle-resolved LEIPES of MAPI single crystal at (b) 300 K and (b) 170 K. Blue triangles indicate the dispersion of the lowest CB extracted from Gaussian fitting of the binding energies. Adapted from [179].

scale with good agreement between the experimental parameters and simulations of proposed structures. To give more fundamental insight into the optoelectronic function of the MA, the spin-resolved CB of MAPI was directly accessed with the SPIPES setup (LPS) for the first time. Based on a 70 meV energy splitting of the conduction band, also supported by first-principle calculations, we report on the apolar character of MA cations in the tetragonal static phase. Even though the current experimental data on the CB is not sufficient to determine effective masses to ascribe Rashba parameters, our combined experiments of TR-XRD and SPIPES point for a dynamical Rashba-Dresselhaus effect in tetragonal MAPI.

4.1 . ATOMIC & ELECTRONIC PROPERTIES OF MAPI

ABX_3 structures are named perovskites after the russian mineralogist Lev Perovski i.e. inorganic minerals such as $BaTiO_3$, $BiFeO_3$, $PbTiO_3$, $SrTiO_3$ among others. Halide perovskites exhibit a similar structure, where the oxide anion is replaced with a halide anion. In general, the A site can be either occupied by an organic (e.g. formamidinium, methylammonium) or inorganic (e.g. Cs) cation, the B site is a metallic cation (Cu, Sn or Pb) and finally an halide anion X=(Br, I, Cl). Notably, the family $MABX_3$ (MA = CH_3NH_3; B = Sn, Pb; X = Cl, Br,

I) is very promising for its use in photovoltaic materials. After the first report on dye-sensitized electrochemical cells with a PCE of 3.8% by A. Kojima et al. [180], the enormous amount of photovoltaic research on the perovskite structures led to further progress on the PCE (Fig. 4.1) [164]. The $CH_3NH_3PbI_3$ is a hybrid halide perovskite consisting of octahedrally coordinated I atoms with a centered Pb as shown in Fig. 4.4 for the I4/mcm space group [181]. The halide atoms are shared by the neighboring metal atoms. The corner-shared network of PbI_6 octahedra has MA cations at the interstices with a dipolar momentum of ~ 2.3 D [182]. At RT, the system crystallizes in a tetragonal phase with lattice constants $a = b = 8.800$ Å and $c = 12.685$ Å [183, 184]. The system becomes cubic above 327 K [172] with Pm3m space group because the hydrogen bonds attaching the cations to the I atoms are weakened, so the mobility of the organic cation within the cage changes and the cations explore now 24 possible orientations, instead of the 8 explored in the tetragonal phase. In the high-temperature phase, the MA cations are dynamically disordered in an almost isotropic potential and at a rate corresponding to the free cation [185, 186].

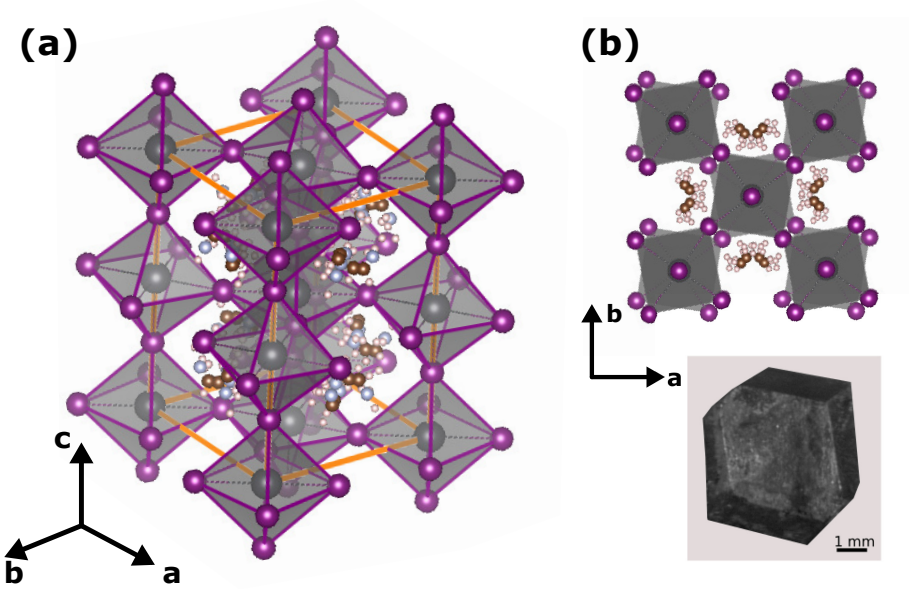

Figure 4.4: (a) Tetragonal MAPI structure (I4/mcm) with unitary cell enclosed by orange volume. The structure consists of inorganic octahedra with I (purple) atoms at the edges that surround a central Pb atom (gray). The MA cations (C: brown, N: blue, H: pink) are distributed at the interstices. (b, up) Neighboring iodine atoms along the c-axis are not colinear in the tetragonal phase but in the cubic one. (b, down) Millimeter-size MAPI single crystal.

The rotation angle of the PbI_6 octahedra is an order parameter of the cubic-tetragonal transition that increases monotonically when decreasing the temperature below RT [183]. The temperature also modifies the pseudo-cubic lattice parameters, $\tilde{a}$=a/$\sqrt{2}$, $\tilde{c}$=c/2 and the cell volume $\tilde{d}$=$\tilde{V}$/2. The cell-volume evolves linearly whereas the lattice constants monotonically as suggested by SC-XRD [183] (Fig. 4.5). Finally, below 165 K an orthorhombic phase is found [173, 187]. In this case, the MA cations are disposed in a head-to-tail sequence to maximize the bonding to the iodine atoms [188, 189].

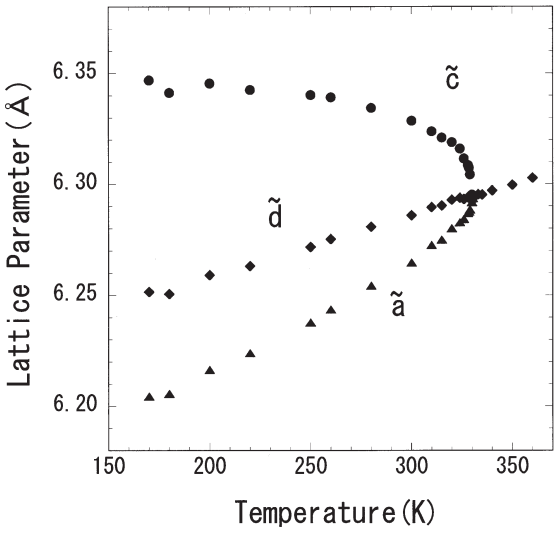

Figure 4.5: Temperature-dependent pseudo-cubic lattice parameters of tetragonal MAPI, ã=a/$\sqrt{2}$ and c̃=c/2, as well as temperature-dependent d̃=Ṽ/2. Reproduced from [183].

4.1.1 . Is MAPI polar or apolar?

In addition to the photovoltaic applications, the room temperature tetragonal phase of MAPI is of special interest due to a controversy on the space group. Either centrosymmetric I4/mcm (4/mmm point group) or non-centrosymmetric I4/cm (4mm point group) space groups have been ascribed to this structural phase as summarized in Table 4.1. Most of the reported studies have been performed with the SC-XRD technique with conflicting results probably related to an increased difficulty to determine the disposition of the organic molecules. The two groups of structural configurations can be distinguished through the lattice parameters and the intensity of particular Bragg reflections, even if the organic cations are light scatterers.

Reference (et al.)	Year	Cubic	Tetragonal	Orthorhombic	Technique
A. Poglitsch [190]	1987	$Pna2_1$†	I4/mcm	Pm3m	XRD
Y. Kawamura [183]	2002	—	I4/mcm	—	SC-XRD
T. Baikie [191]	2013	Pnma	I4/mcm	$Pm\bar{3}m$	SC-XRD
C. Stoumpos [192]	2013	—	I4/cm†	P4mm†	SC-XRD
Y. Dang [193]	2015	—	I4/cm†	—	SC-XRD
M. T. Weller [173]	2015	Pnma	I4/mcm	$Pm\bar{3}m$	Neutron
G. Sharada [194]	2016	Pnma	I4/mcm	$Pm\bar{3}m$	SC-XRD
Min-I Lee [184]	2017	—	I4/mcm	—	SC-XRD

Table 4.1: Reports on crystal structure of MAPI from diffraction experiments. Polar (I4/cm) space groups are indicated by †.

Deducing the space group of the tetragonal structure in our case is by no means evident simply because the reflection conditions for the 4/mmm and 4/m Laue classes are identical as reported in the International Tables for Crystallography [195]. The space group extinction rules for the hkl are not enough to determine whether the system is centrosymmetric (I4/mcm) or non-centrosymmetryc (I4/cm). The experimental diffraction pattern of MAPI monocrystals in the tetragonal phase (200 K) has already been reported [184] for the (h 0 1) and (0 k l) planes (Fig. 4.6) and the structure refinement indicated an I4/mcm space group i.e., an apolar cation distribution. Most of the diffraction studies also concluded in a similar

structure. On the other hand, C. Quarti and collaborators performed DFT optimization with a planewave/pseudopotential approach and the dynamics of the cations was investigated by Car-Parrinello molecular dynamics (CPMD). Therein, three out of the nine structures have a defined MA dipole orientation (polar) and the remaining have a random alignment (apolar) as summarized in Table 4.2. The study also suggests that the polar distribution is energetically more favorable in the static case, in conflict with XRD [184] and second harmonic generation (SHG) rotational anisotropy, both supporting a centrosymmetric I4/mcm space group [171].

The MA cations disposition defines the space group and thus the lack or existence of inversion symmetry in 3D MAPI perovskite. Therefore, the MA also mediates the electronic properties of the system because SOC and inversion asymmetry give rise to splitting of conduction bands through the Rashba-Dresselhaus effect. Thus, as it will be clear in the following, the observation of band splitting in the CB is a direct manner to understand the MA disposition within the inorganic sublattice.

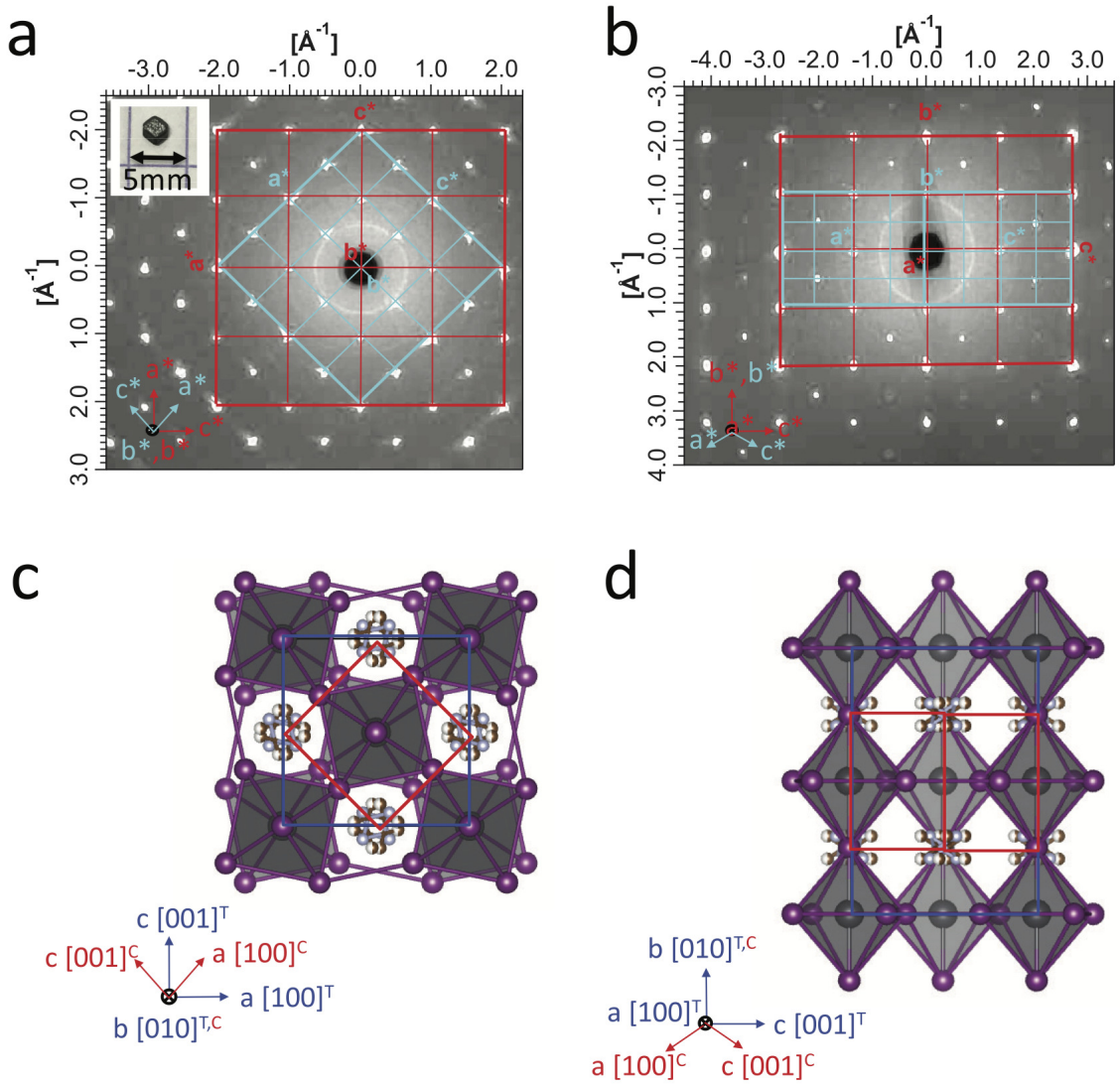

Figure 4.6: X-ray diffraction of MAPI single crystal in the (a) (h o 1) and the (b) (o k l) planes at 200 K. The tetragonal (cubic) reciprocal unit cell is indicated by blue (red) lines. The structure refinement (I4/mcm) is projected in the (c) ac and (d) bc planes. Adapted from [184].

Structure	MA Orientation				Direction	Polarity
	A	B	C	D		
1	1−	1−	1−	1−	[001]	polar
2	1−	1−; 1−	1−	−	[1 − 10][001]	polar
3	2−	2−	−	−	[010][001]	polar
4	1+	1−	1−	1+	−	apolar
5	2+	−	2−	−	−	apolar
6	1+; 1−	−	1+; 1−	−	−	apolar
7	1+; 1−	−	1+; 1−	−	−	apolar
8	1+; 1−	−	1+; 1−	−	−	apolar
9	2−	−	2−	−	−	apolar

Table 4.2: Orientation of methylammonium (MA) cations in the various structural models with and without net molecular alignment from [165]. The MA orientation is shown in Fig. 4.7.

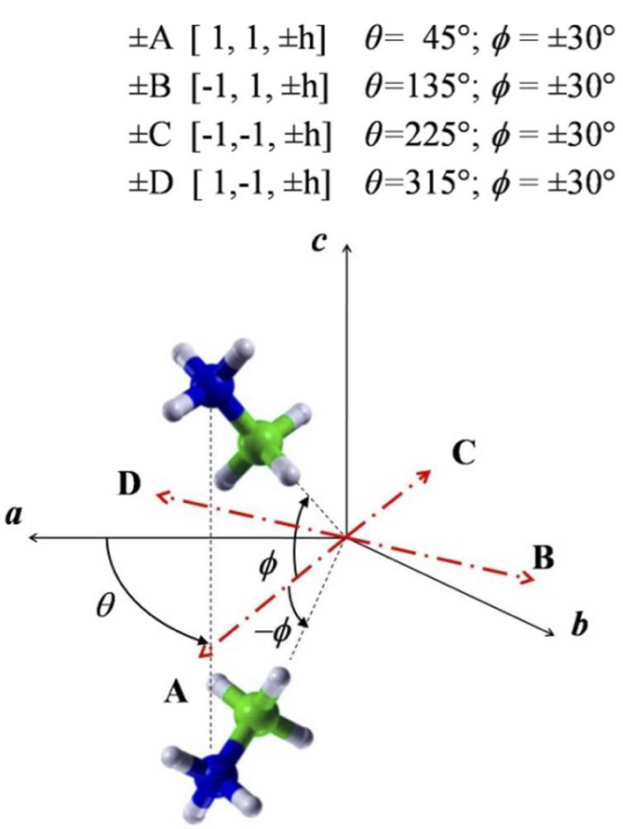

Figure 4.7: Preferred orientations of the organic cation within the perovskite interstice. The crystallographic axes of the perovskite in the tetragonal phase are a, b and c, and the octahedra tilting is along the c-axis, i.e. along the [001] direction. A, B, C and D represent the projection of the MA cation orientations within the ab plane, as measured by the angle θ. The tilting of the molecule with respect to the c-axis is measured by the ϕ angle. Adapted from [165].

4.1.2 . Electronic properties of MAPI

In general, the electronic properties of MAPI are different to those of a typical semiconductor. For instance, the bands around the Fermi level exhibit an anomalous temperature [174] renormalization such that the bandgap reaches a minimum through a phase transition to the orthorhombic (low-temperature) phase, while in typical III-V semiconductors the bandgap de-

creases monotonically with temperature (Fig. 2.5(b)). Additionally, in MAPI both VB and CB have an antibonding character whereas in ionic semiconductors the VB (CB) consist of bonding (antibonding) orbitals. The optoelectronic properties are also affected by a strong atomic SOC due to the inorganic Pb-I sublattice. Interestingly, a larger dependence on SOC is found in the CB rather than the VB [175], in contrast to e.g. GaAs, as shown in Fig. 4.8(a-b). The symmetry breaking causing the spin-splitting of the CB minimum slows the charge-carrier recombination by charge-carrier thermalization at the valleys [169], extending also the exciton lifetime for better photovoltaic performance.

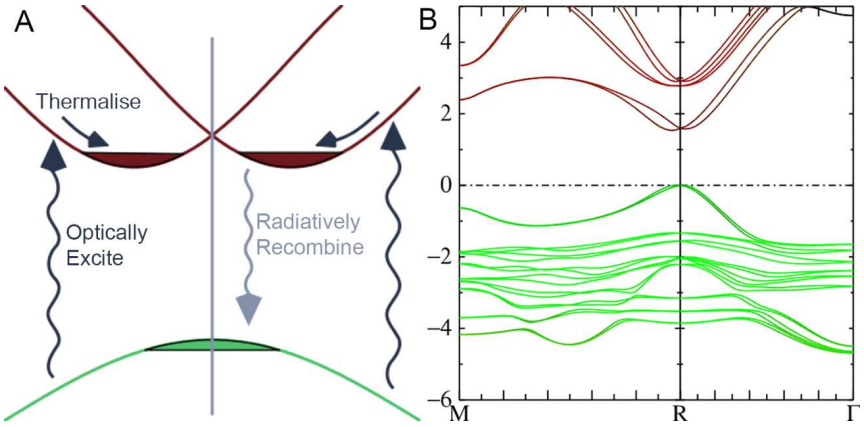

Figure 4.8: (a) Indirect bandgap in MAPI due to Rashba-Dresselhaus splitting. The charge-carrier pairs recombine after thermalization in the CB valleys. (b) Quasi-particle self consistent GW approximation of MAPI band structure. A significant splitting of the conduction band near R and an indirect bandgap (~ 1.75 eV) are observed. Adapted from [175] under a CC attribution license.

To shed light into the puzzling coexistence of a strong absorption and long charge carrier lifetime in MAPI, two variants for explaining the CB spin-splitting have been proposed, either the static or the dynamical Rashba-Dresselhaus effect. We recall the difference between the conventional Rashba (surface) and the Rashba-Dresselhaus (volume) band-splitting from their respective spin textures in Fig. 4.9. As previously mentioned, static Rashba-Dresselhaus occurs in systems with orientational order in the organic cations. A direct-to-indirect bandgap transition is caused by the distortion of the Pb-I sublattice and triggered mainly by the heavy atom because of the Pb $6p$ character of the CB orbital [175]. More precisely, is a consequence of directional local electric fields in the vicinity of the Pb atoms and the distortion of the iodine network [176]. The lattice distortion effects have been observed by PL emission as an indirect-to-direct bandgap transition in polycrystalline MAPI under hydrostatic pressure [196]. The static Rashba-Dresselhaus is ascribed to a non-centrosymmetric phase supported by ferroelectric hysteresis [197] and SHG rotational anisotropy [171]. On the other hand, the dynamical Rashba-Dresselhaus effect is caused by the breaking of the symmetry by the rotation of the MA cations within the interstices of the static inorganic framework in centrosymmetric structures [178] without distortion of the Pb-I framework [171]. Both effects could in principle explain the slow carrier recombination rate.

4.1.3 . Transient phenomena and XRD

In MAPI perovskite, the electron density scatterers are dominated by the heavy elements making difficult to deduce crystallographic properties of the phase-responsible organic cations

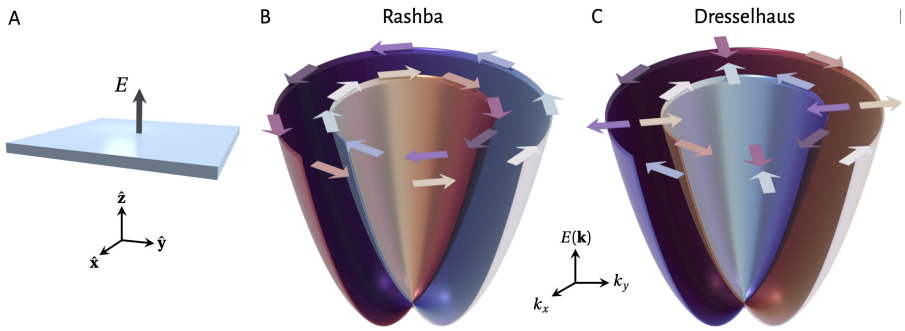

Figure 4.9: (A) In the Rashba-Dresselhaus effect the inversion symmetry of the crystal is broken, for example by an electric field. This lifts the spin degeneracy of the band minimum, and the symmetry dictates whether the system establishes a (B) Rashba or a (C) Dresselhaus spin texture as indicated by the color of the bands and the arrows. Adapted from [178].

by static XRD. The dynamics of the crystal under photoexcitation may shed light into the role of MA cations on the transient states that can only be studied with an appropriated timescale. The orientational dynamics of the $CH_3NH_3^+$ ions occurs in the picosecond scale as experimentally evidenced by complex permittivity [190] and NMR spectroscopy [198]. Thus, a ps resolution is needed between the pump (optical excitation) and the probe (hard X-rays). For the understanding of the light-matter interaction, two more conditions on the pump-probe experiment are needed:

- Temporal synchronization. The arrival of the laser pulse to the volume creates an initial photoexcited condition that can be set as a zero-time reference. Therefore, photoinduced structural changes are probed with an X-ray pulse that arrives after a time delay Δt. For this purpose, the use of high coherence laser sources is beneficial. The characteristic timescale of the electron-lattice processes are summarized in Fig 4.10. In particular, a ps resolution is suitable to observe carrier thermalization from electron-phonon interaction and recombination events occurring in the photoexcited system.

- Spatial overlap. Matching the penetration depth of the energetic X-rays and the laser pump on an explored volume. A parallel beam optics may allow grazing incidences ($> 2°$) of the X-rays thus increasing surface sensitivity [199]. An optimum signal-to-noise ratio can be obtained when the angle of incidence is equal to the critical angle for total external reflection [200]. Below the critical angle for total external reflection, the penetration into the bulk crystal is limited as an evanescent wave.

Before discussing the experimental results let us recall the generalities of X-ray diffraction. Because the wavelength of the hard X-rays (10^{-10}-10^{-11} m) is comparable to the interatomic distance in solids, they are used as a fast probe of the structural disposition of atoms and molecules providing information of the bulk properties of a material. The basic relation between the wavelength of the X-rays and the scattering angle $2\theta_B$ follows from kinematical diffraction theory and is given by the scattering vector $\mathbf{Q}$:

$$|\mathbf{Q}| = 2k \cdot sin\theta_B = \left(\frac{4\pi}{\lambda}\right) sin\theta_B = 2\pi/d_{hkl}, \tag{4.2}$$

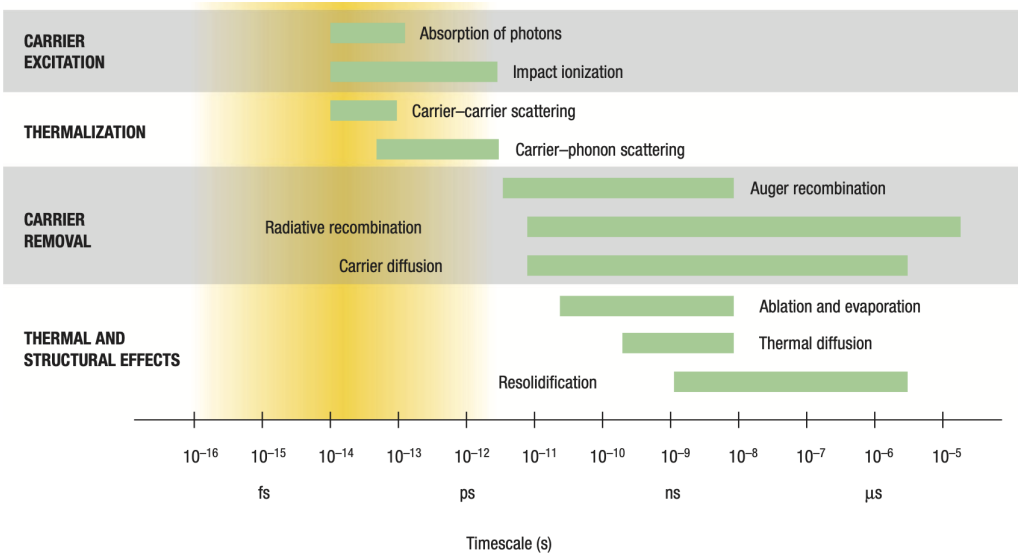

Figure 4.10: Timescale of electronic and structural processes for laser-excited solids. Adapted from [201].

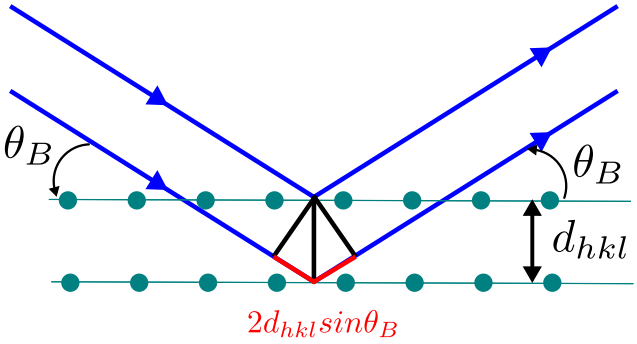

Figure 4.11: Geometrical representation of Bragg's law. When the path difference of the incident wavefronts is a multiple of the wavelength they do interfere constructively and diffract at an angle $2\theta_B$. The path difference is a function of the lattice parameter and the diffraction angle.

where λ is the wavelength of the incident X-ray beam, and d_{hkl} is the interplanar distance of the hkl Bragg reflection. By replacing $k = 2\pi/\lambda$ on Eq. 4.2 the familiar expression of the Bragg's law is retrieved:

$$n\lambda = 2dsin\theta_B. \tag{4.3}$$

The geometrical interpretation of Eq. 4.3 is summarized in Fig. 4.11 where two wavefronts of the same wavelength λ (blue lines) and incident angle θ_B are shown. The rays are reflected from adjacent hkl planes and they can interfere constructively if the path difference between them (red line) is a multiple of λ.

The interplanar distance d_{hkl} of the hkl Miller planes follow from the positions of the j-type atom, or the units, of the lattice in real space, given by

$$\mathbf{r_j} = x_j\mathbf{a_1} + y_j\mathbf{a_2} + z_j\mathbf{a_3}, \tag{4.4}$$

where $\mathbf{a_i}$, $i \in \{1, 2, 3\}$, are the unitary vectors of the cell. The reciprocal space base is constructed from them:

$$\mathbf{b_1} = 2\pi\frac{\mathbf{a_2}\times\mathbf{a_3}}{\mathbf{a_1}\cdot\mathbf{a_2}\times\mathbf{a_3}}, \mathbf{b_2} = 2\pi\frac{\mathbf{a_3}\times\mathbf{a_1}}{\mathbf{a_1}\cdot\mathbf{a_2}\times\mathbf{a_3}}, \mathbf{b_3} = 2\pi\frac{\mathbf{a_1}\times\mathbf{a_2}}{\mathbf{a_1}\cdot\mathbf{a_2}\times\mathbf{a_3}}. \tag{4.5}$$

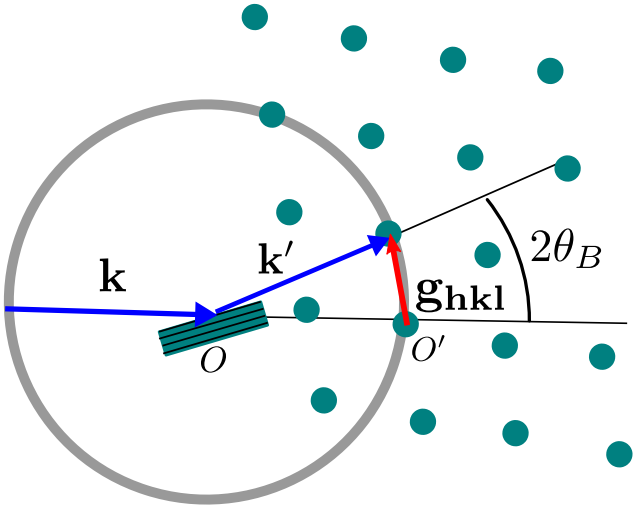

Figure 4.12: Laue condition of diffraction represented in the 2D Ewald sphere. The intersection of the sphere, with radius $|\mathbf{k}|$, and the reciprocal lattice defines the possible Bragg reflections. These reflections are found from reciprocal lattice vectors parting from the O' origin. The bandwith of the incident wave is indicated by the thickness of the circle.

The reciprocal base satisfies $\mathbf{b_i} \cdot \mathbf{a_j} = 2\pi\delta_{ij}$ with δ_{ij}, the Kronecker delta. Therefore, any reciprocal space vector $\mathbf{k}$ can be written as a linear combination of the $\mathbf{b_i}$'s as

$$\mathbf{k} = k_1\mathbf{b_1} + k_2\mathbf{b_2} + k_3\mathbf{b_3}. \tag{4.6}$$

The conditions on the k_i's are to be found. If a vector $\mathbf{K}$ belongs to the reciprocal lattice of a Bravais lattice of points $\mathbf{R}$, then it holds that $e^{i\mathbf{K}\cdot(\mathbf{R}+\mathbf{r})} = e^{i\mathbf{K}\cdot\mathbf{r}}$ for any $\mathbf{r}$. Therefore, it follows that $\mathbf{K}\cdot\mathbf{r} = 2\pi n$, for n integer. Likewise, using the definition of Eq. 4.6 and the lattice vector $\mathbf{R_n} = n_1\mathbf{a_1} + n_2\mathbf{a_2} + n_3\mathbf{a_3}$ we get,

$$\mathbf{K}\cdot\mathbf{R_n} = 2\pi(k_1n_1 + k_2n_2 + k_3n_3) = 2\pi n, \tag{4.7}$$

and since the n_i's are integers, it follows that $k_1 + k_2 + k_3 = n$. Thus, when the coefficients on Eq. 4.6 are integers the plane wave condition is satisfied and a reciprocal lattice vector

$$|\mathbf{g_{hkl}}| = \frac{2\pi}{d_{hkl}}, \tag{4.8}$$

can be defined. It is then clear an inverse proportionality between the lattice parameter of adjacent (hkl) planes to the magnitude of a reciprocal space vector $|\mathbf{g_{hkl}}| \equiv [\text{Å}^{-1}]$. The Laue formulation is an alternative to the geometrical approach for the constructive interference of scattered X-rays:

$$\mathbf{\Delta k} = \mathbf{k}' - \mathbf{k} = \mathbf{g_{hkl}}. \tag{4.9}$$

Eq. 4.9 indicates that constructive interference occurs when the change of wavevector $\mathbf{\Delta k}$, between the incident and reflected waves, is a reciprocal lattice vector. Experimentally, one can search for Bragg reflections by modifying either the magnitude or the direction of the incident $\mathbf{k}$ vector. Because the wavelength of the incident wave is fixed, one can access to reciprocal lattice vectors by the tuning of the incidence angle as schematized in the Ewald sphere of Fig. 4.12.

The Bragg's law (Eq. 4.2) does not provide any information about the scattering intensity $I(hkl)$ of the wavefronts with a constructive interference. Thus, the scattering amplitude of a crystal can be written as

$$\overline{\mathbf{F}}(\mathbf{Q}) = \sum_j f_j(\mathbf{Q}) e^{i\mathbf{Q}\cdot\mathbf{r}_j} \sum_n e^{i\mathbf{Q}\cdot\mathbf{R_n}} = \mathbf{F}(\mathbf{Q})\mathbf{S}(\mathbf{Q}), \tag{4.10}$$

where the first sum of Eq. (4.10) is defined as the unit cell *structure factor* $\mathbf{F}(\mathbf{Q})$ and the second as the *form factor* $\mathbf{S}(\mathbf{Q})$. In one hand, the structure factor sums over the atomic form factor f_j of the j-th atom with respect to its position $\mathbf{r}_j$ relative to a particular lattice site. On the other hand, the form factor sums up over the lattice sites involved in the diffracted intensity via the lattice vectors $\mathbf{R_n} = n_1\mathbf{a_1} + n_2\mathbf{a_2} + n_3\mathbf{a_3}$. It turns out that the conditions of presence and extinction of the reflections follow from the hkl indexation of Eq. 4.10 with proportionality between the Bragg intensity and the structure factor

$$I(hkl) \propto \left|F(hkl)\right|^2. \tag{4.11}$$

Therefore, the reciprocal lattice vector and the structure factor summarize the necessary elements to interpret our XRD results.

4.2 . EXPERIMENTAL RESULTS

In this Section we report direct evidence of the structural change of orientation in the MA cations of three-dimensional MAPI single crystal induced by photon absorption. From time-resolved XRD experiments we conclude that randomly oriented MA^+ ions within the inorganic interstices reorganize in ordered structures to render a net polarization when charge-carrier generation takes place. We find good agreement in the expected modification of the lattice parameter and diffracted intensity after molecular rotation induced by photoexcitation. We have also correlated the structural dynamics of MAPI to its conduction band with spin resolution in order to observe the Rashba-Dresselhaus splitting. Around 70 meV spin-splitting is found in the conduction band of tetragonal MAPI at room temperature.

4.2.1 . Synthesis methods

MAPI single crystals were grown by our collaborators G. Trippé-Allard and E. Deleporte (Laboratoire Aimé Cotton, Université Paris-Saclay). The millimeter-scale crystals were synthesized by the inverse temperature crystallization method [202] where a γ-butyrolactone assisted CH_3NH_3I solution and PbI_2 precursors were used. A stoichiometric ratio of 1:1 was necessary for synthesizing 3D perovskites. The ammonium iodide salt solution is obtained from an ice bath of methylamine (CH_3NH_2) and hydroiodic acid (HI) at ambient atmosphere. This is a common procedure for the hybrid perovskite family [203]. PbI_2 crystals were rinsed and dried after the reaction between solutions of $Pb(NO_3)_2$ and KI. A high-quality sample of these single crystal is shown in Fig. 4.4(b). In the following hours, the TR-XRD experiments were conducted in the as-grown samples as their high susceptibility to degradation, either in air or vacuum conditions, causes the formation of PbI_2 [204].

4.2.2 . Experimental setup

To unveil the cation reorganization in MAPI, single-spot Bragg dynamics was explored with TR-XRD. These pump-probe experiments were conducted at the CRISTAL beamline of synchrotron SOLEIL (France). Fig. 4.13 depicts the overview of the SOLEIL synchrotron with its main elements.The general process of X-ray generation starts by accelerating an electron beam in a linear accelerator (LINAC) until the electrons reach a threshold energy of 100 MeV.

The electrons are then sent towards a second circular accelerator (*Booster*) until they gain an energy of 2.75 GeV which is the necessary input for the storage ring. It is in the storage ring where the electron beam interacts with magnetic dipoles along the ring to maintain a closed trajectory. Additional polepieces with alternated polarity either introduce periodic oscillations or alter the electron trajectory. The deceleration of the wiggling relativistic electrons is responsible of *bremsstrahlung* radiation, from Terahertz to hard X-rays, that supplies each of the 29 available beamlines. The loss of energy due to subsequent deceleration is compensated by the radiofrequency cavity.

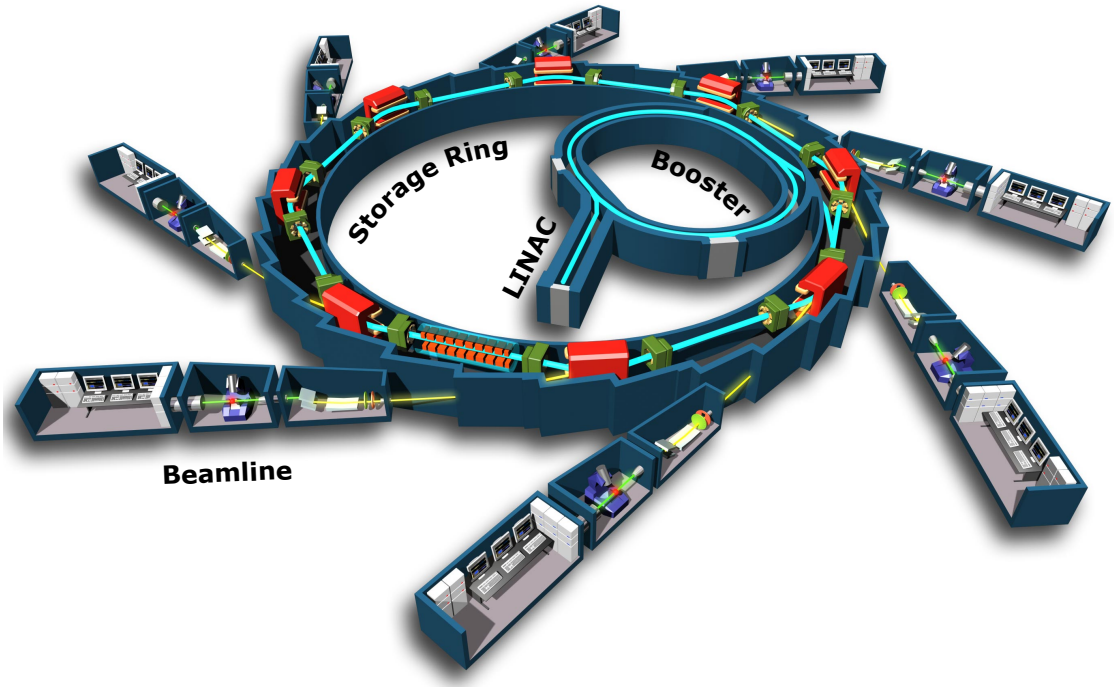

Figure 4.13: Schematics of SOLEIL facility with main elements for the generation of synchrotron radiation.

To satisfy the needs of time resolution, the X-rays are operated in the low-alpha mode that provides electron bunches with a length of few picoseconds [205]. X-rays in between 4 and 30 keV are supplied to the CRISTAL beamline with a U20 undulator in the single-bunch mode. In the CRISTAL beamline, a six-circle (6C) diffractometer (Newport) has a goniometer with an angular accuracy of $\Delta\theta = 0.001^\circ$ for the sample rotation axis and the sphere of confusion is better than 60 μm. The X-ray detection is made with a 2D hybrid pixel detector (XPAD) that can acquire the number and the position of the scattered photons. The XPAD sensor is a Si 500 μm wafer of 560×960 pixels where each pixel is 130×130 μm^2.

TR-XRD was performed on a MAPI single crystal with the experimental arrangement of Fig. 4.14(a). The sample was mounted on the cold finger of an open-loop He cryostat and cool down to 200 K to get a stable condition in the tetragonal phase, then it was oriented in the 6C diffractometer in kappa geometry as shown in 4.14(b).

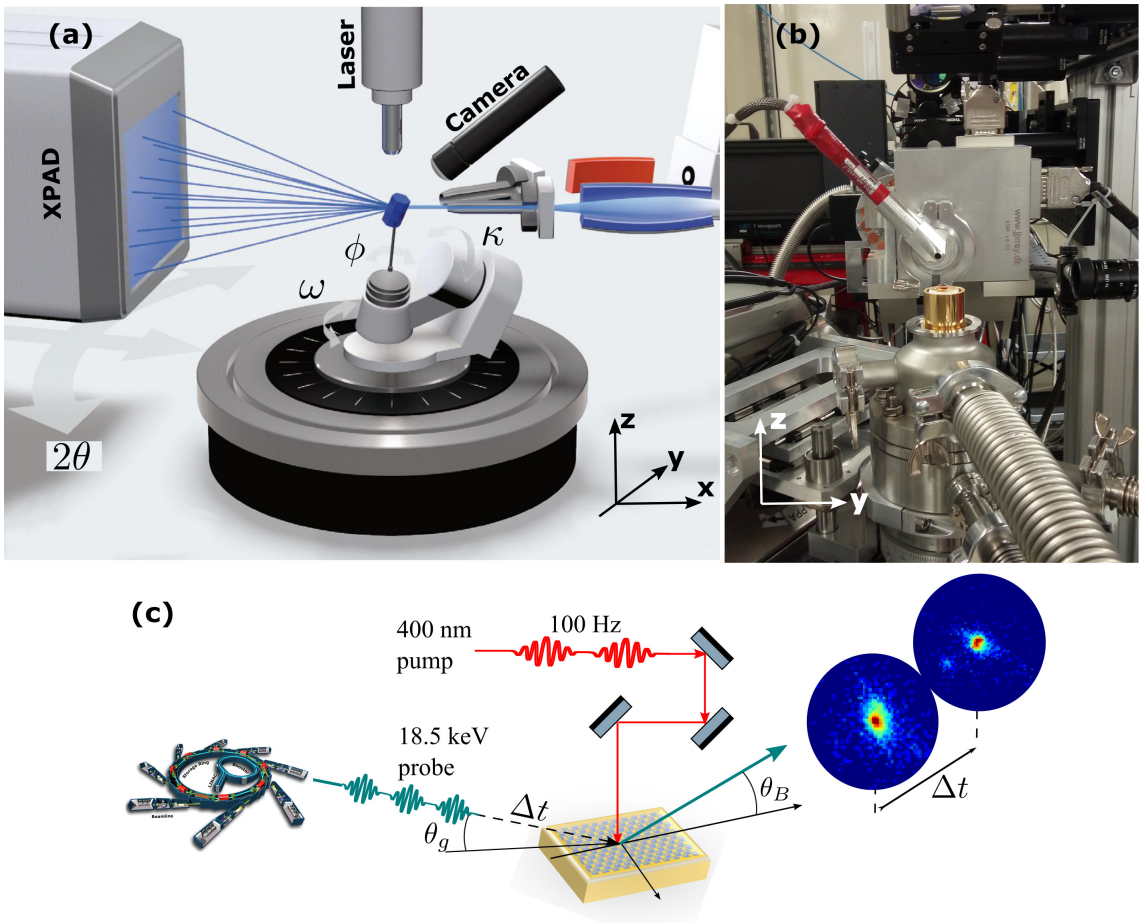

Figure 4.14: (a) Goniometer of the 6C diffractometer in kappa geometry with orientation angles. The incidence of the pump laser is perpendicular to the xy-plane and can be observed with a video camera to determine its cross section. (b) Experimental arrangement of the diffractometer in the CRISTAL beamline facility. (c) TR-XRD experiment on MAPI single crystal: the grazing diffracted intensity and the position of individual Bragg peaks, for consecutive pump-probe events, are registered in the XPAD detector.

Our MAPI samples have an hexagon-like shape surface (4.4(b)) usually exposing their natural $\{100\}$ and $\{112\}$ facets [193]. For the experiments, we oriented the samples with (100) planes parallel to the sample holder as corroborated by the orientation matrix in the *Capoeira* diffractometer control software. The general overview of the experiment is presented in Fig. 4.14(c). Initially, a 400 nm pulsed laser (pump) of 100 Hz repetition rate promotes the formation of charge-carrier pairs at the CB of MAPI. The pump excitation is then followed by 18.511 keV ($\lambda = 0.67$ Å) hard X-ray pulses (probe) after a time delay Δt. Because the width of the X-ray pulses is 10 ps (4k photons each) the time delay is constrained to $\Delta t > 10$ ps. The probe impinges at grazing incidence θ_g to match the penetration depth of the laser beam. Indeed, the penetration depth of the hard X-rays is bigger than the 400 nm pump so that $1° < \theta_B < 2°$ ensures a matching on explored volumes of few tens of nanometers.

4.3 . ORGANIC CATION DYNAMICS IN $CH_3NH_3PbI_3$

Determining suitable Bragg reflections where the structural effects of the MA cation reorganization are present was the preliminary step to perform the experiment. Therefore, the

TR-XRD experiments were conducted on selected Bragg reflections according to the following criteria: (i) simulations of static XRD where the diffracted intensity depending on the MA distribution (polar or apolar) is enhanced and (ii) geometrical availability of the candidate reflections in grazing X-ray irradiation.

The diffracted intensity varies depending on whether the organic cations are disposed in a polar or an apolar distribution. This effect was simulated by our collaborator Min-I Lee (National Taiwan University) using JANA crystallographic software for the structural models proposed by C. Quarti et al. [165]. Here we follow their index nomenclature (Fig. 4.7) i.e., the [1,3] ([4,9]) structures have a polar (apolar) distribution within the inorganic Pb-I sublattice. For our purposes, only the interreticular distance of the probed atomic planes family d_{hkl} and the intensity $I(2\theta_B)$ of the resulting Bragg reflections were compared. As already highlighted, from the Bragg peaks with significant intensity variation with polar or apolar organic cation distribution, only those accessible to grazing irradiation were considered to perform TR-XRD. The simulated diffracted intensities of MAPI in the $(h\ k\ 0)$ plane for polar and apolar MA orientations are shown in Appendix D. The corresponding difference of diffracted intensities between the polar 3 and apolar [4,9] are shown also in Fig. 4.15 represented by a color bar scale where red and blue indicate a higher magnitude difference. On the contrary, white color represents no substantial intensity change. From the same figure, it can be observed that the Bragg (220) have intensity in all the structures (a-f panels), and it was a first candidate for the TR-XRD experiment. In this work, due to the conditions of the goniometer and geometrical constraints of the experimental setup, we studied the (200), $(2\overline{2}2)$ and the (312) Bragg reflections.

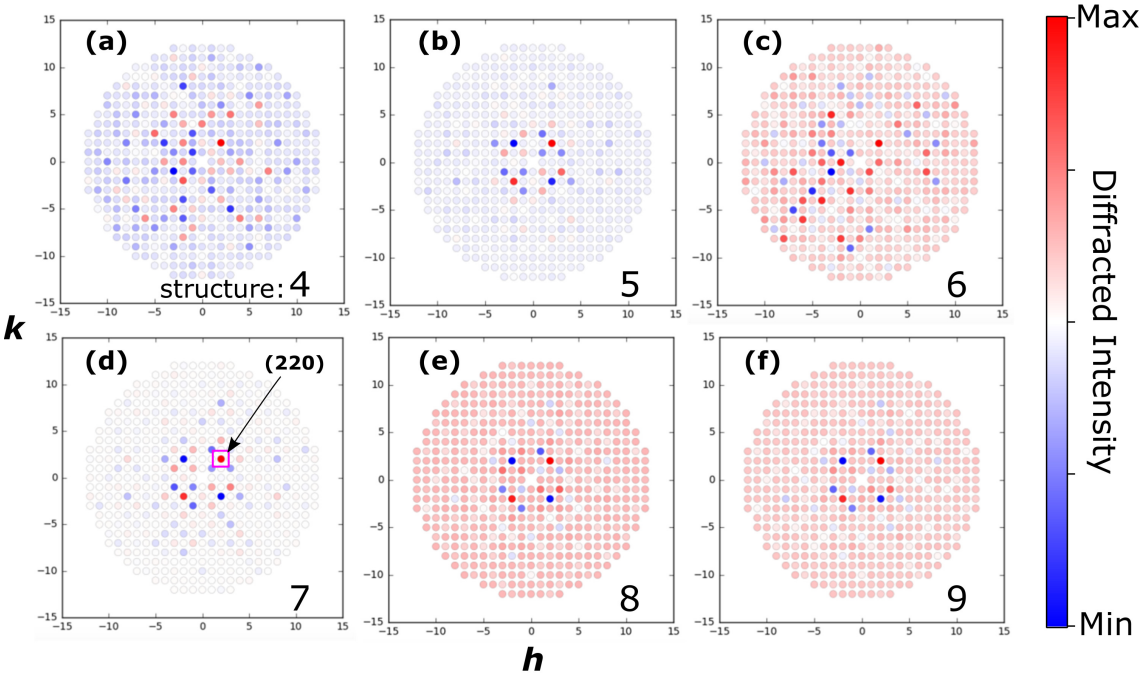

Figure 4.15: Simulated X-ray diffraction intensity difference between polar and apolar structures in the $(h\ k\ 0)$ plane. The nomenclature of the MA distribution corresponds to the structures of Table 4.2. (a)-(f): the intensity of corresponding apolar structures (4 to 9 structures) was subtracted from the intensity of the polar structure 3 (see Appendix D). The (220) Bragg reflection, inside a pink square in (d), is a possible candidate to perform TR-XRD experiments because it appears in all the panels with non-vanishing intensity.

Once the reflections selected, it was necessary to characterize the laser fluence (energy per pulse over the irradiated area A) with a repetition rate of 100 Hz that the sample can stand. Assuming a Gaussian beam we got $A = 0.032$ cm^2, and the fluence was fixed at ~ 0.5 mJ·cm^{-2} by modifying the power input of the laser. This is the fluence where a bimolecular charge recombination is expected in time-resolved photoluminescence (TRPL) [206]. Higher fluences provoke induced thermal excitation and saturation of the system as we show in Fig. 4.16. The figure presents static and dynamic Φ-scans[1] of the (312) reflection with a laser fluence of 1.36 mJ·cm^{-2} where positive and negative delays were used in the pump-probe measurements. It is observed that a shift of $\Phi \sim 0.02°$ between the static and the dynamic measurement occurs for all the different time delays, including negative ones. In a negative time delay, the pump arrives after the probe so that the Bragg peak should appear at the same angle as in the static case which is a clear indication that, by using 1.36 mJ·cm^{-2}, the system does not have time to relax in the timescale of interest.

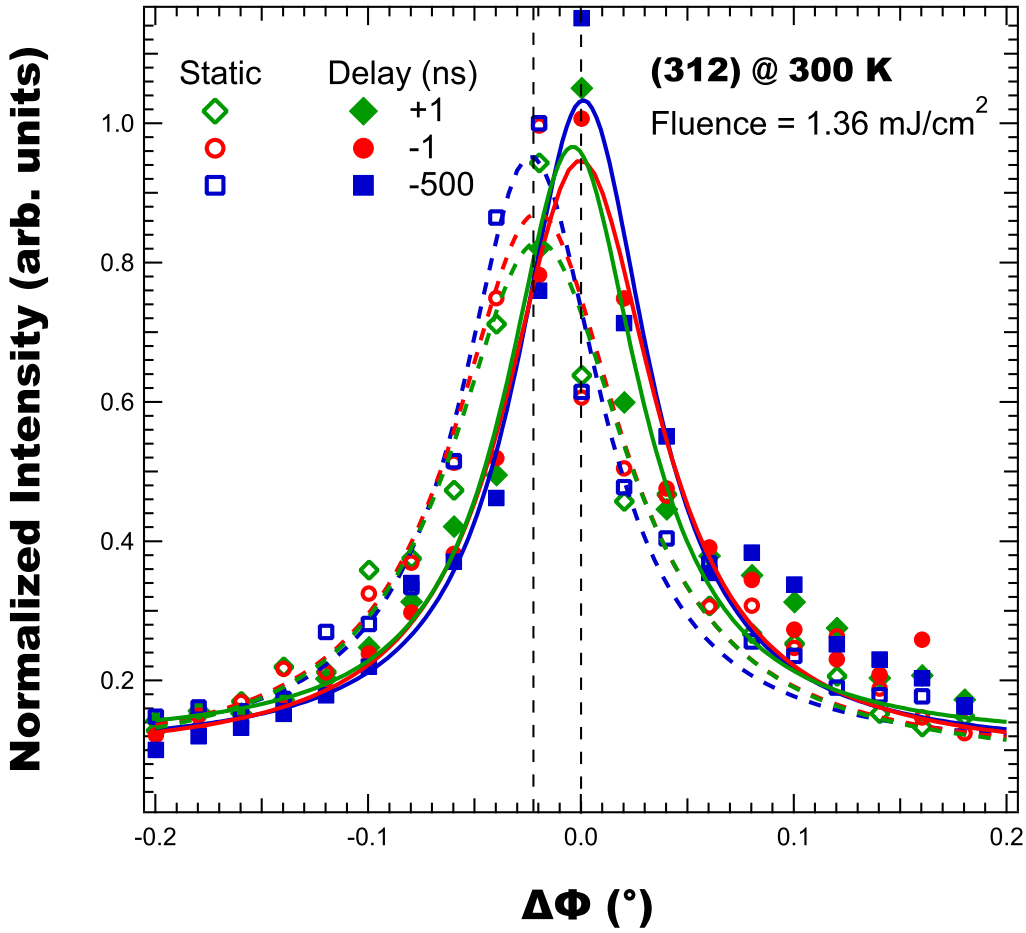

Figure 4.16: Static (empty markers) and dynamic (solid markers) Φ scans of the (312) Bragg of tetragonal MAPI at RT. A laser fluence of 1.36 mJ·cm^{-2} was used in the dynamic measurements. An identical shift of the Bragg reflection for positive and negative time-delays suggest saturation of the system by the pulse energy.

We then analyzed if the sample had been degraded by X-ray irradiation and, to account for precise positions (XPAD) of the selected Bragg reflections into the $I(2\theta_B)$ plots, the Cartesian

[1] In this Chapter, Φ is referred to the goniometer angle indicated in Fig. 4.14.

laboratory frame was transformed to spherical coordinates through the relation between $2\theta_B$ and the detector positioning angles (δ,γ) :

$$cos(2\theta) = cos(\delta) \cdot cos(\gamma). \tag{4.12}$$

Thus, because the PbI_2 is a fingerprint of MAPI degradation, as observed in aged samples at ambient conditions [204] with a strong diffraction intensity at $2\theta_B \sim 5.2°$, we checked that the chosen laser fluence did not degrade the sample by looking for PbI_2 in the XPAD detector. For that, we compared the static diffraction patterns, and the corresponding detector images, of the (312) Bragg at RT before (Fig. 4.17(a)) and after (Fig. 4.17(b)) time-delay scans. We can notice that the diffracted intensity of the (312) reflection remains the same after irradiation preserving its shape in the XPAD detector. No diffraction of PbI_2 nor polycrystalline material was found. With this, the preliminary verifications to perform meaningful experiments were completed and we continued with the dynamical measurements.

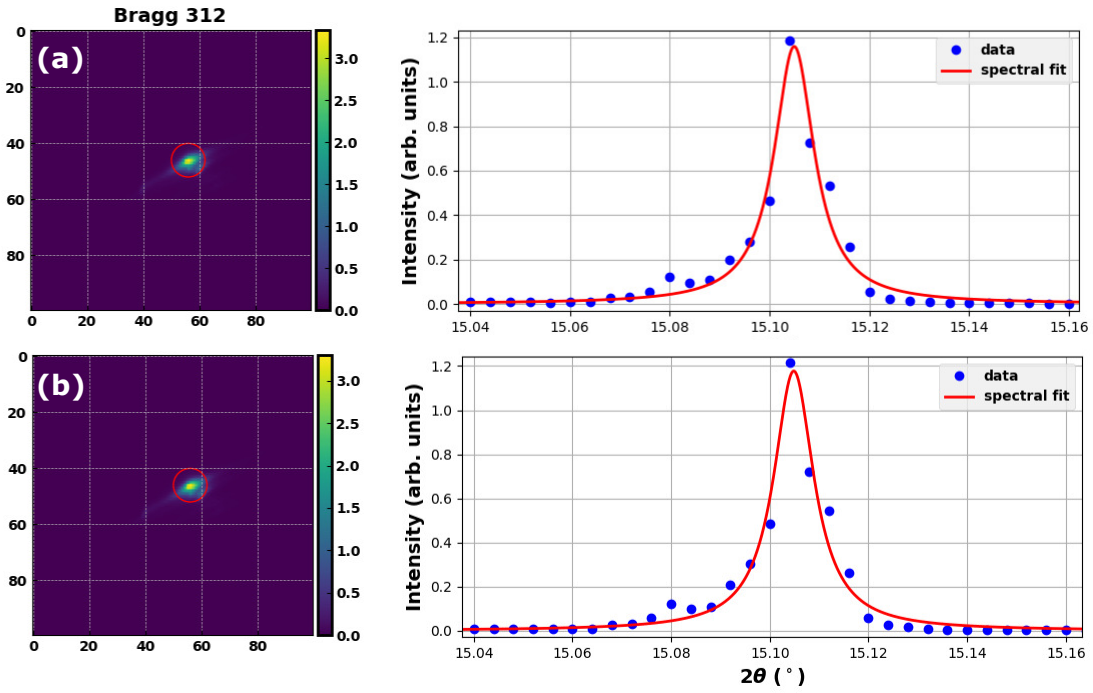

Figure 4.17: Static XRD on the (312) Bragg of MAPI at RT. Left : Logarithmic diffracted intensity projected on the 2D pixel XPAD detector (CCD camera). Right: $I(2\theta)$ plots from the detector images with Lorentzian fitting (red lines). The measurements were taken (a) before and (b) after time-delay scans to discard the formation of PbI_2 from the interaction with the laser pulse and the X-rays.

In a first attempt, laser pulses with 800 nm wavelength were used for the TR-XRD experiments because the energy corresponds to the absorption offset of MAPI: 1.48 eV [193] and 1.55 eV [207] at RT. The pump-probe experiments however, did not show any dynamical signature because the pump energy was insufficient to induce a photoexcited state on the organic cations. Instead, the optical transitions of MAPI were triggered by a 400 nm $(3.1$ eV) laser with a stronger atomic response associated to electronic desexcitation. Just after the arrival of the pump pulse, the occurrence of carrier multiplication is significantly important because the irradiating energy doubles the bandgap. This has been witnessed in time-resolved photoemission (2PPE) that demonstrate a fast carrier cooling with nanosecond-scale characteristic times

[208] whereas the origin of the UV-Vis absorption peak at 480 nm remains unknown [209].

The space group of tetragonal MAPI, in the photoexcited and the equilibrium state, can be obtained from the diffracted intensity in the $I(2\theta)$ relationships. In principle, the space group is usually determined from the Laue symmetry of the crystal and its systematic Bragg absences. The Laue symmetry rules are summarized in the International Tables of Crystallography [195] for the 3D Bravais lattices. Unfortunately, this procedure is not possible in the present case because the explored reflections are in both the centrosymmetric and the non-centrosymmetric classes of the tetragonal structure[2]. Moreover, the R-factor of the single crystal refinement is not helpful in our case to determine the group symmetry because of the small number of acquired reflections in the present experiment[3]. Therefore, our analysis is only based on the experimental structure factor.

We firstly obtained the lattice parameters of MAPI in its tetragonal phase (200 K) from the static rocking curves of the (200), $(2\overline{2}\overline{2})$ and (312) reflections. For that, the θ_B angles were extracted from the 2D pixel detector (Eq. 4.12) and used in the expression for tetragonal structures $1/d_{hkl}^2 = (h^2+k^2)/a^2 + l^2/c^2$. We obtained $a = b \sim 8.881 \pm 0.002$ Å and $c = 12.389 \pm 0.002$ Å for the ground state i.e., without photoexcitation. The experimental modification of the interplanar distance and the reflection intensity after photoexcitation is summarized in Table 4.3. The lattice parameters were obtained from the Bragg position by integrating six different $I(2\theta_B)$ plots in the static and the time-resolved measurement, respectively. The incertitude of the lattice parameter follows from propagating the error of the diffractometer position of δ and γ. These results are very similar to the first-principles modeling of the most stable structures by E. Mosconi et al. [210] where $a = b = 8.86$ Å and $c = 12.66$ Å. Similarly, the lattice constants were experimentally obtained for the photoexcited state rendering $\overline{a} = a - 0.063$ and $\overline{c} = c + 0.258$. In other words, there is an expansion of the c parameter and a contraction of the a parameter. Because the dynamical effect was observed in two Bragg reflections, namely the (312) and the $(2\overline{2}\overline{2})$, we do only report two lattice constants, i.e. a and c. In any case, $a \sim b$ for the tetragonal structure by considering the three reflections: (200), (312) and $(2\overline{2}\overline{2})$, in the static case.

We have compared the lattice parameters of the $(2\overline{2}\overline{2})$ and (312) Bragg with those of the polar and apolar structures proposed by C. Quarti et al. [165]. From the lattice parameter $\Delta d = d_{excited} - d_{static}$ of Table 4.3, the most feasible orientation scenario is a transition from structure 7 to structure 3, as indicated by black arrows in Fig. 4.18. The relative diffracted intensity between structure 7 and structure 3 is also consistent for the $(2\overline{2}\overline{2})$ reflection but not for the (312) where $\Delta I/I_0 \sim -3\%$ from our TR-XRD experiment. To give more insight into the diffracted intensity analysis, we have employed the DFT-optimized structures by F. Brivio et al. (VASP code) [211] to simulate and compare the experimental Bragg intensity $\Delta I/I_0 = (I_{excited} - I_{static})/I_{static}$ to the expected structure factor ratio between apolar and polar ($\dagger$) distributions $\Delta|F| = (|F|^\dagger - |F|)/|F|$. We have experimentally obtained $\Delta I/I_0(2\overline{2}\overline{2}) = +5.9 \pm 1.5\%$ and $\Delta I/I_0(312) = -3.1 \pm 0.8\%$ which is in excellent agreement with the DFT calculations from where $\Delta|F|(2\overline{2}\overline{2}) = +6.0\%$ and $\Delta|F|(312) = -4.4\%$ (Table 4.3).

In overall, our combined analysis of diffracted intensity and lattice parameter indicate for an apolar-to-polar reorganization promoted by photon absorption. Our results on the structural dynamics are in agreement with structural studies of C. Quarti et al. [165] who found that a

[2]Please refer to Table 3.1.4.1 of [195].

[3]Our group have performed the structure refinement of MAPI monocrystals after SC-XRD (200 K) with an R-factor = 0.0302 for the I4/mcm space group [184].

polar cation distribution is linked to a tilt of the octahedra along the $[001]$ whereas an apolar distribution occurs with a tilt on the $[110]$ direction for the structures 8 and 9. In other words, the octahedra rotates along the c-axis for polar distributions of the methylammonium (see Fig. 4.7). Indeed, our sample surface is oriented along the (100) direction which is also parallel to the propagation axis of the laser beam, thus any rotation of the octahedra should appear along the c-axis giving rise to polar cation distribution. The laser effect is thus (i) rotation of the PbI octahedra and (ii) photoexcitation of charge carriers to the CB. Interestingly, we find that the laser beam does not affect the lattice parameter on the direction of incidence were in fact we found a contraction in the a parameter. The complete mechanism of the lattice distortion on the MAPI structure should couple the effects of the reorganizational dynamics of the MA cations and the influence of the photoexcitation processes to the CB. Indeed, the photoexcitation processes inducing a lattice distortion appear only when unoccupied states are populated. No dynamical reorganization was observed by using a laser pump of 800 nm which is probably not enough to populate unoccupied states due to the experimental bandgap. Finally, our findings of the static condition of the MA cations are in contradiction to the calculations for the most energetically favorable polar structures [165] yet in agreement with most of the diffraction studies in tetragonal MAPI (see Table 4.1).

Bragg reflection	d_{static} (Å)	$d_{excited}$ (Å)	Δd ± 0.003 Å	Δd^* (Å)	$\Delta I/I_0$ (%)	$\Delta \lvert F \rvert$ (%)
(200)	4.441	$-$	$-$	$-$	$-$	$-$
$(2\overline{2}2)$	2.801	2.796	-0.005	-0.005	$+5.9 \pm 1.5$	$+6.0$
(312)	2.558	2.543	-0.008	-0.004	-3.1 ± 0.8	-4.4

Table 4.3: Experimental lattice parameter for the static and the photoexcited tetragonal MAPI. The relative intensity of the photoexcited and the static case are in good agreement to the ratio of structure factor $\Delta|F|$ from [211]. The change of lattice parameter Δd is also in good agreement with the results of $(*)$ CPMD calculations [165].

After having analyzed the static and photoexcited states, we concentrate on the temporal evolution between them. We summarize the pump-probe experiments in Fig. 4.19. The curves show the diffraction intensity of tetragonal-phase $(200$ K) MAPI monocrystal as function of time-delay. The standard deviation of each individual data point (average of 73 measurements) is indicated by the error bars. The fluence of the laser pump was set to 0.5 mJ·cm^{-2} to avoid thermal excitations and a repetition rate of 100 Hz was used to avoid saturation on the system. To discriminate dynamical effects from a laser-induced thermal heating of the system, static measurements (without laser pump) were intercalated between the pump-probe shifts (photoexcitation cycles) and are indicated as negative time delays. In Fig. 4.19(a) a time-step of 25 ps was used. We can notice the absence of laser saturation in the static condition of the system. Again, no PbI_2 rings were found after finishing each delay-scan session (~ 9 hrs per Bragg peak). The dynamical effect is clearly visible in a clear rise of the diffracted intensity for positive pump-probe delays. The dynamical effect is particularly reliable for different time-delays since the measurements were acquired in a random order to avoid measurement artifacts coming from a progressive modification of the system.

Characteristic times were extracted by the fitting of the Bragg intensities with a phenomenological exponential:

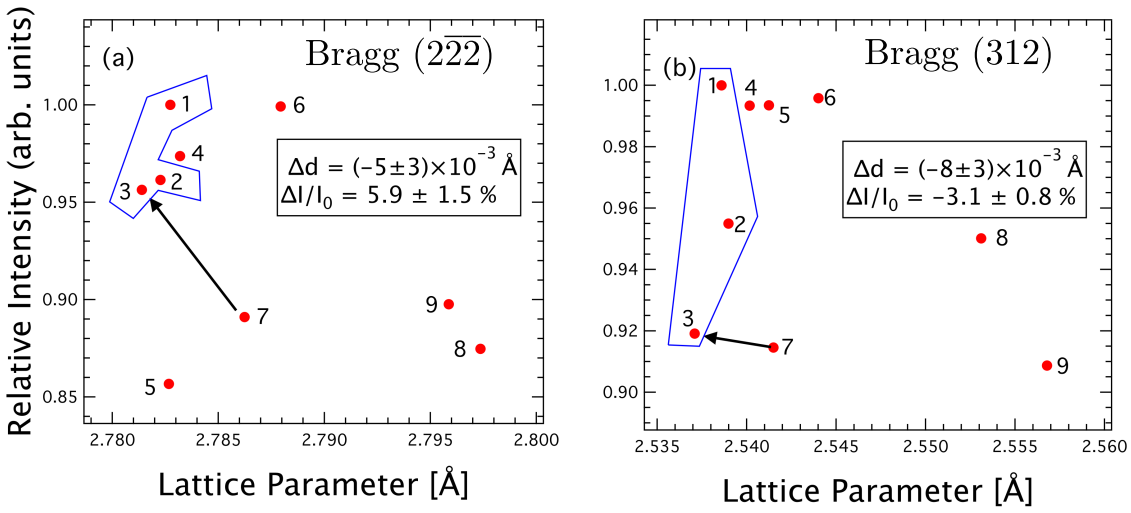

Figure 4.18: Simulated relative intensity and lattice parameter for the (a) $(2\bar{2}\bar{2})$ and the (b) (312) Bragg for possible MA orientations in the tetragonal phase: polar [1,3] and apolar [4,9] structures. The photoexcitation by a laser pump might induce a reorganization of the MA cations in polar dispositions (blue-enclosed) with the most probable structures marked with a black arrow. The experimental values from TR-XRD are indicated in the inset for direct comparison.

$$\Delta I/I_0 = I_0 + I_{max} \cdot \left[1 + exp\left(\frac{t(I_{max}/2) - t}{\tau}\right)\right]^{-1}, \tag{4.13}$$

where τ is the characteristic time of the methylammonium reorganization. We have thus obtained $\tau_{(2\bar{2}\bar{2})} = 19 \pm 8$ ps and $\tau_{(321)} = 7 \pm 4$ ps from 4.19(a). The characteristic time was further corroborated by using a larger time-step of 50 ps for the $(2\bar{2}\bar{2})$ reflection (4.19(b)) from where $\tau_{(2\bar{2}\bar{2})} = 15 \pm 8$ ps. Therefore, we consider $\tau_{(2\bar{2}\bar{2})} = 17 \pm 8$ ps from both measurements. Our estimation of the characteristic time of the transition from apolar to polar orientation is in agreement with the 14 ps rotation time of MA in I4/mcm structures obtained from quasielastic neutron scattering [212] and by CPMD calculations were a 12 ps dynamics [165] was found. We thus propose that charge carrier generation induces the MA reorganization.

An alternative scenario to explain the molecular reorganization is the alignment by non-resonant laser pulses, that could be either adiabatic or non-adiabatic. In the adiabatic situation, the laser field pulse is slow compared to the inherent rotation period of the molecule and the molecule reorganization appears only in the presence of the field. Adiabatic conditions are achieved by commercial laser sources in the ns regime. In the non-adiabatic situation, the laser field pulse is faster than the characteristic rotation period of the molecule. The laser can then induce the molecule in a coherent rotational motion producing a field-free alignment at regularly spaced intervals [213].

In order to distinguish the scenario triggering the MA reorganization, we just recall that we initially tried excitation with 800 nm (1.55 eV) just matching the gap of MAPI. However, the 800 nm excitation did not trigger any dynamics on the diffracted intensity. Since 400 nm (3.10 eV) excitation generates charge carriers, it is thus likely that the MA reorganization is actually caused by the charge-carrier generation and not by laser-induced molecular alignment. Moreover, adiabatic alignment of the molecule can be discarded since the molecular rotation times that we have extracted are comparable to the pulse duration of the X-ray probe.

In the following, we study the unoccupied band structure of tetragonal MAPI, theoretically

and experimentally, to see if our conclusions on the structural reorganization can be confirmed by the Rashba-Dresselhaus splitting in the conduction band.

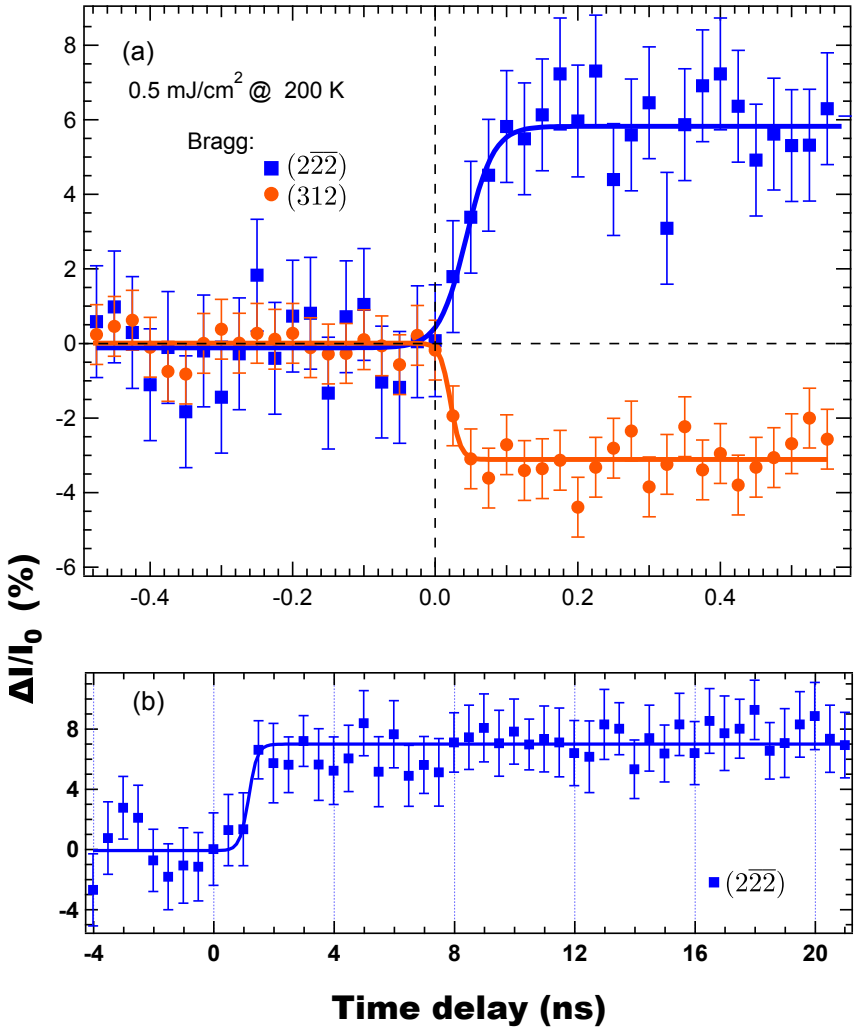

Figure 4.19: Diffraction dynamics of tetragonal MAPI monocrystal as function of time-delay. (a) Diffracted intensity of the (312) and the $(2\bar{2}\bar{2})$ Bragg reflections with a time-step of 25 ps. (b) Diffracted intensity of the $(2\bar{2}\bar{2})$ Bragg with a time-step of 50 ps. The laser fluence is 0.5 mJ·cm^{-2}.

4.3.1 . Unocuppied band dispersion of MAPI

To completely resolve the MAPI band structure, a direct access to the conduction band is necessary. Therefore, we have measured unoccupied states of MAPI monocrystals with spin resolution for the first time. Preliminary results on the conduction band of the tetragonal phase of MAPI based on first-principle calculations allow to conclude on the existence of Rashba-Dresselhaus splitting at room temperature.

We must first identify the effects of SOC on the band structure of MAPI perovskite in the tetragonal phase. For that, ab-initio simulations were performed by our group member Lipin Chen (LPS, Orsay) using the VASP code[4]. The atom structure was relaxed based on the common PBE-GGA functional and the band structure without and with SOC are presented in Fig. 4.20 from where we can clearly observe that the bandgap after considering SOC effects (0.75 eV) reduces significantly compared to the bandgap without SOC (1.65 eV). This bandgap-shrinkage effect after adding the relativistic effects, i.e. spin-orbit coupling, is a well-known effect [171] especially in lead compounds due to the shift of the unoccupied s-p shells [210, 214]. In order to shed more light on this, we extracted the atom-projected band structures (Fig. 4.21) on different atoms, as shown in Fig. 4.21, were we can observe that the Pb and I atoms give their main contribution on the conduction and valence bands close to the Fermi level, respectively. The organic elements (C, H, and N) do only affect very deep states and their contribution around the Fermi level can be neglected. More specifically, based on the orbital-projected band structure of Pb and I atoms (Fig. 4.22), it can be found that the p-orbital contributes significantly to the bands around the Fermi level. This confirms the dominant role of the Pb atoms on the CBM through the empty p-orbital (Fig. 4.22(b)) in agreement with the formal electronic configuration $5d^{10}6s^26p^0$ [211].

Another evident observation is the lift of a two-fold degeneracy of the conduction and valence bands near the bangap after considering the SOC effect (Fig. 4.20(b)): a momentum splitting causing indirect bandgaps is clearly observed in the Y-Γ-Z and U-Γ-V high-symmetry directions. There, non-degenerated states around Γ show energy splittings[5] between 0 to 200 meV. These results clearly indicate that the SOC has a significant effect on the band structure that cannot be neglected, so it has been considered for all the following calculations.

[4]The detailed information about the method is shown in Appendix E

[5]The splitting and interband energies are helpful to compare our experimental SPIPES results as it will be shown in Section 4.3.2.

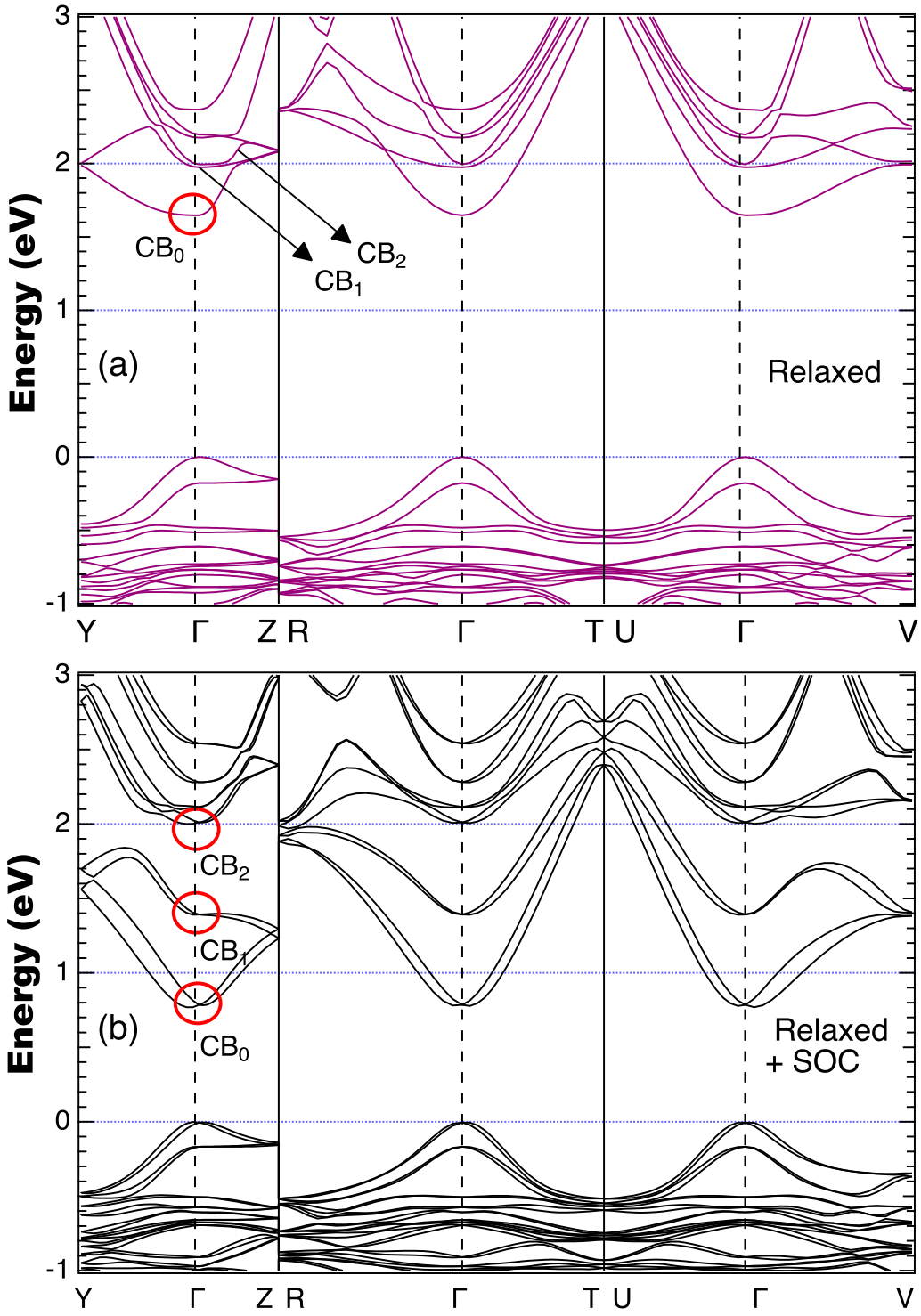

Figure 4.20: (a) Bulk band structure of fully-relaxed tetragonal MAPI: (a) without SOC and (b) with SOC. The spin-orbit coupling introduces a momentum splitting of the conduction band of $\Delta k \sim 0.40$ Å^{-1} in R-Γ-T and also an indirect bandgap in the Y-Γ-Z and U-Γ-V high-symmetry directions. The conduction bands that are considered in the SPIPES experiment (see Section 4.3.2) are encircled in red. The high-symmetry directions are defined as: R=$(1/2, 1/2, 1/2)$, T=$(0, 1/2, 1/2)$, U=$(1/2, 0, 1/2)$, V=$(1/2, 1/2, 0)$, Y=$(0, 1/2, 0)$ and Z=$(0, 0, 1/2)$.

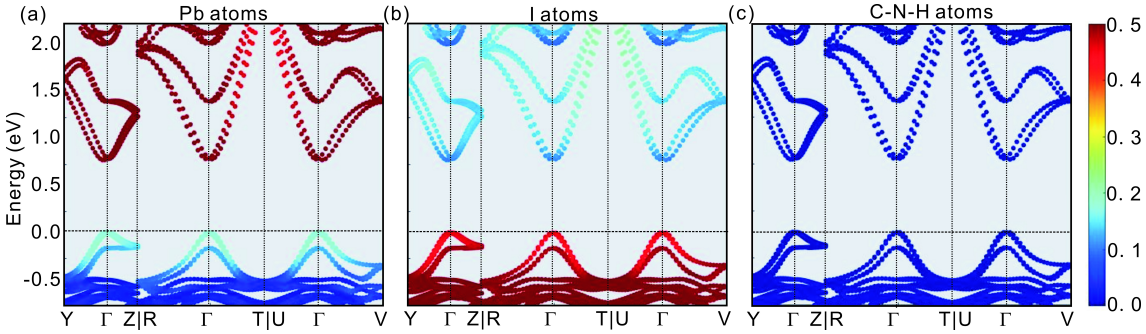

Figure 4.21: Atom-projected bulk band structure of fully-relaxed tetragonal MAPI: (a) Pb, (b) I, (c) C, N and H. The color bar indicates the larger (red) and minor (blue) atomic contribution to the bands nearby the Fermi level. The Pb atoms have a dominant contribution in the conduction properties. The methylammonium cations affect only very deep states.

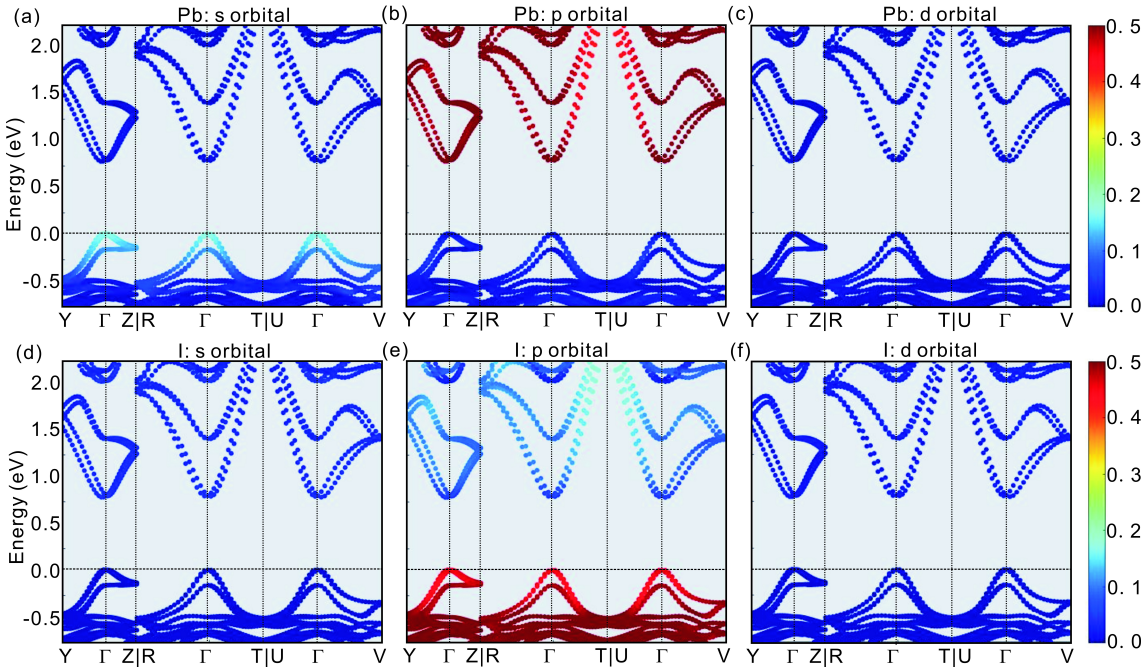

Figure 4.22: Orbital-projected bulk band structure for (a) s, (b) p and (c) d Pb orbitals and (d) s, (e) p and (f) d I orbitals. The color bar indicates highest (red) and lowest (blue) atomic contribution to the bands nearby the Fermi level. The p orbital of the Pb (I) atoms dominates the electronic properties of MAPI at the CB minimum (VB maximum).

After analyzing the bands of the ground state of the system, we simulated the excitation of VB electrons to the CB at Γ-point. In particular, we are interested in the relative change of momentum splitting between the static and the photoexcited systems. Based on VASP software, the photoexcitation was mimicked by transferring one VB electron to the Γ-point of the corresponding empty bands [215] in the primitive cell. Considering that the excitation energy of the optical pump (3.1 eV) is larger than the fundamental bandgap, three simulations considering SOC were performed by populating the electron to CB_0, CB_1 and CB_2 at Γ-point (see Fig. 4.20(b)). The results are summarized in Fig. 4.23. After the excitation of the VB electrons, the fully-relaxed structures show obvious changes with respect to the static system

observed in the lattice distortion (Pb-I bonds), new lattice constants and the band splitting around Γ. We describe and comment these changes in the following.

The lattice constants resulting from the static and dynamic calculations were compared with the corresponding values determined by XRD and TR-XRD experiments. The static lattice parameters after relaxation (with SOC) are $a = 8.901$ Å, $b = 8.913$ Å and $c = 13.183$ Å, showing an acceptable agreement to the experimental lattice data ($a = b = 8.881$ Å, $c = 12.389$ Å) obtained in Section 4.3. The change of lattice constant between the static and the dynamic simulation (VB-CB_0) are $\Delta a = +0.147$ Å, $\Delta b = +0.139$ Å and $\Delta c = +0.321$ Å. Similarly, the experimental change of lattice constants are $\Delta a = -0.063$ Å and $\Delta c = +0.258$ Å i.e., there is good agreement specially in the expansion of the c parameter but quite different for the experimental contraction of a.

Concomitantly with the lattice parameter changes, the band structure is also modified. The momentum splitting is increased in the photoexcited system notably in CB_0. We will focus the discussion on the bands in the Y-Γ-Z direction which was accessed by our SPIPES experiments. The calculations of the static and the VB-CB_0 excitation are compared in Fig. 4.24 with momentum splitting between the two lowest conduction bands of 0.40 Å^{-1} (0.84 Å^{-1}) in the static (photoexcited) case. According to the selection-rules of the Rashba-Dresselhaus effect, the splitting of the bands is larger in structures with a large degree of alignment of the molecules compared to the situation in which the molecules are not aligned [165]. In other words, the higher band splitting in the photoexcited (VB-CB_0) case, when compared to the static calculation, indirectly indicates an apolar-to-polar cation reorganization by photoexcitation in a globally non-centrosymmetric MAPI structure. This is our main conclusion from our TR-XRD experiments. Moreover, populating the CB_1 and CB_2 have a huge impact on the respective band structures (Fig. 4.23(b) and Fig. 4.23(c)) and also in the effective masses. However, since the optimized lattice parameters in these excitations are not in agreement with our experimental estimations (Section 4.3), we limit the discussion to the dynamical effects caused by populating CB_0.

Considering the SOC-induced momentum splitting, the changes of the lattice constants, and the Pb-I bond distortion, we propose that the light excitation modifies the Pb-I framework that subsequently modifies the MA^+ ion configuration. This scenario is also consistent with the atom-projected band structure as the Pb-I atoms give the main contribution to the bands close to the Fermi level in MAPI single crystals. In the following, we extend the theoretical investigations by accessing the unoccupied states of MAPI in the static case.

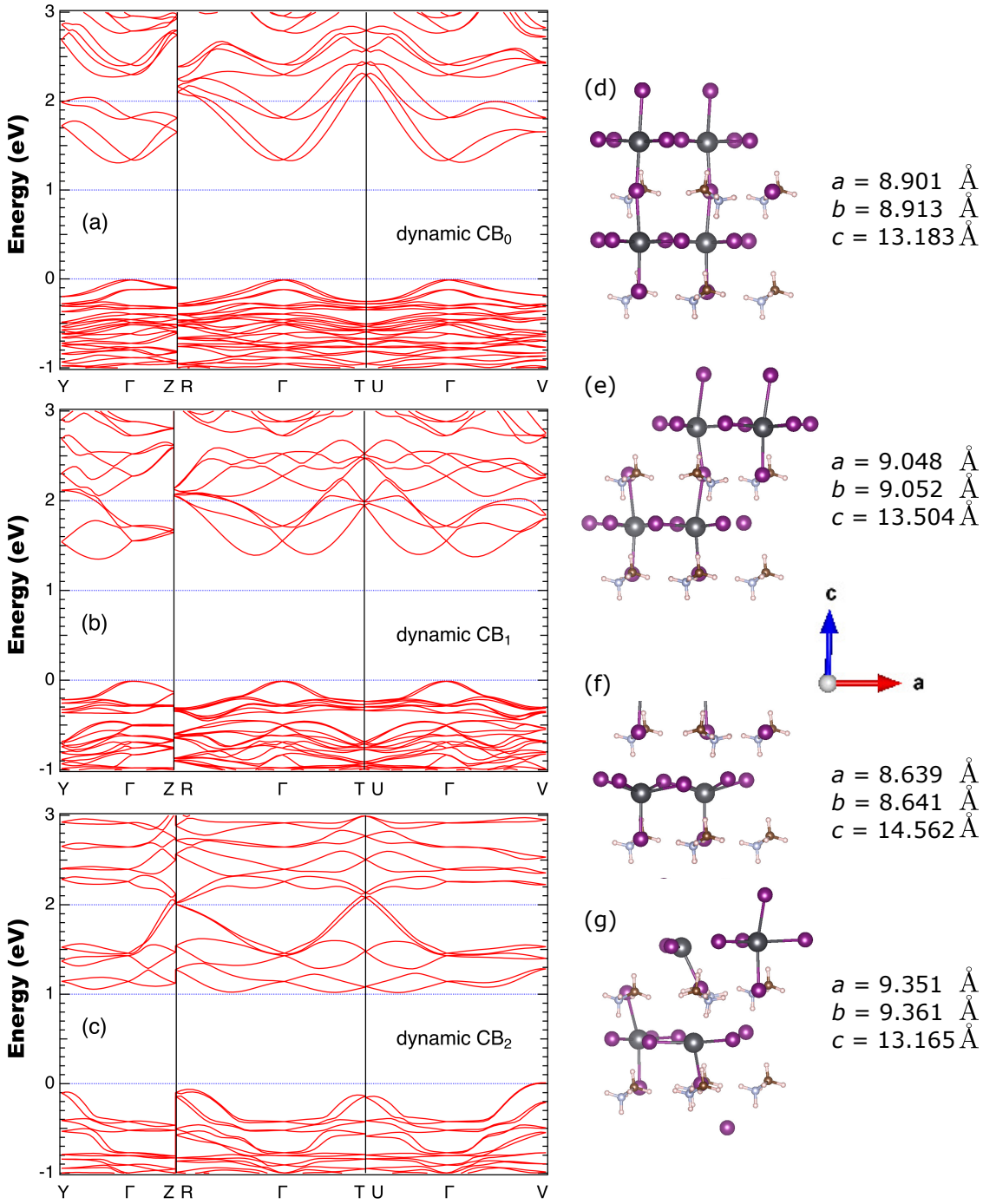

Figure 4.23: Bulk band structure of fully-relaxed tetragonal MAPI with photoexcitation of the highest VB electrons to: (a) CB_0, (b) CB_1 and (c) CB_2 at Γ-point. The relaxed structure (+SOC) of the primitive cell is shown for the (d) static case and the photoexcitation to: (e) CB_0, (f) CB_1 and (g) CB_2, along with their respective cell parameters.

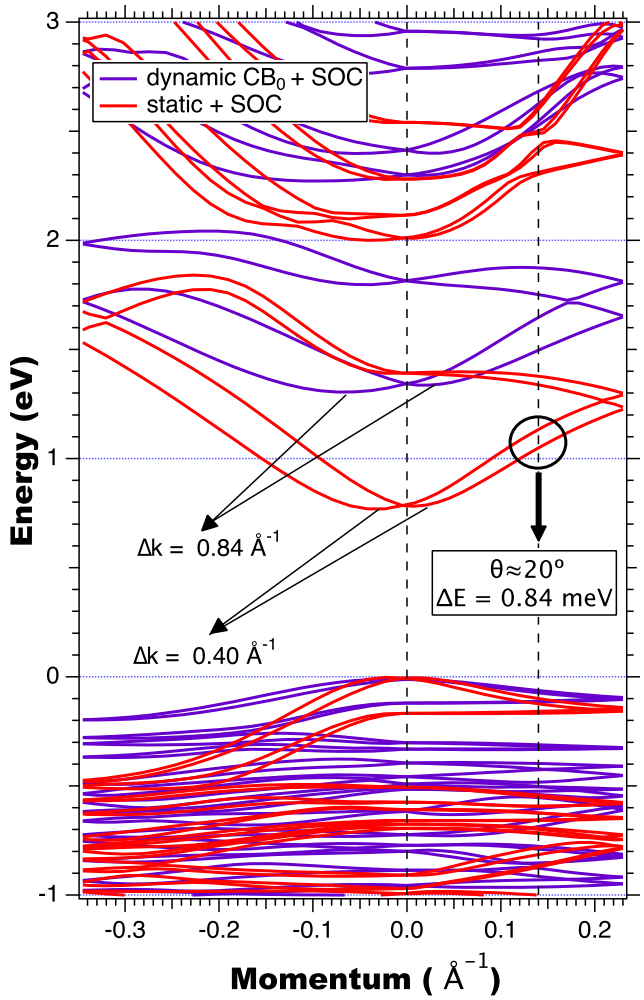

Figure 4.24: Bulk band structure of fully-relaxed tetragonal MAPI in the Y-Γ-Z direction. The static and dynamic (VB-CB_0 photoexcitation) cases are presented. The momentum splitting around Γ are indicated for the CB minimum at each case. Vertical-dashed lines indicate experimentally-accessed reciprocal space points (Section 4.3.2) in good agreement with the theoretical energy splitting of ~ 0.84 eV at $k \sim 0.14$ Å^{-1} ($\theta \sim 20°$).

4.3.2 . Conduction band splitting in MAPI

Let us now analyze if the static structure corresponds to a polar or an apolar configuration by looking at the CB. The p_z orbitals of MAPI were directly accessed by the SPIPES setup at LPS. The experiments were conducted on MAPI single crystals at RT after cleaving the surface in ultra-high vacuum conditions. Previously, millimeter-size MAPI crystals (Fig. 4.25 (a)) were glued on a Ta holder and a ceramic post was attached to the biggest exposed facet ($\{100\}$) with silver epoxy. The sample was then covered with conductive graphite ink to ensure an good electric contact for charge evacuation. Both the graphite ink and the silver epoxy were cured by heating the sample at 360 K over 90 minutes in a hotplate. Once the curing was finished, the electric contact between the sample and the holder was carefully checked to ensure a proper charge evacuation during the measurement. The sample was then introduced in the preparation chamber and cleaved under UHV exposing a fresh surface. LEED (29 eV) was performed on the (100) facet of the crystal and a reduction of the pattern intensity was observed over exposure time (Fig. 4.25 (b)) probably due to a combined effect of the beam current (0.40 μA) and

the beam energy. Anyway, the surface orientation (azimuthal angle ϕ) could be determined and associated with the macroscopical shape of the crystal. Thus, SPIPES was performed on a fresh sample having the same macroscopical shape of the LEED-exposed crystal. The explored reciprocal space direction was the $\overline{\Gamma M}$ (corresponding to Γ-Z in our calculation) by using an electron beam with transverse polarization ($\Phi = 0°$) i.e. perpendicular to $\overline{\Gamma M}$. Transverse polarization of the probe is sensitive to the unoccupied p-orbitals in the Pb-I bonding from the (100) orientation (see Fig. 4.6(d)) and, because of the dominant role of the Pb in the CB around Fermi level, a spin splitting should be observed.

Particular attention was paid to the beam current in order not to degrade the sample during measurements. Probing organometallic perovskites with an electron beam is rather tricky. Degradation by laser [184, 216] or white light illumination [217] in addition to charging upon electron beam bombardment [218] are common effects. In IPES, the organic sample degradation is prevented by decreasing the electron density and up to three orders of magnitude ($\sim 1{\times}10^{-3}$ μA·mm^{-2}) in MAPI monocrystals [219]. Here, the impinging current over the sample was kept at a typical value of 50 nA. The strong interaction of the system with moderated electron current densities (Section 2.2) of ~ 0.5 μA·mm^{-1} was corroborated by the LEED pattern and the SPIPES spectra shown at the bottom of Fig. 4.25(c). We avoided translating the manipulator to irradiate fresh regions of the sample as suggested by J. P. Yang et al. [220] because the presence of domain edges and twinning planes could lead to probing different reciprocal space regions.

The SPIPES spectra of tetragonal MAPI (RT), along the $\overline{\Gamma M}$ direction, is shown in Fig. 4.25 (c). The results show the CB of MAPI for beam incidences at $\theta = 0°$ and $\theta = 20°$. No bias was applied to the sample and the Fermi level was determined from the ideal band structure [221]. Our experiments are in agreement with LEIPES studies [179] (Fig. 4.25) with a similar signal-to-noise ratio and a similar background, although our data have better resolution, reproducing: (i) the relative binding energies namely, the CB_0, CB_1 and CB_2 bands (Table 4.4) and (ii) the shift of such conduction states for $\theta = 0°$ and $\theta = 20°$ spectra[6]. In fact, in LEIPES, the electron beam energy is sweep between 0 and 5 eV, where the effects of the beam broadening are important (see Fig. 3.21). This is a key difference with respect to our setup, where isochromat curves cover typical energies between 5 to 15 eV, that could explain why our data is better resolved. Moreover, our results are spin-resolved for the first time and a splitting of ~ 70 meV is in quantitative agreement to the theoretical expectation (4.20(b)).

[6]Here we are not trying to determine the experimental bandgap of tetragonal MAPI but rather to focus on the relative binding energies of the unoccupied bands and whether or not they present spin splitting.

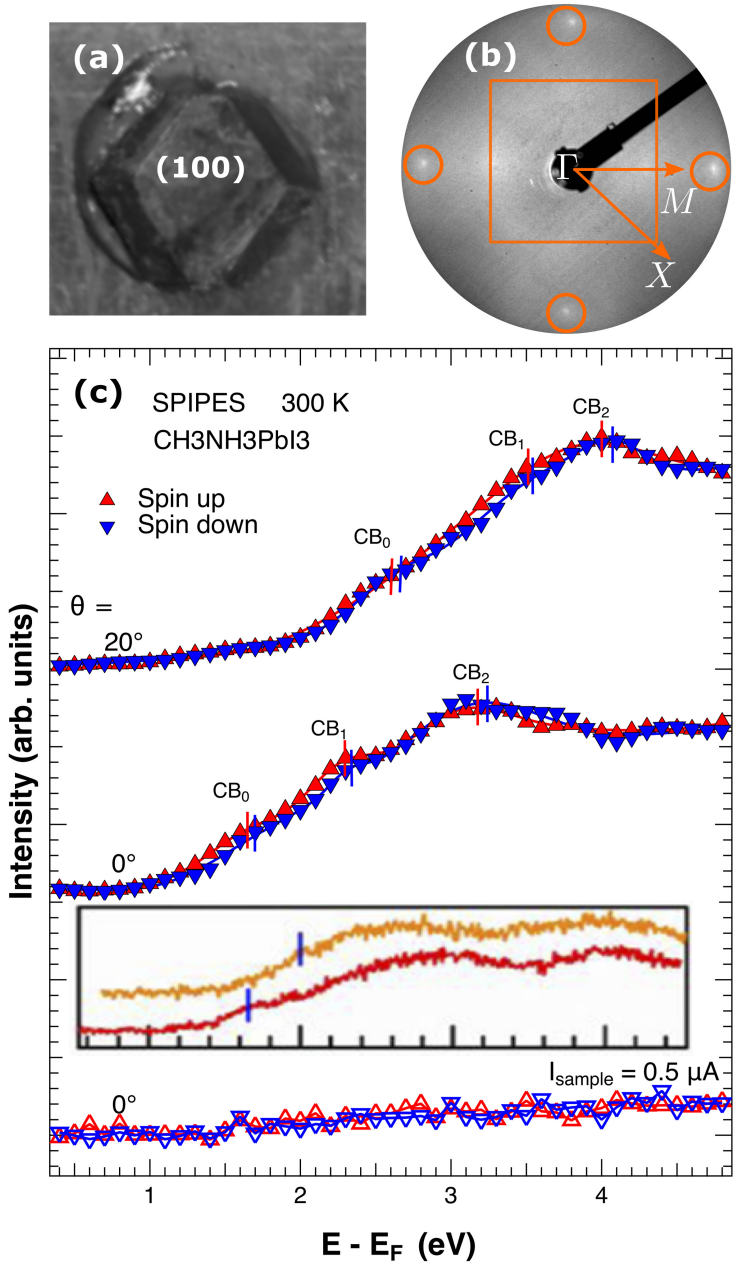

Figure 4.25: (a) Millimeter-size MAPI single crystal exposing natural facet surface oriented in the (100) direction. (b) LEED pattern (29 eV) of as-cleaved MAPI showing high-symmetry paths. The diffraction spots are faint probably due to surface degradation. (c) SPIPES of MAPI perovskite ($\overline{\Gamma M}$) at room temperature taken with our setup. The current over the sample was kept to 50 nA because using higher values ($\sim 0.5\ \mu$A) degrades the system as shown in the lower spectrum (open triangles). Inset: AR-LEIPES of MAPI single crystal along $\overline{\Gamma M}$ (RT) adapted from [179]. The energy scale corresponds to that of our spectra for a direct comparison.

We have fitted the SPIPES spectra of Fig. 4.25 (c), with pseudo-Voigt functions over a linear background, to determine the binding energies of the three identifiable unoccupied states and the spin-splitting of the different states. The shift in binding energy between the up and down states $\Delta CB = CB_i^{\downarrow} - CB_i^{\uparrow}$ at $\theta = 0°$ ($\theta = 20°$) are: $\Delta CB_0 \sim +40$ ($+70$) meV, $\Delta CB_1 \sim +60$ ($+30$) meV and $\Delta CB_2 \sim +80$ ($+70$) meV. Interestingly, considering an average shift to be about 70 meV, we find this value similar to the shift in the direct-to-indirect bandgap

Spin Probe	CB_0 (eV)	CB_1 (eV)	CB_2 (eV)	ΔCB_{10} (eV)	ΔCB_{21} (eV)
down	1.69±0.16	2.34±0.11	3.25±0.16	0.65±0.19	0.91±0.19
up	1.65±0.14	2.29±0.11	3.17±0.18	0.64±0.18	0.88±0.21
integrated†	1.81	2.37	2.88	0.56	0.51

Table 4.4: Room-temperature experimental binding energies of the CB of MAPI at Γ-point and the relative energy between consecutive bands. Spin-resolved energies (LPS) are compared to (†) spin-integrated values from [179].

transition observed in polycrystalline MAPI under hydrostatic pressure [196]. In principle, the CB should be degenerated at Γ-point but it is very likely that the combined effect of finite momentum and energy resolution allows to observe the non-degeneracy at this very point.

We can also compare the experimental difference in energy between consecutive bands at Γ-point with our theoretical calculations. The high-symmetry direction of our SPIPES results $\overline{\Gamma M}$ corresponds to the Γ-Z direction in the band structure calculations (Fig. 4.20) from where $\Delta CB_{10} = CB_1 - CB_0 = 0.61$ eV and $\Delta CB_{21} = CB_2 - CB_1 = 0.62$ eV. We notice the excellent agreement with our experimental data in Table 4.4. Lastly, we consider the calculated shift in energy for the spin up and spin down bands at $k_{\parallel} \sim 0.14$ Å^{-1} ($\theta = 20°$) that is ~ 84 meV also in good agreement with the experimental shift of 70 meV.

Summarizing, our experimental results on the CB of MAPI show band-splitting effects in agreement with the suggestion of Rashba-Dresselhaus splitting. Because the experiments were conducted in the static case which is ascribed to a globally centrosymmetric structure, based on our TR-XRD experiments and ab-initio calculations, there are strong indications that the mechanism of the band splitting in tetragonal MAPI is through a dynamical Rashba-Dresselhaus effect.

4.4 . CONCLUSIONS

We have correlated the electronic and atomic structure of MAPI perovskite by the use of complementary state-of-the-art techniques, TR-XRD (Synchrotron SOLEIL) and SPIPES (LPS, Orsay), in high-quality $CH_3NH_3PbI_3$ single crystals. Our TR-XRD analysis of the structure factor ratio and Bragg intensities suggest a static phase with apolar cations in a tetragonal phase with a I4/mcm symmetry group. The optical excitation induces first an expansion (compression) of the c (a) parameters when the charge-carriers are photoexcited. The modification of lattice parameter and the distortion of the inorganic framework reorients the relaxed MA cations in polar structures. The scenario of centrosymmetric MAPI in the static case is also supported by ab-initio calculations from which the fully-relaxed structures show acceptable agreement in the change of lattice parameter after simulating photoexcitation events. Moreover, SPIPES measurements on the CB reveal a spin-splitting of ~ 70 meV in the CB minimum. Finally, because our TR-XRD analysis indicates an apolar distribution of the MA cations in the static case, it is very likely that the mechanism of band splitting in tetragonal MAPI is highly influenced by the picosecond-scale methylammonium rotations through a dynamical Rashba-Dresselhaus bulk effect.

5 - CONCLUSIONS & PERSPECTIVES

5.1 . SUMMARY

This work has dealt with the experimental study of the Rashba-Bychov at the surface of noble metals and the Rashba-Dresselhaus effects at the bulk of the hybrid perovskite $CH_3NH_3PbI_3$. We have analyzed the manifestation of the spin-orbit coupling in the conduction band by spin-resolved inverse photoemission spectroscopy. For this, we have taken advantage of a new SPIPES setup at LPS. The setup includes a recently developed GaAs-based electron source that allows the tuning of the beam polarization at any desired wavevector while preserving momentum resolution in a low-energy range of operation i.e., from 5 eV up to 200 eV.

In a first part, the operation and capabilities of the new SPIPES setup were tested by the measurement of electronic unoccupied states in low-index noble-metal surfaces: Cu(001) and Au(111). Our data are in good agreement with the literature so that: (i) the setup is satisfactorily working and (ii) a full characterization of the energy, wavevector and spin resolutions was done. More precisely, from the Cu(001) image potential state (n=1) and the Fermi edge, an energy resolution of $\Delta E \sim 200$ meV was obtained. The polarization of the electron source was also investigated by measuring the unoccupied states of the Au(111) system. An effective polarization of $P \sim 0.3$ is found, determined from the L-gap Shockley surface state, in agreement with typical values of the electron beam polarization in GaAs-based sources. With this polarized beam, we observed the splitting of the Au(111) Shockley surface state. Our results are in agreement with ARPES, previous SPIPES measurements and first-principle calculations. A wavevector resolution of $\Delta k \sim 0.07$ Å^{-1} was obtained from the spin asymmetry of the Shockley surface state at the Fermi level. Finally, we demonstrated the 3D tuning of the electron beam polarization vector from the modification of the spectral intensity of the Shockley surface state. The aforementioned commissioning validates the functioning of the spin- and angle-resolved inverse photoemission setup which now grants access to spin-polarized unoccupied states with any orbital composition at any reciprocal space point.

In a second part, the atomic and electronic structure of the prototypical halide perovskite $CH_3NH_3PbI_3$ were studied by time-resolved XRD and SPIPES techniques. More precisely, we investigated the reorganizational dynamics of the methylammonium cations upon light absorption, to elucidate the role of the organic molecules in the electronic properties of the metallorganic system. For that, picosecond-resolved XRD on $CH_3NH_3PbI_3$ single crystals was performed at the CRISTAL beamline in synchrotron SOLEIL. The pump-probe experiments on tetragonal $CH_3NH_3PbI_3$ showed the transient dynamics of the $CH_3NH_3^+$ ions. The results revealed a centrosymmetric space group before the photoexcitation and a non-centrosymmetric structure in the photoexcited state based on the analysis of the experimental Bragg intensities and the lattice constants and their comparison to existing structural models. We thus suggest an apolar-to-polar cation reorganization mediated by the Pb-I cage distortion induced by the photoexcitation of charge-carriers to the conduction band. The scenario of cation reorganization promoted by optical transitions is in agreement with ab-initio calculations of the fully-relaxed $CH_3NH_3PbI_3$ structure, when including relativistic (SOC) effects, and experimentally consistent with the first SPIPES spectra of tetragonal $CH_3NH_3PbI_3$. In one hand, the changes of the lattice parameter, after mimicking photoexcitation to the conduction band, are in agreement with the TR-XRD experiments suggesting also a centrosymmetric structure in the static calculation. Moreover,

spin-polarized states with an energy splitting of ~ 70 meV in the vicinity of the Fermi level, and possibly linked to a dynamical Rashba-Dresselhaus bulk effect, are also in good agreement with a globally centrosymmetric $CH_3NH_3PbI_3$ structure.

5.2 . EXPERIMENTAL PERSPECTIVES

Energy resolution in SPIPES

As demonstrated in this work, GaAs-based electron sources are adequate probes to detect spin-splittings in unoccupied states by SPIPES. Our SPIPES data has shown the influence of the energy resolution on the precise determination of the binding energies. Particularly, the current density over the sample and the GaAs photocathode temperature are two parameters that affect the electron bandwidth energy and thus, the broadening of an inverse photoemission spectrum. The current density mainly depends on the properties of the system under investigation and it can be regulated accordingly. Hence, an optimum control of the GaAs photocathode temperature is highly desirable to increase the total energy resolution of the setup, and it is a perspective to further improve it.

Spin-polarized bulk and surface bands in MAPI

Preliminary data on the conduction states of MAPI revealed polarized states around the Fermi level with an observable SOC of the Pb atoms. One perspective is to perform the full spin-polarized band structure determination of MAPI, to figure out the Rashba coefficients and the effective masses. The origin of the Rashba-Dresselhaus effect can be experimentally studied by investigating the different space group configurations of the MAPI emphasizing on the orthorhombic-tetragonal (165 K) and tetragonal-cubic (327 K) structural transitions. Then, a natural evolution of the topic is to study 2D hybrid perovskite films [222] that possess an enhanced stability [223] and significantly different optoelectronic properties as compared to their 3D counterparts [224, 225]. Hence, quantum confinement effects and the role of p-orbitals (Pb atoms) on the surface states should be addressed experimentally.

2D ferromagnetic semiconductors

Finally, the SPIPES setup is particularly adapted to the study of 2D ferromagnetic semiconductors, where SOC-promoted giant spin-splittings of ~ 450 meV have been predicted by first-principle calculations [226]. Similarly, transition-metal trichalcogenides (TMTC) serve as a base to the semiconductor ferromagnet family $CrXTe_3$ (X = Si, Te), with direct bandgaps of 0.4 eV (Si) and 0.7 eV (Ge) [227, 228], that have potential optoelectronic and spintronic applications due to a ferromagnetic transition with Curie temperatures of 32 K (Si) and 61 K (Ge) [229, 230, 231].

SPIPES is the most suitable experimental technique to investigate the spin character of monolayer direct bandgap TMDCs and TMTCs. Fully disentangling the spin textures of the orbital components in these semiconductors is a straightforward possibility for the SPIPES setup at LPS, without relying in symmetry properties of the surface under study.

Appendix

A . OPTICAL PUMPING OF POLARIZED ELECTRONS

The spin resolution of the IPES setup relies on the production of electron beams with a defined polarization state. A circularly-polarized NIR light beam can eject spin-polarized electrons from NEA GaAs crystals. The change of helicity on the laser system modifies the spin polarization of the electron beam accordingly. In the following, we present the principle of operation of an implemented optical system to automate the tuning between σ^+ and σ^- NIR radiation.

The light propagation along the active elements is referred as in the reference frame of the Fig. 3.3, i.e. along the z-axis. The electric field vector of the laser radiation after traversing the first Glan-Thompson polarizer is

$$\mathbf{E_1} = \hat{\mathbf{x}}cos(\omega t) + \hat{\mathbf{y}}cos(\omega t) = (\hat{\mathbf{x}} + \hat{\mathbf{y}})cos(\omega t) \tag{1}$$

which is a linearly polarized $\mathbf{E}$-field oriented at 45° with respect to the x-axis. The following element is a LC waveplate with a slow and a fast retardation axis. The phase retardation of the slow axis can be adjusted electrically whereas the fast retardation is kept fixed and, without loss of generality, assumed to be equal to zero. Therefore, the effect of the first retarder (LC1) on the electric laser field is

$$\mathbf{E_2} = \hat{\mathbf{x}}cos(\omega t + \delta) + \hat{\mathbf{y}}cos(\omega t - \delta), \tag{2}$$

where a total phase retardation of 2δ has been equally distributed on the vector basis. Eq. 2 is simply transformed to a new orthogonal vector basis

$$\mathbf{E_2} = (\hat{\mathbf{x}} + \hat{\mathbf{y}})cos(\omega t)cos(\delta) - (\hat{\mathbf{x}} - \hat{\mathbf{y}})sin(\omega t)sin(\delta). \tag{3}$$

By comparing to Eq. 1 we can note that LC1 is in fact fully blocking the $(\hat{\mathbf{x}} - \hat{\mathbf{y}})$ component. Therefore if the following polarizer is set parallel to the first one, the resulting electric field is

$$\mathbf{E_3} = (\hat{\mathbf{x}} + \hat{\mathbf{y}})cos(\omega t)cos(\delta) = \mathbf{E_1}cos(\delta). \tag{4}$$

Eq. 4 shows that the phase retardation can modulate the magnitude of $\mathbf{E_3}$ which is totally canceled at $\delta = 90°$. In this manner, the output intensity of the laser is controlled.

The final element is the LC2 retarder that introduces a new phase retardation with respect to the y-component of the linearly polarized electric field. If the phase retardation is adjusted to $\zeta = -3\pi/2$ a circularly polarized state with clockwise helicity (σ^+) results:

$$\mathbf{E_4} = cos(\delta)[\hat{\mathbf{x}}cos(\omega t) + \hat{\mathbf{y}}cos(\omega t - 3\pi/2)] = cos(\delta)[\hat{\mathbf{x}}cos(\omega t) + \hat{\mathbf{y}}sin(\omega t)]. \tag{5}$$

Conversely, if the phase retardation is now $\zeta = -\pi/2$, then

$$\mathbf{E_4} = cos(\delta)[\hat{\mathbf{x}}cos(\omega t) + \hat{\mathbf{y}}cos(\omega t - \pi/2)] = cos(\delta)[\hat{\mathbf{x}}cos(\omega t) - \hat{\mathbf{y}}sin(\omega t)], \tag{6}$$

and a circularly polarized state with counterclockwise helicity (σ^-) results.

B . PHOTON DETECTION : GEIGER-MÜLLER MODE

The equilibrium conditions that give rise to a Poisson distribution in the response of the Geiger-Müller counter were explored. The counting distribution as function of the HV on the GM electrodes is summarized in Fig. 1 for different Ar-acetone combinations. The best gas proportion allows for a stable and longer HV plateau but usually without surpassing 1kV, because the counting may not be at equilibrium. This effect is exemplified in Fig. 1(a) where an abrupt counting avalanche (red lines) can ionize the active gas from the detector. Frequent discharges reduce the lifetime operation of the GM counter. Therefore, even that a partial pressure of about 4 to 4.5% of acetone is within the limits of safety operation, the parameters that have the lower HV value were chosen (Fig. 1(c)).

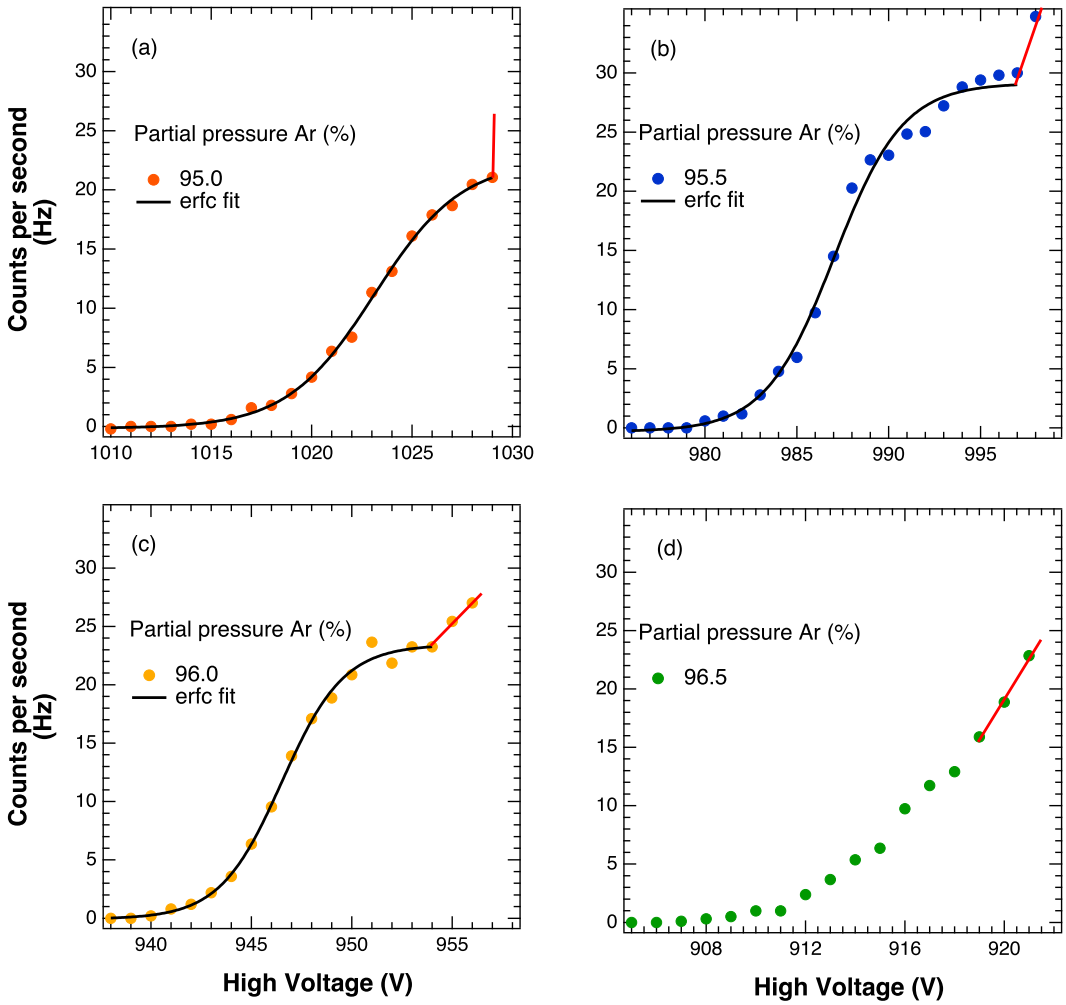

Figure 1: Characterization of gas filling in bandpass detector in the Geiger-Müller mode for a total pressure of 130 mbar of Ar-acetone. The best condition is given by the parameters that reproduce the curve in (c). Red lines indicate Townsend avalanches that discharge the detector.

The CPS in terms of HV can be described by the convolution of a Gaussian $g(t)$ and a Heaviside function $H(t)$ such that $f(V) = g(t) \star H(t)$. Similarly, one can make use of a complementary error function *erfc*, to fit our experimental data as

$$f(V) = \frac{1}{2} erfc((\alpha + \beta V)(\delta V - \gamma)), \tag{7}$$

where,

$$erfc(t) = \frac{2}{\sqrt{\pi}} \int_x^{\infty} e^{-t^2} dt. \tag{8}$$

C . TRANSVERSE POLARIZATION PARAMETERS

The parameters of the rotator lens that were used for acquiring Fig. 3.24 are presented in Fig. 2 where the rotator current evolves linearly with Φ whereas the rotator voltage follows a parabolic trend.

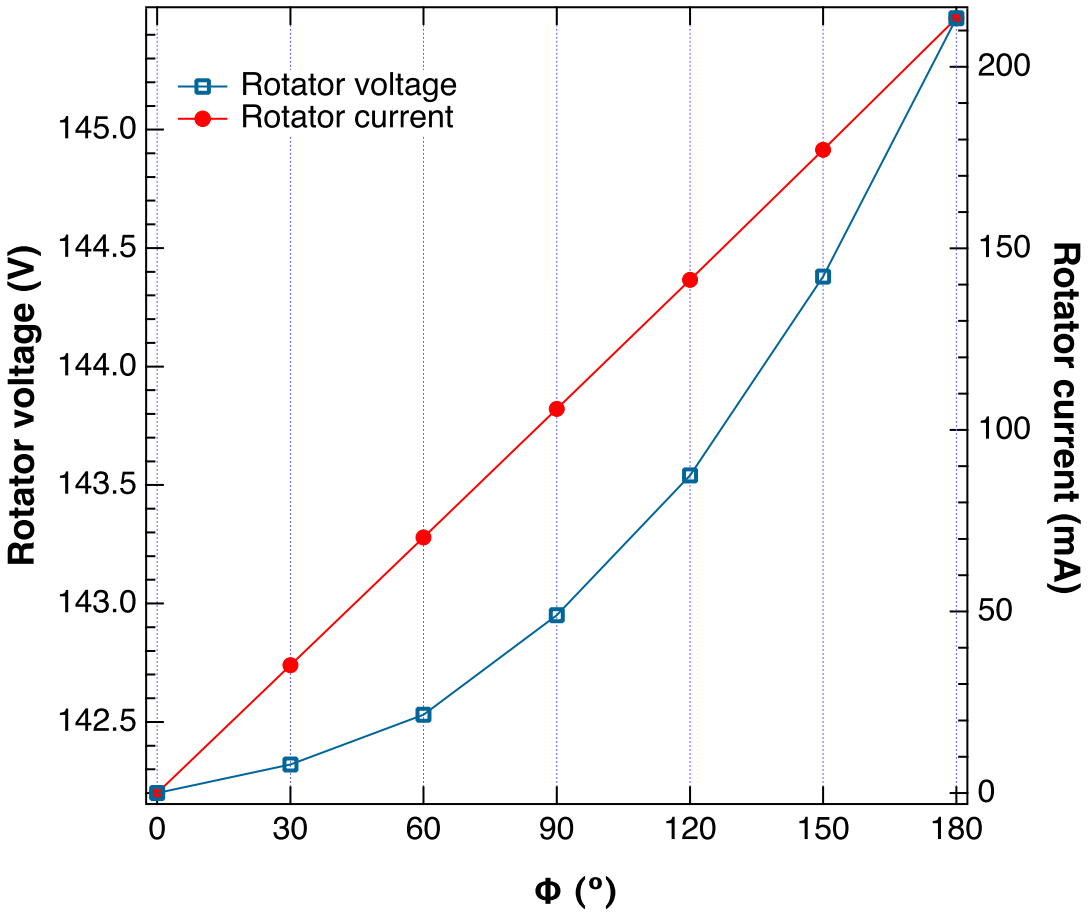

Figure 2: Experimental parameters of the rotator lens for transverse polarization tuning. The positive sign of the rotator current indicate a counterclockwise rotation ($\Phi > 0°$) with respect to the electron beam propagation. Similarly, for clockwise rotations ($\Phi < 0°$) of the spin polarization, the rotator current has the same magnitude but its sign is inverted.

D . DIFFRACTED INTENSITY IN MAPI STRUCTURES

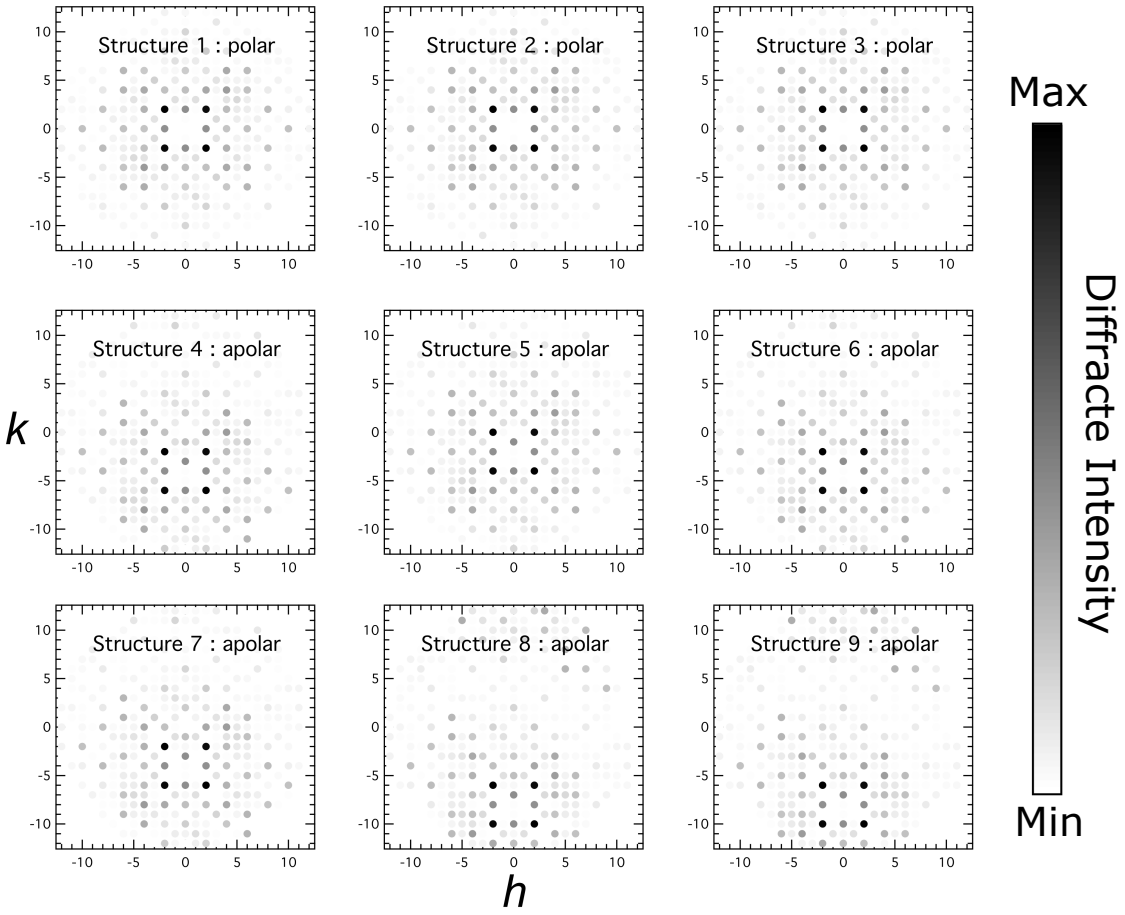

Figure 3: Simulated X-ray diffraction intensity in the (h k 0) plane for 9 different MA cation configurations [165] in MAPI: the structures 1 to 3 are polar and structures 4 to 9 are apolar. A gray-scale bar indicates the intensity of the corresponding Bragg reflections.

E . METHOD FOR DFT CALCULATIONS ON MAPI

The first-principles calculations were carried out within density functional theory (DFT) [232] based on the Vienna ab-initio simulation package VASP [233, 234]. The exchange-correlation potential was adopted by the generalized gradient approximation (GGA) of the Perdew-Burke-Ernzerhof (PBE) functional [235]. The cutoff energy was set as 520 eV. The Brillouin zone was sampled by a Monkhorst-Pack [236, 237] k mesh with size of $3 \times 3 \times 2$. For geometry optimization, the self-consistent field convergence for the total energy and the force variation were set as $10 - 6$ eV and 0.001 eV·Å^{-1}, respectively.

List of Figures

List of Tables

Bibliography

[1] Sebastian David Stolwijk. *Spin-Orbit-Induced Spin Textures of Unoccupied Surface States on Tl/Si(111)*. Springer, 2015.

[2] Stefano Sanvito. Molecular spintronics: The rise of spinterface science. *Nature Physics*, 6(8):562, 2010.

[3] David Hsieh, Yuqi Xia, L Wray, Dong Qian, Arijeet Pal, JH Dil, J Osterwalder, F Meier, G Bihlmayer, CL Kane, et al. Observation of unconventional quantum spin textures in topological insulators. *Science*, 323(5916):919–922, 2009.

[4] Sergey V Eremeev, Ilya A Nechaev, Yu M Koroteev, Pedro M Echenique, and Evgueni V Chulkov. Ideal two-dimensional electron systems with a giant Rashba-type spin splitting in real materials: surfaces of bismuth tellurohalides. *Physical Review Letters*, 108(24):246802, 2012.

[5] SD Stolwijk, H Wortelen, AB Schmidt, and M Donath. Rotatable spin-polarized electron source for inverse-photoemission experiments. *Review of Scientific Instruments*, 85(1):013306, 2014.

[6] Kostya S Novoselov, Andre K Geim, Sergei V Morozov, Dingde Jiang, Yanshui Zhang, Sergey V Dubonos, Irina V Grigorieva, and Alexandr A Firsov. Electric field effect in atomically thin carbon films. *Science*, 306(5696):666–669, 2004.

[7] N David Mermin and Herbert Wagner. Absence of ferromagnetism or antiferromagnetism in one-or two-dimensional isotropic Heisenberg models. *Physical Review Letters*, 17(22):1133, 1966.

[8] Aurelien Manchon, Hyun Cheol Koo, Junsaku Nitta, SM Frolov, and RA Duine. New perspectives for Rashba spin–orbit coupling. *Nature materials*, 14(9):871–882, 2015.

[9] Yabin Fan and Kang L Wang. Spintronics based on topological insulators. volume 6, page 1640001. World Scientific, 2016.

[10] Takehito Yokoyama and Shuichi Murakami. Spintronics and spincaloritronics in topological insulators. *Physica E: Low-dimensional Systems and Nanostructures*, 55:1–8, 2014.

[11] Clément Barraud, Pierre Seneor, Richard Mattana, Stéphane Fusil, Karim Bouzehouane, Cyrile Deranlot, Patrizio Graziosi, Luis Hueso, Ilaria Bergenti, Valentin Dediu, et al. Unravelling the role of the interface for spin injection into organic semiconductors. *Nature Physics*, 6(8):615–620, 2010.

[12] Jl A Wilson and AD Yoffe. The transition metal dichalcogenides discussion and interpretation of the observed optical, electrical and structural properties. *Advances in Physics*, 18(73):193–335, 1969.

[13] Sajid Husain, Rahul Gupta, Ankit Kumar, Prabhat Kumar, Nilamani Behera, Rimantas Brucas, Sujeet Chaudhary, and Peter Svedlindh. Emergence of spin–orbit torques in 2D

transition metal dichalcogenides: A status update. *Applied Physics Reviews*, 7(4):041312, 2020.

[14] Qun-Fang Yao, Jia Cai, Wen-Yi Tong, Shi-Jing Gong, Ji-Qing Wang, Xiangang Wan, Chun-Gang Duan, and JH Chu. Manipulation of the large Rashba spin splitting in polar two-dimensional transition-metal dichalcogenides. *Physical review B*, 95(16):165401, 2017.

[15] Joshua O Island, Aday J Molina-Mendoza, Mariam Barawi, Robert Biele, Eduardo Flores, José M Clamagirand, José R Ares, Carlos Sánchez, Herre SJ Van Der Zant, Roberto D'Agosta, et al. Electronics and optoelectronics of quasi-1D layered transition metal trichalcogenides. *2D Materials*, 4(2):022003, 2017.

[16] Jun Dai, Ming Li, and Xiao Cheng Zeng. Group IVB transition metal trichalcogenides: a new class of 2D layered materials beyond graphene. *Wiley Interdisciplinary Reviews: Computational Molecular Science*, 6(2):211–222, 2016.

[17] Nikhil Sivadas, Matthew W Daniels, Robert H Swendsen, Satoshi Okamoto, and Di Xiao. Magnetic ground state of semiconducting transition-metal trichalcogenide monolayers. *Physical Review B*, 91(23):235425, 2015.

[18] Wei Li, Liujiang Zhou, Oleg V Prezhdo, and Alexey V Akimov. Spin–orbit interactions greatly accelerate nonradiative dynamics in lead halide perovskites. *ACS Energy Letters*, 3(9):2159–2166, 2018.

[19] Mikaël Kepenekian, Roberto Robles, Claudine Katan, Daniel Sapori, Laurent Pedesseau, and Jacky Even. Rashba and Dresselhaus effects in hybrid organic–inorganic perovskites: from basics to devices. *ACS nano*, 9(12):11557–11567, 2015.

[20] Jia Zhang, Ting Wu, Jiashun Duan, Mahshid Ahmadi, Fangyuan Jiang, Yinhua Zhou, and Bin Hu. Exploring spin-orbital coupling effects on photovoltaic actions in Sn and Pb based perovskite solar cells. *Nano energy*, 38:297–303, 2017.

[21] John M Ziman. *Principles of the Theory of Solids*. Cambridge university press, 1972.

[22] Gene Dresselhaus. Spin-orbit coupling effects in zinc blende structures. *Physical Review*, 100(2):580, 1955.

[23] Charles Kittel. Quantum theory of solids, chap. 9, 1963.

[24] Lars Petersen and Per Hedegård. A simple tight-binding model of spin–orbit splitting of sp-derived surface states. *Surface Science*, 459(1-2):49–56, 2000.

[25] S LaShell, BAa McDougall, and E Jensen. Spin splitting of an Au(111) surface state band observed with angle resolved photoelectron spectroscopy. *Physical Review Letters*, 77(16):3419, 1996.

[26] Yua A Bychkov. Properties of 2D electron gas with lifted spectral degeneracy. *JETP Letters*, 39(2):78–81, 1984.

[27] Yu A Bychkov and É I Rashba. Spectrum of a 2D electron gas in an inversion layer. *Soviet Physics Uspekhi*, 28(7):632, 1985.

[28] Friedrich Reinert. Spin–orbit interaction in the photoemission spectra of noble metal surface states. *Journal of Physics: Condensed Matter*, 15(5):S693, 2003.

[29] JB Pendry. New probe for unoccupied bands at surfaces. *Physical Review Letters*, 45(16):1356, 1980.

[30] NV Smith and David Phillip Woodruff. Inverse photoemission from metal surfaces. *Progress in Surface Science*, 21(4):295–370, 1986.

[31] Neville V Smith. Inverse photoemission. *Reports on Progress in Physics*, 51(9):1227, 1988.

[32] JB Pendry. Theory of inverse photoemission. *Journal of Physics C: Solid State Physics*, 14(9):1381, 1981.

[33] Jürgen Henk, Koji Miyamoto, and Markus Donath. Retrieving the initial-state spin polarization from spin-resolved photoemission: Proposal for a case study on W(110). *Physical Review B*, 98(4):045124, 2018.

[34] Volker Dose. Momentum-resolved inverse photoemission. *Surface Science Reports*, 5(8):337–378, 1985.

[35] W Jacob, V Dose, U Kolac, Th Fauster, and A Goldmann. Bulk, surface and thermal effects in inverse photoemission spectra from Cu(100), Cu(110) and Cu(111). *Zeitschrift für Physik B Condensed Matter*, 63(4):459–470, 1986.

[36] Antonio Tejeda and Daniel Malterre. *A Primer in Photoemission: Concepts and Applications*. EDP Sciences, 2020.

[37] FJ Himpsel and T Fauster. Probing valence states with photoemission and inverse photoemission. *Journal of Vacuum Science & Technology A: Vacuum, Surfaces, and Films*, 2(2):815–821, 1984.

[38] M Hoesch, M Muntwiler, VN Petrov, M Hengsberger, L Patthey, M Shi, M Falub, T Greber, and J Osterwalder. Spin structure of the Shockley surface state on Au(111). *Physical Review B*, 69(24):241401, 2004.

[39] M Maniraj, SW D'Souza, J Nayak, Abhishek Rai, Sanjay Singh, BN Raja Sekhar, and SR Barman. High energy resolution bandpass photon detector for inverse photoemission spectroscopy. *Review of Scientific Instruments*, 82(9):093901, 2011.

[40] S Schuppler, N Fischer, Th Fauster, and W Steinmann. Bichromatic two-photon photoemission spectroscopy of image potential states on Ag(100). *Applied Physics A*, 51(4):322–326, 1990.

[41] A Goldmann, M Donath, W Altmann, and V Dose. Momentum-resolved inverse photoemission study of nickel surfaces. *Physical Review B*, 32(2):837, 1985.

[42] F Forstmann. The concepts of surface states. *Progress in Surface Science*, 42(1-4):21–31, 1993.

[43] PM Echenique and JB Pendry. The existence and detection of Rydberg states at surfaces. *Journal of Physics C: Solid State Physics*, 11(10):2065, 1978.

[44] Thomas Fauster. Electron dynamics in image potential states at metal surfaces. *Dynamics at Solid State Surfaces and Interfaces: Current Developments*, pages 53–73, 2010.

[45] V Dose, U Kolac, G Borstel, and G Thörner. Unoccupied surface states in Cu(001). *Physical Review B*, 29(12):7030, 1984.

[46] DA Arena, FG Curti, and RA Bartynski. Unoccupied electronic states of the Cs/Cu(100) and Cs/Cu(111) adsorption systems. *Physical Review B*, 56(23):15404, 1997.

[47] M Donath, M Glöbl, B Senftinger, and V Dose. Photon polarization effects in inverse photoemission from Cu(001). *Solid State Communications*, 60(3):237–240, 1986.

[48] WA Royer and NV Smith. Refracting instrument for ultraviolet inverse photoemission spectroscopy. *Review of Scientific Instruments*, 59(5):737, 1988.

[49] Sune NP Wissing, Christian Eibl, Anna Zumbülte, AB Schmidt, J Braun, J Minár, H Ebert, and M Donath. Rashba-type spin splitting at Au(111) beyond the Fermi level: the other part of the story. *New Journal of Physics*, 15(10):105001, 2013.

[50] H Wortelen, H Mirhosseini, K Miyamoto, AB Schmidt, J Henk, and M Donath. Tuning the spin signal from a highly symmetric unpolarized electronic state. *Physical Review B*, 91(11):115420, 2015.

[51] JJ Scheer and J Van Laar. GaAs-Cs: A new type of photoemitter. *Solid State Communications*, 3(8):189–193, 1965.

[52] M Cardona, NE Christensen, and G Fasol. Relativistic band structure and spin-orbit splitting of zinc-blende-type semiconductors. *Physical Review B*, 38(3):1806, 1988.

[53] Jun-Wei Luo, Gabriel Bester, and Alex Zunger. Full-zone spin splitting for electrons and holes in bulk GaAs and GaSb. *Physical Review Letters*, 102(5):056405, 2009.

[54] H-J Drouhin, C Hermann, and G Lampel. Photoemission from activated gallium arsenide. i. very-high-resolution energy distribution curves. *Physical Review B*, 31(6):3859, 1985.

[55] Daniel T Pierce, F Meier, and P Zürcher. Negative electron affinity GaAs: A new source of spin-polarized electrons. *Applied Physics Letters*, 26(12):670–672, 1975.

[56] Daniel T Pierce and Felix Meier. Photoemission of spin-polarized electrons from GaAs. *Physical Review B*, 13(12):5484, 1976.

[57] Daniel T Pierce, RJ Celotta, G-C Wang, WN Unertl, A Galejs, CE Kuyatt, and SR Mielczarek. The GaAs spin polarized electron source. *Review of Scientific Instruments*, 51(4):478–499, 1980.

[58] CD Thurmond. The standard thermodynamic functions for the formation of electrons and holes in Ge, Si, GaAs, and GaP. *Journal of the Electrochemical Society*, 122(8):1133, 1975.

[59] JS Blakemore. Semiconducting and other major properties of gallium arsenide. *Journal of Applied Physics*, 53(10):R123–R181, 1982.

[60] U Kolac, M Donath, K Ertl, H Liebl, and V Dose. High-performance GaAs polarized electron source for use in inverse photoemission spectroscopy. *Review of Scientific Instruments*, 59(9):1933–1940, 1988.

[61] Nicolas Rougemaille and AK Schmid. Magnetic imaging with spin-polarized low-energy electron microscopy. *The European Physical Journal-Applied Physics*, 50(2), 2010.

[62] P Sáez, R Alley, J Clendenin, J Frisch, R Kirby, R Mair, T Maruyama, R Miller, G Mulhollan, G Prescott, et al. Polarization studies of strained GaAs photocathodes at the SLAC gun test laboratory. In *Proceedings Particle Accelerator Conference*, volume 2, pages 887–889. IEEE, 1995.

[63] MJ Alguard, JE Clendenin, RD Ehrlich, VW Hughes, JS Ladish, MS Lubell, KP Schüler, Guenter Baum, Wilhelm Raith, Roger H Miller, et al. A source of highly polarized electrons at the stanford linear accelerator center. *Nuclear Instruments and Methods*, 163(1):29–59, 1979.

[64] J Van Laar and JJ Scheer. Fermi level stabilization at semiconductor surfaces. *Surface Science*, 3(2):189–201, 1965.

[65] E Pelucchi, S De Rossi, and Franco Ciccacci. Spin polarized photoemission from thin GaAs photocathodes. *Journal of Electron Spectroscopy and related phenomena*, 76:505–509, 1995.

[66] U Fano. Spin orientation of photoelectrons ejected by circularly polarized light. *Physical Review*, 178(1):131, 1969.

[67] M Erbudak and B Reihl. Depolarization of photoelectrons emitted from optically pumped GaAs. *Applied Physics Letters*, 33(7):584–585, 1978.

[68] Stefano Spezia, Dominique Persano Adorno, Nicola Pizzolato, and Bernardo Spagnolo. Temperature dependence of spin depolarization of drifting electrons in n-type GaAs bulks. *arXiv preprint arXiv:1003.2163*, 2010.

[69] R Allenspach, F Meier, and D Pescia. Spin polarized photoemission from GaAs and Ge: Temperature dependence of the threshold polarization. *Applied Physics Letters*, 44(12):1107–1109, 1984.

[70] Xiuguang Jin, Atsushi Mano, Fumiaki Ichihashi, Naoto Yamamoto, and Yoshikazu Takeda. High-performance spin-polarized photocathodes using a GaAs/GaAsP strain-compensated superlattice. *Applied Physics Express*, 6(1):015801, 2012.

[71] T Nishitani, T Nakanishi, M Yamamoto, S Okumi, F Furuta, M Miyamoto, M Kuwahara, N Yamamoto, K Naniwa, O Watanabe, et al. Highly polarized electrons from GaAs–GaAsP and InGaAs–AlGaAs strained-layer superlattice photocathodes. *Journal of Applied Physics*, 97(9):094907, 2005.

[72] HM Al-Khateeb, BG Birdsey, TC Bowen, AS Green, ME Johnston, and Timothy J Gay. A simplified GaAs polarized electron source. *Review of Scientific Instruments*, 70(10):3882–3885, 1999.

[73] Brian S Henderson. Study of negative electron affinity GaAs photocathodes. *Department of Physics and Astronomy, Rice University, Houston, TX*, 2009.

[74] Comparative study of the preparation of negative electron affinity GaAs photocathodes with O2 and with NF3.

[75] Jing Guo and Wenting Qu. Quantum efficiency conversion from the reflection-mode GaAs photocathode to the transmission-mode one. *Optik*, 124(19):4012–4015, 2013.

[76] Richard L Sheffield. High brightness electron sources. In *Proceedings Particle Accelerator Conference*, volume 2, pages 882–886. IEEE, 1995.

[77] N Chanlek, JD Herbert, RM Jones, LB Jones, KJ Middleman, and BL Militsyn. The degradation of quantum efficiency in negative electron affinity GaAs photocathodes under gas exposure. *Journal of Physics D: Applied Physics*, 47(5):055110, 2014.

[78] J Grames, R Suleiman, PA Adderley, J Clark, J Hansknecht, D Machie, M Poelker, and ML Stutzman. Charge and fluence lifetime measurements of a DC high voltage GaAs photogun at high average current. *Physical Review Special Topics-Accelerators and Beams*, 14(4):043501, 2011.

[79] Wei Liu, Shukui Zhang, Marcy Stutzman, and Matt Poelker. Effects of ion bombardment on bulk GaAs photocathodes with different surface-cleavage planes. *Physical Review Accelerators and Beams*, 19(10):103402, 2016.

[80] NG Stoffel and PD Johnson. A low-energy high-brightness electron gun for inverse photoemission. *Nuclear Instruments and Methods in Physics Research Section A: Accelerators, Spectrometers, Detectors and Associated Equipment*, 234(2):230–234, 1985.

[81] M Maniraj and Sudipta Roy Barman. Influence of the contact potential and space-charge effect on the performance of a Stoffel-Johnson design electron source for inverse photoemission spectroscopy. *Review of Scientific Instruments*, 85(3):033301, 2014.

[82] Massimo Ferrario, Mauro Migliorati, and Luigi Palumbo. Space charge effects. *arXiv preprint arXiv:1601.05214*, 2016.

[83] Lamberto Duò, Marco Finazzi, Franco Ciccacci, and Lucio Braicovich. Interaction of oxygen with polycrystalline cobalt studied by inverse-photoemission spectroscopy. *Physical Review B*, 47(23):15848, 1993.

[84] W Sinz. The design of electron guns including thermal effects. *Nuclear Instruments and Methods in Physics Research*, 187(1):259–262, 1981.

[85] Peter W Hawkes and Erwin Kasper. *Principles of electron optics*, volume 2. Academic press, 1996.

[86] Joachim Kessler. *Polarized electrons*, volume 1. Springer Science & Business Media, 1985.

[87] Charles K Sinclair. Electron beam polarimetry. In *AIP Conference Proceedings CONF-980573*, volume 451, pages 23–39. American Institute of Physics, 1998.

[88] Noah Sherman. Coulomb scattering of relativistic electrons by point nuclei. *Physical Review*, 103(6):1601, 1956.

[89] M Hoesch, T Greber, VN Petrov, M Muntwiler, M Hengsberger, W Auwärter, and J Osterwalder. Spin-polarized Fermi surface mapping. *Journal of Electron Spectroscopy and Related Phenomena*, 124(2-3):263–279, 2002.

[90] M Budke, T Allmers, M Donath, and G Rangelov. Combined experimental setup for spin- and angle-resolved direct and inverse photoemission. *Review of Scientific Instruments*, 78(11):113909, 2007.

[91] John Unguris, A Seiler, RJ Celotta, Daniel T Pierce, PD Johnson, and NV Smith. Spin-polarized inverse photoelectron spectroscopy of solid surfaces: Ni(110). *Physical Review Letters*, 49(14):1047, 1982.

[92] M Donath. Spin-resolved inverse photoemission of ferromagnetic surfaces. *Applied Physics A*, 49(4):351–364, 1989.

[93] R Stiepel, R Ostendorf, C Benesch, and H Zacharias. Vacuum ultraviolet photon detector with improved resolution for inverse photoemission spectroscopy. *Review of Scientific Instruments*, 76(6):063109, 2005.

[94] M Nakatake, Y Okamura, S Akiyama, H Namatame, and M Taniguchi. High-resolution photon detection system for inverse-photoemission spectroscopy. *Journal of Electron Spectroscopy and Related Phenomena*, 88:1027–1030, 1998.

[95] L Kipp, M Boehme, H Carstensen, R Claessen, and M Skibowski. Compact grating spectrometer for inverse photoemission spectroscopy. *Review of Scientific Instruments*, 68(5):2144–2148, 1997.

[96] V Dose. VUV isochromat spectroscopy. *Applied Physics*, 14(1):117–118, 1977.

[97] Christian Thiede, Iris Niehues, Anke B Schmidt, and Markus Donath. The acetone bandpass detector for inverse photoemission: operation in proportional and Geiger–Müller modes. *Measurement Science and Technology*, 29(6):065901, 2018.

[98] Glenn F Knoll. *Radiation detection and measurement*. John Wiley & Sons, 2010.

[99] G Denninger, V Dose, and H Scheidt. A VUV isochromat spectrometer for surface analysis. *Applied Physics*, 18(4):375–380, 1979.

[100] KC Prince. Improved inverse photoemission detector. *Review of Scientific Instruments*, 59(5):741–742, 1988.

[101] IG Hill and AB McLean. A comparison of two high performance inverse photoemission bandpass detectors. *Review of Scientific Instruments*, 69(1):261–264, 1998.

[102] JA Lipton-Duffin, AG Mark, GK Mullins, GE Contant, and AB McLean. An inverse photoemission system with large solid angle of detection and adjustable optical bandpass. *Review of Scientific Instruments*, 75(2):445–454, 2004.

[103] D Funnemann and H Merz. 10 eV photon detector for inverse photoemission. *Journal of Physics E: Scientific Instruments*, 19(7):554, 1986.

[104] S Banik, AK Shukla, and SR Barman. Optimal operating conditions and characteristics of acetone/CaF2 detector for inverse photoemission spectroscopy. *Review of Scientific Instruments*, 76(6):066102, 2005.

[105] JA Lipton-Duffin, AG Mark, and AB McLean. Photon detection with n-propanol and C2H6o isomers. *Review of Scientific Instruments*, 73(9):3149–3153, 2002.

[106] V Dose, Th Fauster, and R Schneider. Improved resolution in VUV isochromat spectroscopy. *Applied Physics A*, 40(4):203–207, 1986.

[107] M Budke, V Renken, H Liebl, G Rangelov, and M Donath. Inverse photoemission with energy resolution better than 200 meV. *Review of Scientific Instruments*, 78(8):083903, 2007.

[108] Wayne M Trott, Normand C Blais, and Edward A Walters. Molecular beam photoionization study of acetone and acetone-d6. *The Journal of Chemical Physics*, 69(7):3150–3158, 1978.

[109] Hiroyuki Yoshida. Principle and application of low energy inverse photoemission spectroscopy: a new method for measuring unoccupied states of organic semiconductors. *Journal of Electron Spectroscopy and Related Phenomena*, 204:116–124, 2015.

[110] F Ciccacci, S De Rossi, E Pelucchi, and A Tagliaferri. Spin-resolved electron spectroscopy with highly polarized sources: Inverse photoemission from ferromagnets. *Review of Scientific Instruments*, 68(4):1841, 1997.

[111] Philipp Eickholt, Charlotte Sanders, Maciej Dendzik, Luca Bignardi, Daniel Lizzit, Silvano Lizzit, Albert Bruix, Philip Hofmann, and Markus Donath. Spin structure of K valleys in single-layer WS2 on Au(111). *Physical Review Letters*, 121(13):136402, 2018.

[112] SNP Wissing, AB Schmidt, H Mirhosseini, J Henk, CR Ast, and M Donath. Ambiguity of experimental spin information from states with mixed orbital symmetries. *Physical Review Letters*, 113(11):116402, 2014.

[113] Christian Datzer, Anna Zumbülte, Jürgen Braun, Tobias Förster, Anke B Schmidt, Jianli Mi, Bo Iversen, Philip Hofmann, Jan Minár, Hubert Ebert, et al. Unraveling the spin structure of unoccupied states in Bi2Se3. *Physical Review B*, 95(11):115401, 2017.

[114] G Berti, A Calloni, A Brambilla, G Bussetti, L Duò, and F Ciccacci. Direct observation of spin-resolved full and empty electron states in ferromagnetic surfaces. *Review of Scientific Instruments*, 85(7):073901, July 2014.

[115] Franco Ciccacci, S De Rossi, E Pelucchi, and Alberto Tagliaferri. Spin-resolved electron spectroscopy with highly polarized sources: Inverse photoemission from ferromagnets. *Review of Scientific Instruments*, 68(4):1841–1845, 1997.

[116] Madan S Jagadeesh, Alberto Calloni, Gianlorenzo Bussetti, Lamberto Duò, and Franco Ciccacci. Spin-Resolved PES and IPES Investigation of the Graphene/Ni(111) Interface. *Physica Status Solidi (b)*, 255(3):1700415–5, November 2017.

[117] T Duden and E Bauer. A compact electron-spin-polarization manipulator. *Review of Scientific Instruments*, 66(4):2861–2864, 1995.

[118] V Dose. Image potential surface states. *Physica Scripta*, 36(4):669, 1987.

[119] H. J. Meister. Die bewegung des polarisationsvektors eines Dirac-Teilchens im makroskopischen elektromagnetischen feld. *Zeitschr. f. Physik*, 166:468–476, 1962.

[120] K Jost. Novel design of a 'spherical' electron spectrometer. *Journal of Physics E: Scientific Instruments*, 12(10):1006, 1979.

[121] T Yasue, M Suzuki, K Tsuno, S Goto, Y Arai, and T Koshikawa. Novel multipole Wien filter as three-dimensional spin manipulator. *Review of Scientific Instruments*, 85(4):043701, 2014.

[122] Hiromasa Yasuda, Hiromi Iinuma, Naritoshi Kawamura, Ryo Kitamura, Yasuhiro Kondo, Tsutomu Mibe, Yuga Nakazawa, Masashi Otani, Naohito Saito, Yuki Sue, et al. Development of spin flip analysis for the J-PARC muon g-2/EDM experiment. In *Proceedings of the 3rd J-PARC Symposium (J-PARC2019)*, page 011126, 2021.

[123] John A Nelder and Roger Mead. A simplex method for function minimization. *The Computer Journal*, 7(4):308–313, 1965.

[124] V Dose and G Reusing. Electron-hole pair production and the structure of ultraviolet isochromats. *Applied Physics*, 23(2):131–134, 1980.

[125] P Marchand and L Marmet. Binomial smoothing filter: A way to avoid some pitfalls of least-squares polynomial smoothing. *Review of Scientific Instruments*, 54(8):1034–1041, 1983.

[126] XC Chen, Yu A Litvinov, M Wang, Q Wang, and YH Zhang. Denoising scheme based on singular-value decomposition for one-dimensional spectra and its application in precision storage-ring mass spectrometry. *Physical Review E*, 99(6):063320, 2019.

[127] V Dose, W Altmann, A Goldmann, U Kolac, and J Rogozik. Image-potential states observed by inverse photoemission. *Physical Review Letters*, 52(21):1919, 1984.

[128] DP Woodruff and NV Smith. k-resolved inverse photoemission from Cu(001) and Ni(001). *Physical Review Letters*, 48(4):283, 1982.

[129] Yu Ya Tomashpolsky. Solid surface physics. springer tracts in modern physics. vol. 85 edited by G. Höhler. *Acta Crystallographica Section A: Crystal Physics, Diffraction, Theoretical and General Crystallography*, 35(6):1088–1089, 1979.

[130] DG Dempsey and Leonard Kleinman. Extended-hückel study of the (111), (100), and (110) surfaces of copper. *Physical Review B*, 16(12):5356, 1977.

[131] D Straub and FJ Himpsel. Identification of image-potential surface states on metals. *Physical Review Letters*, 52(21):1922, 1984.

[132] W Von der Linden, M Donath, and V Dose. Unbiased access to exchange splitting of magnetic bands using the maximum entropy method. *Physical Review Letters*, 71(6):899, 1993.

[133] Volker Dose. Ultraviolet bremsstrahlung spectroscopy. *Progress in Surface Science*, 13(3):225–283, 1983.

[134] Thomas J Kreutz, T Greber, Philipp Aebi, and J Osterwalder. Temperature-dependent electronic structure of nickel metal. *Physical Review B*, 58(3):1300, 1998.

[135] G Schönhense. Photoelectron spin-polarization spectroscopy: A new method in adsorbate physics. *Applied Physics A*, 41(1):39–60, 1986.

[136] J Henk, M Hoesch, J Osterwalder, A Ernst, and P Bruno. Spin–orbit coupling in the L-gap surface states of Au(111): spin-resolved photoemission experiments and first-principles calculations. *Journal of Physics: Condensed Matter*, 16(43):7581, 2004.

[137] Katharina T Ritter, Koji Miyamoto, Taichi Okuda, and Markus Donath. Rashba-type splitting of the Au(110) surface state: A combined inverse and direct photoemission study. *Physical Review B*, 104(16):L161101, 2021.

[138] F Forster, G Nicolay, F Reinert, D Ehm, S Schmidt, and S Hüfner. Surface and interface states on adsorbate covered noble metal surfaces. *Surface Science*, 532:160–165, 2003.

[139] F Reinert and G Nicolay. Influence of the herringbone reconstruction on the surface electronic structure of Au(111). *Applied Physics A*, 78(6):817–821, 2004.

[140] D Straub and FJ Himpsel. Spectroscopy of image-potential states with inverse photoemission. *Physical Review B*, 33(4):2256, 1986.

[141] F Meier and D Pescia. Band-structure investigation of gold by spin-polarized photoemission. *Physical Review Letters*, 47(5):374, 1981.

[142] Noboru Takeuchi, Che Ting Chan, and KM Ho. Au(111): A theoretical study of the surface reconstruction and the surface electronic structure. *Physical Review B*, 43(17):13899, 1991.

[143] DP Woodruff, WA Royer, and NV Smith. Empty surface states, image states, and band edge on Au(111). *Physical Review B*, 34(2):764, 1986.

[144] SL Hulbert, PD Johnson, NG Stoffel, WA Royer, and NV Smith. Crystal-induced and image-potential-induced empty surface states on Cu(111) and Cu(001). *Physical Review B*, 31(10):6815, 1985.

[145] A Goldmann, V Dose, and G Borstel. Empty electronic states at the (100), (110), and (111) surfaces of nickel, copper, and silver. *Physical Review B*, 32(4):1971, 1985.

[146] SL Hulbert, PD Johnson, NG Stoffel, and NV Smith. Unoccupied bulk and surface states on Ag(111) studied by inverse photoemission. *Physical Review B*, 32(6):3451, 1985.

[147] J Braun and M Donath. Theory of photoemission from surfaces. *Journal of Physics: Condensed Matter*, 16(26):S2539, 2004.

[148] Peng Zhang, P Richard, T Qian, Y-M Xu, X Dai, and H Ding. A precise method for visualizing dispersive features in image plots. *Review of Scientific Instruments*, 82(4):043712, 2011.

[149] F Forster, S Hüfner, and F Reinert. Rare gases on noble-metal surfaces: an angle-resolved photoemission study with high energy resolution. *The Journal of Physical Chemistry B*, 108(38):14692–14698, 2004.

[150] Riccardo Bertacco and Franco Ciccacci. Oxygen–induced enhancement of the spin-dependent effects in electron spectroscopies of Fe (001). *Physical Review B*, 59(6):4207, 1999.

[151] A Zumbülte, AB Schmidt, and M Donath. Momentum resolution in inverse photoemission. *Review of Scientific Instruments*, 86(1):013908, 2015.

[152] R Matzdorf, A Gerlach, F Theilmann, G Meister, and A Goldmann. New lifetime estimates for d-band holes at noble metal surfaces. *Applied Physics B*, 68(3):393–395, 1999.

[153] SD Kevan. Evidence for a new broadening mechanism in angle-resolved photoemission from Cu(111). *Physical Review Letters*, 50(7):526, 1983.

[154] M Mulazzi, G Rossi, J Braun, J Minár, H Ebert, G Panaccione, I Vobornik, and J Fujii. Understanding intensities of angle-resolved photoemission with circularly polarized radiation from a Cu(111) surface state. *Physical Review B*, 79(16):165421, 2009.

[155] MT Johnson, PJH Bloemen, FJA Den Broeder, and JJ De Vries. Magnetic anisotropy in metallic multilayers. *Reports on Progress in Physics*, 59(11):1409, 1996.

[156] D Oberli, R Burgermeister, S Riesen, W Weber, and HC Siegmann. Total scattering cross section and spin motion of low energy electrons passing through a ferromagnet. *Physical Review Letters*, 81(19):4228, 1998.

[157] JR Cerda, PL De Andres, A Cebollada, R Miranda, E Navas, P Schuster, CM Schneider, and J Kirschner. Epitaxial growth of cobalt films on Cu(100): a crystallographic LEED determination. *Journal of Physics: Condensed Matter*, 5(14):2055, 1993.

[158] JE Ortega, FJ Himpsel, GJ Mankey, and RF Willis. Quantum-well states and magnetic coupling between ferromagnets through a noble-metal layer. *Physical Review B*, 47(3):1540, 1993.

[159] John C Slonczewski. Current-driven excitation of magnetic multilayers. *Journal of Magnetism and Magnetic Materials*, 159(1-2):L1–L7, 1996.

[160] Luc Berger. Emission of spin waves by a magnetic multilayer traversed by a current. *Physical Review B*, 54(13):9353, 1996.

[161] Henry J Snaith. Perovskites: the emergence of a new era for low-cost, high-efficiency solar cells. *The Journal of Physical Chemistry Letters*, 4(21):3623–3630, 2013.

[162] Huanping Zhou, Qi Chen, Gang Li, Song Luo, Tze-bing Song, Hsin-Sheng Duan, Ziruo Hong, Jingbi You, Yongsheng Liu, and Yang Yang. Interface engineering of highly efficient perovskite solar cells. *Science*, 345(6196):542–546, 2014.

[163] Qingfeng Dong, Yanjun Fang, Yuchuan Shao, Padhraic Mulligan, Jie Qiu, Lei Cao, and Jinsong Huang. Electron-hole diffusion lengths>175 μm in solution-grown CH3NH3PbI3 single crystals. *Science*, 347(6225):967–970, 2015.

[164] NREL Transforming Energy. Best research-cell efficiency chart, 2022. https://www.nrel.gov/pv/cell-efficiency.html, last accessed on 2022-05-08.

[165] Claudio Quarti, Edoardo Mosconi, and Filippo De Angelis. Interplay of orientational order and electronic structure in methylammonium lead iodide: implications for solar cell operation. *Chemistry of Materials*, 26(22):6557–6569, 2014.

[166] Shi Liu, Fan Zheng, Nathan Z Koocher, Hiroyuki Takenaka, Fenggong Wang, and Andrew M Rappe. Ferroelectric domain wall induced band gap reduction and charge separation in organometal halide perovskites. *The Journal of Physical Chemistry Letters*, 6(4):693–699, 2015.

[167] Revealing the role of organic cations in hybrid halide perovskite CH3NH3PbI3.

[168] Fenggong Wang, Ilya Grinberg, and Andrew M Rappe. Band gap engineering strategy via polarization rotation in perovskite ferroelectrics. *Applied Physics Letters*, 104(15):152903, 2014.

[169] Tsutomu Miyasaka. Lead halide perovskites in thin film photovoltaics: background and perspectives. *Bulletin of the Chemical Society of Japan*, 91(7):1058–1068, 2018.

[170] Thibaud Etienne, Edoardo Mosconi, and Filippo De Angelis. Dynamical origin of the Rashba effect in organohalide lead perovskites: A key to suppressed carrier recombination in perovskite solar cells? *The Journal of Physical Chemistry Letters*, 7(9):1638–1645, 2016.

[171] Kyle Frohna, Tejas Deshpande, John Harter, Wei Peng, Bradford A Barker, Jeffrey B Neaton, Steven G Louie, Osman M Bakr, David Hsieh, and Marco Bernardi. Inversion symmetry and bulk Rashba effect in methylammonium lead iodide perovskite single crystals. *Nature Communications*, 9(1):1–9, 2018.

[172] Federico Brivio, Jarvist M Frost, Jonathan M Skelton, Adam J Jackson, Oliver J Weber, Mark T Weller, Alejandro R Goni, Aurélien MA Leguy, Piers RF Barnes, and Aron Walsh. Lattice dynamics and vibrational spectra of the orthorhombic, tetragonal, and cubic phases of methylammonium lead iodide. *Physical Review B*, 92(14):144308, 2015.

[173] Mark T Weller, Oliver J Weber, Paul F Henry, Antonietta M Di Pumpo, and Thomas C Hansen. Complete structure and cation orientation in the perovskite photovoltaic methylammonium lead iodide between 100 and 352 K. *Chemical Communications*, 51(20):4180–4183, 2015.

[174] Valerio D'innocenzo, Giulia Grancini, Marcelo JP Alcocer, Ajay Ram Srimath Kandada, Samuel D Stranks, Michael M Lee, Guglielmo Lanzani, Henry J Snaith, and Annamaria Petrozza. Excitons versus free charges in organo-lead tri-halide perovskites. *Nature Communications*, 5(1):1–6, 2014.

[175] Pooya Azarhoosh, Scott McKechnie, Jarvist M Frost, Aron Walsh, and Mark Van Schilfgaarde. Research update: Relativistic origin of slow electron-hole recombination in hybrid halide perovskite solar cells. *APL Materials*, 4(9):091501, 2016.

[176] Federico Brivio, Keith T Butler, Aron Walsh, and Mark Van Schilfgaarde. Relativistic quasiparticle self-consistent electronic structure of hybrid halide perovskite photovoltaic absorbers. *Physical Review B*, 89(15):155204, 2014.

[177] Gabriel J Man, Cody M Sterling, Chinnathambi Kamal, Konstantin A Simonov, Sebastian Svanström, Joydev Acharya, Fredrik OL Johansson, Erika Giangrisostomi, Ruslan Ovsyannikov, Thomas Huthwelker, et al. Electronic coupling between the unoccupied states of the organic and inorganic sublattices of methylammonium lead iodide: A hybrid organic-inorganic perovskite single crystal. *Physical Review B*, 104(4):L041302, 2021.

[178] Martin Schlipf and Feliciano Giustino. Dynamic Rashba-Dresselhaus effect. *Physical Review Letters*, 127(23):237601, 2021.

[179] Jinpeng Yang, Haruki Sato, Hibiki Orio, Xianjie Liu, Mats Fahlman, Nobuo Ueno, Hiroyuki Yoshida, Takashi Yamada, and Satoshi Kera. Accessing the conduction band dispersion in CH3NH3PbI3 single crystals. *The Journal of Physical Chemistry Letters*, 12(15):3773–3778, 2021.

[180] Akihiro Kojima, Kenjiro Teshima, Yasuo Shirai, and Tsutomu Miyasaka. Organometal halide perovskites as visible-light sensitizers for photovoltaic cells. *Journal of the American Chemical Society*, 131(17):6050–6051, 2009.

[181] Koichi Momma and Fujio Izumi. VESTA 3 for three-dimensional visualization of crystal, volumetric and morphology data. *Journal of Applied Crystallography*, 44(6):1272–1276, 2011.

[182] Jarvist M Frost, Keith T Butler, Federico Brivio, Christopher H Hendon, Mark Van Schilfgaarde, and Aron Walsh. Atomistic origins of high-performance in hybrid halide perovskite solar cells. *Nano Letters*, 14(5):2584–2590, 2014.

[183] Yukihiko Kawamura, Hiroyuki Mashiyama, and Katsuhiko Hasebe. Structural study on cubic-tetragonal transition of CH3NH3PbI3. *Journal of the Physical Society of Japan*, 71(7):1694–1697, 2002.

[184] Min-I Lee, Ana Barragán, Maya N Nair, Vincent L R Jacques, David Le Bolloc'h, Pierre Fertey, Khaoula Jemli, Ferdinand Lédée, Gaëlle Trippé-Allard, Emmanuelle Deleporte, Amina Taleb-Ibrahimi, and Antonio Tejeda. First determination of the valence band dispersion of CH3NH3PbI3 hybrid organic–inorganic perovskite. *Journal of Physics D: Applied Physics*, 50(26):26LT02, 2017.

[185] Roderick E Wasylishen, Osvald Knop, and J Bruce Macdonald. Cation rotation in methylammonium lead halides. *Solid State Communications*, 56(7):581–582, 1985.

[186] Osvald Knop, Roderick E Wasylishen, Mary Anne White, T Stanley Cameron, and Michiel JM Van Oort. Alkylammonium lead halides. Part 2. CH3NH3PbX3 (X=Cl, Br, I) perovskites: cuboctahedral halide cages with isotropic cation reorientation. *Canadian Journal of Chemistry*, 68(3):412–422, 1990.

[187] Ioannis Deretzis and Antonino La Magna. Exploring the orthorhombic–tetragonal phase transition in CH3NH3PbI3: the role of atom kinetics. *Nanoscale*, 9(18):5896–5903, 2017.

[188] Tom Baikie, Yanan Fang, Jeannette M Kadro, Martin Schreyer, Fengxia Wei, Subodh G Mhaisalkar, Michael Graetzel, and Tim J White. Synthesis and crystal chemistry of the hybrid perovskite CH3NH3PbI3 for solid-state sensitised solar cell applications. *Journal of Materials Chemistry A*, 1(18):5628–5641, 2013.

[189] IP Swainson, C Stock, SF Parker, L Van Eijck, M Russina, and JW Taylor. From soft harmonic phonons to fast relaxational dynamics in CH3NH3PbBr3. *Physical Review B*, 92(10):100303, 2015.

[190] Albrecht Poglitsch and Daniel Weber. Dynamic disorder in methylammoniumtrihalogenoplumbates (ii) observed by millimeter-wave spectroscopy. *The Journal of Chemical Physics*, 87(11):6373–6378, 1987.

[191] Tom Baikie, Yanan Fang, Jeannette M Kadro, Martin Schreyer, Fengxia Wei, Subodh G Mhaisalkar, Michael Graetzel, and Tim J White. Synthesis and crystal chemistry of the hybrid perovskite (CH3NH3)PbI3 for solid-state sensitised solar cell applications. *Journal of Materials Chemistry A*, 1(18):5628–5641, 2013.

[192] Constantinos C Stoumpos, Christos D Malliakas, and Mercouri G Kanatzidis. Semiconducting tin and lead iodide perovskites with organic cations: phase transitions, high mobilities, and near-infrared photoluminescent properties. *Inorganic Chemistry*, 52(15):9019–9038, 2013.

[193] Bulk crystal growth of hybrid perovskite material CH3NH3PbI3.

[194] G Sharada, Pratibha Mahale, Bhushan P Kore, Somdutta Mukherjee, Mysore S Pavan, Chandan De, Somnath Ghara, A Sundaresan, Anshu Pandey, TN Guru Row, et al. Is CH3NH3PbI3 polar? *J. Phys. Chem. Lett*, 7:2412–2419, 2016.

[195] Massimo Nespolo. International Tables for Crystallography, Volume A, Space-group symmetry. *Acta Crystallographica Section A Foundations and Advances*, 73(3):274–276, 2017.

[196] Tianyi Wang, Benjamin Daiber, Jarvist M Frost, Sander A Mann, Erik C Garnett, Aron Walsh, and Bruno Ehrler. Indirect to direct bandgap transition in methylammonium lead halide perovskite. *Energy & Environmental Science*, 10(2):509–515, 2017.

[197] Yevgeny Rakita, Omri Bar-Elli, Elena Meirzadeh, Hadar Kaslasi, Yagel Peleg, Gary Hodes, Igor Lubomirsky, Dan Oron, David Ehre, and David Cahen. Tetragonal CH3NH3PbI3 is ferroelectric. *Proceedings of the National Academy of Sciences*, 114(28):E5504–E5512, 2017.

[198] Roderick E Wasylishen, Osvald Knop, and J Bruce Macdonald. Cation rotation in methylammonium lead halides. *Solid State Communications*, 56(7):581–582, 1985.

[199] Jens Als-Nielsen and Des McMorrow. *Elements of modern X-ray physics*. John Wiley & Sons, 2011.

[200] Robert Feidenhans. Surface structure determination by X-ray diffraction. *Surface Science Reports*, 10(3):105–188, 1989.

[201] SK Sundaram and Eric Mazur. Inducing and probing non-thermal transitions in semiconductors using femtosecond laser pulses. *Nature Materials*, 1(4):217–224, 2002.

[202] Makhsud I Saidaminov, Ahmed L Abdelhady, Banavoth Murali, Erkki Alarousu, Victor M Burlakov, Wei Peng, Ibrahim Dursun, Lingfei Wang, Yao He, Giacomo Maculan, et al. High-quality bulk hybrid perovskite single crystals within minutes by inverse temperature crystallization. *Nature Communications*, 6(1):1–6, 2015.

[203] Sanjun Zhang, Gaëtan Lanty, Jean-Sébastien Lauret, Emmanuelle Deleporte, Pierre Audebert, and Laurent Galmiche. Synthesis and optical properties of novel organic–inorganic hybrid nanolayer structure semiconductors. *Acta Materialia*, 57(11):3301–3309, 2009.

[204] I Deretzis, A Alberti, G Pellegrino, E Smecca, F Giannazzo, N Sakai, T Miyasaka, and AJAPL La Magna. Atomistic origins of CH3NH3PbI3 degradation to PbI2 in vacuum. *Applied Physics Letters*, 106(13):131904, 2015.

[205] J-P Pollina Lebasque. Low-alpha operation for the SOLEIL storage ring. 2012.

[206] Duyen H Cao, Peijun Guo, Arun Mannodi-Kanakkithodi, Gary P Wiederrecht, David J Gosztola, Nari Jeon, Richard D Schaller, Maria KY Chan, and Alex BF Martinson. Charge transfer dynamics of phase-segregated halide perovskites: CH3NH3PbCI3 and CH3NH3PbI3 or (C4H9NH3) 2 (CH3NH3) n- 1Pb n I3 n+1 mixtures. *ACS applied materials & interfaces*, 11(9):9583–9593, 2019.

[207] Guiming Peng, Xueqing Xu, and Gang Xu. Hybrid organic-inorganic perovskites open a new era for low-cost, high efficiency solar cells. *Journal of Nanomaterials*, 2015:2, 2015.

[208] Zhesheng Chen, Min-i Lee, Zailan Zhang, Hiba Diab, Damien Garrot, Ferdinand Lédée, Pierre Fertey, Evangelos Papalazarou, Marino Marsi, Carlito Ponseca, et al. Time-resolved photoemission spectroscopy of electronic cooling and localization in CH3NH3PbI3 crystals. *Physical Review Materials*, 1(4):045402, 2017.

[209] Guichuan Xing, Nripan Mathews, Shuangyong Sun, Swee Sien Lim, Yeng Ming Lam, Michael Grätzel, Subodh Mhaisalkar, and Tze Chien Sum. Long-range balanced electron- and hole-transport lengths in organic-inorganic CH3NH3PbI3. *Science*, 342(6156):344–347, 2013.

[210] Edoardo Mosconi, Anna Amat, Md K Nazeeruddin, Michael Grätzel, and Filippo De Angelis. First-principles modeling of mixed halide organometal perovskites for photovoltaic applications. *The Journal of Physical Chemistry C*, 117(27):13902–13913, 2013.

[211] Federico Brivio, Alison B Walker, and Aron Walsh. Structural and electronic properties of hybrid perovskites for high-efficiency thin-film photovoltaics from first-principles. *Apl Materials*, 1(4):042111, 2013.

[212] Aurelien Leguy, Jarvist Moore Frost, Andrew P McMahon, Victoria Garcia Sakai, W Kockelmann, ChunHung Law, Xiaoe Li, Fabrizia Foglia, Aron Walsh, Brian C O'regan, et al. The dynamics of methylammonium ions in hybrid organic–inorganic perovskite solar cells. *Nature Communications*, 6(1):1–11, 2015.

[213] Vinod Kumarappan, Simon S Viftrup, Lotte Holmegaard, Christer Z Bisgaard, and Henrik Stapelfeldt. Aligning molecules with long or short laser pulses. *Physica Scripta*, 76(3):C63, 2007.

[214] Pekka Pyykko. Relativistic effects in structural chemistry. *Chemical Reviews*, 88(3):563–594, 1988.

[215] Jinglong Huang, Yinhui Peng, Jiance Jin, Maxim S Molokeev, Xiaobao Yang, and Zhiguo Xia. Unveiling white light emission of a one-dimensional Cu (i)-based organometallic

halide toward single-phase light-emitting diode applications. *The Journal of Physical Chemistry Letters*, 12:12345–12351, 2021.

[216] Shin-ichi Machida, Yasuo Nakayama, Steffen Duhm, Qian Xin, Akihiro Funakoshi, Naoki Ogawa, Satoshi Kera, Nobuo Ueno, and Hisao Ishii. Highest-occupied-molecular-orbital band dispersion of rubrene single crystals as observed by angle-resolved ultraviolet photoelectron spectroscopy. *Physical Review Letters*, 104(15):156401, 2010.

[217] Feng-Shuo Zu, Patrick Amsalem, Ingo Salzmann, Rong-Bin Wang, Maryline Ralaiarisoa, Stefan Kowarik, Steffen Duhm, and Norbert Koch. Impact of white light illumination on the electronic and chemical structures of mixed halide and single crystal perovskites. *Advanced Optical Materials*, 5(9):1700139, 2017.

[218] Kiyohiko Tsutsumi, Hiroyuki Yoshida, and Naoki Sato. Unoccupied electronic states in a hexatriacontane thin film studied by inverse photoemission spectroscopy. *Chemical Physics Letters*, 361(5-6):367–373, 2002.

[219] Jin Yang, Haruki Sato, Hibiki Orio, Xianjie Liu, Mats Fahlman, Nobuo Ueno, Hiroyuki Yoshida, Takashi Yamada, and Satoshi Kera. Accessing the conduction band dispersion in CH3NH3PbI3 single crystals. *arXiv preprint arXiv:2012.13056*, 2020.

[220] Jin-Peng Yang, Matthias Meissner, Takuma Yamaguchi, Xiu-Yun Zhang, Takahiro Ueba, Li-Wen Cheng, Shinichiro Ideta, Kiyohisa Tanaka, Xiang-Hua Zeng, Nobuo Ueno, et al. Band dispersion and hole effective mass of methylammonium lead iodide perovskite. *Solar RRL*, 2(10):1800132, 2018.

[221] Fengshuo Zu, Patrick Amsalem, David A Egger, Rongbin Wang, Christian M Wolff, Honghua Fang, Maria Antonietta Loi, Dieter Neher, Leeor Kronik, Steffen Duhm, et al. Constructing the electronic structure of CH3NH3PbI3 and CH3NH3PbBr3 perovskite thin films from single-crystal band structure measurements. *The Journal of Physical Chemistry Letters*, 10(3):601–609, 2019.

[222] Jakub Jagielski, Sudhir Kumar, Wen-Yueh Yu, and Chih-Jen Shih. Layer-controlled two-dimensional perovskites: synthesis and optoelectronics. *Journal of Materials Chemistry C*, 5(23):5610–5627, 2017.

[223] Xiangxin Tian, Yongzhuan Zhang, Rongkun Zheng, Di Wei, and Jingquan Liu. Two-dimensional organic–inorganic hybrid ruddlesden–popper perovskite materials: preparation, enhanced stability, and applications in photodetection. *Sustainable Energy & Fuels*, 4(5):2087–2113, 2020.

[224] Lakshminarayana Polavarapu, Bert Nickel, Jochen Feldmann, and Alexander S Urban. Advances in quantum-confined perovskite nanocrystals for optoelectronics. *Advanced Energy Materials*, 7(16):1700267, 2017.

[225] Changyong Lan, Ziyao Zhou, Renjie Wei, and Johnny C Ho. Two-dimensional perovskite materials: from synthesis to energy-related applications. *Materials today energy*, 11:61–82, 2019.

[226] Zhiyong Y Zhu, Yingchun C Cheng, and Udo Schwingenschlögl. Giant spin-orbit-induced spin splitting in two-dimensional transition-metal dichalcogenide semiconductors. *Physical Review B*, 84(15):153402, 2011.

[227] LD Casto, AJ Clune, MO Yokosuk, JL Musfeldt, TJ Williams, HL Zhuang, M-W Lin, K Xiao, RG Hennig, BC Sales, et al. Strong spin-lattice coupling in CrSiTe3. *APL materials*, 3(4):041515, 2015.

[228] YF Li, W Wang, W Guo, CY Gu, HY Sun, L He, J Zhou, ZB Gu, YF Nie, and XQ Pan. Electronic structure of ferromagnetic semiconductor CrGeTe3 by angle-resolved photoemission spectroscopy. *Physical Review B*, 98(12):125127, 2018.

[229] Jiaxin Zhang, Xiaochan Cai, Wei Xia, Aiji Liang, Junwei Huang, Chengwei Wang, Lexian Yang, Hongtao Yuan, Yulin Chen, Shilei Zhang, et al. Unveiling electronic correlation and the ferromagnetic superexchange mechanism in the van der waals crystal CrSiTe3. *Physical Review Letters*, 123(4):047203, 2019.

[230] A Milosavljević, A Šolajić, J Pešić, Yu Liu, Cedomir Petrovic, N Lazarević, ZV Popović, et al. Evidence of spin-phonon coupling in CrSiTe3. *Physical Review B*, 98(10):104306, 2018.

[231] GT Lin, HL Zhuang, X Luo, BJ Liu, FC Chen, J Yan, Y Sun, J Zhou, WJ Lu, P Tong, et al. Tricritical behavior of the two-dimensional intrinsically ferromagnetic semiconductor CrGeTe3. *Physical Review B*, 95(24):245212, 2017.

[232] Walter Kohn and Lu Jeu Sham. Self-consistent equations including exchange and correlation effects. *Physical Review*, 140(4A):A1133, 1965.

[233] Georg Kresse and Jürgen Furthmüller. Efficiency of ab-initio total energy calculations for metals and semiconductors using a plane-wave basis set. *Computational Materials Science*, 6(1):15–50, 1996.

[234] Georg Kresse and Jürgen Furthmüller. Efficient iterative schemes for ab initio total-energy calculations using a plane-wave basis set. *Physical Review B*, 54(16):11169, 1996.

[235] John P Perdew, Kieron Burke, and Matthias Ernzerhof. Generalized gradient approximation made simple. *Physical Review Letters*, 77(18):3865, 1996.

[236] Hendrik J Monkhorst and James D Pack. Special points for brillouin-zone integrations. *Physical Review B*, 13(12):5188, 1976.

[237] James D Pack and Hendrik J Monkhorst. " special points for brillouin-zone integrations"—a reply. *Physical Review B*, 16(4):1748, 1977.

[238] Michael M Lee, Joël Teuscher, Tsutomu Miyasaka, Takurou N Murakami, and Henry J Snaith. Efficient hybrid solar cells based on meso-superstructured organometal halide perovskites. *Science*, 338(6107):643–647, 2012.